UNIVERSITAT ROVIRA I VIRGILI

LONG-RANGE BACKSCATTERING COMMUNICATIONS FOR NEXT GENERATION IOT APPLICATIONS

Marc Lázaro Martí

ADVERTIMENT. L'accés als continguts d'aquesta tesi doctoral i la seva utilització ha de respectar els drets de la persona autora. Pot ser utilitzada per a consulta o estudi personal, així com en activitats o materials d'investigació i docència en els termes establerts a l'art. 32 del Text Refós de la Llei de Propietat Intel·lectual (RDL 1/1996). Per altres utilitzacions es requereix l'autorització prèvia i expressa de la persona autora. En qualsevol cas, en la utilització dels seus continguts caldrà indicar de forma clara el nom i cognoms de la persona autora i el títol de la tesi doctoral. No s'autoritza la seva reproducció o altres formes d'explotació efectuades amb finalitats de lucre ni la seva comunicació pública des d'un lloc aliè al servei TDX. Tampoc s'autoritza la presentació del seu contingut en una finestra o marc aliè a TDX (framing). Aquesta reserva de drets afecta tant als continguts de la tesi com als seus resums i índexs.

ADVERTENCIA. El acceso a los contenidos de esta tesis doctoral y su utilización debe respetar los derechos de la persona autora. Puede ser utilizada para consulta o estudio personal, así como en actividades o materiales de investigación y docencia en los términos establecidos en el art. 32 del Texto Refundido de la Ley de Propiedad Intelectual (RDL 1/1996). Para otros usos se requiere la autorización previa y expresa de la persona autora. En cualquier caso, en la utilización de sus contenidos se deberá indicar de forma clara el nombre y apellidos de la persona autora y el título de la tesis doctoral. No se autoriza su reproducción u otras formas de explotación efectuadas con fines lucrativos ni su comunicación pública desde un sitio ajeno al servicio TDR. Tampoco se autoriza la presentación de su contenido en una ventana o marco ajeno a TDR (framing). Esta reserva de derechos afecta tanto al contenido de la tesis como a sus resúmenes e índices.

WARNING. Access to the contents of this doctoral thesis and its use must respect the rights of the author. It can be used for reference or private study, as well as research and learning activities or materials in the terms established by the 32nd article of the Spanish Consolidated Copyright Act (RDL 1/1996). Express and previous authorization of the author is required for any other uses. In any case, when using its content, full name of the author and title of the thesis must be clearly indicated. Reproduction or other forms of for profit use or public communication from outside TDX service is not allowed. Presentation of its content in a window or frame external to TDX (framing) is not authorized either. These rights affect both the content of the thesis and its abstracts and indexes.

UNIVERSITAT ROVIRA I VIRGILI
LONG-RANGE BACKSCATTERING COMMUNICATIONS FOR NEXT GENERATION IOT APPLICATIONS
Marc Lázaro Martí

LONG-RANGE BACKSCATTERING COMMUNICATIONS FOR NEXT-GENERATION IOT APPLICATIONS

Marc Lázaro Martí

TESI DOCTORAL
2023

Long-Range backscattering communications for next-generation IoT applications

by Marc Lázaro Martí

Department of Electronic, Electric and Automatic Control Engineering
Director Dr. Antonio Lázaro
Director Dr. David Girbau

2023

UNIVERSITAT
ROVIRA i VIRGILI

Escola Tècnica Superior d'Enginyeria
Departament d'Enginyeria Electrònica, Elèctrica i Automàtica

Avda. Dels Països Catalans, 26
Campus Sescelades
43007 Tarragona
Tel. (+0034) 977 55 9610
Fax (+0034) 977 55 9605

We STATE that the present study, entitled "Long-Range backscattering communications for next-generation IoT applications", presented by Marc Lázaro Martí for the award of the degree of Doctor, has been carried out under our supervision at the Department of Electronic, Electric and Automatic Control Engineering of this university and that it fulfills all the requirements to be eligible for the International Doctorate Award.

Tarragona, 19th june 2023

Doctoral Thesis Supervisor/s

ANTONIO RAMON LAZARO GUILLEN - DNI 78080752F
Firmado digitalmente por ANTONIO RAMON LAZARO GUILLEN - DNI 78080752F
Fecha: 2023.06.16 14:54:06 +02'00'

Antonio Lázaro Guillén

David Girbau Sala - DNI 77309996G (TCAT)
Firmado digitalmente por David Girbau Sala - DNI 77309996G (TCAT)
Nombre de reconocimiento (DN): c=ES, o=Universitat Rovira i Virgili, 2.5.4.97=VATES-Q9350003A, ou=Empleat públic de nivell mig, sn=Girbau Sala - DNI 77309996G, givenName=David, serialNumber=IDCES-77309996G, cn=David Girbau Sala - DNI 77309996G (TCAT)
Fecha: 2023.06.16 23:29:51 +02'00'

David Girbau Sala

Acknowledgements

I would like to express my most sincere gratitude to my supervisors, Dr. Antonio Ramon Lázaro and Dr. David Girbau, as well as to Dr. Ramon Villarino, for their invaluable guidance and support throughout my PhD journey. I am deeply grateful for providing me with the opportunity to pursue my doctoral studies at the university where I studied, in the city where I grew up, and within the field I am truly passionate about. The knowledge and insights I have gained from them are truly priceless and have contributed significantly to my academic development.

To my loving parents, Angels and Luis, thank you for your unwavering support, love, encouragement, and sacrifices. To my dear siblings, Clara, Francesc, Miriam, and Cristina, thank you for always being by my side. To my love, Melanie, thank you for your support, patience, and incredible belief in me. I can only say that I love you all.

Last but not least, thanks to my friends and colleagues from the university, especially Dr. Marti Boada, Xavi, Ramon, Max, and David, for sharing countless good moments, engaging in insightful conversations, and for all the laughter and good times we have had and that I hope to continue experiencing together. Thank you all.

This work was funded by:

- The Spanish Government under Project RTI2018-096019-B-C31 and grant PRE2019-089028.
- The Spanish Government grant PID2021-122399OB-I00 of the Ministry of Science and Innovation.
- The EU's European Regional Development Fund (ERDF)

Table of Content

UNIVERSITAT ROVIRA I VIRGILI
LONG-RANGE BACKSCATTERING COMMUNICATIONS FOR NEXT GENERATION IOT APPLICATIONS
Marc Lázaro Martí

UNIVERSITAT ROVIRA I VIRGILI
LONG-RANGE BACKSCATTERING COMMUNICATIONS FOR NEXT GENERATION IOT APPLICATIONS
Marc Lázaro Martí

List of Figures

List of Tables

Nomenclature

Acronyms

ABS	anti-lock braking systems
ADAS	Advanced Driver Assistance Systems
AoA	Angle-of-Arrival
ARDS	Acute Respiratory Distress Syndrome
ASK	Amplitude Shift Keying
BackCom	Backscattering Communication
BBCS	Bistatic backscatter communication system
BLE	Bluetooth Low Energy
CSI	channel state information
DHF	Dual Heat Flux
DSB	Double Sideband
FMCW	Frequency-Modulated Continuous Wave
FSK	Frequency Shift Keying
GPR	Ground Penetrating Radars
IC	Integrated Circuit
IMD	Implanted Medical Devices
IoT	Internet of Things
$IR-UWB$	Impulse Radio Ultra Wideband
ISM	Industrial Scientific and Medical
LoS	Line of Sigth
MBCS	Monostatic backscatter communication system
MICS	Medical Implant Communication Service
MTI	Moving Target Indication
NFC	Near Field Communication
NTC	Negative Temperature Coefficient

PM	Particulate Matter
PPG	PhotoPlethysmoGraphy
PSK	Phase Shift Keying
RCS	Radar Cross Section
RCS	Radar Cross-Section
RF	Radio Frequency
$RFID$	Radio Frequency Identification
$RSSI$	Received Signal Strength Indicator
SAR	Synthetic Aperture Radar
SNR	Signal-to-noise ratio
$TDoA$	Time difference of Arrival
$TENG$	Triboelectric Nanogenerator
ToA	Time of Arrival
$WISP$	Wireless Identification and Sensing Platform

Chapter 1

Introduction

1.1 Motivation

Envision a world where countless devices are connected to the Internet, constantly collecting, exchanging, and processing data; not only conventional electronic devices like computers, tablets, or smartphones, but also everyday objects like clothes, furniture, keys, or even your wallet. This is the reality of the Internet of Things (IoT), a rapidly growing network of interconnected devices that is reshaping the way we live, work, and interact with technology. From wearables that track our fitness to smart homes that automatically adjust the lighting and temperature, applications are unbounded. With billions of devices already connected and waiting for billions more in the coming years, the IoT is transforming industries ranging from healthcare to manufacturing, and promises to revolutionize our daily lives in ways we cannot yet imagine [1.1][1.2].

At first glance, connecting mundane objects to the Internet may seem implausible to some, why add unnecessary complexity to everyday things? Collecting the temperature of clothes or detecting the humidity of a plant substrate can be interesting, but is it worth it? Does it really simplify our lives? It is certainly a controversial matter, and answers are always subjective. IoT nodes should always have a social-economic equilibrium, considering resources, costs, social benefits, or security among others, and it is in this balance that the answer lies. A major critique of the IoT field arises from the use of devices that do not respect this balance, since they are usually designed from a flawed perspective, such as a marketing-driven approach, which unfortunately can lead to the

UNIVERSITAT ROVIRA I VIRGILI
LONG-RANGE BACKSCATTERING COMMUNICATIONS FOR NEXT GENERATION IOT APPLICATIONS
Marc Lázaro Martí

creation of dysfunctional devices. However, it should be emphasized that the goal of the IoT is nothing other than improving the well-being of individuals, and never the opposite.

Sir Francis Bacon wrote in his work Meditationes Sacrae -ipsa scientia potestas est-, knowledge itself is power [1.3]. Paraphrasing it in the 21st century, we could say that data is power, and in fact, IoT nodes are providing exceedingly large amounts of data, bringing insightful knowledge in many fields, which would be impossible to obtain through other methods.

The primary milestone for the next generation of IoT devices is to become imperceptible to users, requiring no battery replacements or periodic maintenance. IoT nodes must work seamlessly in the background, freeing users from having to be conscious of them, similar to how anti-lock braking systems (ABS) works in cars or how solar lights turn on and off automatically in smart cities. However, there are several challenges that need to be addressed for the IoT to reach its full potential. Here are some of the main challenges [1.4, 1.5, 1.6]:

- Security: One of the biggest challenges for the next generation of IoT will be to ensure the security of devices and data. As more and more devices are connected to the internet, there will be a greater risk of cyber-attacks and data breaches.
- Interoperability: A significant challenge is the lack of standardization between the wide variety of devices and technologies that are part of the IoT ecosystem, and ensuring that they can communicate and work together seamlessly.
- Privacy: The data collected by IoT devices can be highly sensitive and personal. With the growing amount of data being collected and analyzed by IoT devices, privacy concerns will become more critical than ever. Users will need to have control over their data and be confident that it is being handled securely and ethically.
- Scalability: The next generation of IoT will involve billions of devices and systems, which will require a scalable infrastructure and data processing capabilities.
- Reliability: IoT devices must be reliable and usually be capable to operate effectively in harsh conditions such as extended sun exposure or varying weather, without experiencing malfunctions or failures.

UNIVERSITAT ROVIRA I VIRGILI
LONG-RANGE BACKSCATTERING COMMUNICATIONS FOR NEXT GENERATION IOT APPLICATIONS
Marc Lázaro Martí

- Complexity: The IoT ecosystem is highly complex, with many different devices, protocols, and technologies involved. Managing this complexity and ensuring that the IoT is easy to use and deploy is another challenge.
- Energy Efficiency: Many IoT devices are powered by batteries or other limited power sources, and optimizing their power consumption to extend their battery life is a major challenge. Devices will need to be designed to be energy-efficient and powered by sustainable sources.
- Cost: The cost of IoT devices and systems can be a barrier to adoption, especially in developing countries. To overcome this challenge, IoT technology needs to be made more affordable and accessible to everyone.

Great scientific efforts, both in public and private sectors, are underway to tackle each of these challenges. Although many of them are interconnected, each one of these challenges belongs to different fields and deserves its independent research line. For instance, while privacy must be addressed from the ethical-legal field, security must be addressed through engineering with robust communication protocols, and the optimal way to address interoperability is through standardization bodies. Addressing all of them in the same work would be an impractical and arduous task. Furthermore, it is crucial to acknowledge that a comprehensive solution must account for the interplay between hardware and software, as hardware alone cannot achieve its full potential without the support of suitable software measures.

There is currently a wide range of devices and communication protocols designed specifically for IoT (e.g. MQTT, CoAP, XMPP LoRa, ZigBee, NB-IoT, Z-wave, etc). These protocols are intended to handle a large number of nodes ensuring compliance with the aforementioned requirements, while the devices are optimized to consume minimal amounts of energy. Unfortunately, in many cases, some of the requirements can only be met by sacrificing others, such as reducing energy consumption [1.7] [1.8].

Despite continuous efforts to optimize transceiver power consumption, the power consumption of these devices remains orders above what is required to make them unnoticeable to users. Reducing energy demand below one milliampere is not an easy goal and is a crucial requirement to give a boost to the next generation of IoT devices. To reach this milestone, the hardware design must be approached from a completely different perspective. This is where the

UNIVERSITAT ROVIRA I VIRGILI
LONG-RANGE BACKSCATTERING COMMUNICATIONS FOR NEXT GENERATION IOT APPLICATIONS
Marc Lázaro Martí

work presented in this dissertation focuses.

1.2 Rationale of the research

Consumption, range, and data rate are the three immovable pillars that govern wireless communications. Improving the performance of any one of them always involves, at least, sacrificing one of the other two. This trade-off must always be tailored to meet the requirements of each specific application.

The use of optimized radio frequency (RF) modulations, adjusting active operation cycles, or biasing the circuit below the standard voltage are just some of the techniques used to deal with the aforementioned trade-off, improving one of the three properties while minimizing the negative effect on the others. Even so, the margin of action is limited, especially with commercial hardware.

In order to provide a clearer visual representation of the problem, Figure 1.1 depicts the coverage of the main commercially available wireless technologies as a function of their power consumption. Two primary categories can be distinguished based on their power consumption: active and passive. Active transceivers cover the vast majority of technologies, starting from consumption levels of 10 mA and upwards. These consumption levels require the use of batteries in prototypes, increasing their manufacturing and maintenance costs. However, they are the only ones capable of providing long-range wireless communications and high data rates. Passive transceivers, on the other hand, operate in the range of μA, allowing devices to be powered using energy harvesting techniques or using alternative energy storage systems such as supercapacitors. The most common technology operating under this principle is Radio Frequency Identification (RFID) [1.9].

At first glance, we can observe that there is currently no commercial technology available to achieve wireless communications over tens or hundreds of meters while maintaining power consumption in the range of μA. This capability is an indispensable requirement for a subset of the next generation of IoT devices.

The work of this thesis focuses on the study of backscattering communications based on LoRa wireless technology for low-power, long-range links as an alternative to the recently exposed challenge. The backscattering communication is the basis of RFID and consists of reflecting RF waves instead of directly

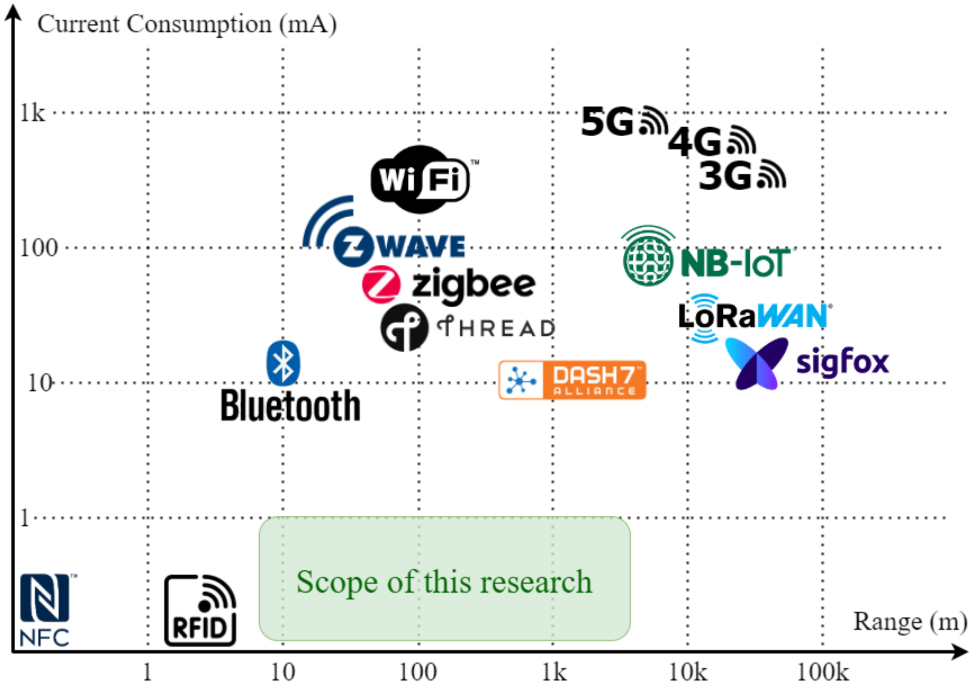

Figure 1.1: Current consumption as a function of read-range for different wireless technologies.

radiating them, reducing the consumption of the device by several orders.

RFID and backscattering communications have been limited to a few meters for several decades. However, with the advent of new, more complex modulations, such as spread spectrum, it has become possible to decouple backscattering communications from conventional RFID, which have historically relied on dedicated readers. This development has opened up a wide range of possibilities and led to very promising results. In the following chapter, backscattering communications will be thoroughly discussed.

The objective of this work is to explore the use of backscatter communications based on LoRa wireless technology as a solution to the aforementioned gap within current available wireless technologies, providing a long-range low-power new wireless technology. This thesis aims to conduct a comprehensive review of the most significant contributions in the design of low-power, long-range backscattering systems. Subsequently, it seeks to make its own contribution in this field by designing a long-range low-power tag and validating its viability in real-world applications. Therefore the main objectives are:

UNIVERSITAT ROVIRA I VIRGILI
LONG-RANGE BACKSCATTERING COMMUNICATIONS FOR NEXT GENERATION IOT APPLICATIONS
Marc Lázaro Martí

1. Introduce the basic principles behind backscatter communications and LoRa wireless technology, highlighting the advantages of LoRa over other modulations such as WiFi, Bluetooth, or ZigBee.
2. Design and implement the tag front-end to maximize the backscattered power and, consequently, the range, but always maintaining the low power consumption constraint.
3. Propose the modulation scheme for the tag and a protocol for establishing the uplink communication, leveraging the key features of LoRa.
4. Evaluate the performance of the proposed tag in diverse applications within the medical, internet of things, and localization fields, thus validating its viability for future commercial applications.

1.3 Structure of the dissertation

After a brief introduction to IoT, where the main challenges in this field have been exposed, and the scope and objectives of this work have been focused, the structure of the dissertation can be introduced, as well as the topics that will be addressed in each chapter. The document is organized as follows:

- Chapter 2 begins with a historical introduction about the discovering and evolution of the backscattering technique, followed by a general review of its most important application fields: radar and RFID. Subsequently, a comprehensive review of the most relevant contributions to the design of bistatic backscatter communication systems is presented, covering both dedicated and ambient configurations.
- Chapter 3 focuses on conducting a theoretical review of the basic principles on the backscattering of electromagnetic fields. To achieve this, the fundamental theory of radar and antennas is reviewed. Furthermore, the basic principles of RFID are also reviewed to mathematically justify the effect of load switching on the antenna termination.
- Chapter 4 addresses all the work carried out regarding the design and implementation of the backscattering tag. In this chapter, various topologies for the front-end design of the tag are discussed, along with two different modulations and communication schemes based on LoRa backscattering

for transmitting the information from the tag. Furthermore, an introduction to LoRa modulation is made to expose the advantages and reasons for its use compared to other modulations. The following chapters present three different applications based on the LoRa backscattering technique described here.

- Chapter 5 studies the application of the backscattering technique in the field of localization. The proposed solution consists in a low-resolution localization system that leverages the low-power consumption of the backscattering tag and the high range provided by LoRa-based backscattering systems. System overview, proof of concept, and comparison over other localization systems are provided.
- Chapter 6 proposes the design of an implanted device using the backscattering technique to establish wireless communication. This chapter focuses on studying the feasibility of using LoRa backscattering communications in high attenuation media, which is the case of the body.
- Chapter 7 presents the design of a smart mask that takes advantage of the low power of LoRa backscattering to implement the wireless communication. The mask integrates a dual-heat sensor capable of accurately measuring body temperature. Additionally, a simple localization system is proposed to determine whether the user wearing the smart mask has entered or exited a building.
- Chapter 8 presents the final conclusions of the thesis.

1.4 List of Contributions

Peer-Reviewed Journal Articles

Feasibility of backscatter communication using LoRAWAN signals for deep implanted devices and wearable applications
M. Lazaro, A. Lazaro and R. Villarino
Sensors, 2020 (vol.20, no.21, p.6342)
DOI: https://doi.org/10.3390/s20216342

Room-level localization system based on LoRa backscatters

UNIVERSITAT ROVIRA I VIRGILI
LONG-RANGE BACKSCATTERING COMMUNICATIONS FOR NEXT GENERATION IOT APPLICATIONS
Marc Lázaro Martí

A. Lazaro, M. Lazaro and R. Villarino
IEEE Access, 2021 (vol.9, p.16004-16018)
DOI: 10.1109/ACCESS.2021.3053144

Smart Face Mask with an Integrated Heat Flux Sensor for Fast and Remote People's Healthcare Monitoring
M. Lazaro, A. Lazaro, R. Villarino and D. Girbau
Sensors, 2021 (vol.21, no.22, p.7472)
DOI: https://doi.org/10.3390/s21227472

Long-Range Wireless System for U-Value Assessment Using a Low-Cost Heat Flux Sensor
M. Lazaro, A. Lazaro, B. González, R. Villarino and D. Girbau
Sensors, 2022 (vol.22, no.19, p.7259)
DOI: https://doi.org/10.3390/s22197259

Peer-Reviewed International Conferences

Smart mask for temperature monitoring with LoRa backscattering communication
M. Lazaro, A. Lazaro, R. Villarino and D. Girbau
2021 6th International Conference on Smart and Sustainable Technologies (SpliTech), Bol and Split, Croatia
IEEE, 2021 (p.1-4)
DOI: 10.23919/SpliTech52315.2021.9566327

Long-Range LoRaWan backscatter based sensors for medical and wearable applications
M. Lazaro, A. Lazaro and R. Villarino
2021 51st European Microwave Conference (EuMC), London, United Kingdom
IEEE, 2022 (p.777-780)
DOI: 10.23919/EuMC50147.2022.9784387

Backscatter Modulation based on Chirp Spread Spectrum (CSS) with enhanced processing gain
M. Lazaro, A. Lazaro, R. Villarino and D. Girbau
2022 3rd URSI Atlantic and Asia Pacific Radio Science Meeting (AT-AP-RASC)

Session Efficient & Green Communications
Gran Canaria, Spain, 29 May – 3 June

Double-gain backscatter modulation based on chirp spread spectrum signals
M. Lazaro, A. Lazaro, R. Villarino and D. Girbau
2022 IEEE 12th International Conference on RFID Technology and Applications (RFID-TA), Cagliari, Italy
IEEE, 2022 (p.63-66)
DOI: 10.1109/RFID-TA54958.2022.9924129

Tag de retrodispersion basado en un amplificador de reflexión con control activo
M. Lazaro, A. Lazaro, R. Villarino and D. Girbau
2023 URSI, XXXVIII Simposio Nacional de la Unión Científica Internacional de Radio, Caceres, Spain
(Accepted) 13th - 15th of September, 2023

Backscatter Tag Based on an Actively-Controlled Reflection Amplifier
M. Lazaro, A. Lazaro, R. Villarino and D. Girbau
2023 26th European Microwave Week (EuMW), Berlin, Germany
(Accepted) 17th - 22th of September, 2023

Comparative Analysis of Two Reflection Amplifier Topologies for Low Power Backscattering Tag Design
M. Lazaro, A. Lazaro, R. Villarino and D. Girbau
2023 20th SBMO/IEEE MTT-S International Microwave and Optoelectronics Conference (IMOC 2023), Barcelona, Spain
(Accepted) 5th - 9th of November, 2023

Co-author collaborations

Seat-occupancy detection system and breathing rate monitoring based

UNIVERSITAT ROVIRA I VIRGILI
LONG-RANGE BACKSCATTERING COMMUNICATIONS FOR NEXT GENERATION IOT APPLICATIONS
Marc Lázaro Martí

on a low-cost mm-Wave radar at 60 GHz
A. Lazaro, M. Lazaro, R. Villarino, and D. Girbau
IEEE Access, 2021 (vol.9, p.115403-115414)
DOI: https://doi.org/10.1109/ACCESS.2021.3105390

New radar micro-Doppler tag for road safety based on the signature of rotating backscatters
A. Lazaro, M. Lazaro, R. Villarino P. de paco
IEEE Sensors Journal, 2020 (vol.21, p.8604-8612)
DOI: https://doi.org/10.1109/JSEN.2020.3048081

Car2Car Communication Using a Modulated Backscatter and Automotive FMCW Radar
A. Lazaro, M. Lazaro, R. Villarino, P. de paco, and D. Girbau
Sensors, 2021 (vol.21, no.11, p.3656)
DOI: https://doi.org/10.3390/s21113656

Spoofing Attacks on FMCW Radars with Low-Cost Backscatter Tags
A. Lazaro, A. Porcel, M. Lazaro, R. Villarino, and D. Girbau
Sensors, 2022 (vol.22, no.6, p.2145)
DOI: https://doi.org/10.3390/s22062145

Smart Spread Spectrum Modulated Tags for Detection of Vulnerable Road Users with Automotive Radar
A. Lazaro, M. Lazaro, R. Villarino, and D. Girbau
Sensors, 2023 (vol.23, no.5, p.2730)
DOI: https://doi.org/10.3390/s23052730

Battery-Less NFC Potentiostat for Electrochemical Point-of-Care Sensors Based on COTS Components
A. Lazaro, R. Villarino, M. Lazaro, N. Canelles, B. Prieto-Simon, D. Girbau
Sensors, 2022 (vol.22, no.19, p.7213)
DOI: https://doi.org/10.3390/s22197213

UNIVERSITAT ROVIRA I VIRGILI
LONG-RANGE BACKSCATTERING COMMUNICATIONS FOR NEXT GENERATION IOT APPLICATIONS
Marc Lázaro Martí

1.5 Bibliography

[1.1] Karim Yaici. IoT forecast: connectivity management platforms 2019–2028. *"IoT Platforms and Technology,"*, 2020.

[1.2] Shadi Al-Sarawi, Mohammed Anbar, Rosni Abdullah, and Ahmad B Al Hawari. Internet of things market analysis forecasts, 2020–2030. In *2020 Fourth World Conference on smart trends in systems, security and sustainability (WorldS4)*, pages 449–453. IEEE, 2020.

[1.3] Francis Bacon. *Meditationes sacrae.* Excusum impensis Humfredi Hooper., 1859.

[1.4] Alireza Souri, Aseel Hussien, Mahdi Hoseyninezhad, and Monire Norouzi. A systematic review of IoT communication strategies for an efficient smart environment. *Transactions on Emerging Telecommunications Technologies*, 33(3):e3736, 2022.

[1.5] Farshad Firouzi, Bahar Farahani, Markus Weinberger, Gabriel DePace, and Fereidoon Shams Aliee. Iot fundamentals: Definitions, architectures, challenges, and promises. *Intelligent Internet of Things: From Device to Fog and Cloud*, pages 3–50, 2020.

[1.6] Saurabh Bagchi, Tarek F Abdelzaher, Ramesh Govindan, Prashant Shenoy, Akanksha Atrey, Pradipta Ghosh, and Ran Xu. New frontiers in iot: Networking, systems, reliability, and security challenges. *IEEE Internet of Things Journal*, 7(12):11330–11346, 2020.

[1.7] A Vinitha, MSS Rukmini, et al. Secure and energy aware multi-hop routing protocol in WSN using Taylor-based hybrid optimization algorithm. *Journal of King Saud University-Computer and Information Sciences*, 34(5):1857–1868, 2022.

[1.8] Hassan El Alami and Abdellah Najid. Optimization of energy efficiency in wireless sensor networks and internet of things: a review of related works. *Nature-Inspired Computing Applications in Advanced Communication Networks*, pages 89–127, 2020.

[1.9] Syed A Ahson and Mohammad Ilyas. *RFID handbook: applications, technology, security, and privacy.* CRC press, 2017.

Chapter 2

Background of backscatter communication

2.1 Discovery and evolution

Backscattering communications have a long and interesting history that dates back to the early days of radar in the 19th century. By then, James C. Maxwell had already published his work "A Dynamical Theory of the Electromagnetic Field" [2.1], establishing the theoretical foundations of electromagnetic waves: Maxwell's equations. Maxwell's work was the culmination of a set of evidences presented by scientists such as Hans Christian Orsted, André-Marie Ampère, and Michael Faraday during the 18th century that suggested a link between electricity and magnetism. Faraday showed that electricity could influence the behavior of a magnet and vice versa, planting the seed for Maxwell's work. The scientific community had been skeptical for more than a decade about the idea of Maxwell's fields until his theory was proven in 1888 by Heinrich R. Hertz [2.2]. By the end of the 18th and early 19th centuries, wireless communications were becoming a reality thanks to the work of Hertz himself, Aleksander Popov, Nikola Tesla, and Guglielmo Marconi with the creation of the first Morse code transceivers. In the first decade of the century, the work of Ernst F.W. Alexanderson and Reginals Fessenden made the first radio broadcast[2.3] and amplitude modulation possible. At the dawn of World War I, wireless communications were still in the beginning stage and the main method of communication was wired. However, after the incessant destruction of communication

UNIVERSITAT ROVIRA I VIRGILI
LONG-RANGE BACKSCATTERING COMMUNICATIONS FOR NEXT GENERATION IOT APPLICATIONS
Marc Lázaro Martí

lines, they soon realized the great advantage of wireless communications, and the 4 years of conflict were vital for the improvement of radio communications. The invention of the vacuum tube in 1904 by physicist John Ambrose Fleming [2.4] and its subsequent industrial production in 1916 allowed radio transceivers to be miniaturized and integrated into planes, cars, and boats. By 1918, with the end of the war, two-way radio communications and radio broadcasting were already a reality.

After the war, the study of electromagnetic fields was booming, and another major breakthrough was on the horizon: radio detection and ranging (radar). Years earlier, while attempting to prove Maxwell's theoretical work, Hertz discovered that radio waves were affected by metal objects and experimented with reflectors to observe this effect. The reflection of radio waves is known as backscattering, and it was the foundation for subsequently developing radar. Later, in 1904, Christian Hülsmeyer delved into Hertz's observations, determining that reflected radio waves could be used to detect distant metal objects, and he patented a naval detection system. The system, a predecessor to radar, did not attract much attention at the time. In 1917, Nikola Tesla established the theoretical principles of modern radar. In the 1930s, the pre-war environment in the face of the threat of World War II caused several countries to begin developing radar in parallel. The current radar model was created in 1935 in England by Robert Watson-Watt. However, Germany, the United States, Japan, and the Soviet Union developed their own radars in parallel, primarily for military purposes, such as Freya, Wurzburg, and SCR-268/270. With the outbreak of World War II, radar evolution progressed rapidly, driven by the war. The main problem with radar at that time was that it could not differentiate between enemy and allied targets. To solve this problem, the backscattered radar signals began to be modulated, giving rise to identification friend or foe (IFF) transponders. The race against time to win the war allowed for an increase in operating frequency, surpassing the pre-established barrier in the VHF band and giving rise to the first microwave radars. The main advantages of the frequency increase were the reduction in antenna size and the increase in precision due to narrow beam widths. One of the most important microwave radars was the SCR-584 [2.5]. After the war, although the development of radar slowed down, new advances such as the monopulse tracking radar, phased-array radar, synthetic-aperture radar (SAR), and pulse Doppler radar continued [2.6].

UNIVERSITAT ROVIRA I VIRGILI
LONG-RANGE BACKSCATTERING COMMUNICATIONS FOR NEXT GENERATION IOT APPLICATIONS
Marc Lázaro Martí

In 1945, the Second World War came to an end, marking the start of a new era: radio-frequency identification (RFID). American inventor Leon Theremin created a completely passive listening device to spy on the Soviet Union. Although this device was not an identification tag but an audio modulation device, it is considered the predecessor of RFID because of its complete passivity, much like RFID tags. Three years later, in 1948, Harry Stockman published his work *"Communication by Means of Reflected Power"* [2.7], which examined the theoretical basis of communications through backscatter. In his conclusions, Stockman stated the following:

> *-Evidently considerable research and development work has to be done before the remaining basic problems in reflected-power communication are solved, and before the field of useful applications is explored.-*
>
> Harry Stockman

As expected, without any apparent military applications, it took more than two decades for several companies to show interest in RFID. However, the development of RFID was already underway. In 1964, Roger F. Harrington presented a general formulation for electromagnetic backscatter in his work *"Theory of Loaded Scatters"* [2.8]. From 1970, the number of academic contributions in the field of RFID skyrocketed, and private entities began to show interest in the potential applications of RFID tags in fields such as transportation, inventory control, animal tagging, and personnel control. Mario W. Cardullo officially patented the first RFID tag with rewritable memory in 1973. Shortly thereafter, in 1975, scientists Alfred Koelle, Steven Depp, and Robert Freyman presented a notable contribution titled "Short-Range Radio-Telemetry for Electronic Identification Using Modulated Backscatter" [2.9]. It described a simple and cost-effective electronic identification system capable of operating at distances of tens of meters, encouraging large-scale commercialization of RFID. By the end of the 20th century, millions of RFID tags were being used around the world [2.10]. It is worth mentioning that the evolution of RFID, like much of electronics, can be attributed to the invention of the transistor by William B. Shockley, John Bardeen, and Walter Brattain in 1948 and its subsequent evolution into field-effect transistors [2.11].

Currently, the field of backscattering continues to generate a lot of interest, not only for further improving existing technologies such as radar and RFID but

UNIVERSITAT ROVIRA I VIRGILI
LONG-RANGE BACKSCATTERING COMMUNICATIONS FOR NEXT GENERATION IOT APPLICATIONS
Marc Lázaro Martí

also for developing modern backscattering communications. In the 21st century, scientific efforts have focused on addressing two of the main limitations of RFID: the imperative use of dedicated readers and the limited communication range, which had long been restricted to few meters. In 2013, Joshua R. Smith et al. from the University of Washington presented their work "Ambient Backscatter: Wireless Communication Out of Thin Air" which proposed a communication system powered solely by RF signals from the environment. This breakthrough removed the first limitation of RFID, the need for dedicated readers. Over the last decade, researchers have successfully studied the use of various ambient signals as a carrier source and decoding backscatter communications using non-dedicated receivers. In 2017, the second limitation of RFID and backscatter communications was finally overcome with the introduction of the first long-range backscatter communication system based on LoRa signal reflection, with a maximum range of nearly half a kilometer [2.12]. Today, the system has been further improved to enable communication at distances of over 1 kilometer [2.13]. Figure 2.1 depicts the key discoveries and significant events in the evolution of backscatter communications.

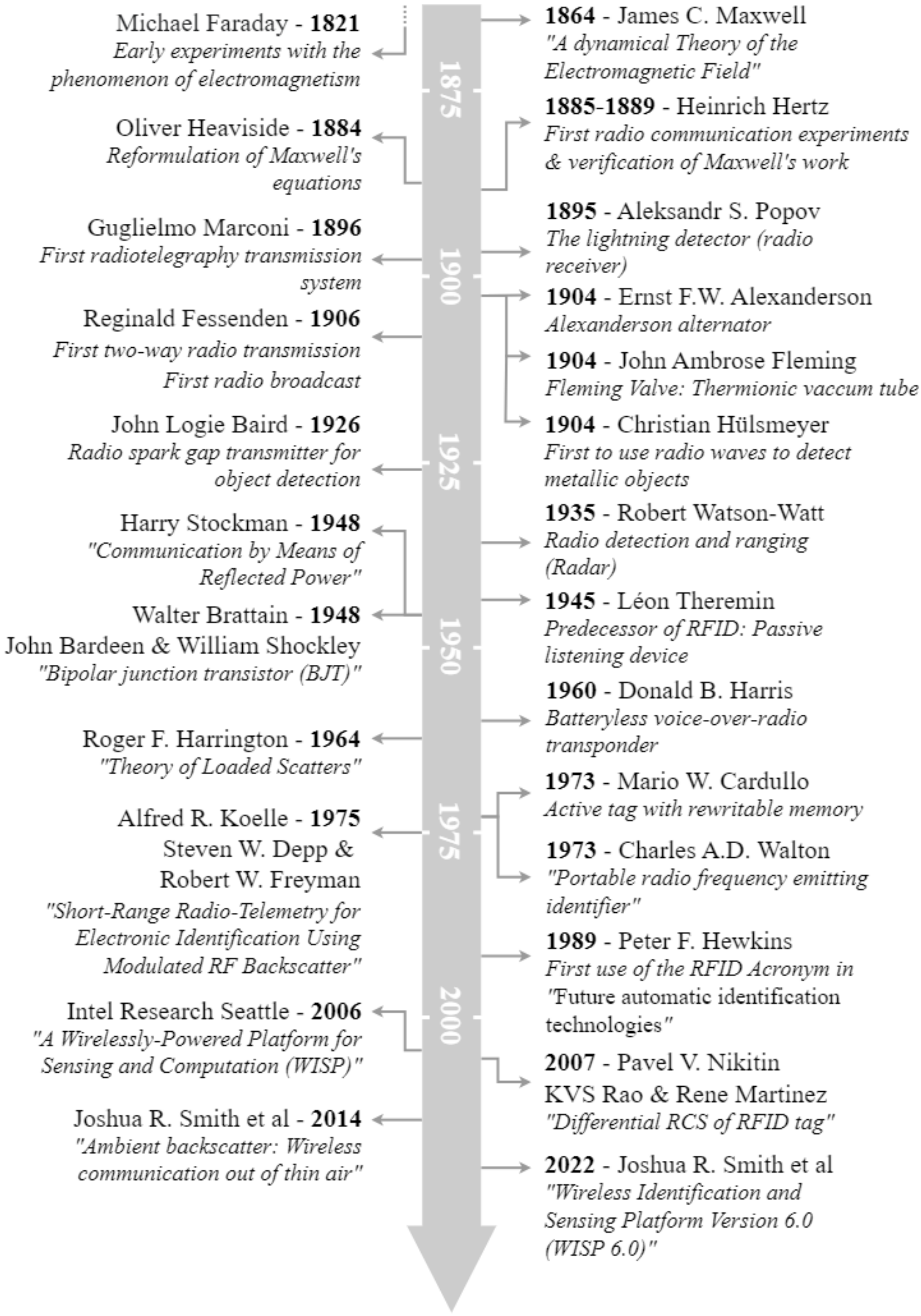

Figure 2.1: Cronologic evolution of RF backscattering

2.2 State of the art

This section provides a comprehensive overview of the latest research and developments in backscattering communications (BackCom). BackCom systems consist of three essential components: a carrier transmitter, a backscatter (modulator), and a backscatter receiver. These systems can be categorized based on various criteria such as topology, application, power requirements, or modulation. One commonly used method for differentiation is based on the transmitter-receiver topology: monostatic or bistatic. Figure 2.2 illustrates the classification of main BackCom systems and sets a guideline for the structuration of this section. Accordingly, the first and second subsections will cover monostatic backscatter communication systems (MBCS) and bistatic backscatter communication systems (BBCS), respectively. BBCS will be analyzed more extensively than MBCS, since the actuation field of this work focuses on this system architecture. Finally, the LoRa backscatter systems proposed in the literature will be evaluated in more detail in the last section.

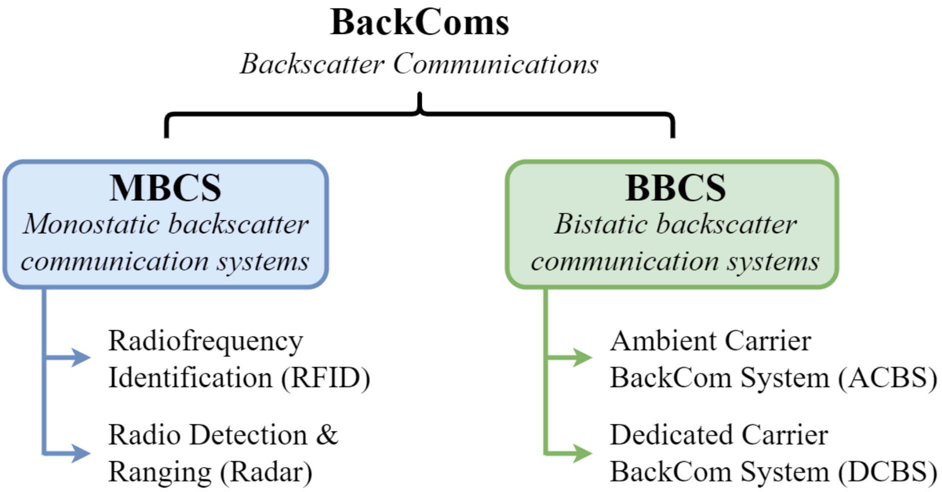

Figure 2.2: BackCom system categorization.

2.2.1 Monostatic backscatter communication systems

Monostatic BackCom architectures integrate both carrier source and backscatter receiver in the same device, by definition called a transceiver[1], but usually known as a reader. Co-locating the carrier source and backscatter receiver introduces an undesired self-interference to the system leading to what is known as doubly near-far problem[2], limiting the communication range and adding extra complexity to the reader design. To cope with this problem, active cancellation techniques are required, increasing the cost of the reader [2.14]. Moreover, in MBCS signals suffer from a round-trip path loss (source-to-tag and tag-to-receiver) causing the signal-to-noise ratio (SNR) at the receiver to drop with the fourth power of the reader-to-tag distance [2.15]. When the tag is far from the reader, this particular loss translates into higher energy outage probabilities and a lower backscattered signal strength [2.16], reducing the reader coverage.

The main backscattering technologies that employ monostatic architectures are radar and RFID. Although both work on the same principle (obtain information from backscattered signals), there are significant differences between them. The main purpose of radar is to detect and track nearby objects without the need to add transponders to the target. In radar systems, the backscatter signal is not actively modulated, and target identification depends entirely on its radar cross-section (RCS). On the other hand, RFID involves adding a transponder[3], commonly referred to as a tag, to specific objects. These tags modulate the backscattered signal by altering one or several of its physical properties (amplitude, frequency, or phase) in order to send data to the reader. Figure 2.3 illustrates an MBCS for both radar and RFID applications.

Although neither RFID nor radar are the main focus of this thesis, there are

---

[1] Transceiver: Device that can both transmit and receive signals for communication or detection purposes. In RFID is commonly referred to as a "reader". A Radar is a transceiver.

[2] The doubly near-far problem is a problem in wireless communication systems where a strong interferer signal causes the receiver to adjust its gain and sensitivity level, making it difficult to detect a weaker signal that arrives at the same time or shortly afterward. This problem occurs when the ratio between the power of the stronger and weaker signals is similar to the ratio between the power of the stronger and weaker noises in the channel. In such cases, the receiver may reduce its gain to avoid distortion from the strong signal, but this also reduces the ability to detect the weaker signal. This problem can occur in many types of wireless communication systems, including cellular networks, satellite communications, and RFID systems.

[3] Transponder: Device that emits a signal in response to another receiving signal. In RFID is commonly referred to as a "tag".

many similarities in the design of transponders, sensing techniques, modulation schemes, applications, and energy harvesting techniques that make it important to provide a general review of these sibling technologies. Such a review can lead to insightful ideas that are of particular interest for the development of this and future research.

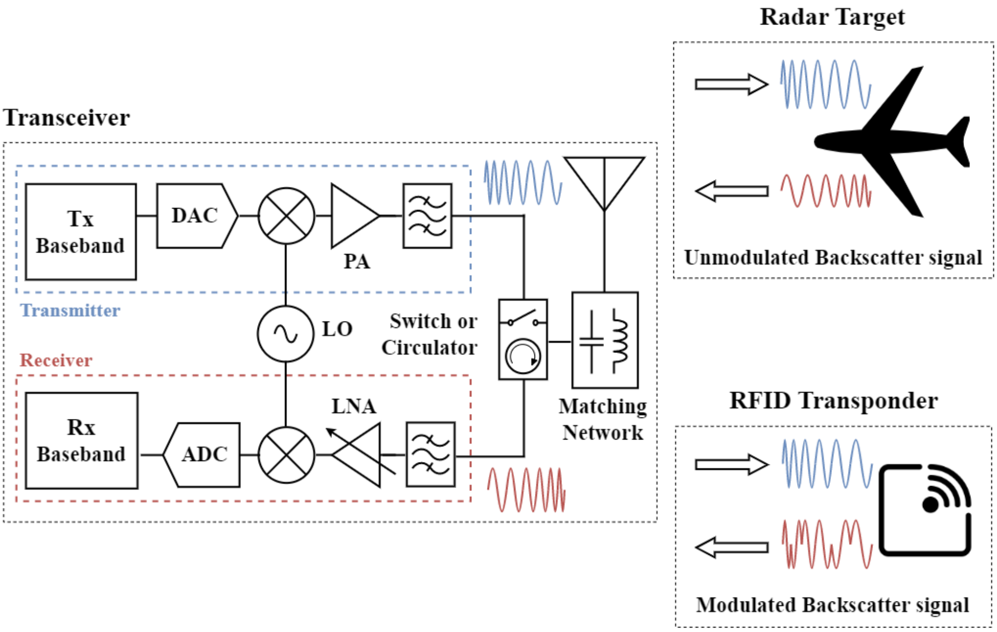

Figure 2.3: Monostatic backscatter communication systems topology.

2.2.1.1 Radar-based systems

Research within the field of radar often focuses on enhancing transceivers capabilities, such as range and resolution, through the integration of cutting-edge components, the design of new topologies, or the implementation of more advanced signal-processing algorithms. While these research fields are beyond the scope of this thesis, there is a growing area of research within the radar field aimed at increasing the detectability of radar targets through the use of reflectors and active transponders.

Several contributions in the literature propose to extend the primary detection capabilities of radars by providing targets with backscattering-based transponders [2.17][2.18][2.19][2.20]. The tag establishes an uplink towards

UNIVERSITAT ROVIRA I VIRGILI
LONG-RANGE BACKSCATTERING COMMUNICATIONS FOR NEXT GENERATION IOT APPLICATIONS
Marc Lázaro Martí

radar to share data, such as an identifier or sensor value. Radars are used in a wide range of fields, and the most common ones can be classified into two main categories: continuous wave radar and pulsed radar. Among the most used ones we can find the frequency-modulated continuous wave (FMCW) radar, synthetic aperture radar (SAR), and moving target indication (MTI) radar. The work in [2.21] presents a mathematical model that can simultaneously image, localize, and establish one-way uplink communication between tagged objects and the radar using backscattering transponders. The proposed system employs SAR techniques and offers several advantages, including tag-vs-clutter discrimination, multiple access among tags, and improved SNR in localization. Similar contributions are presented in [2.22][2.23]. With the relentless increase in the operating frequency of radars, transponder design for X-band [2.24], Ku-band, K-band, Ka-band[2.25], and mmWave-band [2.26] has generated great interest. High available bandwidth at millimeter wave band is favorable for high resolution ranging.

FMCW radars are widely used in the automotive industry to enable advanced driver assistance systems (ADAS). Radars excel at detecting metallic objects; however, their performance is poor when it comes to detecting pedestrians or objects made of other materials like plastic or wood. For this reason, there is a growing research effort to increase the detectability of vulnerable targets that go unnoticed by automotive radars. [2.27] presents a microdoppler tag based on the signature of rotating backscatters, allowing the target to be detected in presence of strong clutter. In contrast to conventional active load-modulated transponders, this one is based on a rotating reflector. Recently, a double-antenna backscattering transponder has been proposed in the literature; this device can be used to generate spoofing attacks on FMCW vehicle radars [2.28], establish inter-car communication (e.g., turn lights on, car stopped, car in reverse, etc.) [2.29], and increase the detectability of vulnerable objects such as pedestrians, cyclists, road workers, and, more recently, scooter riders, particularly in urban areas [2.30]. The transponder includes an amplifier between both antennas to increase its RCS, and has been designed to operate in the 24 GHz band using both a pair of 7-element series-fed array antennas or a pair of patch antennas with two dielectric lenses.

Beyond the automotive sector, this tag-radar architecture is also considered in other fields of application. Ground penetrating radars (GPR) are used, among

UNIVERSITAT ROVIRA I VIRGILI
LONG-RANGE BACKSCATTERING COMMUNICATIONS FOR NEXT GENERATION IOT APPLICATIONS
Marc Lázaro Martí

other purposes, to measure soil moisture. The main disadvantage is that the radar must be close to the ground or even in contact with it. Some studies have presented a hybrid system with backscattering tags to overcome this drawback [2.31][2.32]. Also in the medical field, various radar-based systems, such as CW Doppler and FMCW radars, are being studied to monitor respiration and vital signs with backscattering tags [2.33][2.34]. Moreover, a similar configuration is used in [2.35] to implement an indoor localization system using an impulse radio ultra-wideband (IR-UWB) radar with low-power tags.

2.2.1.2 RFID-based systems

Parallel advancements in the design of both readers and tags have driven the progress of RFID technology. The main research lines have focused on enhancing techniques for processing the backscattered signal, enhancing reader sensitivity, reducing manufacturing costs, increasing the amount of data encoded/stored by the tag, and exploring new applications. These research lines have been crucial in advancing RFID technology, making it more efficient and cost-effective, and expanding its potential uses in various fields. Beyond identification, RFID is currently used for diverse applications such as sensing, localization, and authentication. Healthcare [2.36], agriculture [2.37], transportation [2.38], and retail [2.39] are some of the main fields where RFID is used; however, the implementation fields of RFID are countless. For instance, in [2.40], RFID technology is evaluated as a system to study the behavior of bees. In recent years, RFID sensors based on polymers and nanomaterials have gained a lot of interest due to their capability to measure a wide variety of physical parameters such as temperature, humidity, pH, pressure, gases, biological compounds, and mechanical stress [2.41]. Figure 2.4 shows an example of an RFID sensor.

One of the main advantages of RFID technology and the reason for its widespread adoption in countless applications is the low cost of tags. With the desire to reduce definitively the consumption of the tag to zero, chipless technology emerged, completely eliminating any type of electronics in the tag. Nowadays, RFID tags can be classified into two major groups: chipped and chipless. The former is the most commonly used in the commercial field, and its development is mainly driven by the private sector. Chipped tags can be classified according to several criteria, such as the frequency band where they operate (LF, HF, UHF, MW), power source (active, semi-passive, or passive), genera-

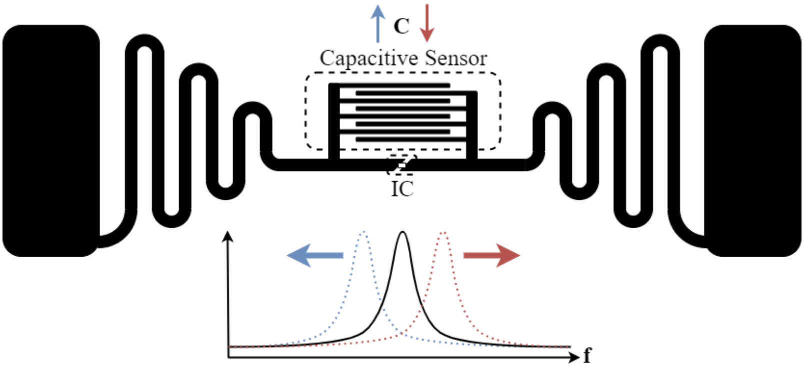

Figure 2.4: Capacitive RFID sensor diagram.

tion and performance of the integrated circuit (IC) (Higgs, Monza, UCODE, NTAG, etc.), or communication field (near-field or far-field).

On the other hand, chipless tags, technology that seeks to eliminate tag consumption entirely, are mainly classified by the domain where data is encoded: frequency domain, time domain, spatial domain, or hybrid systems. In each of these subgroups, there exist several data codification techniques. The frequency domain is the first and most studied system in chipless literature, followed by the time domain. In the former, the most common technique consists of encoding information in frequency peaks through resonators [2.42], while in the latter, data is usually encoded by means of delay lines [2.43][2.44]. Hybrid systems appear to cope with the encoding capacity limitations of the aforementioned techniques and consist of encoding information using two or even three domains, for example, acting on frequency and time delay of the backscattered signal simultaneously [2.45][2.46]. The spatial domain, also known as the image domain, differs substantially from the others, as the tag's information is extracted by scanning the tag by sections [2.47]. This technique heavily depends on the resolution of the reader and is therefore usually only used at frequencies above 10 GHz. Figure 2.5 shows the classification of RFID transponders.

In 2006, a significant breakthrough in transponder side design was achieved with the introduction of the Wireless Identification and Sensing Platform (WISP). This innovation resulted from a collaboration between Intel Research Seattle and the University of Washington [2.48]. Prior to the development of WISP, RFID tags were limited to being non-programmable black boxes, preventing researchers from conducting experiments with them. WISP revolutionized the

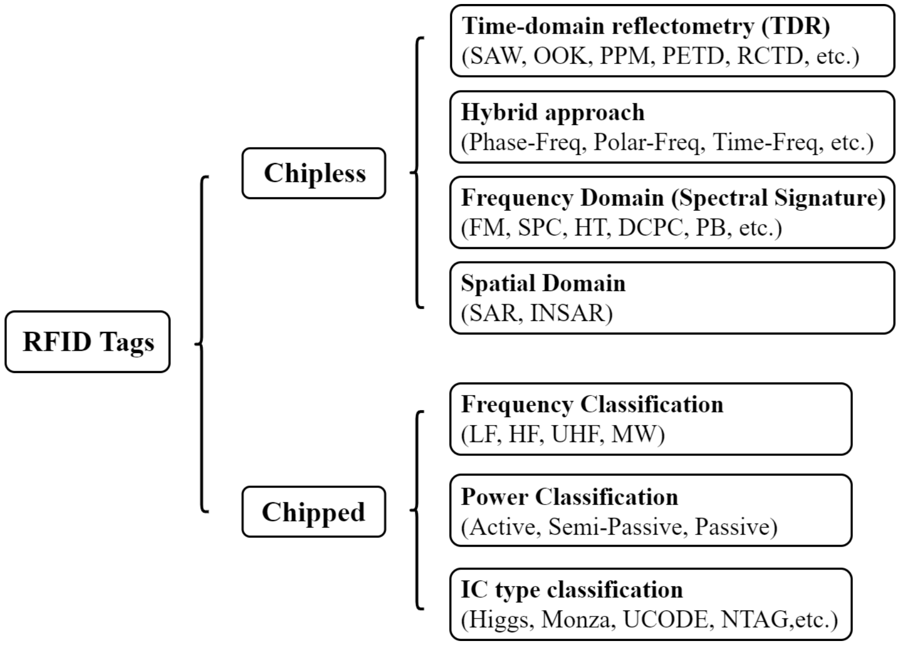

Figure 2.5: RFID transponder classification.

field by introducing the first battery-free embedded transponder that integrated an MSP430 microcontroller, enabling it to be read and powered by commercial UHF readers. Over time, the WISP has undergone substantial enhancements, improving its performance and incorporating various low-power sensors capable of operating solely on harvested energy from RF signals and ambient light. Figure 2.6 illustrates the latest version of the WISP device released in 2022 [2.49].

Another important branch of RFID is Near-Field Communication (NFC) technology. The typical operating frequency of NFC is 13.56 MHz, within the high frequency (HF) band. Unlike conventional RFID, NFC uses inductive coupling as a means of communication and energy transmission, limiting the communication range to a few centimeters. NFC devices use coil antennas to concentrate the magnetic field and maximize the coupling between the two devices. The most well-known application of NFC is contactless cards, initially for bank cards, but nowadays also used in identification cards such as national identity documents or public transportation cards.

The recent integration of this technology into smart devices has encouraged the development of passive NFC tags in a wide range of fields, opening the door

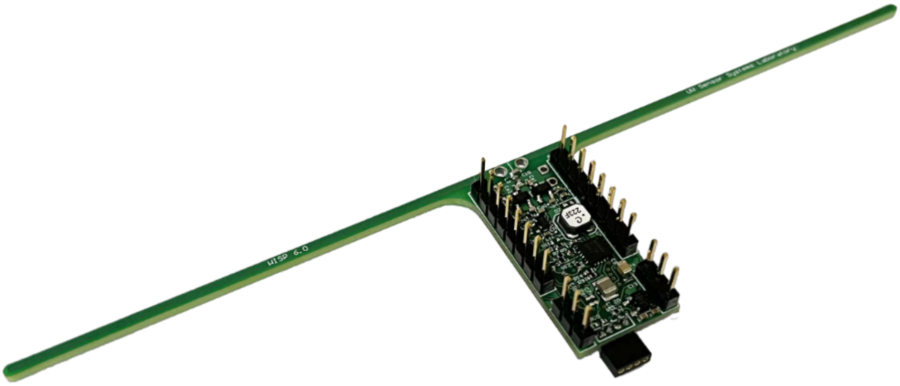

Figure 2.6: Wireless identification and sensing platform (WISP) version 6.0 [2.49].

to NFC sensors [2.50]. Some of the most recent contributions in the literature propose novel applications such as a battery-less bicycle tire pressure sensor based on a force-sensing resistor [2.51], a flexible epidermal NFC tag for sensing sweat [2.52] and a battery-less NFC potentiostat for measuring glucose strips and other electrochemical Point-of-Care sensors [2.53].

2.2.2 Bistatic backscatter communication systems

In contrast to MBCS, in bistatic architectures carrier source and backscatter receiver are deployed separately as described in figure 2.7. BBCS adds certain advantages to the system compared with MBCS, reason why it has recently been adopted as the architecture for next-generation long-range backscattering systems. Individual design of the carrier source and the backscatter receiver reduces their complexity, and consequently their cost. In most scenarios, losses in BBCS systems never reach the round-trip path loss. Only when the tag is equidistant from the transmitter and the receiver, the system will exhibit the same losses as in the monostatic configuration. However, considering that the tag does not have a static location, in most cases, it will not fulfill the aforementioned condition. Moreover, the doubly near-far problem can be mitigated by dislocating the carrier source and backscatter receiver, and even more, deploying multiple carrier sources, allowing far targets to harvest enough energy from nearby power beacons to reach the minimum required power level at the backscatter receiver. The strategic placement of carrier emitters can greatly enhance the coverage of the system [2.54].

However, compared with its monostatic counterpart, dislocating carrier source and backscatter receiver introduce a new problem to be addressed: a carrier frequency offset (CFO) between the source and the receiver. This miss-synchronization severely affects the system throughput [2.15] and is especially problematic for low-data rates communications. Historically, periodogram or preamble techniques have been proposed to compensate for the CFO problem [2.55]. However, more recent research proposes a novel interface cancellation scheme for BBCS that does not suffer from CFO, avoiding the long processing times that periodogram techniques can require in some scenarios [2.56].

Within BBCS there are two major groups: those that require a dedicated deployment, and those using ambient signals from legacy devices, also known as ambient backscatter communication (AmBC) systems. Subsequently, an overview of the principal contributions in both fields will be examined.

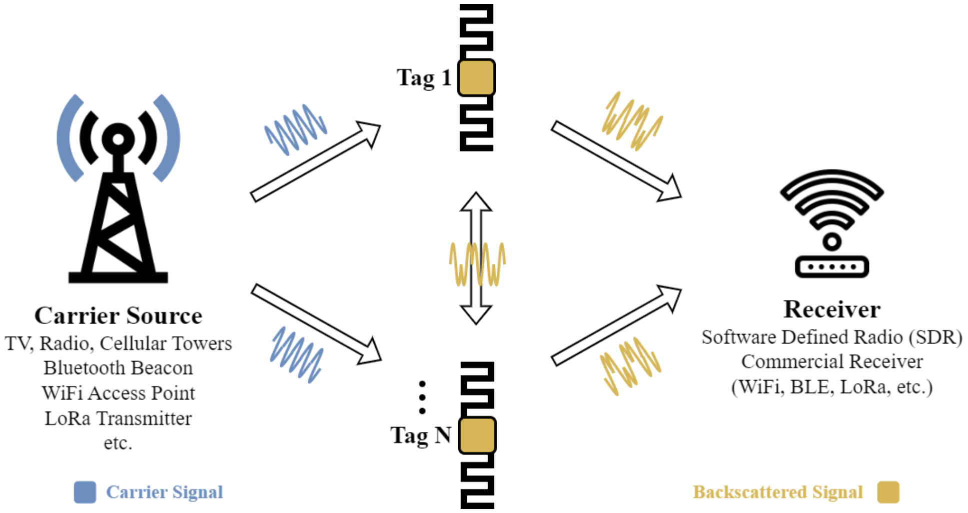

Figure 2.7: RFID transponder classification.

2.2.2.1 Dedicated carrier-based system

Despite the appeal of using ambient signals as a carrier and power source for backscatter communications, this configuration is not always feasible, especially in areas with little or no coverage, such as high mountain zones or garages. Dedicated carrier-based systems can not only cope with these situations, but

UNIVERSITAT ROVIRA I VIRGILI
LONG-RANGE BACKSCATTERING COMMUNICATIONS FOR NEXT GENERATION IOT APPLICATIONS
Marc Lázaro Martí

may even be a preferable option over AmBC systems to meet certain coverage, reliability, and performance requirements. In contrast to AmBC, where transmitters are fixed in specific locations, the use of a dedicated carrier source adds control over an extra variable in the system design, the transmitter, which results in several advantages. Carrier source location can be carefully determined as a function of the environment to maximize system performance, and multiple carrier sources can be deployed, providing coverage to dead zones, which would be impossible with a single carrier source. In addition, the use of dedicated carrier sources gives control over parameters such as the output power and carrier modulation, avoiding the problem of modulating the tag information onto already modulated and time-varying signals, making it easier for the receiver to decode the information.

BBCS based on multiple dedicated carrier sources (also called power beacons), has been extensively studied in the literature to increase system coverage [2.57]. The placement of carrier sources is not trivial, and an appropriate arrangement can maximize the guaranteed coverage distance (GCD) [2.54]. Additionally, by using multiple carrier emitters, transmitted power can be reduced by a factor of 50 [2.58]. A recent contribution proposes the addition of an intelligent reflecting surface (IRS) to assist tag-to-reader backscatter communication: phase changes introduced by the IRS are addressed by implementing a miniaturization-maximization algorithm, and a multiple-tag scenario is considered [2.59].

While there is plenty of research work successfully addressing the main challenges of BBCS through novel coding schemes, multi-antenna techniques, anti-collision protocols, channel modeling, and so on, the implementation of these systems with dedicated devices typically needs to be done from scratch on general-purpose equipment like FPGAs. This approach can be expensive and discourages large-scale commercial adoption. As a result, some contributions propose hybrid systems compatible with existing wireless modulations and commodity receivers but still employing dedicated carrier sources, starting the transition to ambient backscattering architectures. Some of the most relevant contributions of BBCS based on dedicated carrier emitter have been summarized in Table 2.1.

A WiFi BBCS is presented in [2.60]. In the proposed system, a dedicated carrier source emits a frequency tone that the backscatter transponder uses

UNIVERSITAT ROVIRA I VIRGILI
LONG-RANGE BACKSCATTERING COMMUNICATIONS FOR NEXT GENERATION IOT APPLICATIONS
Marc Lázaro Martí

to directly synthesize 802.11b packets, later demodulated by commodity WiFi receivers. The idea was tested experimentally with an FPGA, and power consumptions were simulated with the design of an application-specific integrated circuit (ASIC). The results stated a power consumption of 14.5 μW and 59.2 μW for 1 $Mbps$ and 11 $Mbps$ data rates, respectively. A comparable implementation, which is compatible with standard Bluetooth receivers, is outlined in [2.61]. The proposed backscatter tag effectively synthesizes BLE advertisement packets (unidirectional uplink communication) from a CW carrier signal. The backscattered BLE packets are indistinguishable from those generated by a BLE transmitter, maintaining the same channel, modulation scheme, and packet structure, and neither hardware nor firmware alterations are required to enable commodity BLE devices to demodulate the backscattered signal. The experimental results demonstrate communication ranges of up to 9.4 m with a data rate of 1 $Mbps$, providing performance similar to that of active BLE radios but with a power consumption significantly lower.

Likewise, the abovementioned system design can be extrapolated to many other modulations such as ZigBee (802.15.4)[2.62] or LoRa [2.63][2.64]. LoRa, which stands for Long-Range, is a widely adopted wireless technology in the Internet of Things (IoT) that utilizes chirp spread spectrum (CSS) modulation to encode information. CSS modulation offers several advantages, including high resilience to interference and high processing gain, resulting in extended communication ranges. As a result, backscatter communications based on this modulation leverage these properties to enhance the coverage of the backscattering system. Research studies such as LoRea [2.63], LoRa Backscatter [2.64], and Full-Duplex LoRa Backscatter [2.65] report communication ranges of up to 3.4 km, 2.8 km, and 92 m, respectively, under specific conditions such as the tag-to-transmitter distance, the gain of the antennas, the power of the transmitter and the type of scenario (indoor/outdoor).

As research tends to use ubiquitous commodity devices either in dedicated or ambient BBCS, the line that distinguishes both groups becomes blurred. Finding a classification criterion that applies to any backscattering system seems difficult, if not impossible. Some works consider any architecture with no control over the transmitter as ambient BBCS, such as those based on TV or FM carriers. On the other hand, others consider any system that does not require the deployment of dedicated transceivers as ambient BBCS, such as those based on ubiquitous commodity transceivers. It should be noted that the main difference between these two groups is the control over the carrier signal. In this work, any architecture in concordance with the second definition has been considered an ambient BBCS and assessed in the following section. Table 2.1 summarizes the stated features of most relevant contributions in dedicated BBCS found in the literature.

				Performance		
Ref	Year	Carrier	Receiver	Consumption	Throughput	Tag-Rx
[2.57] [2.58] [2.15]	2012 2013 2014	Frequency Tone (867 MHz)	Custom (SDR:USRP)	n/a	1 $kbps$	134 m (Tx: 13 dBm)
[2.61]	2015	Frequency Tone (2.4 GHz)	Commodity (BLE)	28 nW (FE) Ctrl(FPGA)	1 $Mbps$	9.4 m
[2.55]	2015	Frequency Tone (868 MHz)	Custom (SDR:USRP-2)	n/a	1 $Mbps$	150 m 13 dBm
[2.60]	2016	Frequency Tone (2.4 GHz)	Commodity (WiFi)	14.5 - 59.2 μW (IC)	1 $Mbps$ - 11 $Mbps$	9.1 - 30.5 m
[2.62]	2016	Frequency Tone (2.4 GHz)	Commodity (ZigBee)	n/a (FPGA)	250 $kbps$	20 cm 0 dBm
[2.64]	2017	Frequency Tone (905 MHz)	Commodity (LoRa: SX1276)	9.25 μW (IC)	18 bps - 37.5 $kbps$	237.5 m (2.8 km, Tx-Tag: 5 m)
[2.63]	2017	Frequency Tone (CC2420) (0.86-2.4 GHz)	Custom (CC1310-868) (CC2500-2.4)	70 μW (868) 650 μW (2.4)	2.9/197 $kbps$ (868/2.4)	3.4 km (868) 225 m (2.4)
[2.66]	2019	Frequency Tone (USRP+UBX-30) (900 MHz)	Custom (USRP+UBX-40)	45.2 μW (IC)	1 $kbps$	n/a
[2.65]	2021	Frequency Tone (ADF4351) (900 MHz)	Custom (Tx-Rx co-loc) (SX1276+ADF)	(Receiver) 112 mW(30dBm) 3.04 W (4dBm)	366 bps - 13.6 $kbps$	103 m

Table 2.1: Comparison between the most relevant contribution in BBCS based on dedicated devices.

2.2.2.2 Ambient carrier-based systems

Joshua R. Smith and Alanson P. Sample, the two main researchers in the WISP project, conceived the idea of powering tags with energy harvested from ambient RF signals, thereby freeing the system from the imperative use of conventional RFID readers. Despite the bulky antenna used in preliminary tests, they successfully collected $60\mu W$ at a range of 4 km from a TV tower. As a proof of concept, a commercial temperature and humidity sensor was pow-

UNIVERSITAT ROVIRA I VIRGILI
LONG-RANGE BACKSCATTERING COMMUNICATIONS FOR NEXT GENERATION IOT APPLICATIONS
Marc Lázaro Martí

ered up [2.67]. Later, the harvesting sensitivity of the system was enhanced allowing sensor node operation at a distance of 10.4 km from a TV transmitter, and over 200 m from a cellular base transceiver station [2.68]. An important milestone was reached in 2013 with the first ambient backscatter communication (AmBC) system presented by Smith et al. This innovative system enabled inter-communication between several backscattering tags using TV transmissions as the sole source of power, without the need for specifically deployed transmitters or receivers. The proposed tags integrated a backscatter transmitter and receiver allowing communication among them at distances up to 0.76 *m* with a predefined data rate of 0.1, 1, or 10 *kbps* [2.69]. Since then, research on AmBC systems has gained momentum. In 2014, an improved version of the backscatter transmitter and receiver, named *μmo* and *μcode* respectively, were introduced in [2.70]. Proposed receiver (*μmo*) implemented a low-power multi-antenna design to separate the noisy TV transmission from the backscatter transmitter data, resulting in a 100-fold increase in data rate, from 10 kbps to 1 Mbps, and an extended range up to 24 meters. On the other hand, for the design of the *μcode* transmitter, a novel coding scheme that eliminates the need for transmitter-receiver synchronization was proposed, thereby reducing the complexity of demodulating tag information at the receiver side.

WiFi transmissions are also proposed as a potential technology to harness backscatter communications. Nowadays, it is difficult to find an urban area without WiFi networks. Smartphones, wearables, tablets, and laptops all integrate WiFi capabilities, making it highly appealing to be used in AmBC systems, not only as carrier emitters but also as receivers. First WiFi AmBC system was proposed in [2.71]. The novel approach proposed a full duplex communication capable of connecting RF-powered tags to the internet by means of commodity WiFi devices. The uplink communication is implemented by modulating the existent WiFi channel information, while the downlink communication is implemented with the presence or absence of WiFi packets. Results stated a communication range of up to 2.1 *m* and a data rate of up to 1 *kbps*. A similar approach is presented by Ishizaki et al in [2.72]. The proposed system directly harvests energy from the WiFi access point (AP), achieving a power of 30.8 μW at a distance of 30 *cm*. The output power of the AP was set to 24 *dBm*. The results state data rates of 5.5 *kbps* and 2.25 *kbps* at distances of 30 *cm* and 40 *cm* from the AP, respectively.

UNIVERSITAT ROVIRA I VIRGILI
LONG-RANGE BACKSCATTERING COMMUNICATIONS FOR NEXT GENERATION IOT APPLICATIONS
Marc Lázaro Martí

Since then, many systems have been proposed to enhance the key properties of BBCS: consumption, throughput, and range. The trade-off between these three parameters makes it difficult to achieve remarkable performance in all three. Consequently, each contribution aims to enhance the system in concordance with the application. In order to summarize all the ambient BBCS available in the literature, Table 2.3 exposes the vast majority of contributions made to date sorted chronologically. This table summarizes the results of each work as a guide but does not pretend to be a comparison, since it wouldn't be faithful. The lack of standardization in the presentation of results makes it difficult to compare systems since not all the test settings are stated. Maximum communication ranges are highly dependent on the transmitter power and the tag-to-transmitter distance. Throughput and BER can be drastically increased and reduced, respectively, at the cost of increasing consumption or reducing the distance. Carrier modulation affects the system's performance. Unfortunately, the before-mentioned settings are not always exposed in the contributions.

Systems implemented in FPGAs are often accompanied by the design and simulation of an ASIC, yielding results in the range of several tens of μW. On the other hand, systems implemented with commercial off-the-shelf (COTS) components tend to fall within that range for analog modulations but quickly scale up to several hundreds of μW for digital modulations ranging from few bps to several $Mbps$. The vast majority of proposals present communication speeds in the range of $kbps$. However, some contributions focus on maximizing the speed ([2.73]: 11 $Mbps$, [2.74]: 10.61 $Mbps$) at the expense of sacrificing power consumption, a consequence of using higher-frequency oscillators. On the other hand, the communication range varies from 0.3 m [2.72] to 2.2 km [2.13]. However, this measurement is not very meaningful as it is usually obtained with the tag placed very close to the transmitter. A more reliable characterization would be to evaluate and report the maximum movement area of the tag. LoRa technology-based systems stand out for achieving the highest communication ranges. On the other hand, systems operating in the 2.4 GHz band, such as those based on WiFi and Bluetooth, tend to excel in attaining higher data rates.

				Performance		
Ref	Year	Carrier	Receiver	Consumption	Throughput	Tag-Rx
[2.72]	2011	WiFi (2.4 GHz)	Commodity (WiFi)	30.8 μW	5.5 $kbps$	0.3 m
[2.69]	2013	TV (539 MHz)	Tag[4]	0.79 μW (FE)	10 $kbps$	2.5 m
[2.70]	2014	TV & RFID (539 & 915 MHz)	Tag	(μcode) 8.9 μW (μmo) 422 μW	(μcode) 1 $kbps$ (μmo) 1 $Mbps$	(μcode) 24.3 m (μmo) 2.13 m
[2.71]	2014	WiFi (2.4 GHz)	Commodity (WiFi)	9.65 μW (FE)	1 $kbps$	2.1 m
[2.75]	2015	WiFi (2.4 GHz)	Commodity (WiFi)	3.15-15.75 μW	5 $Mbps$ (1 $Mbps$)	1 m (5 m)
[2.76]	2016	WiFi (2.4 GHz)	Commodity (WiFi)	n/a	100 $kbps$ (1 $Mbps$)	50 m (8 m)
[2.77]	2016	WiFi (2.4 GHz)	Commodity (WiFi)	33 μW (IC)	300 $kbps$ (LOS) 200 $kbps$ (NLOS)	54 m (LOS) 32 m (NLOS)
[2.73]	2016	BLE (2.4 GHz)	Commodity (WiFi & ZigBee)	28 μW (IC)	2 $Mbps$ (up to 11 $Mbps$)	27.4 m
[2.78]	2016	WiFi & BLE (2.4GHz)	Commodity (WiFi & BLE)	45 μW (IC)	313.8 bps (WiFi) 45.8 bps (BLE) 48.7 $kbps$ (FS)	4.8 m (WiFi) 4.4 m (BLE) 3.6 m (FS)
[2.79]	2017	FM (88-108 MHz)	Commodity (FM)	11.07 μW (IC)	3.2 $kbps$	18.2 m
[2.80]	2017	FM (88-108 MHz)	Commodity (FM)	313 μW	500 bps	2 m
[2.81]	2017	FM (88-108 MHz)	Commodity (FM)	0.677 mW (2.838 mW)	50 bps (2.5 $kbps$)	5 m
[2.82]	2017	FM (88-108 MHz)	Commodity (FM)	24 μW(1.2 V) 58 μW(1.79 V)	Analog frequency modulation	15 m (indoor) 26 m (outdoor)
[2.83]	2017	WiFi, BLE & ZigBee (2.4 GHz)	Commodity (WiFi,BLE, & ZigBee)	30 μW	60 $kbps$ 15 $kbps$ (multi)	42 m
[2.84]	2017	FM, TV& Cellular (88-900 MHz)	Custom (SDR)	n/a	158 bps	22 m
[2.85]	2018	FM (88-108 MHz)	Commodity (FM)	24 μW	FM mod P-FSK (1 $kbps$) S-BPSK (0.5 $kbps$)	15 m (indoor) 26 m (outdoor)
[2.86]	2018	Basestation	Tag (AM)	3.48 μW	n/a (AM)	9.4 m (RF) 15.2 m (Light)

...

Table 2.2: Comparison of AmBC systems proposed in the literature (Part 1).

---

[4] Tag integrates both transmitter and receiver capabilities, allowing tag intercommunication

[5] Analog frequency modulation refers to a modulation technique where there is no digital data. The signal varies based on a physical magnitude, such as a capacitive sensor. Analog modulation cannot be directly compared to digital modulations in terms of bits per second (bps). However, an approximate bps value can be extrapolated based on the resolution of the analog demodulator receiver.

Ref	Year	Carrier	Receiver	Consumption	Throughput	Tag-Rx
...						
[2.87]	2018	WiFi (2.4 GHz)	Commodity (WiFi)	n/a	50 $kbps$	14 m
[2.88]	2018	WiFi (2.4 GHz)	Commodity (WiFi)	14.2 mW (FPGA)	200 bps	8 m (tag-tag: 0.4 m)
[2.89] [2.90]	2018 (2020)	WiFi (2.4 GHz)	Commodity (WiFi)	10 μW	4-40 $kbps$	8 m (20 m)
[2.12]	2018	LoRa Gateway (900 MHz)	Commodity (LoRa)	220 μW	6.25 $kbps$ (SF7) 97 bps (SF12)	300 m (SF7) 800 m (SF12)
[2.91] [2.92]	2019 (2020)	WiFi (2.4 GHz)	Custom (SDR: USRP)	n/a (FPGA)	700 $kbps$	0.6 m
[2.93]	2019	SDR (WiFi, FM, TV) (91-2400 MHz)	Commodity (WiFi, FM, TV)	800 μW 50 μW (listen)	10 $kbps$	10 m (FM) 9 m (TV) 3.5 m (WiFi)
[2.94]	2020	LoRa (900 MHz)	Custom (SDR: USRP)	300 μW	9.9 - 121.4 $kbps$	71.4 - 225.6 m
[2.95]	2020	BLE (2.4 GHz)	Commodity (BLE)	n/a (FPGA)	2.8 $kbps$	23 m
[2.96]	2020	BLE (2.4 GHz)	Commodity (BLE)	37 μW (IC)	16.6 $kbps$	25 m (indoor) 56 m (outdoor)
[2.97]	2020	WiFi (2.4 GHz)	Commodity (WiFi)	464 μW 32 μW (IC)	240 $kbps$ (single) 246 $kbps$ (multi)	21.3 m
[2.98]	2020	WiFi, BLE & ZigBee (2.4 GHz)	Commodity (WiFi, BLE & ZigBee)	279 mW	278.4 $kbps$	28 m (WiFi) 22 m (BLE) 20 m (ZigBee)
[2.99]	2020	ZigBee (2.4 GHz)	Commodity (WiFi)	2 mW (FPGA) 38.7 μW (IC)	200 $kbps$	27 m
[2.100]	2020	LTE (680 MHz)	Custom LTE Rx (SDR: USRP)	>4.5 mW 158.6 μW	3.63 $Mbps$	97.5 m
[2.101]	2021	BLE (2.4 GHz)	Commodity (BLE)	2.03 mW (FPGA)	8.275 $kbps$ (LOS)	20 m (LOS) 14 m (NLOS)
[2.102]	2021	WiFi (2.4 GHz)	Custom & Commercial (SDR: USRP)	n/a	237.8 $kbps$	16 m
[2.103]	2021	WiFi (2.4 GHz)	Commercial (WiFi)	30 μW (IC)	500 $kbps$	30 m
[2.74]	2021	WiFi (2.4 GHz)	Custom WiFi (SDR: USRP)	30.2 μW (IC)	62.3 $kbps$ - 10.61 $Mbps$	48.76 m
[2.104]	2021	ZigBee (2.4 GHz)	Commodity (ZigBee)	n/a (FPGA)	13 $kbps$ (LOS) 10.3 $kbps$ (NLOS)	15 m
[2.13]	2021	LoRa (433 MHz)	Custom (SDR:USRP N210)	320 μW	120 bps	2.2 km
[2.105]	2021	LoRa (900 mHz)	Custom (SDR:USRP N210)	Receiver: 0.3 mW	39.5–199.4 $kbps$	50-200 m
[2.106]	2022	LoRa (433 MHz)	Custom (COTS design)	Receiver: 93.2 (IC)	19.6 $kbps$	180 m
[2.107]	2023	BLE (2.4 GHz)	Commodity (ZigBee)	n/a	218 $kbps$ (LOS) 204 $kbps$ (NLOS)	24 m 20 m (BER<1%)
[2.108]	2023	LTE (R&S SMBV100) (486 MHz)	Custom (SDR:USRP)	n/a (Rasp. Pi)	n/a	21 m (LOS)

Table 2.3: Comparison of AmBC systems proposed in the literature (Part 2).

UNIVERSITAT ROVIRA I VIRGILI
LONG-RANGE BACKSCATTERING COMMUNICATIONS FOR NEXT GENERATION IOT APPLICATIONS
Marc Lázaro Martí

2.2.3 LoRa backscattering systems

This section provides a more specific review of backscattering systems based on LoRa. Unlike Bluetooth and WiFi-based systems, LoRa signals are not as common nowadays. As a result, LoRa-based systems are often implemented with dedicated transceivers. However, thanks to projects like Helium or LoRaWAN, the deployment of LoRa gateways has experienced exponential growth in recent years. Helium encourages the installation of LoRa gateways to provide coverage for IoT nodes in smart cities. While most urban areas have a significant number of hotspots, coverage tends to decrease significantly in suburban areas. If the number of LoRa gateways continues to increase, LoRa-based backscattering systems may be able to operate without the need for dedicated transmitters.

A backscattering tag capable of synthesizing LoRa packets employing a voltage-controlled oscillator is presented in [2.64]. This system uses a frequency tone as a carrier source and a LoRa commercial receiver to demodulate the backscattered signal. A harmonic cancellation mechanism is also introduced to improve the spectral efficiency. The system has been implemented using an FPGA and its power consumption has been simulated using Cadence and Synopsis software toolkits. Alternatively, [2.109] proposes an IQ impedance modulator to synthesize LoRa packets by modulating the phase of the reflected wave instead of its instantaneous frequency.

Moreover, [2.12] presents the implementation of a backscattering tag that uses LoRa ambient transmissions as a carrier source. In contrast to systems based on unmodulated carrier sources, which do not require tag-carrier synchronization, the tag proposed integrates a LoRa packet detection circuit to synchronize the tag modulation with the intermittent LoRa ambient transmissions. Tag achieves that by correlating the incoming signal with a predefined up-chirp saved in its memory. The tag modulates the incident LoRa packets by circularly shifting some of the symbols. An FPGA has been used for the tag implementation. The backscattered signal has been demodulated with a USRP SDR. Experimental results exhibit a maximum data rate of 6.25 *kbps*.

The above-mentioned systems shift the backscattered signal to an adjacent channel to avoid the interference of the carrier. The work presented in [2.94], modulates the tag information directly in the LoRa carrier band using a simple On-Off keying (OOK) modulation. This work proposes a novel algorithm to split

UNIVERSITAT ROVIRA I VIRGILI
LONG-RANGE BACKSCATTERING COMMUNICATIONS FOR NEXT GENERATION IOT APPLICATIONS
Marc Lázaro Martí

the carrier from the tag signal and allow super low power consumption on the tag as a result of the low frequency required by the in-band OOK modulation. The results state data-rates of up to 199.4 *kbps*, considerably higher than prior works [2.12]. However, the proposed system requires an SDR to demodulate the tag information.

A LoRa backscattering system with parallel decoding, which enables 101 parallel tag transmission, is presented in [2.13]. The tag integrates an envelope detector to detect the presence of LoRa packets. The maximum stated range is 2.2 km under specific conditions (Bandwidth: 500 kHz, Transmitter power: 30 dBm, tag close to transmitter), however, the wake-up envelope detector circuit limits the range of the tag to 104m away from the transmitter. Once more, all the implementation relies on an SDR for the demodulation.

Prior works implement a LoRa packet detection by means of a cross-correlation [2.12] and a moving average filter [2.94]. However, any of them can demodulate the LoRa packet payload. The work carried out in [2.106] copes with this problem and outperforms the detection range with a maximum detection range of 148.6 m in comparison to the 30.6 m and 42.4 m stated in [2.94] and [2.12], respectively.

A full-duplex LoRa backscattering reader (monostatic architecture) is presented in [2.65]. The proposed implementation achieves 78 dB of self-interference cancellation in a low-cost, long-range, and small-form-factor reader design, making it suitable for integration into smartphones. The reader can demodulate LoRa backscattered packets at distances up to 91.5 m and 15.3 m when the transmission power is set to 30 and 20 dBm, respectively.

Many recent researches focus on improving the performance of LoRa backscattering systems. However, many of them achieve it using innovative modulation systems and demodulation algorithms implemented on general-purpose hardware, such as FPGAs and SDRs. Nonetheless, it is challenging to find proposals implemented solely with commercial LoRa transceivers. Despite the recent advances in the field, very few applications can be found leveraging the outstanding properties of LoRa backscattering communications. An automatic irrigation system based on LoRa backscattering is presented in [2.110]. In [2.65], the authors introduce two brief proof of concepts to design a smart contact lens and an aerial surveillance system for precision agriculture. However, the proposed applications are barely developed. Moreover, a long-range cyclist sensing is presented in [2.111].

2.3 Bibliography

[2.1] James Clerk Maxwell. VIII. A dynamical theory of the electromagnetic field. *Philosophical transactions of the Royal Society of London*, (155):459–512, 1865.

[2.2] Dieter J Cichon and Wiener Wiesbeck. The Heinrich Hertz wireless experiments at Karlsruhe in the view of modern communication. 1995.

[2.3] Ira Brodsky. How Reginald Fessenden put wireless on the right technological footing. In *IEEE GLOBECOM 2008-2008 IEEE Global Telecommunications Conference*, pages 1–5. IEEE, 2008.

[2.4] HF Dylla and Steven T Corneliussen. John Ambrose Fleming and the beginning of electronics. *Journal of Vacuum Science & Technology A: Vacuum, Surfaces, and Films*, 23(4):1244–1251, 2005.

[2.5] Ivan A Getting. SCR-584 radar and the Mark 56 naval gun fire control system. *IEEE Aerospace and Electronic Systems Magazine*, 5(10):3–15, 1990.

[2.6] Merrill I Skolnik. *Radar handbook*. McGraw-Hill Education, 2008.

[2.7] Harry Stockman. Communication by means of reflected power. *Proceedings of the IRE*, 36(10):1196–1204, 1948.

[2.8] Roger F Harrington. Theory of loaded scatterers. In *Proceedings of the institution of electrical engineers*, volume 111, pages 617–623. IET, 1964.

[2.9] Alfred R Koelle, Steven W Depp, and Robert W Freyman. Short-range radiotelemetry for electronic identification, using modulated RF backscatter. *Proceedings of the IEEE*, 63(8):1260–1261, 1975.

[2.10] Peter H Siegel. Microwaves Are Everywhere: RFID-Do You Know Where Your Pet Is? *IEEE Journal of Microwaves*, 1(3):679–688, 2021.

[2.11] Jeremy Landt. The history of RFID. *IEEE potentials*, 24(4):8–11, 2005.

[2.12] Yao Peng, Longfei Shangguan, Yue Hu, Yujie Qian, Xianshang Lin, Xiaojiang Chen, Dingyi Fang, and Kyle Jamieson. PLoRa: A passive long-range data network from ambient LoRa transmissions. In *Proceedings of the 2018 Conference of the ACM Special Interest Group on Data Communication*, pages 147–160, 2018.

[2.13] Jinyan Jiang, Zhenqiang Xu, Fan Dang, and Jiliang Wang. Long-range ambient LoRa backscatter with parallel decoding. In *Proceedings of the 27th Annual International Conference on Mobile Computing and Networking*, pages 684–696, 2021.

[2.14] Muhammad Usman Sheikh, Boxuan Xie, Kalle Ruttik, Hüseyin Yiğitler, Riku Jäntti, and Jyri Hämäläinen. Ultra-low-power wide range backscatter communication using cellular generated carrier. *Sensors*, 21(8):2663, 2021.

[2.15] John Kimionis, Aggelos Bletsas, and John N Sahalos. Increased range bistatic scatter radio. *IEEE Transactions on Communications*, 62(3):1091–1104, 2014.

[2.16] Shin Hyuk Choi and Dong In Kim. Backscatter radio communication for wireless powered communication networks. In *2015 21st Asia-Pacific Conference on Communications (APCC)*, pages 370–374. IEEE, 2015.

[2.17] Itay Cnaan-On, Stewart J Thomas, Jeffrey L Krolik, and Matthew S Reynolds. Multichannel backscatter communication and ranging for distributed sensing with an FMCW radar. *IEEE Transactions on Microwave Theory and Techniques*, 63(7):2375–2383, 2015.

[2.18] Itay Cnaan-On, Stewart J Thomas, Matthew S Reynolds, and Jeffrey L Krolik. Multichannel radar backscatter communication and localization. In *2014 IEEE International Conference on Acoustics, Speech and Signal Processing (ICASSP)*, pages 76–80. IEEE, 2014.

[2.19] Antonio Lazaro, Javier Lorenzo, Ramon Villarino, and David Girbau. Backscatter transponder based on frequency selective surface for FMCW radar applications. *Radioengineering*, 23(2):632–641, 2014.

[2.20] A Lazaro, J Lorenzo, R Villarino, and D Girbau. Modulated corner reflector using frequency selective surfaces for FMCW radar applications. In *2015 European Microwave Conference (EuMC)*, pages 111–114. IEEE, 2015.

[2.21] Xiaojie Fu, Andreas Pedross-Engel, Daniel Arnitz, Claire M Watts, Apoorva Sharma, and Matthew S Reynolds. Simultaneous imaging, sensor tag localization, and backscatter uplink via synthetic aperture radar. *IEEE Transactions on Microwave Theory and Techniques*, 66(3):1570–1578, 2017.

[2.22] Jian-Feng Gu, Kuangda Wang, and Ke Wu. System architecture and signal processing for frequency-modulated continuous-wave radar using active backscatter tags. *IEEE transactions on signal processing*, 66(9):2258–2272, 2017.

[2.23] Luca Venturino, Emanuele Grossi, Marco Lops, Jeremy Johnston, and Xiaodong Wang. Radar-enabled ambient backscatter communication. *arXiv preprint arXiv:2208.07061*, 2022.

[2.24] J Lorenzo, A Lazaro, R Villarino, and D Girbau. Active backscatter transponder for FMCW radar applications. *IEEE Antennas and Wireless Propagation Letters*, 14:1610–1613, 2015.

[2.25] Axel Strobel, Christian Carlowitz, Robert Wolf, Frank Ellinger, and Martin Vossiek. A millimeter-wave low-power active backscatter tag for FMCW radar systems. *IEEE transactions on microwave theory and techniques*, 61(5):1964–1972, 2013.

[2.26] Wadim Stein, Anna Aleksieieva, Sven Roehr, and Martin Vossiek. Phase modulated 61 GHz backscatter transponder for FMCW radar-based ranging. In *GeMiC 2014; German Microwave Conference*, pages 1–4. VDE, 2014.

[2.27] Antonio Lazaro, Marc Lazaro, Ramon Villarino, and Pedro De Paco. New radar micro-Doppler tag for road safety based on the signature of rotating backscatters. *IEEE Sensors Journal*, 21(6):8604–8612, 2020.

[2.28] Antonio Lazaro, Arnau Porcel, Marc Lazaro, Ramon Villarino, and David Girbau. Spoofing attacks on fmcw radars with low-cost backscatter tags. *Sensors*, 22(6):2145, 2022.

[2.29] Antonio Lazaro, Marc Lazaro, Ramon Villarino, David Girbau, and Pedro de Paco. Car2car communication using a modulated backscatter and automotive fmcw radar. *Sensors*, 21(11):3656, 2021.

[2.30] Antonio Lazaro, Marc Lazaro, Ramon Villarino, and David Girbau. Smart spread spectrum modulated tags for detection of vulnerable road users with automotive radar. *Sensors*, 23(5):2730, 2023.

[2.31] Colleen Josephson, Bradley Barnhart, Sachin Katti, Keith Winstein, and Ranveer Chandra. Rf soil moisture sensing via radar backscatter tags. *arXiv preprint arXiv:1912.12382*, 2019.

[2.32] Colleen Josephson, Manikanta Kotaru, Keith Winstein, Sachin Katti, and Ranveer Chandra. Low-cost in-ground soil moisture sensing with radar backscatter tags. In *ACM SIGCAS conference on computing and sustainable societies*, pages 299–311, 2021.

[2.33] Aditya Singh and Victor M Lubecke. Respiratory monitoring and clutter rejection using a CW Doppler radar with passive RF tags. *IEEE Sensors Journal*, 12(3):558–565, 2011.

[2.34] Alessandro DiCarlofelice, Emidio DiGiampaolo, and Piero Tognolatti. mm-Wave chipless RFID tag for healthcare applications. In *2020 XXXIIIrd General Assembly and Scientific Symposium of the International Union of Radio Science*, pages 1–3. IEEE, 2020.

[2.35] Yuan Zhou, Choi Look Law, and Jingjing Xia. Ultra low-power RFID tag with precision localization using IR-UWB. In *2011 IEEE MTT-S International Microwave Symposium*, pages 1–4. IEEE, 2011.

[2.36] Moutaz Haddara and Anna Staaby. RFID applications and adoptions in healthcare: a review on patient safety. *Procedia computer science*, 138:80–88, 2018.

[2.37] Rakiba Rayhana, Gaozhi Xiao, and Zheng Liu. RFID sensing technologies for smart agriculture. *IEEE Instrumentation & Measurement Magazine*, 24(3):50–60, 2021.

[2.38] Sim Liew Fong, Amir Ariff Azham bin Abu Bakar, Falah YH Ahmed, and Arshad Jamal. Smart transportation system using RFID. In *Proceedings of the 2019 8th International Conference on Software and Computer Applications*, pages 579–584, 2019.

[2.39] Maja Škiljo, Petar Šolić, Zoran Blažević, Lea Dujić Rodić, and Toni Perković. Uhf rfid: Retail store performance. *IEEE Journal of Radio Frequency Identification*, 6:481–489, 2021.

[2.40] P Nunes-Silva, M Hrncir, JTF Guimarães, H Arruda, L Costa, G Pessin, JO Siqueira, P De Souza, and VL Imperatriz-Fonseca. Applications of RFID technology on the study of bees. *Insectes sociaux*, 66:15–24, 2019.

[2.41] Filippo Costa, Simone Genovesi, Michele Borgese, Andrea Michel, Francesco Alessio Dicandia, and Giuliano Manara. A review of RFID sensors, the new frontier of internet of things. *Sensors*, 21(9):3138, 2021.

[2.42] Durga Prasad Mishra and Santanu Kumar Behera. Resonator Based Chipless RFID: A Frequency Domain Comprehensive Review. *IEEE Transactions on Instrumentation and Measurement*, 2022.

[2.43] Mohammadali Forouzandeh and Nemai Chandra Karmakar. Chipless RFID tags and sensors: A review on time-domain techniques. *Wireless Power Transfer*, 2(2):62–77, 2015.

[2.44] David Girbau, Ángel Ramos, Antonio Lazaro, Sergi Rima, and Ramón Villarino. Passive wireless temperature sensor based on time-coded UWB chipless RFID tags. *IEEE Transactions on Microwave Theory and Techniques*, 60(11):3623–3632, 2012.

[2.45] Arnaud Vena, Etienne Perret, and Smail Tedjini. Chipless RFID tag using hybrid coding technique. *IEEE Transactions on Microwave Theory and Techniques*, 59(12):3356–3364, 2011.

[2.46] Fatemeh Babaeian and Nemai Chandra Karmakar. Hybrid chipless RFID Tags-A pathway to EPC global standard. *IEEE Access*, 6:67415–67426, 2018.

[2.47] Dong Huu Nguyen, Mohammad Zomorrodi, and Nemai Chandra Karmakar. Spatial-based chipless RFID system. *IEEE Journal of Radio Frequency Identification*, 3(1):46–55, 2019.

[2.48] Joshua R Smith, Alanson P Sample, Pauline S Powledge, Sumit Roy, and Alexander Mamishev. A wirelessly-powered platform for sensing and computation. In *UbiComp 2006: Ubiquitous Computing: 8th International Conference, UbiComp 2006 Orange County, CA, USA, September 17-21, 2006 Proceedings 8*, pages 495–506. Springer, 2006.

[2.49] Rohan Menon, Rohit Gujarathi, Ali Saffari, and Joshua R Smith. Wireless Identification and Sensing Platform Version 6.0. 2022.

[2.50] Martí Boada, Antonio Lazaro, David Girbau, and Ramón Villarino. *Battery-less NFC Sensors for the Internet of Things*. John Wiley & Sons, 2022.

[2.51] Marti Boada, Antonio Lazaro, Ramon Villarino, Ernest Gil-Dolcet, and David Girbau. Battery-less NFC bicycle tire pressure sensor based on a force-sensing resistor. *IEEE Access*, 9:103975–103987, 2021.

[2.52] Adina Bianca Barba, Giulio Maria Bianco, Luca Fiore, Fabiana Arduini, Gaetano Marrocco, and Cecilia Occhiuzzi. Design and manufacture of flexible epidermal NFC device for electrochemical sensing of sweat. In *2022 IEEE International Conference on Flexible and Printable Sensors and Systems (FLEPS)*, pages 1–4. IEEE, 2022.

[2.53] Antonio Lazaro, Ramon Villarino, Marc Lazaro, Nicolau Canellas, Beatriz Prieto-Simon, and David Girbau. Battery-Less NFC Potentiostat for Electrochemical Point-of-Care Sensors Based on COTS Components. *Sensors*, 22(19):7213, 2022.

[2.54] Xiaolun Jia and Xiangyun Zhou. Power beacon placement for maximizing guaranteed coverage in bistatic backscatter networks. *IEEE Transactions on Communications*, 69(11):7895–7909, 2021.

[2.55] Nikos Fasarakis-Hilliard, Panos N Alevizos, and Aggelos Bletsas. Coherent detection and channel coding for bistatic scatter radio sensor networking. *IEEE Transactions on Communications*, 63(5):1798–1810, 2015.

[2.56] Qin Tao, Yihao Li, Caijun Zhong, Shuai Shao, and Zhi Zhang. A novel interference cancellation scheme for bistatic backscatter communication systems. *IEEE Communications Letters*, 25(6):2014–2018, 2021.

[2.57] John Kimionis, Aggelos Bletsas, and John N Sahalos. Bistatic backscatter radio for tag read-range extension. In *2012 IEEE International Conference on RFID-Technologies and Applications (RFID-TA)*, pages 356–361. IEEE, 2012.

[2.58] John Kimionis, Aggelos Bletsas, and John N Sahalos. Bistatic backscatter radio for power-limited sensor networks. In *2013 IEEE Global Communications Conference (GLOBECOM)*, pages 353–358. IEEE, 2013.

[2.59] Xiaolun Jia, Xiangyun Zhou, Dusit Niyato, and Jun Zhao. Intelligent reflecting surface-assisted bistatic backscatter networks: Joint beamforming and reflection design. *IEEE Transactions on Green Communications and Networking*, 6(2):799–814, 2021.

[2.60] Bryce Kellogg, Vamsi Talla, Shyamnath Gollakota, and Joshua R Smith. Passive wi-fi: Bringing low power to wi-fi transmissions. In *13th {USENIX} Symposium on Networked Systems Design and Implementation ({NSDI} 16)*, pages 151–164, 2016.

[2.61] Joshua F Ensworth and Matthew S Reynolds. Every smart phone is a backscatter reader: Modulated backscatter compatibility with bluetooth 4.0 low energy (ble) devices. In *2015 IEEE international conference on RFID (RFID)*, pages 78–85. IEEE, 2015.

[2.62] Carlos Pérez-Penichet, Frederik Hermans, Ambuj Varshney, and Thiemo Voigt. Augmenting IoT networks with backscatter-enabled passive sensor tags. In *Proceedings of the 3rd Workshop on Hot Topics in Wireless*, pages 23–27, 2016.

[2.63] Ambuj Varshney, Oliver Harms, Carlos Pérez-Penichet, Christian Rohner, Frederik Hermans, and Thiemo Voigt. Lorea: A backscatter architecture that achieves a long communication range. In *Proceedings of the 15th ACM Conference on Embedded Network Sensor Systems*, pages 1–14, 2017.

[2.64] Vamsi Talla, Mehrdad Hessar, Bryce Kellogg, Ali Najafi, Joshua R Smith, and Shyamnath Gollakota. Lora backscatter: Enabling the vision of ubiquitous connectivity. *Proceedings of the ACM on interactive, mobile, wearable and ubiquitous technologies*, 1(3):1–24, 2017.

[2.65] Mohamad Katanbaf, Anthony Weinand, and Vamsi Talla. Simplifying Backscatter Deployment: Full-Duplex LoRa Backscatter. In *NSDI*, pages 955–972, 2021.

[2.66] Mehrdad Hessar, Ali Najafi, et al. Netscatter: Enabling large-scale backscatter networks. In *Proceedings of the 16th USENIX Symposium on Networked Systems Design and Implementation (NSDI'19)*, 2019.

[2.67] Alanson Sample and Joshua R Smith. Experimental results with two wireless power transfer systems. In *2009 IEEE Radio and Wireless Symposium*, pages 16–18. IEEE, 2009.

[2.68] Aaron N Parks, Alanson P Sample, Yi Zhao, and Joshua R Smith. A wireless sensing platform utilizing ambient RF energy. In *2013 IEEE Topical Conference on Biomedical Wireless Technologies, Networks, and Sensing Systems*, pages 154–156. IEEE, 2013.

[2.69] Vincent Liu, Aaron Parks, Vamsi Talla, Shyamnath Gollakota, David Wetherall, and Joshua R Smith. Ambient backscatter: Wireless communication out of thin air. *ACM SIGCOMM computer communication review*, 43(4):39–50, 2013.

[2.70] Aaron N Parks, Angli Liu, Shyamnath Gollakota, and Joshua R Smith. Turbocharging ambient backscatter communication. *ACM SIGCOMM Computer Communication Review*, 44(4):619–630, 2014.

[2.71] Bryce Kellogg, Aaron Parks, Shyamnath Gollakota, Joshua R Smith, and David Wetherall. Wi-Fi backscatter: Internet connectivity for RF-powered devices. In *Proceedings of the 2014 ACM Conference on SIGCOMM*, pages 607–618, 2014.

[2.72] Haruya Ishizaki, Hidetoshi Ikeda, Yoichi Yoshida, Tadashi Maeda, Tadahiro Kuroda, and Masayuki Mizuno. A battery-less WiFi-BER modulated data transmitter with ambient radio-wave energy harvesting. In *2011 Symposium on VLSI Circuits-Digest of Technical Papers*, pages 162–163. IEEE, 2011.

[2.73] Vikram Iyer, Vamsi Talla, Bryce Kellogg, Shyamnath Gollakota, and Joshua Smith. Inter-technology backscatter: Towards internet connectivity for implanted devices. In *Proceedings of the 2016 ACM SIGCOMM Conference*, pages 356–369, 2016.

[2.74] Xin Liu, Zicheng Chi, Wei Wang, Yao Yao, Pei Hao, and Ting Zhu. Verification and Redesign of OFDM Backscatter. In *NSDI*, pages 939–953, 2021.

[2.75] Dinesh Bharadia, Kiran Raj Joshi, Manikanta Kotaru, and Sachin Katti. Backfi: High throughput wifi backscatter. *ACM SIGCOMM Computer Communication Review*, 45(4):283–296, 2015.

[2.76] Pengyu Zhang, Dinesh Bharadia, Kiran Joshi, and Sachin Katti. Enabling backscatter communication among commodity wifi radios. In *Proceedings of the 2016 ACM SIGCOMM Conference*, pages 611–612, 2016.

[2.77] Pengyu Zhang, Dinesh Bharadia, Kiran Joshi, and Sachin Katti. Hitchhike: Practical backscatter using commodity wifi. In *Proceedings of the 14th ACM Conference on Embedded Network Sensor Systems CD-ROM*, pages 259–271, 2016.

[2.78] Pengyu Zhang, Mohammad Rostami, Pan Hu, and Deepak Ganesan. Enabling practical backscatter communication for on-body sensors. In *Proceedings of the 2016 ACM SIGCOMM Conference*, pages 370–383, 2016.

[2.79] Anran Wang, Vikram Iyer, Vamsi Talla, Joshua R Smith, and Shyamnath Gollakota. FM Backscatter: Enabling Connected Cities and Smart Fabrics. In *NSDI*, volume 17, pages 3154630–3154650, 2017.

[2.80] Spyridon-Nektarios Daskalakis, John Kimionis, Ana Collado, Manos M Tentzeris, and Apostolos Georgiadis. Ambient FM backscattering for smart agricultural monitoring. In *2017 IEEE MTT-S International Microwave Symposium (IMS)*, pages 1339–1341. IEEE, 2017.

[2.81] Spyridon Nektarios Daskalakis, John Kimionis, Ana Collado, George Goussetis, Manos M Tentzeris, and Apostolos Georgiadis. Ambient backscatterers using FM broadcasting for low cost and low power wireless applications. *IEEE Transactions on Microwave Theory and Techniques*, 65(12):5251–5262, 2017.

[2.82] Georgios Vougioukas and Aggelos Bletsas. 24μ Watt 26m range batteryless backscatter sensors with FM remodulation and selection diversity. In *2017 IEEE International Conference on RFID Technology & Application (RFID-TA)*, pages 237–242. IEEE, 2017.

[2.83] Pengyu Zhang, Colleen Josephson, Dinesh Bharadia, and Sachin Katti. Freerider: Backscatter communication using commodity radios. In *Proceedings of the 13th International Conference on emerging Networking EXperiments and Technologies*, pages 389–401, 2017.

[2.84] Chouchang Yang, Jeremy Gummeson, and Alanson Sample. Riding the airways: Ultra-wideband ambient backscatter via commercial broadcast systems. In *IEEE INFOCOM 2017-IEEE Conference on Computer Communications*, pages 1–9. IEEE, 2017.

[2.85] Georgios Vougioukas and Aggelos Bletsas. Switching frequency techniques for universal ambient backscatter networking. *IEEE Journal on Selected Areas in Communications*, 37(2):464–477, 2018.

[2.86] Vamsi Talla, Bryce Kellogg, Shyamnath Gollakota, and Joshua R Smith. Battery-free cellphone. *Proceedings of the ACM on Interactive, Mobile, Wearable and Ubiquitous Technologies*, 1(2):1–20, 2017.

[2.87] Jia Zhao, Wei Gong, and Jiangchuan Liu. Spatial stream backscatter using commodity wifi. In *Proceedings of the 16th Annual International Conference on Mobile Systems, Applications, and Services*, pages 191–203, 2018.

[2.88] Jia Zhao, Wei Gong, and Jiangchuan Liu. X-tandem: Towards multi-hop backscatter communication with commodity wifi. In *Proceedings of the 24th Annual International Conference on Mobile Computing and Networking*, pages 497–511, 2018.

[2.89] Ali Abedi, Mohammad Hossein Mazaheri, Omid Abari, and Tim Brecht. Witag: Rethinking backscatter communication for wifi networks. In *Proceedings of the 17th ACM Workshop on Hot Topics in Networks*, pages 148–154, 2018.

UNIVERSITAT ROVIRA I VIRGILI
LONG-RANGE BACKSCATTERING COMMUNICATIONS FOR NEXT GENERATION IOT APPLICATIONS
Marc Lázaro Martí

[2.90] Ali Abedi, Farzan Dehbashi, Mohammad Hossein Mazaheri, Omid Abari, and Tim Brecht. Witag: Seamless wifi backscatter communication. In *Proceedings of the Annual conference of the ACM Special Interest Group on Data Communication on the applications, technologies, architectures, and protocols for computer communication*, pages 240–252, 2020.

[2.91] Xin He, Weiwei Jiang, Meng Cheng, Xiaobo Zhou, Peng-Jun Wan, Panlong Yang, and Brian Kurkoski. GuardRider: Towards Sustainable Backscattering System over WiFi in the Wild. *arXiv preprint arXiv:1912.06493*, 2019.

[2.92] Xin He, Weiwei Jiang, Meng Cheng, Xiaobo Zhou, Panlong Yang, and Brian Kurkoski. Guardrider: Reliable WiFi backscatter using reed-Solomon codes with QoS guarantee. In *2020 IEEE/ACM 28th International Symposium on Quality of Service (IWQoS)*, pages 1–10. IEEE, 2020.

[2.93] Zerina Kapetanovic, Ali Saffari, Ranveer Chandra, and Joshua R Smith. Glaze: Overlaying occupied spectrum with downlink iot transmissions. *Proceedings of the ACM on Interactive, Mobile, Wearable and Ubiquitous Technologies*, 3(4):1–21, 2019.

[2.94] Xiuzhen Guo, Longfei Shangguan, Yuan He, Jia Zhang, Haotian Jiang, Awais Ahmad Siddiqi, and Yunhao Liu. Aloba: rethinking ON-OFF keying modulation for ambient LoRa backscatter. In *Proceedings of the 18th Conference on Embedded Networked Sensor Systems*, pages 192–204, 2020.

[2.95] Maolin Zhang, Si Chen, Amiya Nayak, and Wei Gong. Enabling multi-channel backscatter communication for Bluetooth low energy. In *ICC 2020-2020 IEEE International Conference on Communications (ICC)*, pages 1–6. IEEE, 2020.

[2.96] Maolin Zhang, Jia Zhao, Si Chen, and Wei Gong. Reliable backscatter with commodity ble. In *IEEE INFOCOM 2020-IEEE Conference on Computer Communications*, pages 1291–1299. IEEE, 2020.

[2.97] Xin Liu, Zicheng Chi, Wei Wang, Yao Yao, and Ting Zhu. VMscatter: A Versatile MIMO Backscatter. In *NSDI*, pages 895–909, 2020.

[2.98] Wei Gong, Longzhi Yuan, Qiwei Wang, and Jia Zhao. Multiprotocol backscatter for personal IoT sensors. In *Proceedings of the 16th International Conference on emerging Networking EXperiments and Technologies*, pages 261–273, 2020.

[2.99] Jinhwan Jung, Jihoon Ryoo, Yung Yi, and Song Min Kim. Gateway over the air: Towards pervasive internet connectivity for commodity iot. In *Proceedings of the 18th International Conference on Mobile Systems, Applications, and Services*, pages 54–66, 2020.

[2.100] Zicheng Chi, Xin Liu, Wei Wang, Yao Yao, and Ting Zhu. Leveraging ambient lte traffic for ubiquitous passive communication. In *Proceedings of the Annual conference of the ACM Special Interest Group on Data Communication on the applications, technologies, architectures, and protocols for computer communication*, pages 172–185, 2020.

UNIVERSITAT ROVIRA I VIRGILI
LONG-RANGE BACKSCATTERING COMMUNICATIONS FOR NEXT GENERATION IOT APPLICATIONS
Marc Lázaro Martí

[2.101] Maolin Zhang, Si Chen, Jia Zhao, and Wei Gong. Commodity-level BLE backscatter. In *Proceedings of the 19th Annual International Conference on Mobile Systems, Applications, and Services*, pages 402–414, 2021.

[2.102] Qiwei Wang, Si Chen, Jia Zhao, and Wei Gong. Rapidrider: Efficient wifi backscatter with uncontrolled ambient signals. In *IEEE INFOCOM 2021-IEEE Conference on Computer Communications*, pages 1–10. IEEE, 2021.

[2.103] Manideep Dunna, Miao Meng, Po-Han Wang, Chi Zhang, Patrick P Mercier, and Dinesh Bharadia. SyncScatter: Enabling WiFi like synchronization and range for WiFi backscatter Communication. In *NSDI*, pages 923–937, 2021.

[2.104] Zhaoyuan Xu and Wei Gong. Homoscatter: Towards efficient connectivity for ZigBee backscatter system. *arXiv preprint arXiv:2111.02140*, 2021.

[2.105] Xiuzhen Guo, Longfei Shangguan, Yuan He, Jia Zhang, Haotian Jiang, Awais Ahmad Siddiqi, and Yunhao Liu. Efficient ambient LoRa backscatter with On-Off keying modulation. *IEEE/ACM Transactions on Networking*, 30(2):641–654, 2021.

[2.106] Xiuzhen Guo, Longfei Shangguan, Yuan He, Nan Jing, Jiacheng Zhang, Haotian Jiang, and Yunhao Liu. Saiyan: Design and implementation of a low-power demodulator for LoRa backscatter systems. In *Proc. USENIX NSDI*, pages 437–451, 2022.

[2.107] Zhaoyuan Xu and Wei Gong. BumbleBee: Enabling the Vision of Pervasive ZigBee Backscatter Communication. In *2023 IEEE International Conference on Pervasive Computing and Communications (PerCom)*, pages 252–261. IEEE, 2023.

[2.108] Jingyi Liao, Xiyu Wang, Kalle Ruttik, Riku Jantti, and Phan-Huy Dinh-Thuy. Ambient FSK Backscatter Communications using LTE Cell Specific Reference Signals. *arXiv preprint arXiv:2301.13664*, 2023.

[2.109] Daniel Belo, Ricardo Correia, Yuan Ding, Spyridon Nektarios Daskalakis, George Goussetis, Apostolos Georgiadis, and Nuno Borges Carvalho. IQ impedance modulator front-end for low-power LoRa backscattering devices. *IEEE Transactions on Microwave Theory and Techniques*, 67(12):5307–5314, 2019.

[2.110] Siaka Konate, Changli Li, and Lizhong Xu. LoRa Backscatter Automated Irrigation Approach: Reviewing and Proposed System. In *2020 6th International Conference on Robotics and Artificial Intelligence*, pages 205–213, 2020.

[2.111] Haotian Jiang, Jiacheng Zhang, Xiuzhen Guo, and Yuan He. Sense me on the ride: Accurate mobile sensing over a LoRa backscatter channel. In *Proceedings of the 19th ACM Conference on Embedded Networked Sensor Systems*, pages 125–137, 2021.

Chapter 3

Theory of backscatter communication

This chapter focuses on addressing the entire theoretical part regarding the backscattering technique relevant to the work of this thesis. Thus, Section 3.1 begins with a brief introduction to radar cross-section. Section 3.2 deals with the fundamental theory of antennas relevant in the field of backscattering. Finally, Section 3.3 and Section 3.4 address the differential radar cross-section of the tag and mathematically justifies the behavior of the backscattered signal due to the load modulation.

3.1 Radar Cross-Section

Objects naturally reflect impinging electromagnetic fields based on their radar cross-section (σ), which depends on the object's morphology, including its shape and materials. A larger σ indicates that the target reflects more power back to the source, while a smaller σ means that the target reflects less power back. The σ determines the magnitude of the backscattered power in comparison to that of an ideal sphere with a cross-sectional area of 1 m^2. It should be noted that the radar cross-section also depends on the incident angle. While σ of simple geometric objects can be calculated theoretically, more complex targets require a direct measurement or a simulation. Figure 3.1 shows the maximum radar cross-section (σ_{max}) for three different targets (sphere, flat plate, and corner) along with an approximate 180° axial plane pattern to illustrate the differences between them [3.1].

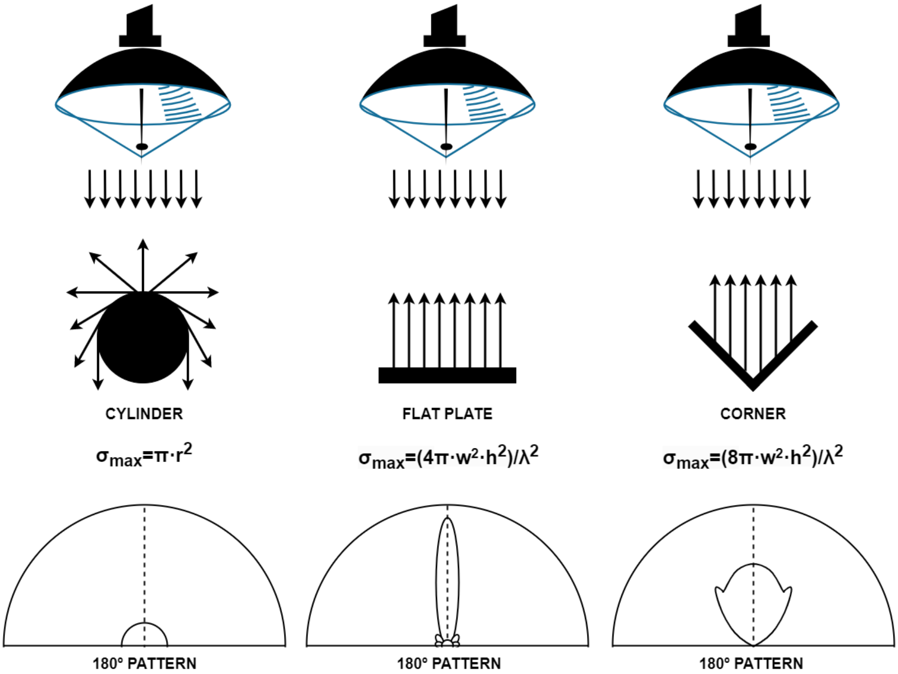

Figure 3.1: Radar cross-section representation for 3 different objects: sphere, flat plate, and corner.

3.2 Tag backscattered power

The concept of radar cross-section extends beyond the radar field and plays an important role in any backscattering system. In contrast to the static σ of radar targets (what can be considered a kind of intrinsic analog modulation), backscatter transponders modulate their characteristic σ to encode digital information in the scattered signal. To achieve this, the reflection coefficient of the transponder antenna is modulated by loading it with different impedances. This technique is known as load modulation and is the basis of the RFID and backscattering systems.

The theoretical basis behind antenna scattering has been extensively studied in the literature by Green [3.2], Harrington [3.3], Kraus [3.4], Hansen [3.5] and more recently by Balanis [3.6], Nikitin [3.7], Yen [3.8], and Bletsas [3.9], among others. Typically, a combination of circuit and field theory is employed to determine the scattered power of a loaded antenna.

The backscattered field can be divided into two main contribution modes called the structural mode and the antenna mode. The structural mode occurs due to the current induced on the surface of the antenna by the interaction with an electromagnetic field. This mode is independent of the load impedance and can be measured when the antenna is conjugate-matched, meaning that maximum power is transferred to the load, leaving only the structural scattering field. On the other hand, the antenna mode depends on the antenna load and applies to any load other than the antenna complex conjugated. Therefore, part of the energy is absorbed by the load, while another part is re-radiated by the antenna due to the reflection caused by the impedance mismatch.

The equivalent circuit of a loaded antenna (or a tag) is depicted in Figure 3.2, where the antenna has been substituted with a Thevenin generator. This method evaluates the antenna mode rather than the structural mode and it is considered an accurate approach for modeling canonical minimum scattering (CMS)[1] antennas [3.7], which are widely used in the UHF band. Despite the inherent limitations of this approach, it can effectively determine the load-dependent power backscattered by the tag [3.7].

In Figure 3.2, Z_a is the impedance of the antenna ($Z_a = R_a + jX_a$), Z_{load}

---

[1] A canonical minimum scattering antenna is defined as one that becomes 'invisible' when the accessible waveguide terminals are open-circuited [3.10].

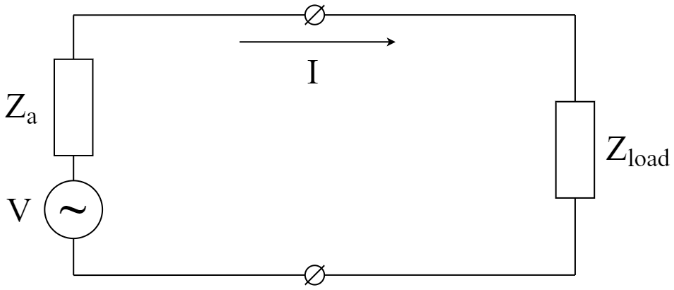

Figure 3.2: Equivalent circuit of a loaded antenna.

is the impedance of the load ($Z_{load} = R_{load} + jX_{load}$), V is the open circuit voltage received by the antenna, and I is the current induced by the incident electromagnetic field. In practice, not all power dissipated in the resistance R_a is backscattered; instead, some of it is dissipated as heat in the antenna ($R_a = R_{scatt} + R_{loss}$). However, assuming a lossless antenna ($R_{loss} = 0$), the backscattered power P_a can be mathematically defined as follows:

$$P_a = \frac{1}{2}|I|^2 R_a = \frac{|V|^2 R_a}{2|Z_a + Z_{load}|^2} \tag{3.1}$$

Likewise, the power delivered to the antenna termination (P_{load}) can also be calculated. When the load impedance is not conjugate matched to that of the antenna, the ratio of power delivered to the load or backscattered will depend on the reflection coefficient at the antenna terminals, mathematically described as:

$$\Gamma = \frac{Z_{load} - Z_a^*}{Z_{load} + Z_a} \tag{3.2}$$

The Thevenin equivalent circuit does not consider the contribution of the structural mode. Therefore, the field backscattered by the antenna, represented as $\vec{E}a$, can be alternatively described in a more general notation, applicable to any antenna, as follows:

$$\vec{E}_a(Z_{load}) = \vec{E}_s + \vec{E}_{tag}\Gamma \tag{3.3}$$

where $\vec{E}_s$ is the structural mode, which is the term independent of the load, and $\vec{E}_{tag}$ is the antenna mode (also known as tag mode). It can be noted that when the antenna is matched with the complex conjugate impedance, the reflection coefficient is zero ($\Gamma = 0$), remaining only the structural scattering field.

Let's consider an impinging electromagnetic wave that generates a power density at the specific location of the tag. The energy flux density of an electromagnetic field passing through a delimited surface is denoted as the Poynting vector $\vec{S}$ (W/m^2) and mathematically defined by the vector product of the electric $\vec{E}$ (V/m) and the magnetic $\vec{H}$ (A/m) field components ($\vec{S} = \vec{E} \times \vec{H}$). As a result of the product of two time-varying fields, the Poynting vector takes different values at different instants of time. This specific magnitude is known as the instantaneous Poynting vector and is not particularly interesting in practice. Therefore, it is typically integrated over a period of time to obtain an average power density (S).

To calculate the average power density delivered by the carrier source to the tag, an isotropic transmitter that uniformly radiates an electromagnetic field over free space is considered. Power is distributed uniformly over the entire surface of the sphere ($P_t/4\pi r^2$). In practice, isotropic transmitters do not exist and the power density depends on the antenna's radiation pattern ($D(\theta, \phi)$). However, by considering that the antenna's maximum gain points towards the tag's coordinates, the power density at the tag can be mathematically determined by:

$$S = \frac{P_t G_t}{4\pi r^2} \tag{3.4}$$

where P_t is the transmitted power, G_t the gain of the transmitter antenna, and r the distance between the transmitter and the tag. The ratio of the power available at the terminals of the antenna (P_{load}) to the incident power density (S) is an area A_{eff} coined as the effective area or effective aperture of the antenna:

$$A_{eff} = \frac{P_{load}}{S} = \frac{|V|^2 R_{load}}{2S|Z_a + Z_{load}|^2} = \frac{\lambda^2}{4\pi} G_{tag} \tag{3.5}$$

which can be expressed as a function of wavelength (λ) and the tag's antenna gain (G_{tag}) [3.6][3.7]. Any of the powers dissipated in the antenna can be expressed as an aperture: effective aperture (A_{eff}), loss aperture (A_{loss}), scattering aperture (A_{scatt}) and collecting aperture (A_c), which results of the sum of the previous three ($A_c = A_{scatt} + A_{loss} + A_{eff}$). One can note that radar cross section and antenna apertures have the same units (m^2). This is

UNIVERSITAT ROVIRA I VIRGILI
LONG-RANGE BACKSCATTERING COMMUNICATIONS FOR NEXT GENERATION IOT APPLICATIONS
Marc Lázaro Martí

because, in fact, the radar cross-section of the antenna σ is nothing more than the scattering aperture A_{scatt} of the antenna.

Being introduced the power density, all the powers dissipated in the antenna $(P_{loss}, P_{scatt}, P_{load})$ and its analogous apertures, we can express the radar cross section with more commonly used parameters [3.7]:

$$\sigma = \frac{(\lambda G_{tag} R_a)^2}{\pi |Z_a + Z_{load}|^2} \tag{3.6}$$

It can be noted that when the antenna is open-circuited ($Z_{load} = \infty$), the tag does not reflect anything ($\sigma = 0$). Otherwise, when the antenna is conjugate matched ($Z_{load} = Z_a^*$), radar cross-section will be equal to the effective aperture multiplied by the tag antenna gain ($\sigma = A_{eff} G_{tag} = \lambda^2 G_{tag}^2 / 4\pi$). Finally, when the antenna is terminated with a short circuit ($Z_{load} = 0$), the radar cross-section depends on the ratio between the real and the imaginary part of the antenna impedance, reaching the maximum ($\sigma = \lambda^2 G_{tag}^2 / pi$) when antenna impedance is purely resistive ($Z_a = R_a$). The radar cross-section of the tag can be expressed as a function of the reflection coefficient [3.2]:

$$\sigma = \frac{\lambda^2}{4\pi} G_{tag} |C - \Gamma|^2 \tag{3.7}$$

where C represents a complex parameter independent of the load and related to the structural scattering mode of the antenna [3.8]. For instance, when the tag antenna is a thin dipole $C \simeq 1$ [3.6]. Finally, knowing the radar cross-section, power at the receiver can be determined by means of the classical radar equation:

$$P_r = \frac{P_t G_t G_r \lambda^2 \sigma}{(4\pi)^3 d_t^2 d_r^2} \tag{3.8}$$

where G_r is the gain of the receiver antenna, and d_t and d_r are the distances from the transmitter to the tag and the tag to the receiver, respectively.

3.3 Tag differential Radar Cross-Section

RFID and backscattering tags modulate the reflection coefficient at their antenna terminals to encode information in the backscattered signal. This is achieved by loading the antenna with different impedances. While most tags use only two states (two loads) for modulation, it is possible to implement high-order modulations with multi-state load-modulated tags. Figure 3.3 illustrates the equivalent circuit of a backscattering tag, where Z_0 and Z_1 represent two distinct load impedances. The modulating signal that controls the switch is denoted as $p(t)$, the carrier signal as $c(t)$, and the signal reflected by the tag as $r(t)$.

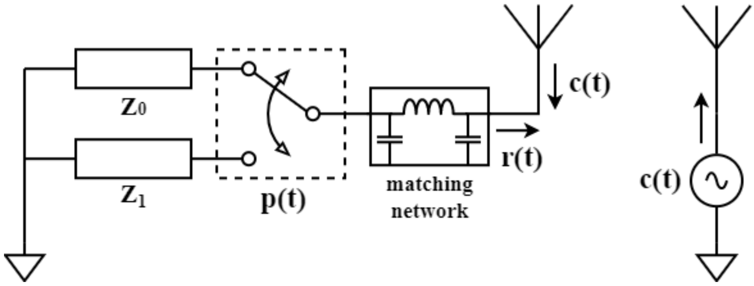

Figure 3.3: Equivalent circuit of a backscatter tag.

With the switch continuously toggling between two antenna load terminations, the scattering aperture of the tag needs to be redefined based on the reflection coefficients produced by each load. As the information is included in the difference in the backscattered field between the two states, it is used the differential radar cross-section ($\Delta\sigma$). In the context of Figure 3.3, which illustrates the two impedances Z_0 and Z_1, $\Delta\sigma$ can be mathematically defined as [3.11]:

$$\Delta\sigma = \frac{\lambda^2}{4\pi} G_{tag}^2 |\Gamma_0 - \Gamma_1|^2 m \tag{3.9}$$

where Γ_0 and Γ_1 are the complex power wave reflection coefficients associated to Z_0 and Z_1, respectively, and m is the modulation factor that is a function of the first Fourier coefficient of the modulating signal $p(t)$. Assuming a square wave with an ideal 50% duty cycle, m takes a value of $1/\pi^2$. Subsequently, the power at the receiver defined in 3.8 can be recalculated as a function of $\Delta\sigma$:

$$P_r = \frac{P_t G_t G_r \lambda^2 \Delta\sigma}{(4\pi)^3 d_t^2 d_r^2} \tag{3.10}$$

Can be noted from 3.9 that the power transmitted by the tag depends on the difference between Γ_0 and Γ_1. By using an open-circuit $Z_0 = \infty$ and a short-circuit $Z_1 = 0$, unitary positive and negative reflection coefficients are generated

UNIVERSITAT ROVIRA I VIRGILI
LONG-RANGE BACKSCATTERING COMMUNICATIONS FOR NEXT GENERATION IOT APPLICATIONS
Marc Lázaro Martí

($\Gamma_0 = 1$, $\Gamma_1 = -1$), thus maximizing the differential radar cross-section of the tag:

$$\Delta\sigma_{max} = \frac{\lambda^2}{\pi} G_{tag} m \tag{3.11}$$

Ideally, the two states Γ_0 and Γ_1, are on opposite sides of the real axis of the Smith chart when using an open-circuit and a short-circuit. In practice, however, parasitic elements in the circuit adds a reactive component to the load, shifting the reflection coefficients to the complex plane. The key to maximizing $\Delta\sigma$ is to keep the reflection coefficients 180º out-of-phase with each other.

3.4 Load modulation

In its simplest form, using only two loads, the backscattered signal can be modulated in frequency (FSK, Frequency Shift Keying), phase (PSK, Phase Shift Keying), or amplitude (ASK, Amplitude Shift Keying). The phase and amplitude directly depend on the complex impedance observed from the antenna terminals. Specifically, the phase relies on reactance, while the amplitude relies on the resistance of the load. On the other hand, the frequency depends on the load switching frequency.

When the antenna load switches between two states, the result is identical to an RF mixing process, where the incoming RF signal at the antenna $c(t)$ is multiplied by the load switching frequency $p(t)$. From Figure 3.3, assuming that $p(t)$ is close to an ideal square wave signal, inherent in the load-switching process, the resulting backscattered signal $r(t)$ can be described mathematically as follows:

$$\begin{aligned} r(t) &= p(t) \cdot c(t) \\ &= A \cdot cos(\omega_c t + \phi_0) \cdot sgn(cos(\omega_p t)) \\ &= \frac{2A}{\pi} \sum_{n=1,3..}^{\infty} \frac{1}{n} [cos((\omega_c - n\omega_p)t) - cos((\omega_c + n\omega_p)t)] \end{aligned} \tag{3.12}$$

where A is the amplitude of the backscattered signal, ω_c is the center frequency of the carrier, ω_p is the switching frequency of $p(t)$, ϕ_0 is the phase shift of $c(t)$ relative to $p(t)$, and sgn is the sign function. To ease the mathematical modeling, $c(t)$ has been considered a frequency tone. $p(t)$ is the square wave, synthesized in the load-switching process.

Similarly, we can model the periodically switched reflection coefficient with a square wave of amplitude $\Delta\sigma$ and frequency f_p. Therefore, after the Fourier series development of the square wave, the resultant spectrum, which is given as an infinite sum of delta functions located at each of the harmonics, can be mathematically defined as:

$$\Gamma(f) = \sum_{n=-\infty}^{n=+\infty} c_n \delta(f-(f_c+nf_p)) + \sum_{n=-\infty}^{n=+\infty} c_n \delta(f+(f_c+nf_p)) \tag{3.13}$$

where c_n are the Fourier coefficients, and f_c is the central frequency of the incident signal at the tag location. For a square waveform with duty cycle δ_c, the coefficients c_n are given by:

$$c_n = \begin{cases} \frac{1}{2}\Gamma_{avg} & , n = 0 \\ \frac{1}{2}|\Delta\Gamma|\delta_c(\frac{sin(n\pi\delta_c)}{n\pi\delta_c}) & , n \neq 0 \end{cases} \tag{3.14}$$

where Γ_{avg} is the average power reflection coefficient between Z_0 and Z_1 states. Using equation (3.13) and (3.13), the backscattered field can be written as:

$$\begin{aligned} \overrightarrow{E}_{scatt}(Z_{load}) = (\overrightarrow{E}_s + \frac{1}{2}\overrightarrow{E}_m\Gamma_{avg})(\delta(f-f_c)+\delta(f-f_c)) \\ + \overrightarrow{E}_m \sum_{n\neq 0} c_n\delta(f-(f_c+nf_p) \\ + \overrightarrow{E}_m \sum_{n\neq 0} c_n\delta(f+(f_c+nf_p)) \end{aligned} \tag{3.15}$$

Therefore, the first term in (3.15) results in the non-modulated term and depends on the structural mode of the tag. The second term represents the modulated sidebands that are a function of the antenna mode. Coefficients of higher amplitude in the Fourier expansion ($n = \pm 1$), are those that result in the components at the frequencies $f_c \pm f_p$.

Two important drawbacks can be seen from equations (3.12) and (3.15). First, the load switching generates a double sideband (DSB) modulation with two mirror copies on each side of the carrier ($\omega_c \pm \omega_p$), the backscattered signal, and the image. Second, the square-wave signal generates harmonics. To graphically show the two mentioned problems a frequency tone at 868 MHz has been backscattered. Figure 3.4 and Figure 3.5 show the measurements of the backscattered signal for 4 different frequencies (100 kHz - 400 kHz) and for several duty cycles (10% - 90%). It can be noted that when the tag is modulated with a 50% duty cycle square signal, the backscattered signal generates half of the harmonics than for other duty cycles (only odd harmonics) and provides the maximum power at these harmonics, as expected from the mathematical development of the Fourier series for a square signal with different duty cycles. Note that the backscattered field at first harmonic is proportional to the radar cross-section defined in equation (3.9).

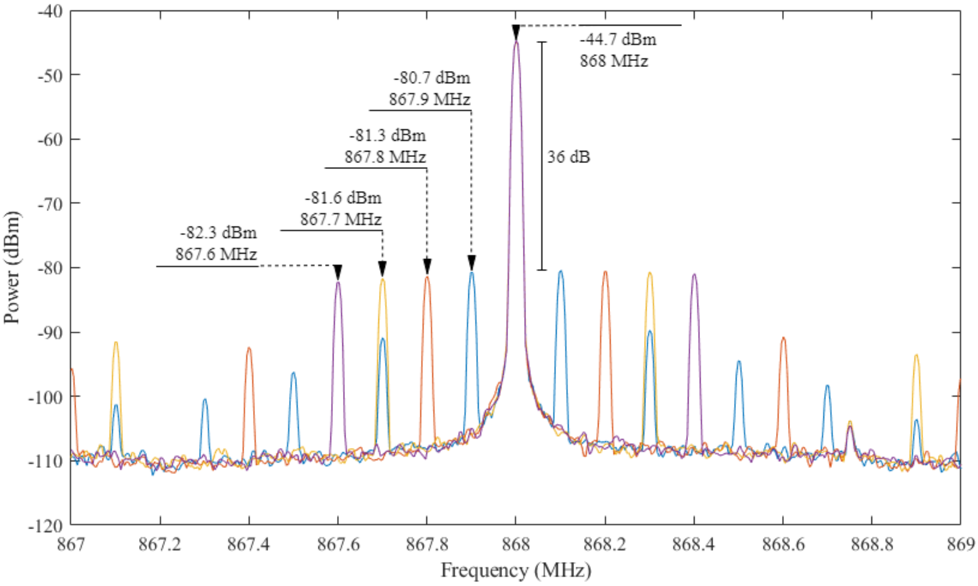

Figure 3.4: Spectrum of the backscattered signal for four different switching frequencies. Carrier wave: frequency tone at $f_c = 868MHz$.

3.5 Bibliography

[3.1] Naval Air Warfare Center. Electronic warfare and radar systems engineering handbook. *Electronic Warfare Division, Pont Mugu, CA*, 1997.

[3.2] Robert Blair Green. *The general theory of antenna scattering.* The Ohio State University, 1963.

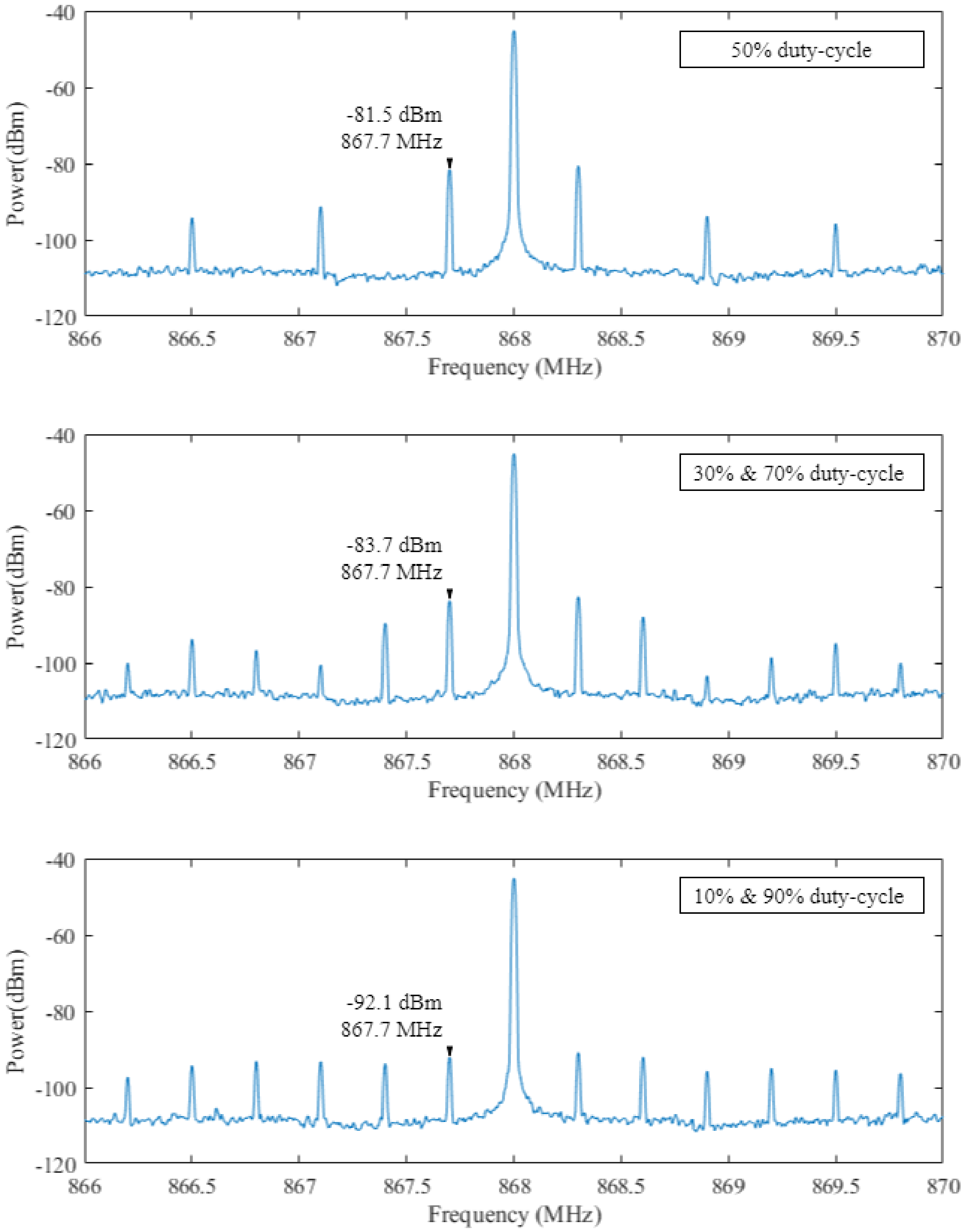

Figure 3.5: Spectrum of the backscattered signal when tag is modulated with an square wave of frequency $f_p = 300kHz$ for several duty cycles. Carrier wave: frequency tone at $f_c = 868MHz$.

UNIVERSITAT ROVIRA I VIRGILI
LONG-RANGE BACKSCATTERING COMMUNICATIONS FOR NEXT GENERATION IOT APPLICATIONS
Marc Lázaro Martí

[3.3] Roger F Harrington. Small resonant scatterers and their use for field measurements. *IRE Transactions on Microwave Theory and Techniques*, 10(3):165–174, 1962.

[3.4] John D Kraus, Ronald J Marhefka, and Ahmad S Khan. *Antennas and wave propagation*. Tata McGraw-Hill Education, 2006.

[3.5] Robert C Hansen. Relationships between antennas as scatterers and as radiators. *Proceedings of the IEEE*, 77(5):659–662, 1989.

[3.6] Constantine A Balanis. *Antenna theory: analysis and design*. John wiley & sons, 2016.

[3.7] Pavel V Nikitin and KV Seshagiri Rao. Theory and measurement of backscattering from RFID tags. *IEEE Antennas and Propagation Magazine*, 48(6):212–218, 2006.

[3.8] Chih-Chuan Yen, Alfonso E Gutierrez, Dharmaraj Veeramani, and Daniel Van Der Weide. Radar cross-section analysis of backscattering RFID tags. *IEEE Antennas and Wireless Propagation Letters*, 6:279–281, 2007.

[3.9] Aggelos Bletsas, Antonis G Dimitriou, and John N Sahalos. Improving backscatter radio tag efficiency. *IEEE Transactions on Microwave Theory and Techniques*, 58(6):1502–1509, 2010.

[3.10] WK Kahn and H Kurss. Minimum-scattering antennas. *IEEE Transactions on Antennas and Propagation*, 13(5):671–675, 1965.

[3.11] Pavel V Nikitin, KVS Rao, and Roberto D Martinez. Differential RCS of RFID tag. *Electronics letters*, 43(8):1, 2007.

UNIVERSITAT ROVIRA I VIRGILI
LONG-RANGE BACKSCATTERING COMMUNICATIONS FOR NEXT GENERATION IOT APPLICATIONS
Marc Lázaro Martí

Chapter 4

Backscattering Tag Design

This chapter covers all the work carried out in the design of the backscattering tag. It is divided into three main parts. The first part addresses two different implementations for the tag's front-end: one based on conventional load modulation and the other integrating a reflection amplifier to improve the backscattered power. One system emphasizes minimizing the tag's energy consumption, while the other prioritizes communication range. The choice between the two depends on the specific requirements of the application. The second part explores two different tag modulations based on LoRa. Finally, in the last part, the power consumption of the proposed implementations is summarized, and an energy harvesting system is proposed to power the tag.

4.1 Tag front-end

4.1.1 Load-modulated backscattering tag

Load-modulated backscattering tags can be classified as passive or active depending on the topology implemented in the front-end. While passive tags aim to ensure low-profile and battery-free designs, active tags sacrifice these properties to enhance the communication range. Passive tags integrate an energy harvesting system to power up the tag, typically using RF energy harvesting techniques that take advantage of the ever-present carrier as an energy source. To accomplish this, a portion of the incident RF signal is directed to a rectifying circuit, while the remaining portion is backscattered. Passive tags switch between a matched impedance, ensuring maximum power transfer to the rectifying circuit (harvesting state, $\Gamma_0 \approx 0$), and an unmatched impedance (reflecting state, $\Gamma_1 \leq 1$). This results in a differential reflection coefficient of $|\Delta\Gamma| = |\Gamma_1 - \Gamma_0| \leq 1$. On the other hand, active tags, which lack RF energy harvesting capabilities, can maximize the backscattered power by using antipodal reflection coefficients (ideally, $\Gamma_0 \simeq -1$, $\Gamma_1 \simeq 1$), resulting in $|\Delta\Gamma| \simeq 2$. However, no load-modulated tag can exhibit a $|\Delta\Gamma|$ higher than 2. Figure 4.1 illustrates the ideal reflection coefficients for the two aforementioned load-modulated systems.

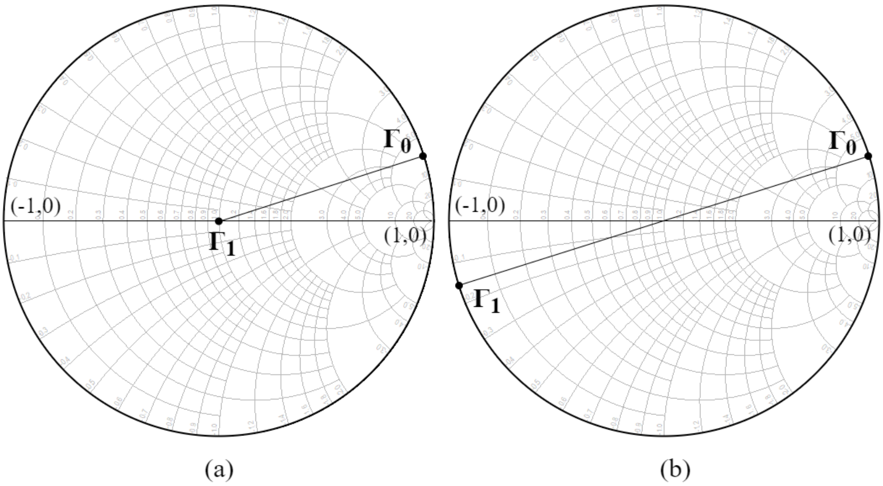

Figure 4.1: Tag reflection coefficients for two different load-modulation configuration: (a) to maximize $\Delta\sigma$ and (b) integrating energy harvesting capabilities.

Since the passive tags powered by the carrier signal energy are limited by the maximum operating range of the RF energy harvesting circuit, is better to opt for the implementation of an active tag, allowing to maximize $|\Delta\Gamma|$, as described in Figure 4.1a. The system diagram of the implemented load-modulated front-end is the same as the one proposed in Figure 3.3 of section 3.3, when antenna termination is toggled between two states with an RF switch. The two antipodal states have been generated using a short circuit and an open circuit. The switch used is an SPDT ADG902 CMOS reflective switch from Analog devices with a typical insertion loss of 0.8 dB at 1 GHz [4.1].

A PCB with the ADG902 switch connected to an SMA connector through a 50 Ω transmission line has been manufactured to characterize the front-end with a Vector Network Analyzer (VNA). Figure 4.2 shows an image of the PCB with the ADG902 and a diagram of the measurement setup.

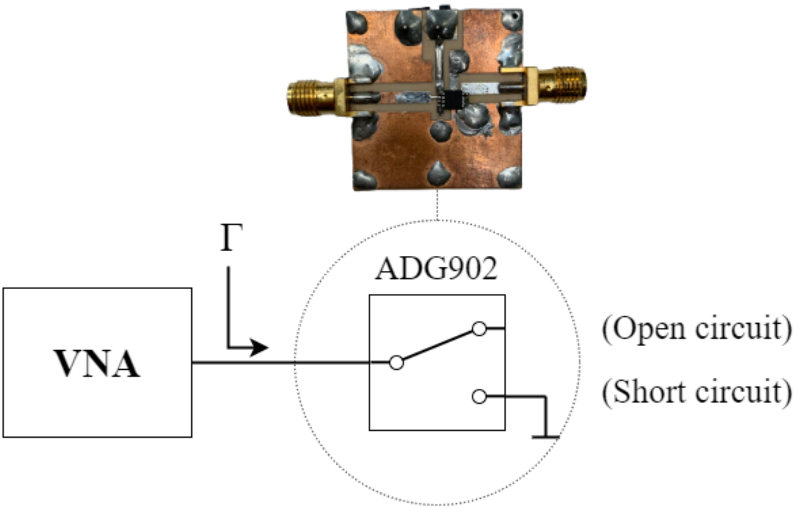

Figure 4.2: Photograph of the ADG902 characterization board with a diagram of the measurement setup.

Figure 4.3 shows the measured reflection coefficient when the switch is on the state Z_{SC} (loaded with a short circuit) and the state Z_{OC} (loaded with an open circuit). A marker at 868 MHz shows that the two states have a phase difference close to 180º. Losses of 1.5 dB with respect to the ideal short circuit and open circuit are obtained due to the insertion loss of the switch.

Figure 4.4 illustrates the ratio between the measured differential reflection coefficient and the maximum differential reflection coefficient for an ideal open

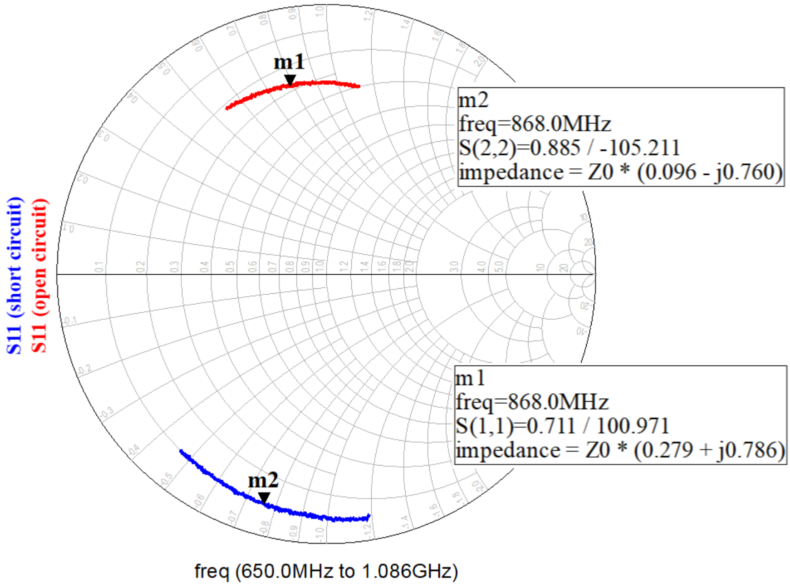

Figure 4.3: Measured reflection coefficients of the ADG902 SPDT switch for state 1 (open-circuit) and state 2 (short-circuit) at 868 MHz

circuit and short circuit ($|\Delta\Gamma|^2/4$). The ratio decreases as the frequency increases due to the higher insertion loss of the switch. The implemented prototype exhibits a loss of -2 dB compared to the ideal case for the 868 MHz ISM band.

4.1.2 Amplified backscattering Tag

To overcome the differential reflection coefficient constraint discussed in the previous subsection ($|\Delta\Gamma| \leq 2$), an effective solution is to integrate a reflection amplifier within the tag front-end. To do so, the antenna is directly terminated with the reflection amplifier. When the amplifier is disabled, it generates a reflection coefficient of $\Gamma_0 = Be^{j\phi_0} < 1$, where B and ϕ_0 are the amplitude and the phase of the complex reflection amplifier of the amplifier disabled. On the other hand, when the amplifier is enabled, it produces a reflection coefficient of $\Gamma_1 = \sqrt{G}e^{j\phi_1} > 1$, where G and ϕ_1 represents the gain and phase of the amplifier in this state (proportional to the negative impedance generated by the amplifier). By toggling between these two states—enabling and disabling the amplifier— the backscattered signal can be modulated. The maximum value of the differential reflection coefficient, $|\Delta\Gamma|$, occurs when $B = 1$ and $\phi_0 = \phi_1 + \pi$,

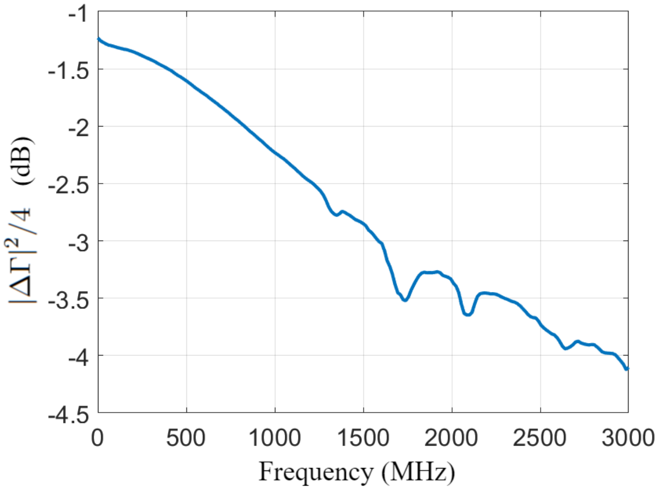

Figure 4.4: Ratio between the measured differential reflection coefficient and the ideal differential reflection coefficient as a function of the frequency for the ADG902 switch.

while the minimum value is obtained when $B = 1$ and $\phi_0 = \phi_1$. Therefore, the differential reflection coefficient falls within the following range: $(\sqrt{G} - 1) \leqslant |\Delta\Gamma| \leqslant (\sqrt{G} + 1)$. However, it's important to note that by turning the amplifier on and off, only one of the two states can take advantage of the amplification. To further increase $|\Delta\Gamma|$, a phase-shift modulator connected between the reflection amplifier and the antenna can be used to generate two antipodal states while the reflection amplifier is always on, resulting in $|\Delta\Gamma| = 2\sqrt{G}$ [4.2]. Figure 4.5 depicts the reflection coefficients when the backscatter signal is modulated enabling and disabling the amplifier and using a phase-shifter while the amplifier remains always on. This section focuses on implementing the last mentioned system, depicted in Figure 4.6.

Several works in the literature propose integrating amplifiers into tags to extend the communication range. While some systems suggest using two-antenna topologies, where one antenna receives the carrier signal, amplifies it, and transmits it through the other antenna, this approach is not universally applicable. Using two antennas carries the risk of feedback, where the amplified signal loops back through the tag's receiving antenna, resulting in oscillation and interferences in the frequency spectrum. This technique can be employed in automotive applications where radar systems operate at 24 GHz (K-band) and 77 GHz

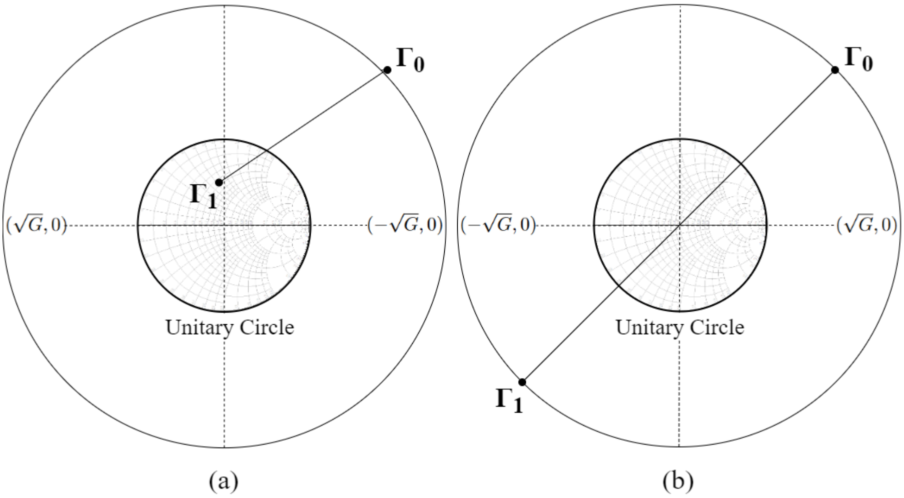

Figure 4.5: Reflection coefficients of the tag with a reflection amplifier for two different modulation systems: (a) by turning the amplifier on and off, and (b) through a phase modulator while the amplifier remains always on.

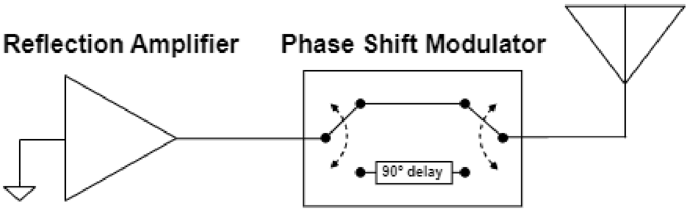

Figure 4.6: Diagram of the active backscattering tag based on a reflection amplifier along with a phase-shift modulator.

(W-band) [4.3]. At these frequencies, the isolation between the antennas is high and the signal attenuates rapidly, reducing the likelihood of system oscillation. Moreover, radar applications are suitable for utilizing highly directional antennas, further minimizing the probability of oscillation, as the interaction between pedestrians or vehicles typically occurs in specific directions. On the contrary, in the UHF band, this technique is not commonly used for two reasons: the operating frequency and the use of omnidirectional antennas. At 868 MHz, which is a widely used UHF tag operation frequency, the signal attenuation is much lower, and the use of directional antennas is usually not feasible due to application requirements. Therefore, reflection amplifier-based topologies are more suitable for designing tags in UHF applications, and this section will focus on exploring this topology. Figure 4.7 illustrates the two different described topologies for the design of amplified backscattering tags.

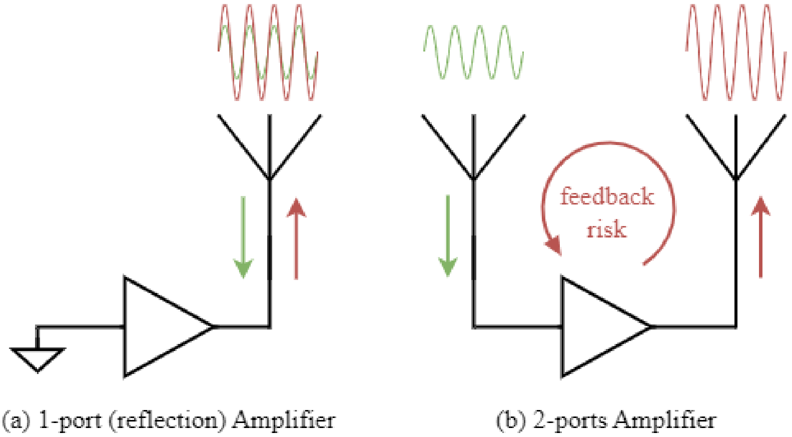

(a) 1-port (reflection) Amplifier (b) 2-ports Amplifier

Figure 4.7: Illustration of a backscattering tag based on a 1-port reflection amplifier (a) and 2-ports reflection amplifier (b).

Reflection amplifiers are a unique class of amplifiers that harness the principles of wave reflection to achieve amplification. Unlike conventional amplifiers that rely solely on gain elements like transistors, reflection amplifiers utilize impedance mismatches and wave interactions to enhance the amplitude of signals. The concept of reflection amplification is rooted in the transmission line theory and the phenomenon of signal reflection. When a signal encounters an impedance mismatch at the interface of two transmission lines or components, a portion of the signal is reflected back towards the source. Reflection amplifiers exploit this reflection by carefully designing the impedance characteristics of the system to achieve signal amplification. By skillfully manipulating impedance mismatches, the reflected signal can be combined with the incoming signal in a constructive manner, resulting in an amplified output [4.4].

One of the major advantages of reflection amplifiers is their inherent broadband nature, allowing them to operate over a wide frequency range. Furthermore, they can offer high linearity, low noise figures, and good power efficiency. These characteristics make reflection amplifiers suitable for applications such as radio frequency (RF) and microwave systems, where high performance and broad frequency coverage are essential [4.5].

Several devices, including IMPATT diodes, tunnel diodes, Gunn diodes, bipolar transistors, and FET transistors, can be used in their simplest form

UNIVERSITAT ROVIRA I VIRGILI
LONG-RANGE BACKSCATTERING COMMUNICATIONS FOR NEXT GENERATION IOT APPLICATIONS
Marc Lázaro Martí

to synthesize this type of amplifier. Among them, tunnel diodes have gained widespread attention as an excellent option due to their super-low power consumption [4.6]. However, designs based on bipolar transistors demonstrate comparable performance within the micro-ampere range [4.2]. Therefore, both devices will be subsequently assessed and compared for the implementation of low-power reflection amplifiers within the backscattering tag front-end.

A comparison of various previous contributions on the design of reflection amplifiers is provided in Table 4.1. It is worth noting that MBD2057 tunnel diodes exhibit the best efficiency, with an outstanding power consumption of 18 μW. Additionally, using the same device, the maximum gain, with a value of 51 dB is reported for an input power of -100 dBm. Transistor-based models show more modest results, with a maximum gain of 36.19 dB for an input power of -60 dBm. The minimum power consumption reported for transistor-based designs is 325 μW, achieved using a BFT25A bipolar junction transistor.

UNIVERSITAT ROVIRA I VIRGILI
LONG-RANGE BACKSCATTERING COMMUNICATIONS FOR NEXT GENERATION IOT APPLICATIONS
Marc Lázaro Martí

Ref	Year	Device	Frequency (GHz)	Consumption (μW)	P_{in} (dBm)	Gain (dB)
[4.7]	2021	NE3509M04 GaAs HJ-FET	2.37 2.57	1530 5500	-60 -50	36.19 35.83
[4.8]	2021	GI307A TD	0.097	90	-50	23
[4.9]	2021	MBD2057-E28 TD	5.8	40	-90	50
[4.10]	2020	AI301A GaAs TD	0.41 0.82	144	-43	30 20
[4.11]	2020	MBD2057-E28 TD	5.8	18	-100	51
[4.6]	2019	1N3712 Ge TD	0.86	65	-60	35
[4.12]	2019	NE3509M04 GaAs FET	2.45	-	-	11.5
[4.13]	2018	MBD5057-E28 Ge TD	5.8	45	-75	40
[4.14]	2018	MBD5057-E28 Ge TD	5.8	20.4	-81	35
[4.15]	2017	NE3509M04 GaAs FET	1.8 (2.4)	2400	-25	21.9 13
[4.16]	2017	AI301A GaAs TD	0.89	200	-30	17
[4.17]	2017	AI201A GaAs TD	0.915	178	-30	13
[4.18]	2016	2um Resonant TD	5.8	420	8.6	-25.4
[4.19]	2015	MBD5057-E28 Ge TD	5.45	45	-70	34.4
[4.2]	2014	BFT25A BJT	0.915	325	-50 -30	10.2 4.9
[4.20]	2014	BFT25A BJT	0.9	605	-50 -30	30 14.92
[4.21]	2014	BFT25A BJT	0.9	664	-50 -20	29 9
[4.22]	2014	InP 0.9 Resonant TD	5.7	125	-	10.4
[4.23]	2013	BFP405 Si BJT	5.25	2000	-25	13

Table 4.1: Comparison of the reflection amplifiers proposed in the literature.

4.1.2.1 Tunnel diode-based reflection amplifier

Tunnel diodes, also known as Esaki diodes, are specialized semiconductor devices that exhibit a unique behavior known as quantum tunneling as a result of the high doping of the p-n junction. Developed in the 1950s by Leo Esaki, tunnel diodes are characterized by their ability to efficiently and rapidly transfer charge carriers through the energy barrier of a semiconductor material. This intriguing phenomenon allows tunnel diodes to operate at extremely high frequencies and to exhibit negative resistance, making them valuable components in various electronic applications. Unlike traditional diodes that rely on majority carrier conduction, tunnel diodes exploit the quantum mechanical phenomenon of electron tunneling. This occurs when electrons can pass through a potential barrier, even though classically they would not possess enough energy to overcome it. The delicate interplay between the band structure of the semiconductor material and the applied voltage leads to a pronounced tunneling effect. Due to their unique characteristics, tunnel diodes find application in areas that require fast switching speeds, high-frequency oscillators, low-noise amplifiers, and microwave circuits. Their ability to operate in the terahertz frequency range makes them suitable for cutting-edge technologies such as telecommunications, radar systems, and high-speed digital communication [4.24]. Therefore taking advantage of the beforementioned properties, a reflection amplifier based on an AI301A tunnel diode is designed, manufactured, and characterized. The circuit schematic for the proposed reflection amplifier is depicted in Figure 4.8.

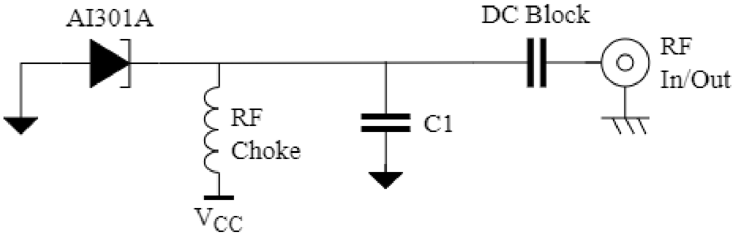

Figure 4.8: Circuit schematic of the proposed AI301A-based reflection amplifier.

The first step is to characterize the tunnel diode in DC to find the ideal polarization point. DC characterization has been done with a U2722A modular source unit (SMU) from Keysight. Figure 4.9 shows the measured IV polarization curve of the AI301A tunnel diode. At low biasing voltage, tunnel diodes presents a differential negative resistance region where current decreases while voltage increases. This characteristic is of particular interest in the design of resonators and amplifiers. As observed from the measured IV curve, the tunnel diode sharply reverses its current at 0.108 mV and 0.64 mV. However, the tunnel diode can only be polarized to leverage the differential negative resistance within the range from 0.108 mV to 0.300 mV, maximizing the gain from 114 mV to 122 mV (>20 dB).

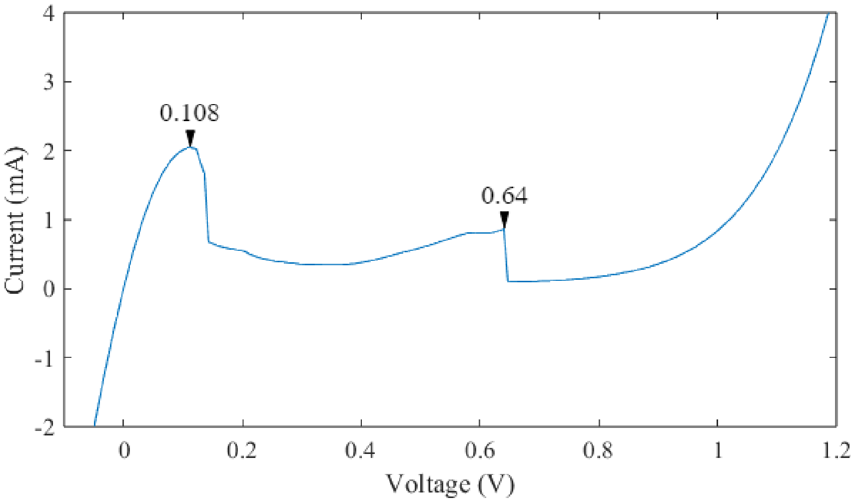

Figure 4.9: Measured IV curve of the AI301A tunnel diode.

Once the suitable biasing point is determined (114 mV, 1 mA), the S-parameters of the tunnel diode at this biasing point can be measured using the VNA to proceed with the design. The layout of the reflection amplifier has been designed and simulated using ADS. Figure 4.10 shows the layout and a photograph of the final prototype. Capacitor C1 has been connected through a stub to ease the frequency adjustment process. Instead of a straight stub, it has been implemented using meanders to reduce the size of the board. The reflection amplifier has been manufactured on Rogers 4003C of 32 mils thick. Figure 4.11 and Figure 4.12 show the reflection amplifier gain as a function of the biasing voltage and the input power, respectively.

Figure 4.11 shows how the tunnel diode successfully amplifies the reflected signal in the UHF band. It can be observed that the amplifier gain requires a very precise power supply, as variations as low as 3 mV significantly affect the

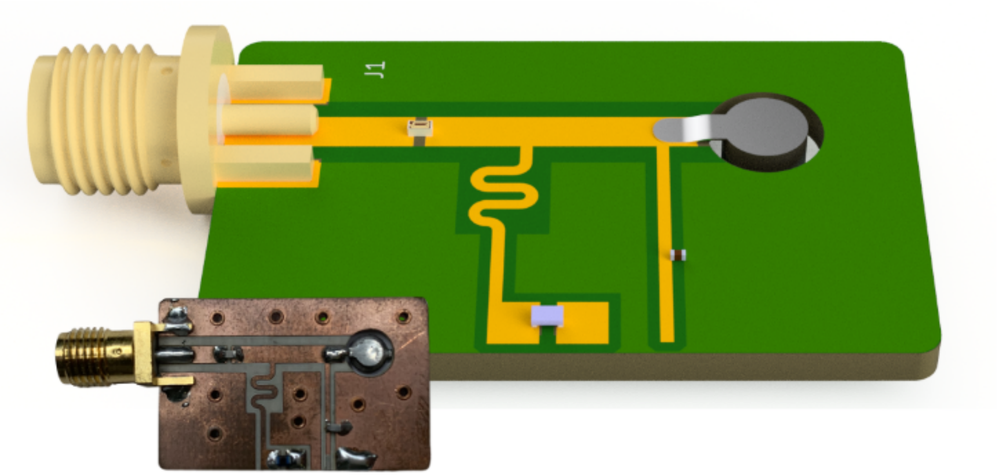

Figure 4.10: Render and photography of the designed AI301A-based reflection amplifier.

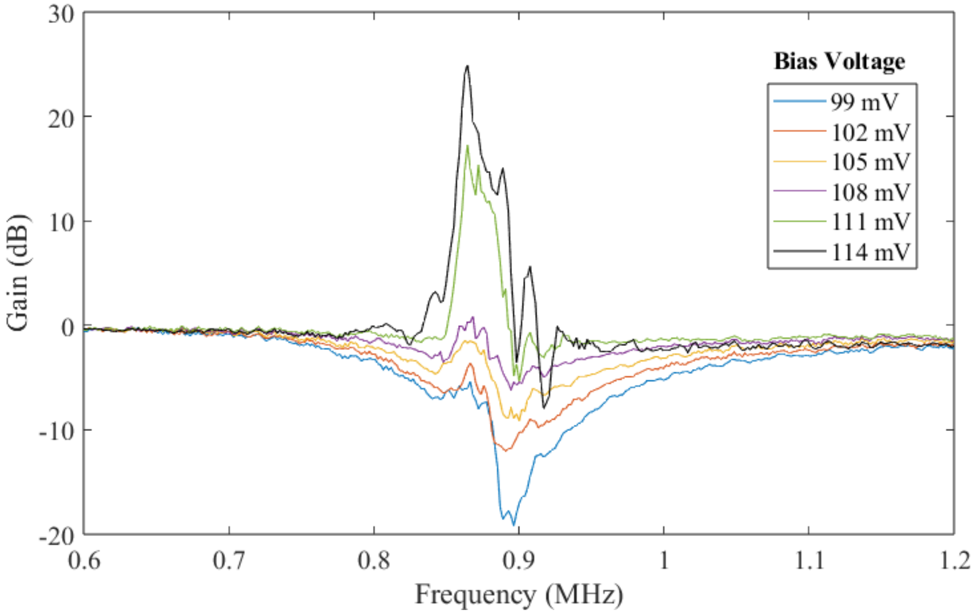

Figure 4.11: Measured gain (S_{11}) of the AI301A-based reflection amplifier as a function of the biasing voltage.

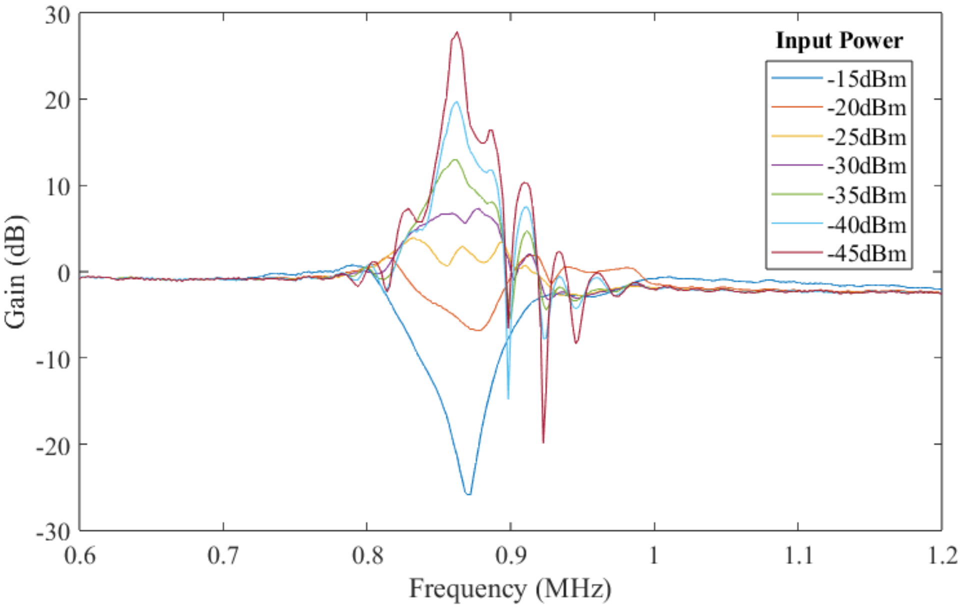

Figure 4.12: Measured gain (S_{11}) of the AI301A-based reflection amplifier as a function of the input power.

amplifier's behavior.

As expected, in Figure 4.12 can be observed how the amplifier gain decreases with an increase in input power due to the gain compression. In reflection amplifiers, as the input power increases, the reflected signal also becomes stronger, making the active element (the tunnel diode in this case) to reach its saturation limit. At this point, the tunnel diode can no longer amplify the signal linearly and starts to distort it.

4.1.2.2 Transistor-based reflection amplifier

The design of a reflection amplifier with a transistor does not differ much from the design of an oscillator. In fact, the basic principle is the same: to generate positive feedback to amplify the signal at the collector. However, the reflection amplifier is carefully biased to operate near the unstable region, but without reaching oscillation. The design of the reflection amplifier is based on the topology of a Colpitts oscillator. The schematic of the proposed circuit is shown in Figure 4.13.

Traditionally, the design of an oscillator or a reflection amplifier involves

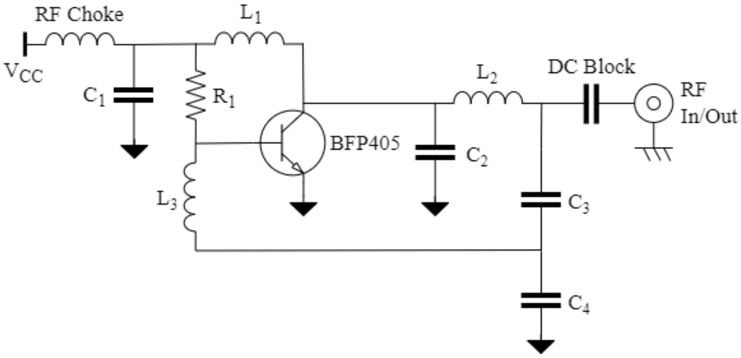

Figure 4.13: Circuit diagram of the proposed BFP405-based reflection amplifier.

adjusting the components of the resonant tank circuit to determine the desired oscillation frequency and carefully defining the bias point of the transistor to ensure stable operation. Additionally, impedance matching is essential for optimizing power transfer and overall performance, as it affects the reflected signals fed back to the amplifier, resulting in either an increase or decrease in gain based on their relative phase (constructive or destructive interference).

The reflection amplifier has been designed and tuned in ADS using discrete components. Alternatively, it can be designed solely with microstrip stubs, which reduces costs but increases the layout size. In practice, the use of discrete components simplifies the amplifier adjustment process as it eliminates the need for layout modifications. Hybrid designs are a favorable option as they combine the benefits of both systems, offering cost-effectiveness and flexibility for system adjustments. The layout and photography of the designed and manufactured amplifier are presented in Figure 4.14. The manufactured reflection amplifier has been integrated directly with the phase shift modulator described in the next subsection.

The amplifier has been implemented using a BFP405 SIEGET NPN bipolar transistor from Infineon and adjusted to operate at the 868 MHz ISM band. The values of the discrete components used are the following: $C_1 = 470pF$, $C_2 = 2.8pF$, $C_3 = 6.8pF$, $C_4 = 1.2pF$, $L_1 = 20nH$, $L_2 = 35nH$, $L_3 = 11.6nH$, $R_1 = 355k\Omega$, $C_{DC-block} = 1nF$, $L_{RF-choke} = 100nH$. The biasing point of the reflection amplifier has been adjusted to be 1.8 V, matching the minimum voltage required for any microcontroller.

Figure 4.15 shows the measured IV curve of the amplifier. In contrast to the

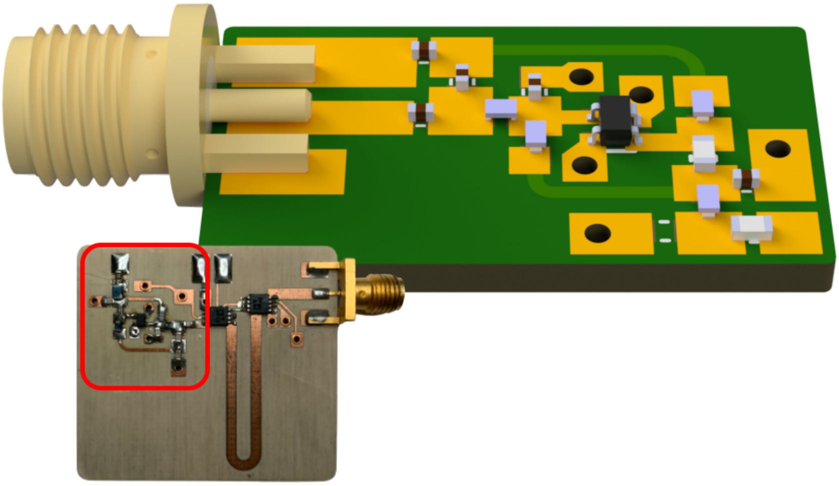

Figure 4.14: Render and photography of the designed BFP405-based reflection amplifier.

tunnel diode IV curve, the transistor-based reflection amplifier increases its current continuously while voltage increases. Just like in the previous subsection, the gain of the amplifier has been characterized based on the bias voltage and input power. The results are depicted in Figures 4.16 and 4.17, respectively.

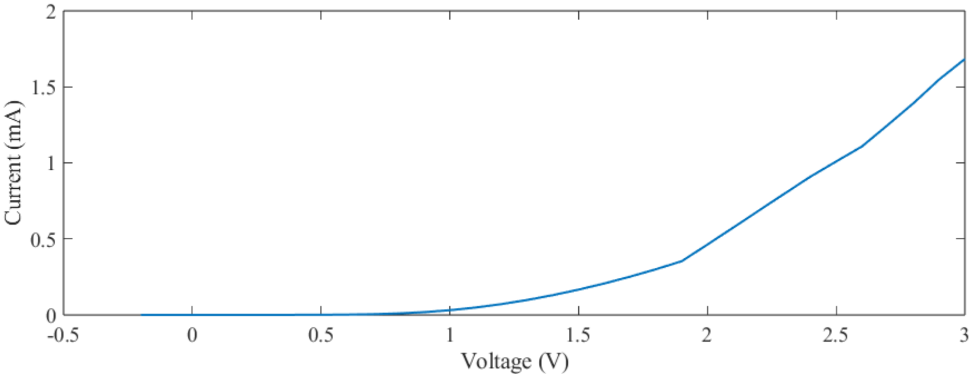

Figure 4.15: Measured IV curve of the BFP405-based reflection amplifier.

Although the power consumption of the tunnel diode-based reflection amplifier (114 μW) is significantly lower compared to the transistor-based reflection amplifier (612 μW), when the amplifiers have to be integrated within a full sys-

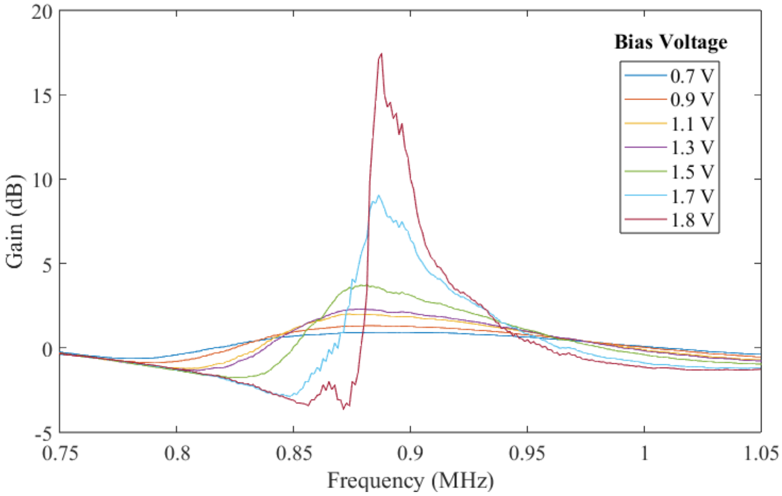

Figure 4.16: Measured gain (S_{11}) of the BFP405-based reflection amplifier as a function of the biasing voltage.

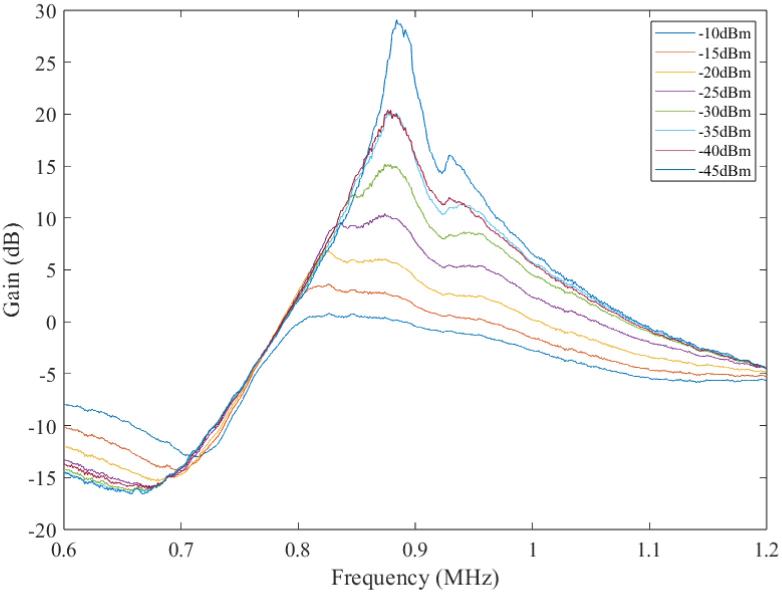

Figure 4.17: Measured gain (S_{11}) of the BFP405-based reflection amplifier as a function of the input power.

UNIVERSITAT ROVIRA I VIRGILI
LONG-RANGE BACKSCATTERING COMMUNICATIONS FOR NEXT GENERATION IOT APPLICATIONS
Marc Lázaro Martí

tem, the tunnel diode version requires to reduce the minimum supply voltage of the microcontroller by more than one order, from 1.8 V to 114 mV. This down-conversion is not trivial, and no commercially available solutions can be found. A dedicated multi-stage step-down DC-DC converter should be designed with an efficiency high enough to not exceed the power consumption of the transistor version. It seems more favorable to use energy harvesting techniques to power the tunnel diode-based reflection amplifier, but the current consumption and the narrow biasing voltage margin suppose a challenge. A fair comparison between the efficiency of both amplifiers requires considering the power supply conditioning. The transistor-based reflection amplifier has been designed to operate at a voltage of 1.8 V to avoid any conversion losses.

Therefore, although the transistor-based amplifier exhibits a more modest gain-consumption efficiency compared to the tunnel diode when analyzed individually, it proves to be more efficient within the context of a full system integration, since it does not require voltage conversions and has a lower current consumption. Additionally, with the transistor-based design, the biasing voltage can vary almost 1 V still exhibiting gain.

4.1.2.3 Phase shift modulator

As mentioned, the backscattering tag can be modulated by turning on and off the amplifier, thus absorbing or amplifying the impinging signal. However, backscattered power can be maximized keeping the amplifier always on and shifting the phase of the signal by means of a phase modulator. The modulator connects the antenna directly to the reflection amplifier, or alternately through a 90º delay line. As the signal travels twice through the modulator, finally two reflection coefficients shifted 180º one to the each other can be generated. Phase shift modulator has been implemented using two ADG918 SPDT switches and characterized using a vector network analyzer. Figure 4.18 shows a render and a photograph of the prototype. The size of the phase-shift modulator can be reduced using a meander line instead of a straight line or using a coplanar waveguide instead of a microstrip waveguide to reduce the width of the 50 Ω line.

Figure 4.19a and Figure 4.19b show the S-parameter measurements for both states (open-circuit and short-circuit). Figure 4.20a and Figure 4.20b show the measurement of the insertion-loss and the phase shift for both states overlapped

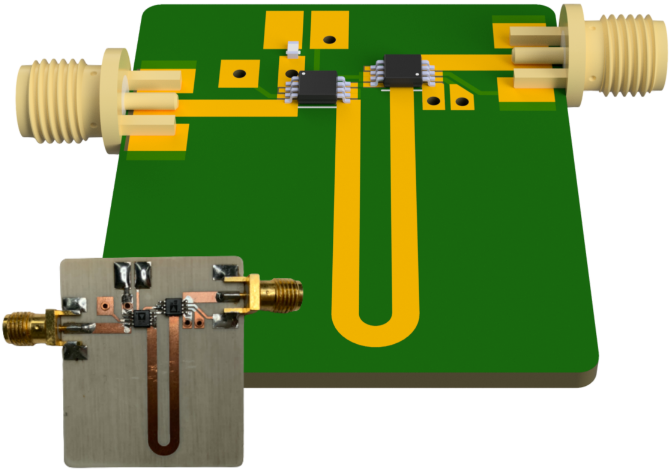

Figure 4.18: Render and photography of the designed phase shift modulator.

to compare the difference. The insertion loss is close to 1.8 dB in both states and good matching is observed with a return loss below 24 dB. Modulator insertion loss must be assessed in concordance with the amplifier gain and can be expressed mathematically as [4.2]:

$$IL(dB) > -10\log\frac{1}{2}\cdot\frac{1}{2\sqrt{G}} \tag{4.1}$$

where IL is the insertion loss of the phase-shift modulator and G is the gain of the reflection amplifier. If the system design does not ensure compliance with Equation (4.1), it is preferable to opt for an on-off amplifier modulation (as depicted at the beginning of the section in Figure 4.5a), avoiding the losses inserted by the modulator, and only amplifying one of the two states. However, the measured gain of both reflection amplifiers is high enough to compensate for the round trip insertion loss of the switches (3.6 dB).

The phase shift modulator has been tested with the BFP405 reflection amplifier. Figure 4.21 shows the two states generated by the phase modulator when the amplifier is on (blue) and off (red). It can be appreciated that the blue states are outside the unitary reflection coefficient circle. Since the blue state includes the gain of the amplifier and the losses of the modulator, the reflection coefficient higher than one proves the fulfillment of the equation 4.1.

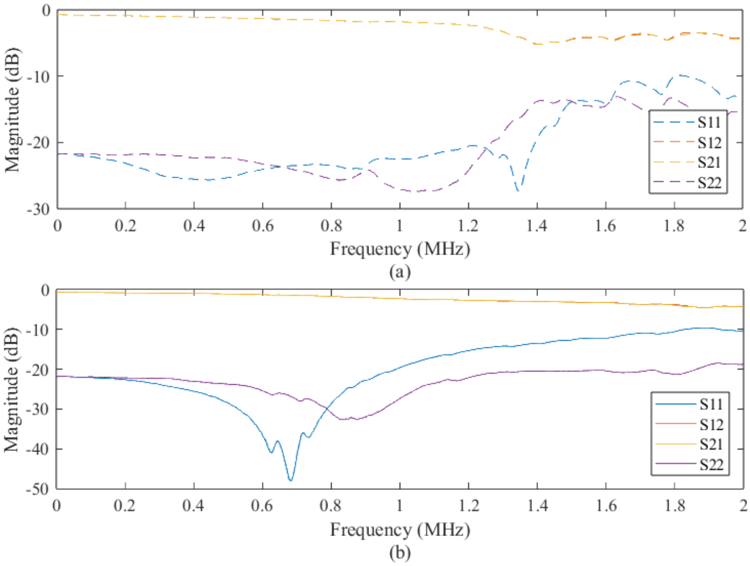

Figure 4.19: S-parameter measurements of the phase-shift modulator in both states: open circuit (a) and short-circuit (b).

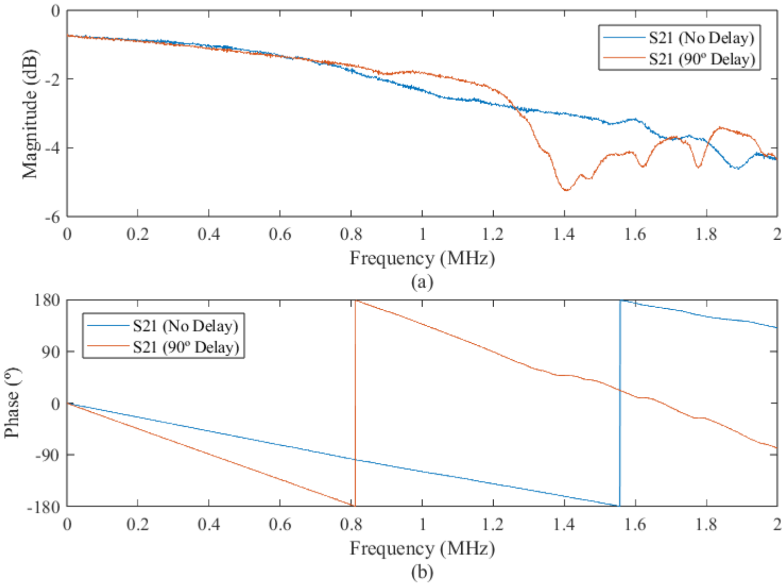

Figure 4.20: Insertion loss (S_{21})(a) and phase delay (b) characterization of the reflection amplifier for both states (90º phase shift (blue) and 0º phase shift (orange)).

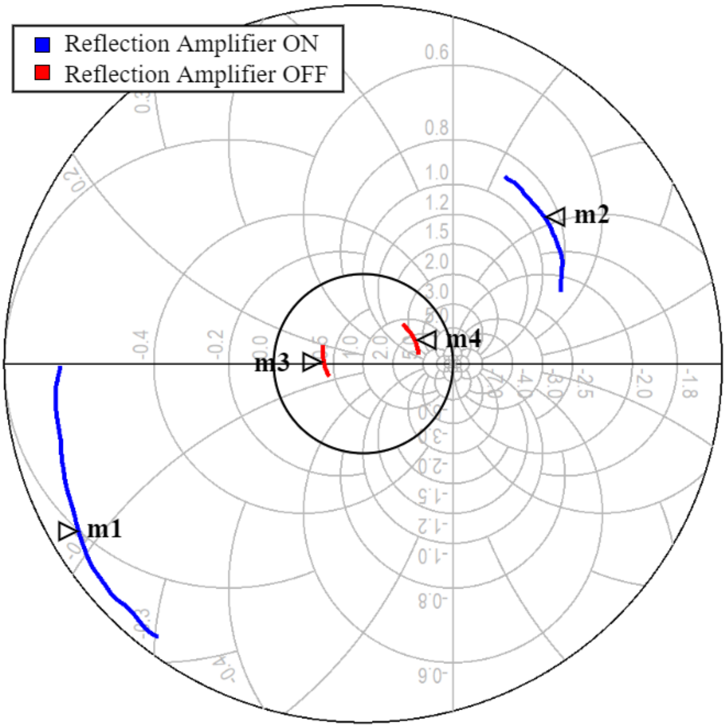

Marker	State	[Mag/Deg]	Impedance
m1	0°	[3.68/ − 149.54°]	$Z_0 \cdot (-0.60 - j0.18)$
m2	180°	[2.60/39.34°]	$Z_0 \cdot (-1.54 - j0.88)$
m3	0°	[0.44/177.07°]	$Z_0 \cdot (0.39 - j0.02)$
m4	180°	[0.63/27.86°]	$Z_0 \cdot (2.13 - j2.09)$

Figure 4.21: Measured reflection coefficient S_{11} for the two states generated by the phase modulator ($0^{\underline{o}}$ and $180^{\underline{o}}$ shift) when the amplifier is turned on (blue) and off (red). Frequency range from 855 MHz to 885 MHz. Markers placed at 868 MHz.

4.1.2.4 Amplifier current monitoring

Despite the significant research in the literature on the design and integration of reflection amplifiers in the tag's front-end, some challenges need to be addressed further. As observed in the previous sections, the behavior of reflection amplifiers depend on the input power. At certain power levels, there is a risk that the amplifier may start to oscillate, thus generating interference in the spectrum. Furthermore, current consumption increases with higher input powers. Therefore, keeping the reflection amplifier continuously powered in all scenarios does not appear to be a good practice. To address this issue, an active control approach is proposed to enable or disable the reflection amplifier based on its power consumption, which is directly proportional to the incident power. To achieve this, it is suggested to integrate a current sensor into the amplifier's power supply line. A schematic of the system is shown in Figure 4.22.

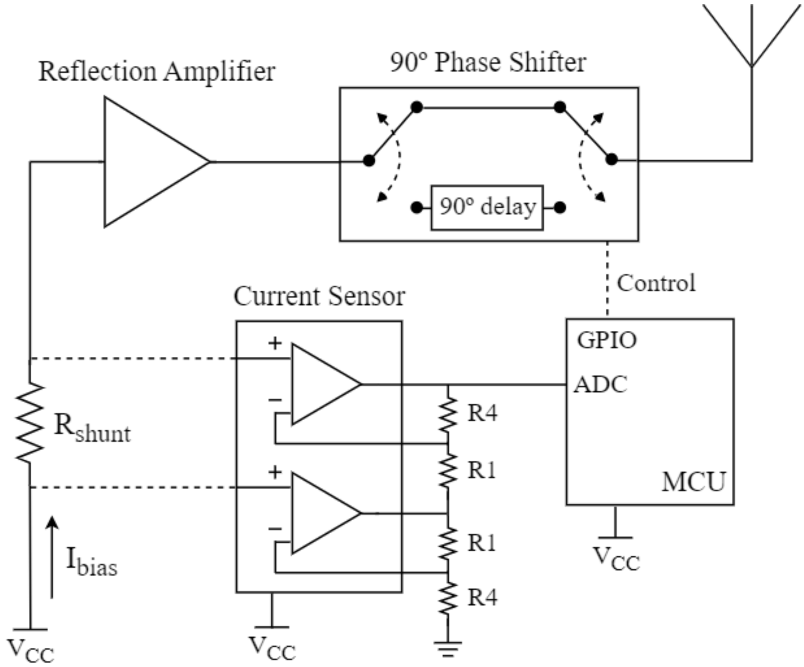

Figure 4.22: Measured reflection amplifier biasing current as a function of the RF input power.

The current sensor has been implemented by placing a shunt resistance at the input of the reflection amplifier bias. The shunt resistance voltage drop is amplified with an op-amp in differential topology and measured by a microcontroller (MCU). The current sensing accuracy depends on the gain of the amplifier, on the resolution of the MCU analog-to-digital converter (ADC), and on the voltage drop, which in turn depends on the magnitude of the shunt resistance and the current flowing through it.

The current sensor design has been adjusted for an 8-bit Attiny417 MCU, which integrates a 10-bit ADC. Many low-power microcontrollers integrate ADCs of this same resolution. Given a reference voltage of 0.55 V, the ADC can measure voltage variations of 0.537 mV. The reflection amplifier current draw ranges from 280 μA up to almost 1 mA. However, the current sensor is designed to turn the amplifier on and off for current values between 280 and 400 μA. Higher currents always disable the amplifier.

A 10 Ω shunt resistance is used, which results in voltage drop from 2.8 mV to 4 mV. Resistors R1 and R4, depicted in Fig. 4.22, are set to 1 $k\Omega$ and 100 $k\Omega$, respectively, setting a gain of 101. With this configuration, the operational amplifier output voltage ranges from 282.8 to 404 mV. In other words, the minimum detectable current step is 0.5 μA. To implement the current sensor a MAX9916 has been used, which integrates two 20 μA rail-to-rail Op-Amps. Building the differential amplifier with both op-amps results in a total current draw of 40 μA. However, the current consumption of the sensor can be further reduced to a few μA by using integrated current sensors such as the MAX9634, rendering the power consumption practically negligible compared to that of the reflection amplifier.

Fig. 4.23 shows the current consumption of the amplifier in relation to the input RF power. Oscillations have been observed in the spectrum analyzer for input powers exceeding -25 dBm. However, even at -40 dBm, a marginal increase in current can be discerned, providing an opportunity to deactivate the amplifier, thus reducing 300 μA the current consumption of the system. With power levels of approximately -40 dBm, the backscattering tag can effectively work without the need for the reflection amplifier.

Although in practice many wireless transmissions tend to be below -40 or -50 dBm at few meters from the transmitter, this is not always the case. For example, a commercial LoRa transmitter, which can emit 20 dBm, with a monopole antenna (3 dBi gain) can perfectly reach -25 dBm at a distance of 3m in direct line-of-sight.

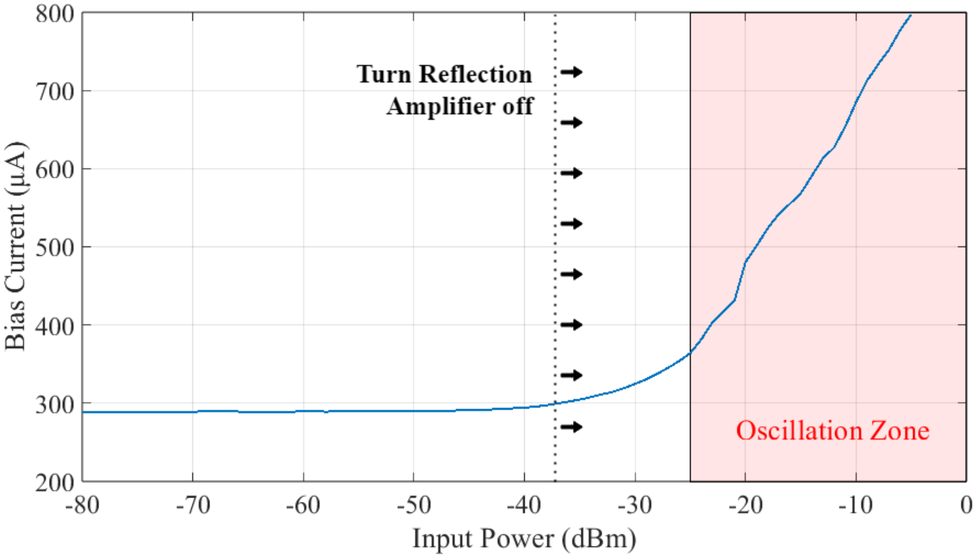

Figure 4.23: Measured reflection amplifier biasing current as a function of the RF input power.

Considering that backscattering tags are designed for the IoT field, where many nodes coexist, it is not uncommon to assume that some of them could eventually be located a few meters or centimeters away from the transmitter. In such cases, these nodes may start to oscillate, consequently disabling the communications of all the other nodes. Thus, the active control of this type of amplifier is mandatory if they are integrated into backscattering tags. This practice becomes even more necessary in reflection amplifiers based on tunnel diodes, which present a less stable behavior.

4.1.3 Backscattered power comparison

This brief section shows the gain introduced by the reflection amplifier compared to the conventional load-modulated front end. Both tunnel diode-based and transistor-based reflection amplifier gains have been compared to the conventional front-end. Measurement has been taken in monostatic configuration with two 9 dBi UHF RFID antennas located 1 meter away from the tag. Absorbing panels have been used behind the tag to reduce interferences. Measurements are presented in figure 4.24. The peak backscattered power in the first harmonic is -95.05 dB, -78.65 dB, and -76.55 dB for the conventional load modulated, the transistor-based, and the tunnel diode-based reflection amplifier, respectively. The switching frequency of the tag has been set to be 100 kHz. The SIEGET BJT transistor has been polarized at 1.75 V and the tunnel diode at 114 mV.

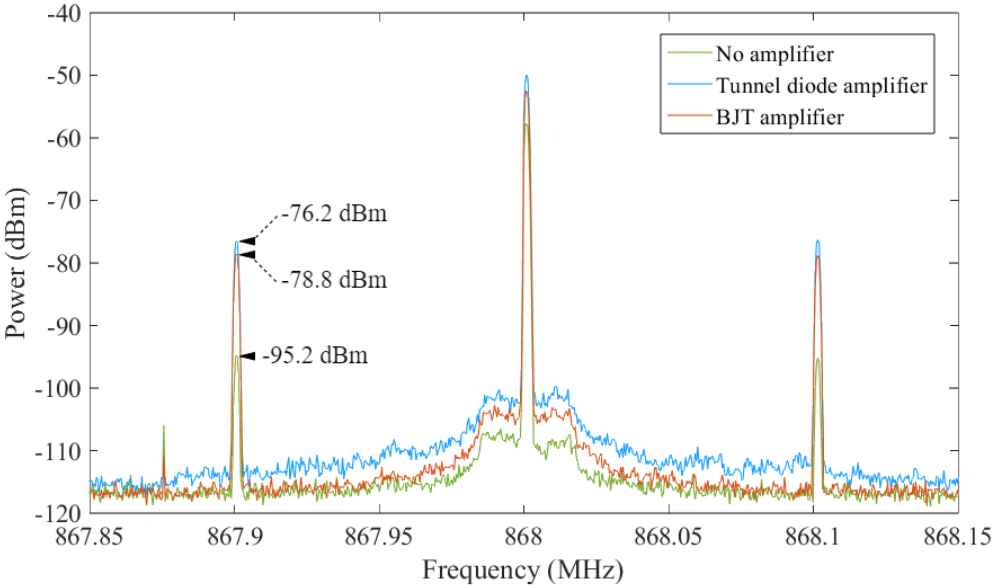

Figure 4.24: Comparison between the proposed front-ends: passive load-modulation (green), transistor-based reflection amplifier (red), and tunnel diode-based reflection amplifier (blue).

4.2 Tag and carrier modulation

The backscattering systems proposed in this thesis utilize LoRa transmissions as the carrier signal, unlike other works that are based on other types of modulations (WiFi, BLE, etc.) or direct non-modulated carriers (frequency tones). This section discusses the modulation of the carrier and tag. Firstly, an introduction to LoRa modulation is provided in order to understand the advantages it brings when used as a carrier. Then, two different tag modulations are presented: one implemented by simply enabling and disabling the backscattered signal, and another consisting of modulating the tag's switching frequency to generate a down-chirp signal that is inverse to the impinging up-chirps of the carrier.

Before proceeding, it is necessary to clarify the following: In previous sections, the term modulation has been used to refer to the process of switching between multiple loads or turning the amplifier on and off. In this section, we will also address tag modulation, but at a higher level, discussing the architecture of the backscattering system and data transmission methods employed in the practice.

Throughout this subsection, the same nomenclature defined in Section 3.3 is used, where $p(t)$ represents the signal that controls the switch, $c(t)$ is the carrier signal, $r(t)$ is the backscattered signal, and Z_0 and Z_1 represent the two termination states of the antenna, being Z_0 an open circuit and Z_1 a short circuit.

4.2.1 Carrier modulation: LoRa Primer

LoRa[1] is a wireless modulation technology patented by Semtech, specially designed for long-range communications with a low power consumption [4.25]. It stands out for its ability to provide robust connectivity over long distances while operating in unlicensed frequency bands [4.26]. LoRa modulation is specifically designed to optimize the trade-off between range, capacity, and power consumption, making it suitable for a wide range of applications, especially for the Internet of Things (IoT). Since it operates in the sub-GHz frequency bands, typically using frequencies such as 433 MHz, 868 MHz, or 915 MHz, depending on the regulatory domain (Asia, Europe, or America). Recently, Semtech released a LoRa IC operating at 2.4 GHz [4.27], enabling worldwide operation without being constrained by specific regulations. The use of these lower frequencies enables LoRa signals to propagate over longer distances and penetrate obstacles more effectively than higher-frequency wireless technologies.

LoRa uses a proprietary modulation scheme called Chirp Spread Spectrum (CSS), which modulates the data onto chirp[2] by circularly shifting them as described in Figure 4.25.

Figure 4.26 shows the direct measurement of a LoRa packet. The wide bandwidth of the chirp signals enables LoRa devices to achieve high sensitivity

---

[1] LoRa, which stands for Long Range, defines the physical (PHY) layer of the Open Systems Interconnection (OSI) model. On the other hand, LoRaWAN is a medium access control (MAC) layer protocol maintained by the LoRa Alliance. These two terms should not be confused.

[2] A chirp, often called a sweep signal, is a signal in which the frequency increases (up-chirp) or decreases (down-chirp) with time

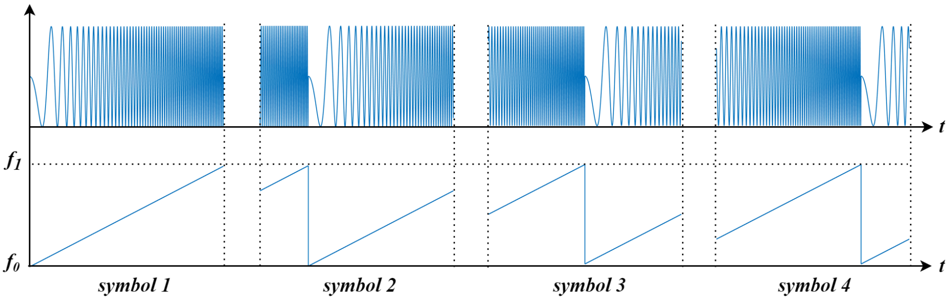

Figure 4.25: Chirp circularly-shift modulation used in LoRa to encode symbols.

and robustness against noise and interference, allowing LoRa to coexist with other wireless technologies in the same frequency band. Furthermore, the use of error correction techniques ensures reliable communication even in harsh environments with high levels of interference. LoRa transceivers typically allow users to adjust the chirp bandwidth from 7.8 to 500 kHz, however, only three of these (125, 200, and 500 kHz) are supported by the LoRaWAN protocol. LoRa supports different spreading factors, ranging from 7 to 12, which determine the data rate (from 0.3 $kbit/s$ to 27 $kbit/s$) and communication range (up to 5 and 15 km in urban and rural areas, respectively). Higher spreading factors provide a longer range but lower data rates, while lower spreading factors offer higher data rates but a shorter range. This flexibility allows LoRa to adapt to various application requirements, balancing the trade-off between range and data throughput [4.28].

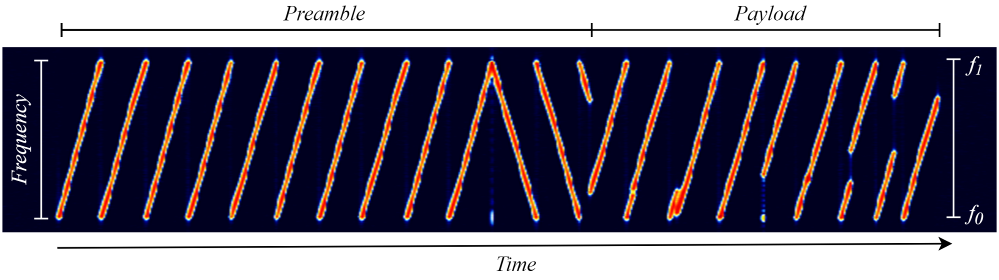

Figure 4.26: Measurements of a LoRa packet transmission.

The remarkable communication range of LoRa modulation is attributed to the high sensitivity of the receivers, which can reach as low as -148 dBm [4.25]. This sensitivity allows the demodulation of signals up to 20 dB below the noise floor, surpassing the capabilities of other modulations [4.29]. This outstanding property of LoRa modulation is indeed attributed to the demodulation process performed at the receiver, where the incoming up-chirps are multiplied by down-chirps of same period and bandwidth, resulting in a frequency tone with a high processing gain. Figure 4.27 demonstrates the measurement and demodulation of a LoRa packet using MATLAB. The figure illustrates the recorded up-chirps of the LoRa signal, the down-chirp demodulation sequence, and the resulting demodulated levels obtained through the multiplication of these two.

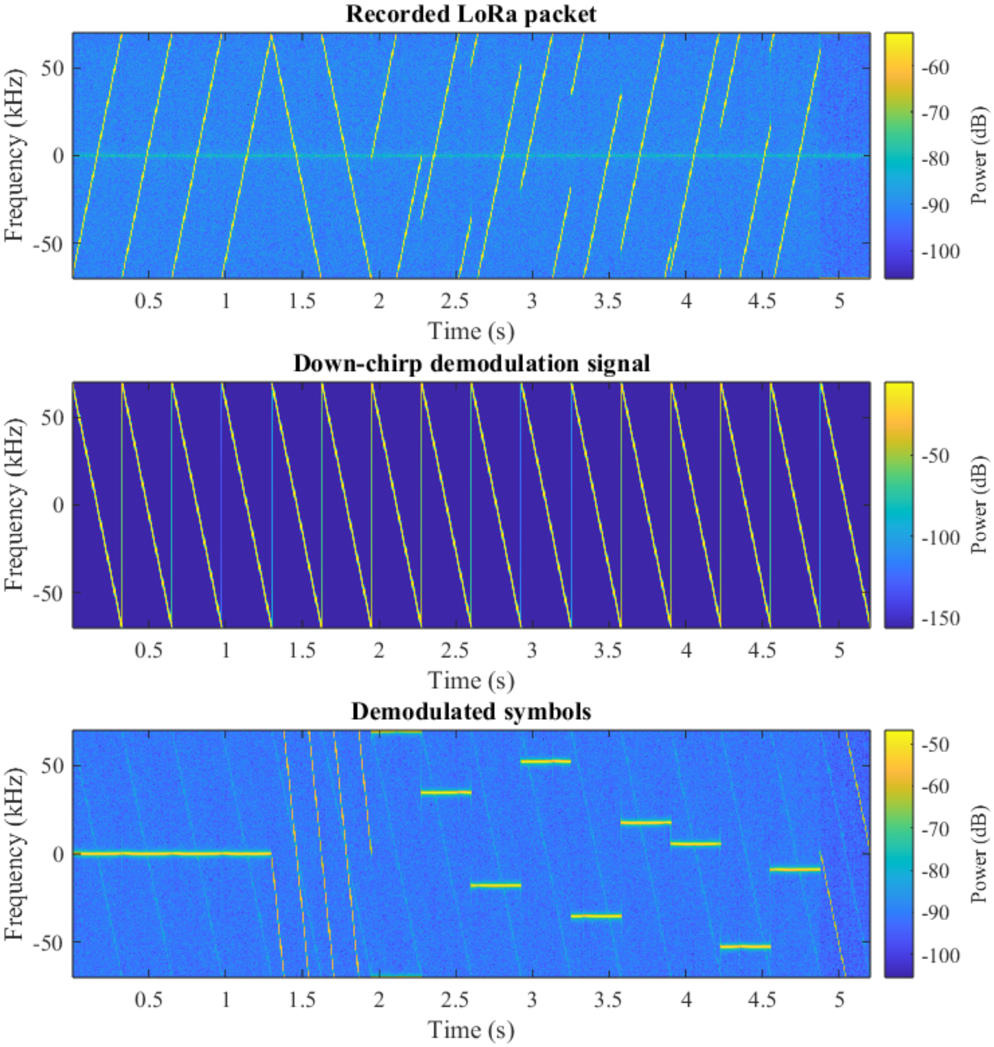

Figure 4.27: Matlab LoRa packet demodulation.

UNIVERSITAT ROVIRA I VIRGILI
LONG-RANGE BACKSCATTERING COMMUNICATIONS FOR NEXT GENERATION IOT APPLICATIONS
Marc Lázaro Martí

Therefore, among all the mentioned advantages of LoRa modulation, the processing gain, receiver sensitivity, and communication range of several kilometers are the key features that make LoRa modulation ideal for compensating the weak backscattered tag transmission caused by the two-way propagation losses. This significantly enhances the communication of the backscatter system, which would be impossible with any other type of modulation.

4.2.2 Tag modulation: On-Off keying

The backscattered signal's amplitude, phase, and frequency can be modulated based on the load properties and switching frequency, as described in the first section of this chapter. In contrast to the conventional ASK and FSK modulations commonly employed in RFID, the modulation proposed in this thesis is based on the principle coined as frequency-shift (FS) backscattering [4.30]. The FS-backscattering technique involves shifting the backscattered signal to a non-overlapping adjacent channel by periodically switching between the loads at a constant frequency. By relocating the backscattered signal to a clean adjacent channel, the interference generated by the carrier is minimized, thus enhancing the signal-to-noise ratio (SNR) at the receiver. Once the frequency shift is applied, the tag's digital information can be encoded using various methods. For instance, by turning the switching signal $p(t)$ on and off, we can implement a binary amplitude modulation in the adjacent channel, commonly known as on-off keying (OOK) modulation. On the other hand, by switching at two different frequencies, a binary frequency-shift keying (B-FSK) modulation can be achieved. It should be noted that the primary distinction between traditional and FS-backscattering modulations lies in the constant frequency switching employed to shift the backscattering uplink towards an unoccupied channel. Figure 4.28 illustrates the difference between the control signal $p(t)$ for the implementation of an ASK modulation using the traditional way or using the FS-backscattering technique.

The proposed system to implement the tag-to-receiver uplink communication is a LoRa-packet OOK modulation. The system deployment is depicted in Figure 4.29. A LoRa transmitter is set to generate the carrier signal at a center frequency f_c. The tag, which is modulated at a frequency f_p, backscatters the impinging LoRa packets to an adjacent channel ($f_c \pm f_p$) where the LoRa receiver is listening. Can be noted that the receiver cannot directly demodulate

UNIVERSITAT ROVIRA I VIRGILI
LONG-RANGE BACKSCATTERING COMMUNICATIONS FOR NEXT GENERATION IOT APPLICATIONS
Marc Lázaro Martí

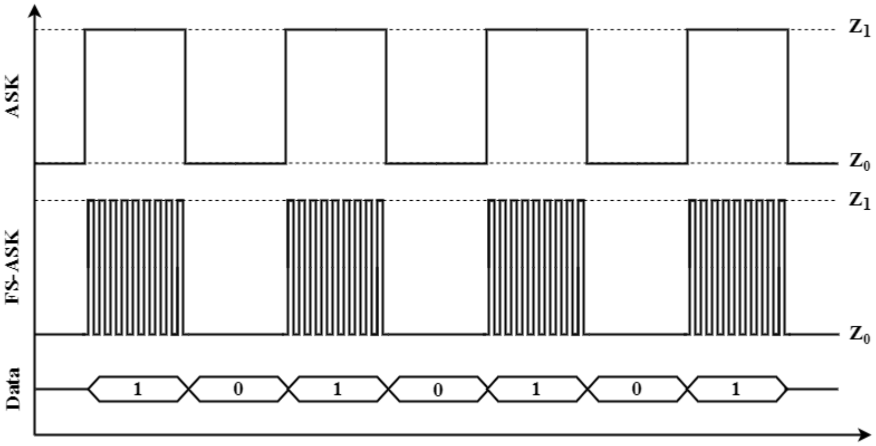

Figure 4.28: Representation of the control signal $p(t)$ on a backscattering tag to implement an ASK modulation in the traditional way or using the FS-backscattering technique.

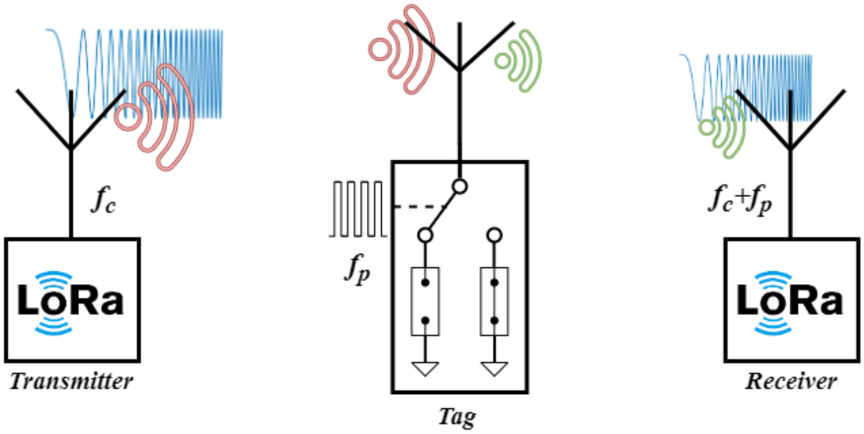

Figure 4.29: Diagram of the system architecture for the proposed OOK modulation

UNIVERSITAT ROVIRA I VIRGILI
LONG-RANGE BACKSCATTERING COMMUNICATIONS FOR NEXT GENERATION IOT APPLICATIONS
Marc Lázaro Martí

the LoRa packets of the transmitter, but only those backscattered by the tag. The advantage of this method is that neither the carrier transmission nor the shifted packets are modified at all, allowing any commercial off-the-shelf LoRa receiver to directly demodulate the backscattered packet. The communication system implements a packet-level modulation, where digital ones and zeros are encoded in the presence or non-presence of packets. This communication system does not alter the original LoRa transmission and is independent of the packet payload.

The LoRa transmitter node is continuously sending packets, whose duration (packet air-time) depends on the number of symbols sent, which in turn depends on the LoRa packet configuration: spreading factor (SF), bandwidth, preamble length (default to 8), coding rate (CR), sync word (default to 0x12) and, of course, the payload. For example, for a packet with the following configuration: SF: 12, BW: 125 kHz, CR: 1, preamble: 8 symbols, and payload: 10 bytes), the time on air is around a second (991.23 ms).

Figure 4.30 shows the spectrogram and waterfall plot obtained from measurements of the OOK modulation described in this subsection. The spectrogram is generated using the phase and quadrature (IQ) samples captured with a software-defined radio (SDR). The waterfall plot is created by stacking the instantaneous measured power level within a periodic frame of time. The LoRa transmitter is configured to transmit packets at 868 MHz with a spreading factor of 12 and a bandwidth of 125 kHz. The backscattering tag's switching frequency was set to 300 kHz, generating two sideband channels at 867.7 MHz and 868.3 MHz. By disabling the tag's switching frequency, it is possible to observe how the sideband transmissions are cut off.

The communication has been implemented following the scheme depicted in Figure 4.31, based on the well-known asynchronous serial port protocol. Tag data is encoded in frames. The frame length depends on the number of bits required to send the tag information, which in fact varies with the application. Frame length can be fixed or variable. In this last case, it is recommended to send a field within the frame indicating the total length of the frame. Additionally, parity bits, checksums, or CRC bits can be added to enhance transmission reliability. For the proof of concept, a byte is more than enough to encode a temperature value, an identifier, or a simple indicator. The tag sends a byte of data and two start/stop bits to indicate the start and the stop of the payload.

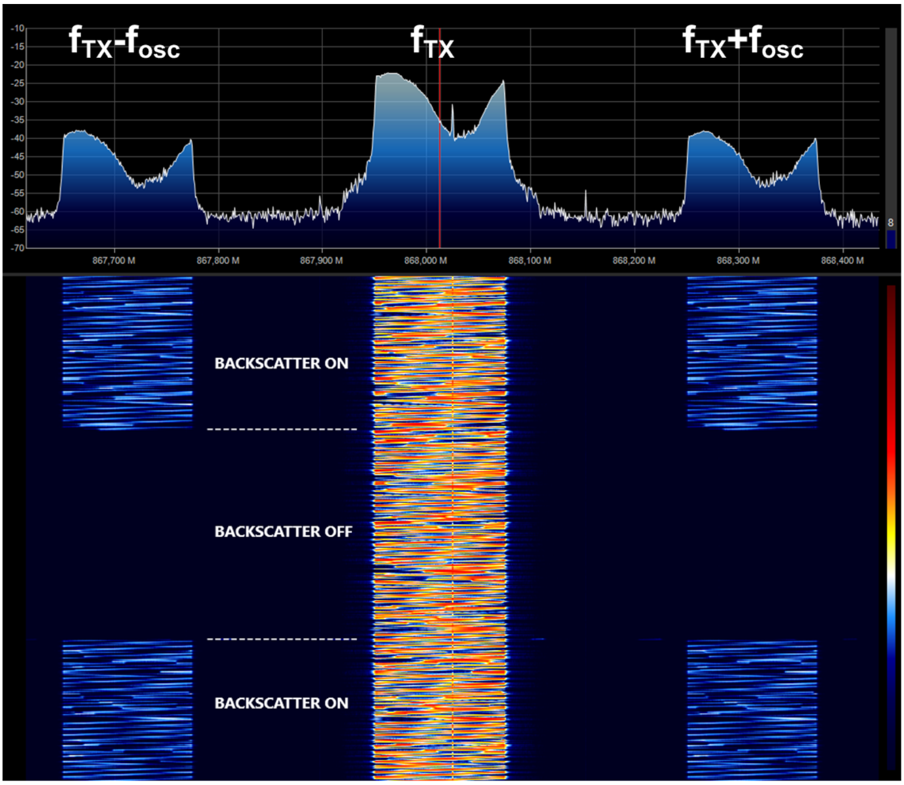

Figure 4.30: Measured spectrogram with backscatter on and off showing the shift of LoRa channel to offset channels when the backscatter is on.

Therefore, the frame length is 10 bits. The LoRa packet air-time has been adjusted to be the minimum as possible, thus increasing the communication data rate. Therefore, for a spreading factor of 7, a bandwidth of 250 kHz, a preamble length of 6, and the minimum payload, the packet air-time is reduced to 18 ms. The duration of each bit (32 ms) is the sum of a LoRa packet and the gap between each one of them, which has been set to be 14 ms. As the backscatter leaves a minimum time between frames equal to its frame length ($10 \cdot 32\ ms$) and considering the values mentioned above, the system can send frames every 640 ms, therefore the data rate is 12.5 $bits/s$.

Depending on the scenario, there are several strategies for managing collisions between tag transmissions. One method is to deliberately reduce the communication range of the tags if the application allows it. By increasing or reducing the spreading factor and bandwidth of LoRa packets, the processing gain at the receiver varies proportionally, thereby increasing or reducing the

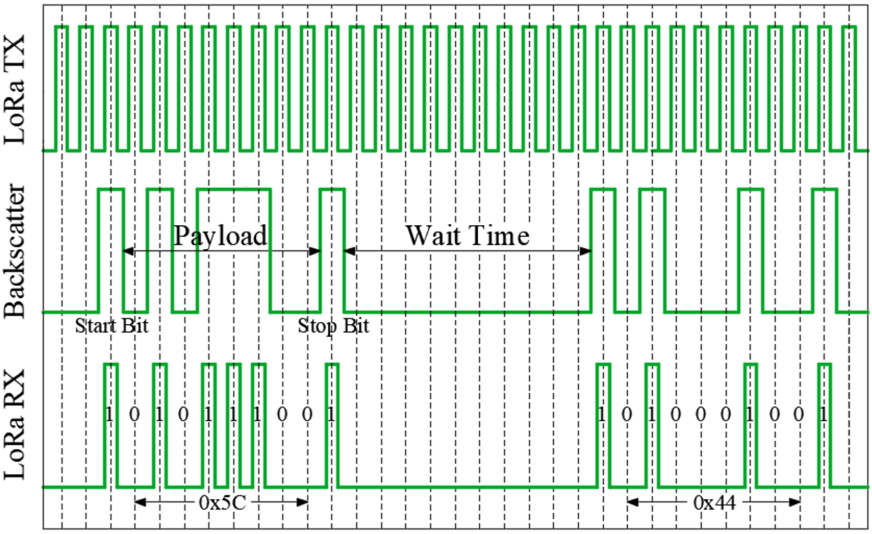

Figure 4.31: Block diagram showing the data transmission using the reflection of the transmitted packets.

range. This approach effectively reduces collisions since only tags within a constrained area can send packets. Another method involves randomly adjusting the waiting time between frame transmissions, which eliminates periodic collisions between transmissions from different backscatters.

The communication protocol can be implemented in a low-power 8-bit microcontroller (MCU) from the AtTiny family from Microchip. The switch control signal $p(t)$ can be generated in several ways, using the integrated pulse width modulation (PWM) function of the MCU or integrating an oscillator in the tag which is enabled or disabled by the MCU. These two methods have their own advantages and disadvantages. While the dedicated oscillator exhibits a higher frequency accuracy, it normally consumes more than the PWM function of the MCU. Fortunately, LoRa receivers can measure the frequency shift from the expected central frequency and the packet received central frequency, dynamically correcting the frequency offsets due to the backscatter oscillator drifts, whether it is the internal of the MCU, or the dedicated one. The optimal system should be studied based on the specific components, as running the entire MCU at 300 kHz may be less efficient than running it at 32 kHz to control an external oscillator of 300 kHz. It all depends on the power consumption of the MCU running at 300 kHz with all the functions disabled (ADC, DAC, Timers, etc.).

UNIVERSITAT ROVIRA I VIRGILI
LONG-RANGE BACKSCATTERING COMMUNICATIONS FOR NEXT GENERATION IOT APPLICATIONS
Marc Lázaro Martí

4.2.3 Tag down-chirp modulation

4.2.3.1 Operation principle

One inconvenience of the backscattering technique is the mirrored harmonic generation on both sides of the carrier signal, which creates undesired interference across a wide range of frequencies. This issue has been addressed in the literature through a single-sided backscattering front-end that emulates a complex modulation signal $p(t)$ using four complex impedances [4.31][4.32]. In this section, a novel tag modulation based on LoRa backscattering is proposed, which achieves similar spectrum efficiency as single-sideband backscattering, but through a completely different approach. As will be seen in more detail, the proposed modulation in this section involves the unspreading of one sideband of the backscattered signal, thereby increasing its peak power. Simultaneously, the other sideband is spread by a factor of two, effectively disguising it as noise for the other channels. In practice, the double-spread sideband always remains below the noise floor.

The modulation described in this section stems from the demodulation process used in LoRa communications [4.25][4.33]. LoRa encodes information circularly shifting a base chirp (up-chirp), which starts at f_0 and finishes at $f_0 + BW$. Equation (4.2) describes mathematically the base chirp signal $c(t)$ sent by the LoRa transmitter.

$$c(t) = e^{j2\pi(f_0 t + \frac{BW}{2T}t^2)}, \qquad 0 \leq t \leq T \tag{4.2}$$

where BW is the bandwidth, T is the period and f_0 is the initial frequency of the chirp. To demodulate the transmitted chirps the receiver multiplies the incoming signal by a complex conjugate time-reversed chirp $c^*(T-t)$ (down-chirp) with the same bandwidth and period as the transmitted chirp. The signal $r(t)$ resulting from multiplying the up-chirp and the down-chirp is described by 4.3. One can realize that $r(t)$ perfectly matches with the equation of a complex sinusoidal signal $Ae^{j(\omega t + \phi)}$.

$$r(t) = e^{j2\pi((2f_0 + BW)t + (2f_0 - B)\frac{T}{2})}, \qquad 0 \leq t \leq T \tag{4.3}$$

Since the load-switching process multiplies the incoming signal $c(t)$ by the switch modulation signal $p(t)$, the idea lies in directly modulating the switching frequency of the tag with a down-chirp signal with the same bandwidth and spreading factor than $c(t)$, consequently bouncing the complex sinusoidal signal $r(t)$. The result of this operation is the backscattering of a frequency tone with the consequent processing gain. Figure 4.32 shows a diagram of the modulation process described in this subsection.

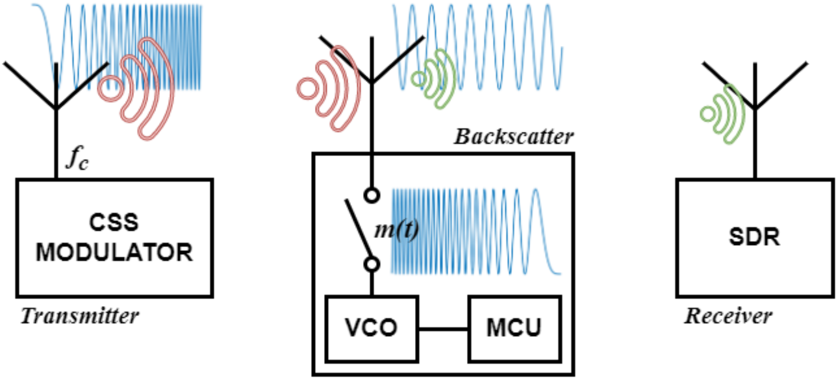

Figure 4.32: Backscatter modulation diagram to bounce a sinusoidal tone from an incoming CSS signal.

In conventional backscattering of CSS signals, this processing gain is obtained at the receiver side when the signal is demodulated, in contrast to the method proposed here, where the signal is directly backscattered from the tag already with the processing gain. The aforementioned processing gain can be determined mathematically by the ratio between the data rate of the spreading sequence R_c (chips/second), and the real data rate R_b (bits/second) of the communication, as described by (4.4).

$$G_p = 10 \cdot log_{10}(\frac{R_c}{R_b}) \tag{4.4}$$

4.2.3.2 Communication scheme

At this point, the tag's information can be encoded in several ways. The simplest is to enable and disable $p(t)$ to generate an amplitude modulation. Alternatively, we can change the frequency of the backscattered tone by circularly shifting $p(t)$, thus creating an FSK modulation. Furthermore, by changing the slope of the down-chirp modulation -modifying BW or SF- to not match that of the carrier, another CSS modulation with a wider or thicker spectrum can be created. The

UNIVERSITAT ROVIRA I VIRGILI
LONG-RANGE BACKSCATTERING COMMUNICATIONS FOR NEXT GENERATION IOT APPLICATIONS
Marc Lázaro Martí

range of possibilities is wide.

To encode the tag's information the following method is proposed. Data is encoded implementing an OOK modulation over the backscattered frequency tone. Therefore, a digital one is transmitted when $p(t)$ is modulated with a down-chirp and the frequency tone is backscattered. On the contrary, cutting off the modulation $p(t)$ nothing is backscattered, which is equivalent to a digital zero. At this point, information could already be sent following the communication scheme presented in the previous section. However, to further increase the detectability of the tag, it is proposed to use a Barker sequence to encode the information and provide a second processing gain to the system. A Barker code is a binary sequence with the ideal auto-correlation property. This method consists of encoding individual bits with a digital sequence that the receiver unambiguously recognizes, which abruptly decreases the probability of error. This method is commonly used in direct sequence spread spectrum (DSSS) modulations. In the experiments performed in the laboratory, a 7-bit sequence -[1110010]- with a peak to side-lobe ratio of 16.9 dB is used.

Therefore the proposed modulation achieves a double processing gain by first modulating the tag with a down-chirp, thereby reflecting a frequency tone with the first processing gain, and second, by encoding the tag's information with a Barker sequence, providing the second processing gain to the modulation. These processing gains depend on the resolution of the DAC and the length of the Barker sequence, respectively. Therefore, they can be adjusted depending on the application.

4.2.3.3 Carrier-Tag Syncronization

Since the backscattering tag does not integrate any receiver, there is no synchronization between the carrier LoRa transmission and the down chirp generated in the tag. Figure 4.33 illustrates the effect of multiplying an up-chirp and a down-chirp miss-synchronized. Non-synchronized chirp multiplication generates two frequency tones with a separation between them equal to the chirp bandwidth (BW). The chirp bandwidth used in the simulation of Figure 4.33 has been set to 125 kHz. It can be observed that processing gain is distributed between the two frequency tones. Therefore, maximum processing gain is obtained when the up-chirp and down-chirp are synchronized, while the minimum is when one is shifted half of the chirp period relative to the other.

UNIVERSITAT ROVIRA I VIRGILI
LONG-RANGE BACKSCATTERING COMMUNICATIONS FOR NEXT GENERATION IOT APPLICATIONS
Marc Lázaro Martí

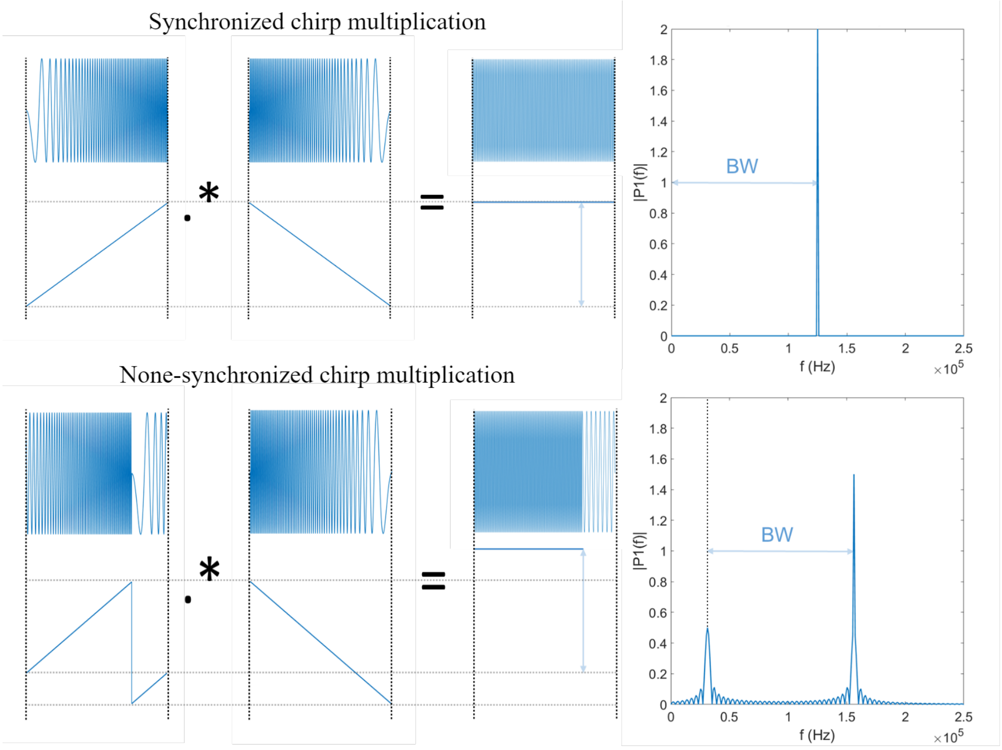

Figure 4.33: Misalignment effect on chirp multiplication

Figure 4.34a shows the measured spectrum when the down-chirp is deliberately shifted with respect to the impinging LoRa transmission. It clearly shows the processing gain distribution above mentioned. Figure 4.34b shows a 3D diagram of the measured right backscattered sideband, where the black-shadowed slide is the case when carrier up-chirp and tag down-chirp are perfectly synchronized.

This effect difficult the tag data demodulation, since the receiver does not know the frequency of the backscattered tone signal, which in fact can vary with each tag transmission when random waiting delays between packet transmissions are used. Beyond that, simple carrier or tag oscillator drift can shift the frequency of the backscattered tone. Since tag data is encoded using a known Barker sequence, a Matlab demodulation algorithm that performs the correlation between the measured IQ samples and the Barker sequence for all the frequencies from $f_c + (f_p - (BW/2))$ to $f_c + (f_p + (BW/2))$ is implemented. The maximum correlation peak determines the frequency of the backscattered

UNIVERSITAT ROVIRA I VIRGILI
LONG-RANGE BACKSCATTERING COMMUNICATIONS FOR NEXT GENERATION IOT APPLICATIONS
Marc Lázaro Martí

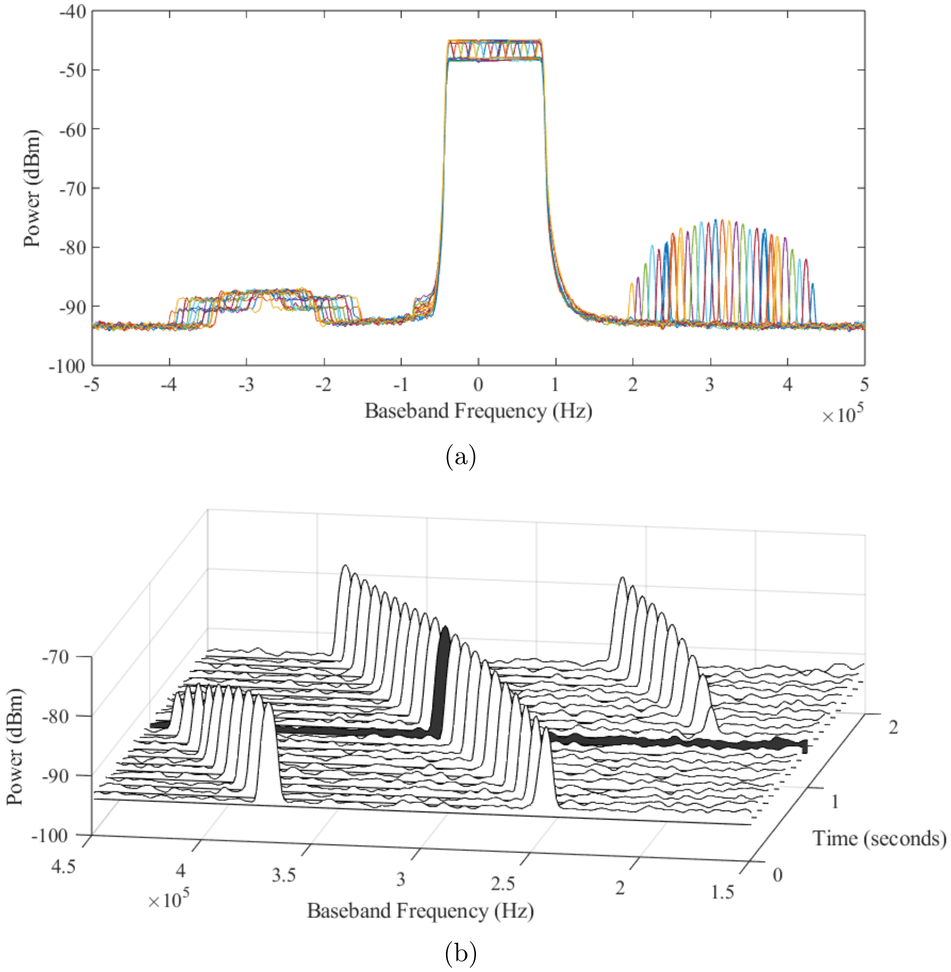

(a)

(b)

Figure 4.34: Misalignment effect on chirp multiplication

signal. By utilizing lower frequency increments (Δf) for the correlation sweep, the accuracy of peak identification can be enhanced at the cost of increased processing time. Once the backscatter frequency is determined, the complete packet data can be demodulated. The algorithm's code has been included in the annex section.

4.2.3.4 Tag implementation

The down-chirp has been synthesized in the tag with a voltage-controlled oscillator (VCO) controlled by the digital-to-analog converter (DAC) of the MCU.

The tag prototype has been implemented using an 8-bit AtTiny417 MCU from Microchip, an LTC6990 VCO from Analog Devices, and the already-mentioned ADG902. Figure 4.35 shows the prototype of the tag. Must be noted that the ability of the tag to synthesize the chirps depends on the resolution of the DAC. The total power consumption of the implemented tag is 635 μA and the cost is 4.34 $.

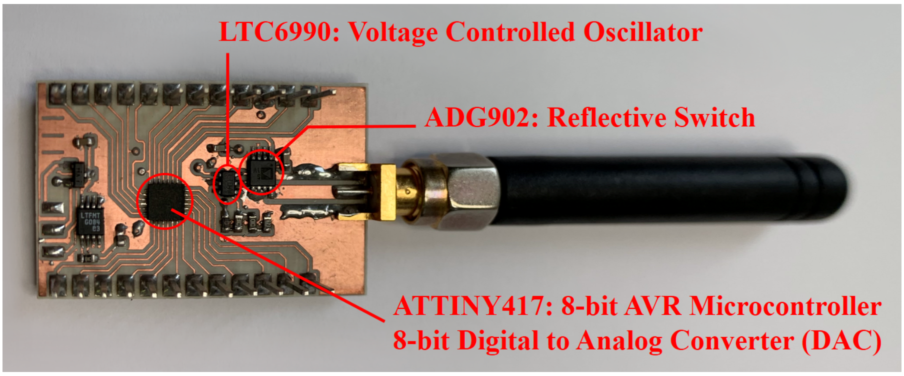

Figure 4.35: Top view of the tag's prototype.

4.2.3.5 Experimental results

To compare the power peak of the reflected signal between the conventional OOK modulation and the down-chirp modulation proposed in this subsection, the resulting spectrum for both methods has been superimposed in Figure 4.36. For the experiments, the bandwidth (BW) and the spreading factor (SF) of the LoRa transmitter were set to 125kHz and 12. Finally, as observed in Figure 4.36, a processing gain of 13.41 dB was obtained.

The measurements presented in this section were taken in bistatic mode. The receiver was placed at a distance of 20 meters from the transmitter, and the tag moved linearly along the distance between both. The power and the frequency of the transmitter were set to 20 dBm and 868 MHz. The tag's signal was recorded using the Adalm Pluto SDR and subsequently processed with Matlab. Figure 4.37 shows the IQ signal recorded with the SDR at a distance of 13 meters from the transmitter and 7 meters from the receiver. Figure 4.38 shows the correlation of the incoming signal with the Barker sequence, where the demodulated data can be clearly appreciated. To test the communication, a fixed hexadecimal number -0x97- was transmitted by the tag.

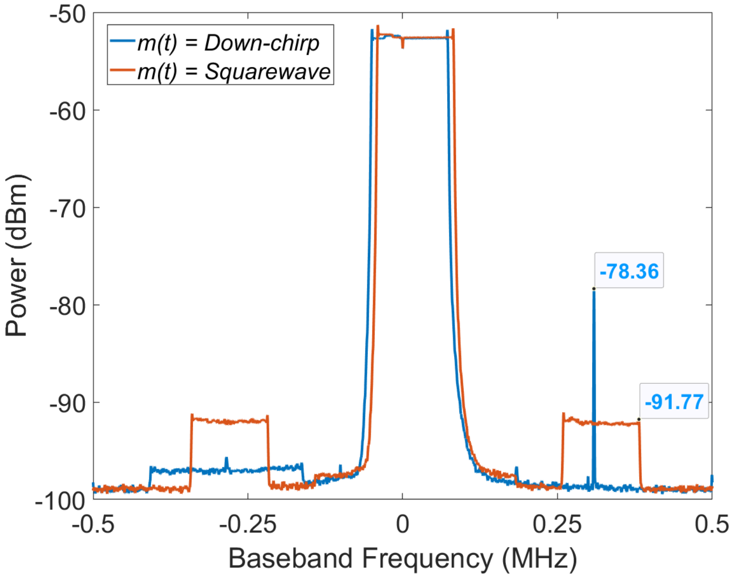

Figure 4.36: Spectrum comparison between conventional backscatter and down-chirp modulated backscatter. Source signal: CSS modulation (Up-chirp), $f_c = 868MHz$, $BW = 125KHz$ and $SF = 12$. Conventional Backscatter signal (Orange): Squarewave, $f_c = 300kHz$, duty cycle $= 50\%$. Down-chirp backscatter signal (Blue): CSS modulation (Down-chirp), $f_c = 300kHz$, $BW = 125KHz$ and $SF = 12$.

The data rate of the communication, without considering the Barker code, can be calculated as a function of the chirp duration, which in turn depends on the BW and the SF. Each chirp encodes one bit. With the $BW = 125kHz$ and $SF = 12$ aforementioned, a data rate of 30.31 $bits/s$ can be achieved. Taking into consideration the Barker code, the data rate is reduced to 4.36 $bits/s$. However, these communication speeds are not the maximum rates. In fact, it is possible to modulate shorter chirps within the period of a base chirp, allowing more bits to be encoded in a single chirp. Higher modulation data rates and their effect over the range and consumption should be further explored.

Finally mention that the proposed down-chirp modulation presents two trade-offs in terms of processing gain: the down-chirp modulation gain can reach up to 25.33 dB with a 12-bit resolution DAC, thereby increasing power consumption, while the Barker sequence gain can reach up to 22.3 dB of gain with a 13-bit Barker sequence, resulting in a reduced communication data rate.

UNIVERSITAT ROVIRA I VIRGILI
LONG-RANGE BACKSCATTERING COMMUNICATIONS FOR NEXT GENERATION IOT APPLICATIONS
Marc Lázaro Martí

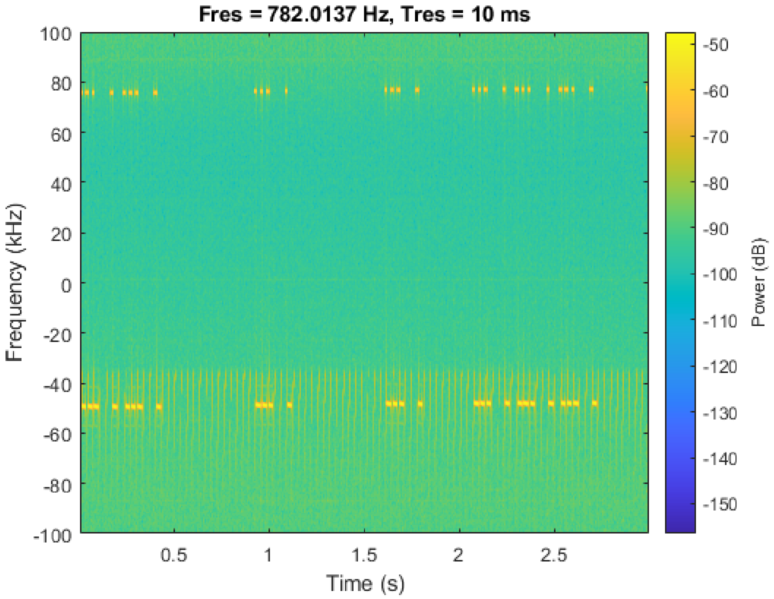

Figure 4.37: IQ recording of the backscattered signal encoded with the 7-bit barker sequence.

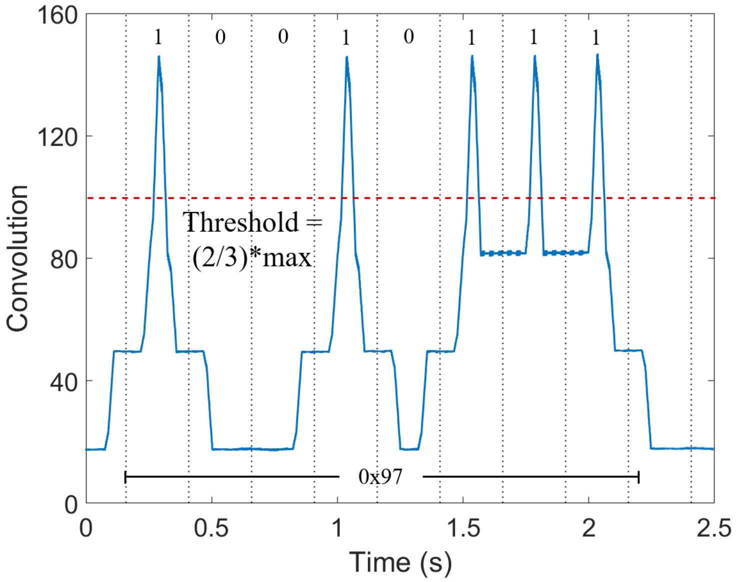

Figure 4.38: Convolution of the backscattered signal with the Barker sequence. Tag demodulated data: 0x97, [10010111].

4.3 Tag power consumption

This section addresses the tag energy consumption and summarizes the power consumed by each component employed to implement the modulations and front-ends aforementioned. Must be noted that the final power consumption of the tag depends not only on the components but also on the operation frequency. Table 4.2 summarizes the power consumption.

Component	frequency	Voltage	Current	Power consumption
		Backscattering front-end		
RF switch ADG902 [4.1]	868 MHz	1.8 V	<1 μA	~1 μW
RF switch ADG918 [4.34]	868 MHz	1.8 V	<1 μA	~1 μW
BJT HBFP405 [4.35]	868 MHz	1.8 V	280 μA	504 μW
Tunnel Diode AI301A [4.36]	868 MHz	114 mV V	1.2 mA	136.8 μW
VCO LTC6990 [4.37]	237.5 - 362.5 kHz	2.25 V	180 μA	405 μW
Oscillator LTC6907 [4.38]	300 kHz	3 V	36 μA	108 μW
MAX9916 [4.39]	-	1.8 V	36 μA	64.8 μW
MAX9634 [4.40]	-	1.8 V	1 μA	~1 μW
DAC (AtTiny417) [4.41]	-	1.8 V	96 μA	172.8 μW
		Control unit		
MCU AtTiny402/417 [4.42]	32 kHz	1.8 V	7 μA	12.6 μW
	1 MHz prescaled	1.8 V	455 μA	819 μW

Table 4.2: Summary of power consumption for the components used in the implementations.

From Table 4.2, it is evident that the importance lies not only in the components used but also in the operating frequency and voltage. For the load modulation front-end, the microcontroller can be directly used to generate the switching frequency with the PWM functionality, or it can be used along with an oscillator only as a baseband digital modulator. The former configuration requires running the clock at 1 MHz to generate the 300 kHz switching frequency. On the contrary, the last configuration (MCU + LTC6907) allows running the MCU with the low power 32 kHz clock in order to enable or disable the external oscillator, making it a more efficient option. Despite using a prescaler to reduce clock frequency from 1 MHz to ∼300 kHz, the consumption still remains considerably higher than when using the 32 kHz clock. Another consideration is that the 32 kHz clock works well in LoRa packet level OOK modulation, but is impractical for synthesizing down-chirps or higher data rate modulations.

From Table 4.2, it can be observed that the components have different minimum operating voltages. As mentioned in the amplified front-end section, when biasing voltages are not matched, the implementation becomes less efficient, since requires using regulators, converters, or, in the worst case, voltage dividers. For instance, let's consider the LTC6990 and LTC6907, which have minimum operating voltages of 2.25V and 3V, respectively. One option is to study their behavior when biased below the minimum voltage. While it is not recommended, this technique would likely work with the LTC6990 but may not be effective with the LTC6907, leaving only the conversion option. Therefore, the power consumption of the regulator should be added to the previous table. Fortunately, regulators designed for voltage conversions between standard biasing voltages, such as in this case (3 V to 1.8 V), typically exhibit high efficiency.

Radiofrequency energy harvesting techniques have not been studied in this thesis since the minimum signal strength required to power up the tag limits the communication coverage, and because the reflected power is reduced by a factor of 4, as demonstrated in section 3.2. Therefore, light energy harvesting is considered the best option to power up the tag. The AEM10941 has been used, since it can start harvesting energy from an input power as low as 3 μW at 380 mV. Energy can be stored in a Li-ion battery, a supercapacitor, or a Lithium Ion Capacitor (LIC). Li-ion batteries stands out by it high stored energy compared to supercapacitors. On the other hand, supercapacitor stand out by its instantaneous power. LIC combines many of the advantages of supercapacitors and Li-ion batteries. Figure 4.39 shows a 60 mAh LiPo battery, a LIC capacitor of 1.6 F, a standard supercapacitor of 1 F, and a thin-form CAP-XX supercapacitor of 220 mF.

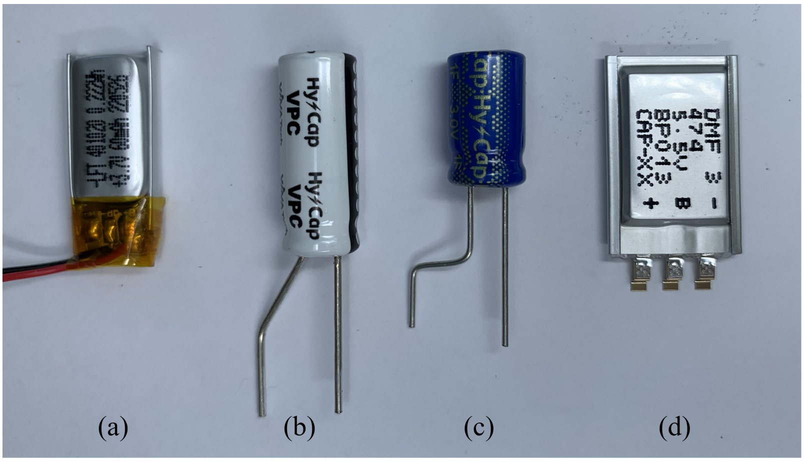

Figure 4.39: Different storage elements: (a) Lithium Polymer battery, (b) Lithium-ion capacitor, (c) supercapacitor, (d) thin-profile supercapacitor

Light energy harvesting system has been tested with an indoor LL200-2.4-37 flexible solar cell from PowerFilm capable to provide an open circuit voltage $V_{oc} = 2.2V$ and short circuit current $I_{sc} = 60\mu A$ under 200 lux illuminance conditions and $V_{oc} = 2.9V$ and $I_{sc} = 200\mu A$ under 1000 lux illuminance conditions. Indoor light levels usually range from 100 to 1000 lux [4.43]. Energy is stored in a 220 mF CAP-XX supercapacitor with a leakage current of only 3 μA. The main feature of this CAP-XX supercapacitor is its very high power density and high energy storage capacity in a space-efficient prismatic package with only 2.2 mm thickness, making it ideal for low-profile tag designs. Figure 4.40 shows the energy harvester system with the flexible solar cell, the energy manager, and the CAP-XX supercapacitor. The capacitor is capable to keep energy all night long. By duty cycling the tag operation, tag should work perpetually. The advantage of using supercapacitors is that their lifespan is much longer than Li-ion batteries. Comparing them by number of charge-cycles, Li-ion batteries have an average of 500 to 10.000 cycles, while supercapacitors range from 100.000 to a million cycles.

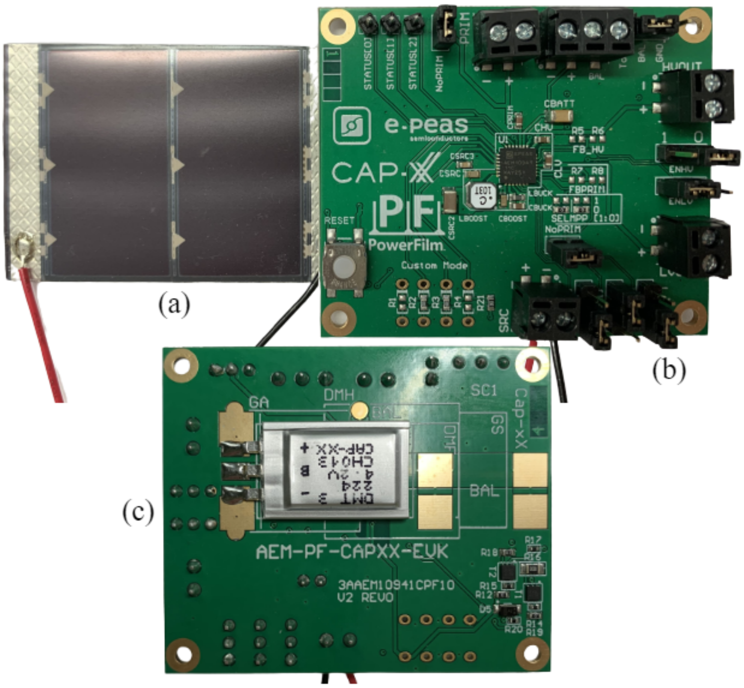

Figure 4.40: Light energy harvesting system (AEM10941 Evaluation Kit): (a) flexible solar cell, (b) front view of the board, (c) Rear view of the board with the CAP-XX supercapacitor.

UNIVERSITAT ROVIRA I VIRGILI
LONG-RANGE BACKSCATTERING COMMUNICATIONS FOR NEXT GENERATION IOT APPLICATIONS
Marc Lázaro Martí

4.4 Conclusions

In this section, the work related to the implementation of the backscattering tag has been addressed. From the work carried out in this chapter, several conclusions can be drawn regarding tag front-end design and the implementation of the modulation scheme, including the physical medium modulation and uplink communication protocol.

Different topologies have been studied for the implementation of the backscattering tag. On one hand, the conventional load-modulated front-end has been examined. This system stands out for its extremely low power consumption, as it only requires an RF switch with minimal current consumption, making it suitable for passive implementations or applications with super low power requirements. Subsequently, the integration of a reflection amplifier in the tag front-end has been studied for applications requiring longer communication ranges. The two main low-power reflection amplifier topologies found in the literature (tunnel diode-based and transistor-based reflection amplifiers) have been successfully designed, manufactured, and characterized. The main advantage of the tunnel diode-based amplifier is its high gain and low power requirements, which has sparked significant interest recently. However, due to its low bias voltage, this high efficiency diminishes when integrated into a complete system, as logic circuits operate at much higher voltages, necessitating the use of converters to integrate them into the same tag. On the contrary, despite exhibiting modest efficiencies, the transistor-based reflection amplifier can operate at voltages that match those of microcontrollers, making the overall integration more efficient. Therefore, based on this premise, it can be concluded that the transistor-based reflection amplifier appears to be a better option for the design of backscattering tags.

Reflection amplifiers are pseudo-oscillators strategically designed to amplify without starting to oscillate and their behavior depends on the input power. Therefore, its integration into backscattering tags poses some challenges that have not been addressed in the literature. For input powers high enough, the reflection amplifier can start to oscillate, generating interferences in the spectrum and potentially disabling all neighbor communications, since the noise floor increases within the tag band. Furthermore, keeping the amplifier always turned on is not an efficient practice for energy management and reduces the tag's lifespan. Therefore, the integration of a current sensor to activate and deactivate the reflection amplifier as a function of the input power is proposed, thus solving the two aforementioned issues.

For the communication implementation, two different backscattering modulations have been presented, along with an uplink communication scheme. Each modulation exhibits its own advantages and weaknesses. The OOK LoRa-packet modulation stands out for its low power consumption and compatibility with commercial off-the-shelf LoRa receivers for demodulation. However, due to the backscatter information being piggybacked by LoRa packets, the achieved data rate is not particularly high in terms of speed.

On the other hand, the down-chirp modulation implements a more optimal spectrum utilization and takes advantage of the processing gain inherent to LoRa modulation. Furthermore, an additional processing gain is achieved by encoding the tag information with a 7-bit Barker sequence. However, this modulation requires more power due to the integration of a VCO and the higher MCU clock speed required for synthesizing the LoRa down-chirps, and it must be demodulated using a SDR. Since the tag information is demodulated with a SDR, further work could be done exploring the maximum communication data-rate as a function of the tag power consumption.

4.5 Bibliography

[4.1] Analog Devices. *ADG901/ADG9020 Hz to 4.5 GHz, 40 dB Off Isolation at 1 GHz,17 dBm P1dB at 1 GHz SPST Switches*, 8 2003. Rev. D: Initial Version.

[4.2] John Kimionis, Apostolos Georgiadis, Ana Collado, and Manos M Tentzeris. Enhancement of RF tag backscatter efficiency with low-power reflection amplifiers. *IEEE Transactions on Microwave Theory and Techniques*, 62(12):3562–3571, 2014.

[4.3] Antonio Lazaro, Marc Lazaro, Ramon Villarino, David Girbau, and Pedro de Paco. Car2car communication using a modulated backscatter and automotive fmcw radar. *Sensors*, 21(11):3656, 2021.

[4.4] AP Venguer, JL Medina, RA Chávez, A Velázquez, A Zamudio, and GN Il'in. Theoretical and experimental analysis of resonant microwave reflection amplifiers. *Microwave Journal*, 47(10):80–93, 2004.

UNIVERSITAT ROVIRA I VIRGILI
LONG-RANGE BACKSCATTERING COMMUNICATIONS FOR NEXT GENERATION IOT APPLICATIONS
Marc Lázaro Martí

[4.5] JO Scanlan and JT Lim. A design theory for optimum broadband reflection amplifiers. *IEEE Transactions on Microwave Theory and Techniques*, 12(5):504–511, 1964.

[4.6] Ambuj Varshney, Andreas Soleiman, and Thiemo Voigt. Tunnelscatter: Low power communication for sensor tags using tunnel diodes. In *The 25th Annual International Conference on Mobile Computing and Networking*, pages 1–17, 2019.

[4.7] Diogo Matos, Ricardo Correia, and Nuno Borges Carvalho. Dual-Band FET-Based Reflection Amplifier for Backscatter Modulator Performance Enhancement. *URSI Radio Science Letters*, 3:39, 2021.

[4.8] Jia Hu, Linling Zhong, Tao Ma, Zhe Ding, and Zhanqi Xu. Long-range FM backscatter tag with tunnel diode. *IEEE Microwave and Wireless Components Letters*, 32(1):92–95, 2021.

[4.9] Ajibayo Adeyeye, Charles Lynch, Aline Eid, Jimmy Hester, and Manos Tentzeris. 5.8-GHz low-power tunnel-diode-based two-way repeater for non-line-of-sight interrogation of RFIDs and wireless sensor networks. *IEEE Microwave and Wireless Components Letters*, 31(6):794–797, 2021.

[4.10] Karan Gumber, Corinne Dejous, and Simon Hemour. Harmonic reflection amplifier for widespread backscatter Internet-of-Things. *IEEE Transactions on Microwave Theory and Techniques*, 69(1):774–785, 2020.

[4.11] Aline Eid, Jimmy Hester, and Manos M Tentzeris. A 5.8 GHz Fully-Tunnel-Diodes-Based 20 μW, 88mV, and 48 dB-Gain Fully-Passive Backscattering RFID Tag. In *2020 IEEE/MTT-S International Microwave Symposium (IMS)*, pages 607–610. IEEE, 2020.

[4.12] Seiran Khaledian, Farhad Farzami, Besma Smida, and Danilo Erricolo. Two-way backscatter communication tag using a reflection amplifier. *IEEE Microwave and Wireless Components Letters*, 29(6):421–423, 2019.

[4.13] Francesco Amato, Christopher W Peterson, Brian P Degnan, and Gregory D Durgin. Tunneling RFID tags for long-range and low-power microwave applications. *IEEE Journal of Radio Frequency Identification*, 2(2):93–103, 2018.

[4.14] Francesco Amato, Hakki M Torun, and Gregory D Durgin. RFID backscattering in long-range scenarios. *IEEE Transactions on Wireless Communications*, 17(4):2718–2725, 2018.

[4.15] Farhad Farzami, Seiran Khaledian, Besma Smida, and Danilo Erricolo. Reconfigurable dual-band bidirectional reflection amplifier with applications in Van Atta array. *IEEE Transactions on Microwave Theory and Techniques*, 65(11):4198–4207, 2017.

[4.16] Farhad Farzami, Seiran Khaledian, Besma Smida, and Danilo Erricolo. Ultra-low power reflection amplifier using tunnel diode for RFID applications. In *2017 IEEE International Symposium on Antennas and Propagation & USNC/URSI National Radio Science Meeting*, pages 2511–2512. IEEE, 2017.

[4.17] Seiran Khaledian, Farhad Farzami, Danilo Erricolo, and Besma Smida. A full-duplex bidirectional amplifier with low DC power consumption using tunnel diodes. *IEEE Microwave and Wireless Components Letters*, 27(12):1125–1127, 2017.

[4.18] Jongwon Lee and Kyounghoon Yang. RF power analysis on 5.8 GHz low-power amplifier using resonant tunneling diodes. *IEEE Microwave and Wireless Components Letters*, 27(1):61–63, 2016.

[4.19] Francesco Amato, Christopher W Peterson, Brian P Degnan, and Gregory D Durgin. A 45 μW bias power, 34 dB gain reflection amplifier exploiting the tunneling effect for RFID applications. In *2015 IEEE International Conference on RFID (RFID)*, pages 137–144. IEEE, 2015.

[4.20] John Kimionis, Manos M Tentzeris, Apostolos Georgiadis, and Ana Collado. Inkjet-printed reflection amplifier for increased-range backscatter radio. In *2014 44th European Microwave Conference*, pages 5–8. IEEE, 2014.

[4.21] John Kimionis, Apostols Georgiadis, Sangkil Kim, Ana Collado, Kyriaki Niotaki, and Manos M Tentzeris. An enhanced-range RFID tag using an ambient energy powered reflection amplifier. In *2014 IEEE MTT-S International Microwave Symposium (IMS2014)*, pages 1–4. IEEE, 2014.

[4.22] Jongwon Lee, Jooseok Lee, and Kyounghoon Yang. Reflection-type RTD low-power amplifier with deep sub-mW DC power consumption. *IEEE microwave and wireless components letters*, 24(8):551–553, 2014.

[4.23] Pak Chan and Vincent Fusco. Full duplex reflection amplifier tag. *IET Microwaves, Antennas & Propagation*, 7(6):415–420, 2013.

[4.24] RN Hall. Tunnel diodes. *IRE Transactions on Electron Devices*, 7(1):1–9, 1960.

[4.25] Semtech Corporation. Semtech Application Note AN1200.22, LoRa Modulation Basics. Technical report, Semtech Corporation, 05 2015.

[4.26] Umber Noreen, Ahcène Bounceur, and Laurent Clavier. A study of LoRa low power and wide area network technology. In *2017 International Conference on Advanced Technologies for Signal and Image Processing (ATSIP)*, pages 1–6. IEEE, 2017.

[4.27] Gwendoline Hochet Derevianckine, Alexandre Guitton, Oana Iova, Baozhu Ning, and Fabrice Valois. Opportunities and Challenges of LoRa 2.4 GHz. *IEEE Communications Magazine*, 2023.

[4.28] Semtech Corporation. *Application note AN1200.22 LoRa Modulation Basics*, May 2015. Rev. 2.

[4.29] Stewart J Thomas, Jordan S Besnoff, and Matthew S Reynolds. Modulated backscatter for ultra-low power uplinks from wearable and implantable devices. In *Proceedings of the 2012 ACM workshop on Medical communication systems*, pages 1–6, 2012.

[4.30] Pengyu Zhang, Mohammad Rostami, Pan Hu, and Deepak Ganesan. Enabling practical backscatter communication for on-body sensors. In *Proceedings of the 2016 ACM SIGCOMM Conference*, pages 370–383, 2016.

[4.31] Vikram Iyer, Vamsi Talla, Bryce Kellogg, Shyamnath Gollakota, and Joshua Smith. Inter-technology backscatter: Towards internet connectivity for implanted devices. In *Proceedings of the 2016 ACM SIGCOMM Conference*, pages 356–369, 2016.

[4.32] Pengyu Zhang, Dinesh Bharadia, Kiran Joshi, and Sachin Katti. Hitchhike: Practical backscatter using commodity wifi. In *Proceedings of the 14th ACM Conference on Embedded Network Sensor Systems CD-ROM*, pages 259–271, 2016.

[4.33] Tulasi R Haritsa, BM Yashu, U Kumar, and MN Suma. Mathematical characterization and simulation of LoRa. *Wireless Personal Communications*, 115(2):1481–1506, 2020.

[4.34] Analog Devices. *ADG918/ADG919: Wideband 4 GHz, 43 dB Isolation at 1 GHz, CMOS 1.65 V to 2.75 V, 2:1 Mux/SPDT*, 5 2016. Rev. E.

[4.35] Infineon Technologies. *BFP405: Surface mount wideband silicon NPN RF bipolar transistor*, 01 2019. Rev. 2.0.

[4.36] Russian tunnel diode. *AI301A (A301A), Gallium Arsenide, Switching applications, I_p=2mA, V_p=180mV, V_{pp}=0.65V, $I_p/I_v = 4$.*

[4.37] Analog Devices(Linear Technologies). *LTC6990: TimerBlox: Voltage Controlled Silicon Oscillator*, 1 2020. Rev. D.

UNIVERSITAT ROVIRA I VIRGILI
LONG-RANGE BACKSCATTERING COMMUNICATIONS FOR NEXT GENERATION IOT APPLICATIONS
Marc Lázaro Martí

[4.38] Analog Devices(Linear Technologies). *Micropower, 40kHz to 4MHz Resistor Set Oscillator in SOT-23*, 6 2005. Rev. A.

[4.39] Analog Devices(Maxim Integrated). *MAX9914–MAX9917: 1MHz, 20A, Rail-to-Rail I/O Op Amps with Shutdown*, 11 2014. Rev. 3.

[4.40] Analog Devices(Maxim Integrated). *MAX9634: nanoPower, 4-Bump UCSP/SOT23, Precision Current-Sense Amplifier*, 7 2021. Rev. 6.

[4.41] Microchip Technology. *ATtiny417/814/816/817 tinyAVR 1-series. MCU de 8 Bits, AVR Family ATtiny417 Series Microcontrollers, AVR, 20 MHz, 4 KB, 24 Pines, VQFN*, 12 2020. Rev. D.

[4.42] Microchip Technology. *ATtiny202/204/402/404/406 tinyAVR 0-series. MCU de 8 Bits, AVR Family ATtiny402 Series Microcontrollers, AVR, 20 MHz, 4 KB, 8 Pines, SOIC*, 04 2021. Rev. A.

[4.43] Ian Mathews, Paul J King, Frank Stafford, and Ronan Frizzell. Performance of III–V solar cells as indoor light energy harvesters. *IEEE Journal of Photovoltaics*, 6(1):230–235, 2015.

Chapter 5

Backscattering for Localization Applications

5.1 Introduction

In recent years, indoor localization systems have generated great interest due to their potential applications [5.1][5.2][5.3]. Most of the methods proposed in the literature, as well as commercial systems, focus on improving localization precision [5.4]. In some applications, such as autonomous robot guidance [5.5], localization accuracy is fundamental because they require an exact location in a coordinate system. Performance depends greatly on the method used: (time of arrival (ToA), time difference of arrival (TDoA), angle of arrival (AoA), or received signal strength indicator (RSSI); and it also depends on the environment, attenuation introduced by objects, movement, and the localization algorithm employed. Depending on the localization method, different wireless systems have been explored: Wi-Fi, Bluetooth, UWB, modulated continuous wave (FMCW) radar, RFID, etc. LoRa-based localization systems have recently been proposed for indoor and outdoor environments [5.6][5.7][5.8][5.9]. Some of these systems were compared in [5.10][5.11]. Their precision often increases with the number of anchors [5.12][5.13] and these systems require LoS (Line-of-Sight) scenarios [5.14].

Another interesting group of localization techniques includes those that are based on fingerprint classification. In this case, the system estimates the location of an object by matching received signal strength indicator (RSSI) measure-

UNIVERSITAT ROVIRA I VIRGILI
LONG-RANGE BACKSCATTERING COMMUNICATIONS FOR NEXT GENERATION IOT APPLICATIONS
Marc Lázaro Martí

ments with the closest location fingerprints. The RSSI measurements are often obtained from Wi-Fi access points [5.15] or Bluetooth beacons [5.16], [5.17] in indoor applications or Sigfox, LoRaWAN [5.18] or mobile communications in large areas [5.19]. However, these methods require a calibration of the system by recording the exact location on a map. Two main groups of techniques have been reported for classification in these systems: neural networks [5.20][5.21] and machine learning techniques [5.22]. The main drawback of previous localization methods is that the high number of anchors and the manual calibration procedure decrease the system's return on investment (ROI). However, there are other applications in which knowing an approximate area, such as a room [5.17][5.23][5.24] is sufficient. Within the various medical applications, monitoring activities of daily living (ADL) [5.25][5.26][5.27][5.28] constitute an example of the second group. A major challenge for these applications is that the tracking devices must be noninvasive and private because they are intended to be used by the elderly. Therefore, the devices must be worn and the battery lifetime must be very long to avoid continuous recharges that can cause the user to stop using the system. Both the installation of the localization system and the cost mean that a reduced number of anchors capable of covering large areas (e.g. care facilities or hospitals) have to be installed. From a practical perspective, it should be noted that in most indoor localization methods, when the number of anchors used is small (or when the cost of installing several anchors is prohibitive), the precision is around several meters [5.16]. In other words, they can be used to roughly recognize a room.

The main goal and novelty of this chapter is that it describes the study of the performance and viability of an indoor room-level localization system based on LoRa signal backscattering. This work aims to contribute to the improvement of human and social welfare through the application of the system in fields such as patient management in hospitals and care facilities, capacity monitoring in establishments of different types, autonomous buildings, etc. Compared to other systems based on active beacons (e.g. Bluetooth, Wi-Fi, or UWB), LoRa backscatter stands out for its lower power consumption and long range due to the high sensitivity of LoRa receivers. This LoRa backscatter device can be embedded in a wristband or any other wearable device, thereby obviating the need for uncomfortable, heavy electronics. The localization system is made up of several LoRa receivers distributed in different rooms, a LoRa transmitter located at a central point, and the backscatter device, which is carried or worn by an individual. Commercial low-cost LoRa modules have been used in the experiments to validate the system. A simple algorithm based on the reception of the highest signal strength was used to determine the position (the room where the user is). In order to improve accuracy, different machine learning algorithms are compared. In these cases, algorithm training was accomplished by acquiring a set of samples while the user moves randomly within each of the rooms. The random point acquisition greatly accelerates the training procedure. It is only necessary to know which room the samples were taken in, and not the coordinates of the receivers or the transmitter. Parameters such as transmitter power and propagation model are also not necessary to program the algorithms. This simplifies the training procedure and practical implementation in real environments.

The chapter is organized as follows. Section 5.2 describes the system, including the proof of concept prototype for the LoRa backscatter. A propagation model is proposed to check the algorithm based on simulated data. The simulated results are described in Section 5.3. Experimental results are presented in section 5.4. Section 5.5 compares the features of the proposed room-level localization technique with other localization technologies. Finally, section 5.6 summarizes the conclusions.

5.2 System architecture overview

The use of a backscattering device to reflect the data signal from a LoRa transmitter to an adjacent channel as described in section 4.2.2 of chapter 4 is here proposed. A set of LoRa receivers tuned to this shifted channel receive the data packets and measure the received signal strength indicator (RSSI) and signal-to-noise ratio (SNR) for each one. The LoRa receivers are placed in different rooms, so each room can be identified by comparing the RSSI collected by the receivers. The receiver with the highest RSSI level determines the location of the backscatter. Advanced fingerprint algorithms can be employed to improve the decision. A diagram of a possible scenario is shown in Figure 5.1. The LoRa backscatter stands out for its low power consumption compared to other beacons because it does not have to generate RF signals or process the incoming LoRa packets.

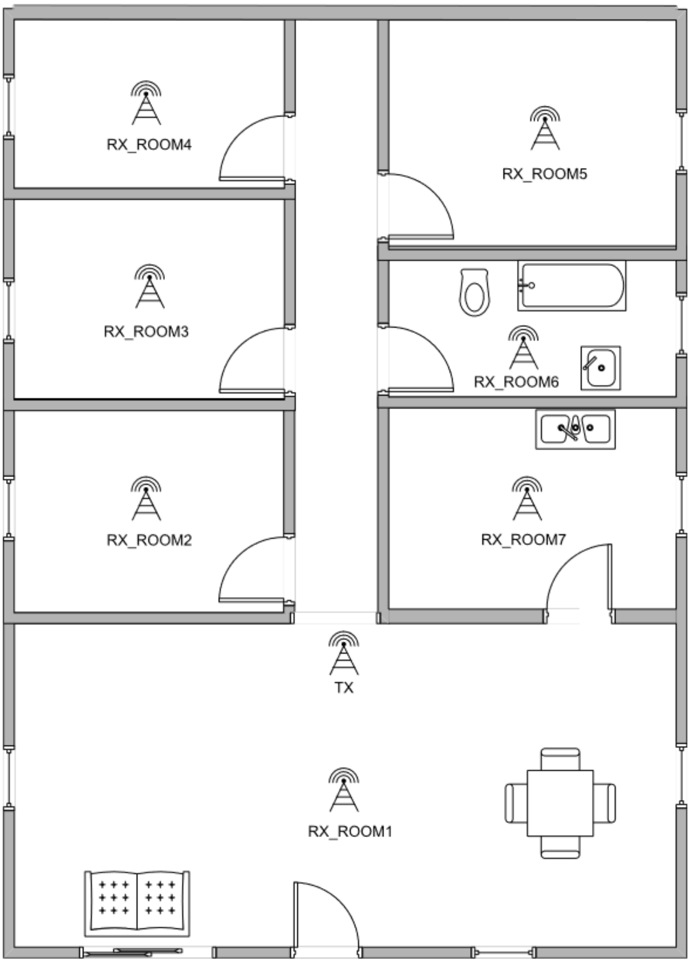

Figure 5.1: Example of typical Tx and Rx placement on a house

For the system implementation, several low-cost LoRa32 development boards, from the brand TTGO, are used. These boards integrate an ESP32 microcontroller from Espressif and a Semtech SX1276 transceiver. The ESP32 provides Wi-Fi and Bluetooth connectivity, while the SX1276 enables LoRa connectivity, making it a versatile triple-wireless technology transceiver. The SX1276 transceiver can operate across a frequency range from 137 MHz to 1020 MHz, covering European, North American, and Asian ISM bands. One advantage of the SX1276 transceiver is its high tolerance to frequency deviations, enabling demodulation of packets with significant frequency deviation. Moreover, in the rare case of being unable to demodulate the data due to considerable frequency

UNIVERSITAT ROVIRA I VIRGILI
LONG-RANGE BACKSCATTERING COMMUNICATIONS FOR NEXT GENERATION IOT APPLICATIONS
Marc Lázaro Martí

shift, the SX1276 includes an automatic frequency correction (AFC) functionality to readjust the reception frequency. System implementation has been done with the European/American version of the LoRa32 board, which operates at the 868 MHz ISM band. The SX1276 allows to set up several parameters of the radio and the LoRa packets. For the experiments, transmission power has been left to default (17 dBm). However, it can be adjusted from 2 dBm up to 20 dBm, if necessary. The cost of the LoRa32 boards is less than 10 \$ and no hardware modification is needed, making the full deployment of the system cheap and easy.

A Wi-Fi link is used to send the data to a cloud database. Alternatively, the data can be transmitted among nodes via point-to-point LoRa links or directly to a LoRa gateway, which uploads the data to a cloud database. This second method can be used in industrial environments or in buildings without coverage in some areas or without any coverage at all. Data are transferred to the cloud by means of the MQTT (Message Queue Telemetry Transport) protocol. Each receiver publishes the RSSI and SNR measurements in a MQTT topic. To avoid errors arising from lost packets or uploading delays, the transceiver sends each packet with an identifier, which might be just a counter. This makes it possible to synchronize the data from the receivers. After the tag transmission, each receiver publishes a message to the MQTT broker with the packet identifier, the room identifier, and the measured RSSI and SNR.

5.2.1 Backscatter prototype

For the tag prototype, the LoRa packet-level OOK modulation described in chapter 4 is used. This modulation has been chosen for two reasons: to keep the tag's power consumption as low as possible and to enable demodulation with commercial LoRa receivers, thereby reducing the overall implementation cost. Figure 5.2 shows a render of the PCB and an image of the manufactured prototype, which has been mounted into a 3D-printed wristband. The tag integrates a wideband low-profile ceramic antenna (P/N: 0900AT43A0070) from Johanson Technology, designed to operate in the 868 and 915 MHz bands. The antenna consists of a ceramic monopole and an additional printed line used to adjust the frequency of the antenna at the 868 MHz band. To enhance impedance matching, an LC matching network with SMD components is designed with the aid of the VNA. To switch between the open circuit and the short circuit the already

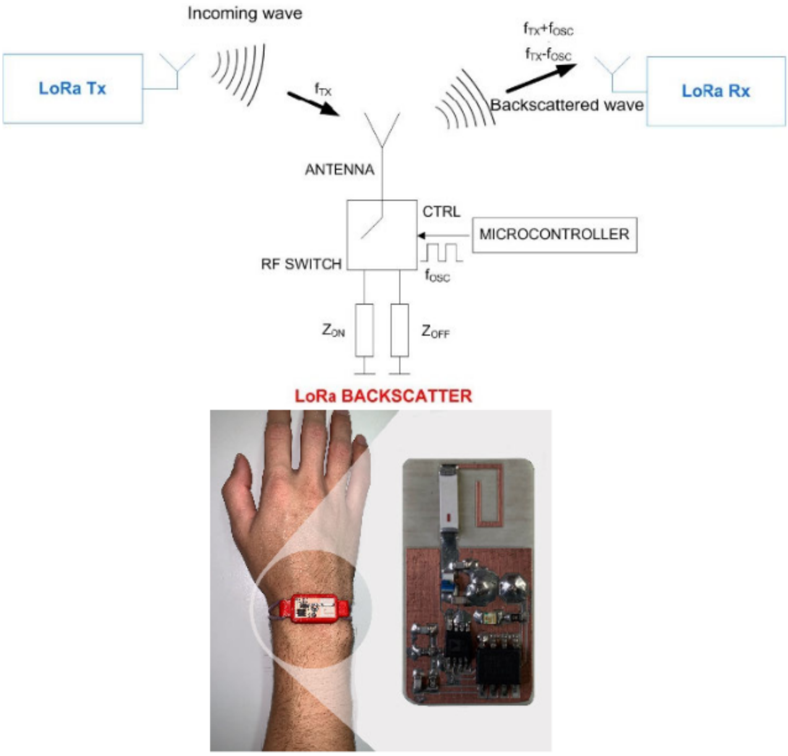

Figure 5.2: Block diagram of the backscattering system (top) and photograph of a prototype (bottom)

mentioned ADG902 is used, and the control signal has been directly generated using the PWM function of the AtTiny402 microcontroller. The microcontroller generates the tag identifier baseband data transmitted via backscattering. The total current consumption when the microcontroller wakes up, working at a 1 MHz clock speed with an operating voltage of 3.3 V, is 890 μA. This total value is considerably lower than that of Bluetooth LE modules that typically require 7 to 15 mA when they are in the reception or transmission states. One interesting aspect to mention is that the backscatter device has no transmission or reception mode, since it is not capable of processing or generating RF signals. Therefore, the tag periodically backscatters the identifier by reflecting the LoRa packets, and is a task of the receiver to get this information.

5.2.2 Propagation model

The method proposed is based on the measurement of the RSSI from different receivers tuned to the frequency channel shifted by the backscattering tag. In this section, an empirical model to perform simulations of coverage area and localization rates is proposed. The received power (P_R) can be expressed as in an RFID system using the radar equation [5.29]:

$$P_R = \frac{P_T G_T}{4\pi d_T^2} \cdot \Delta\sigma \cdot \frac{1}{4\pi d_R^2} \cdot \frac{\lambda^2}{4\pi} \cdot G_R \tag{5.1}$$

where P_T is the transmitted power, G_T the transmitter antenna gain, G_R is the receiver antenna gain, $\Delta\sigma$ is the differential radar cross-section of the tag, and d_T and d_R are the distance from the transmitter to the tag and from the tag to the receiver, respectively. The receiver power increases when the tag is close to the transmitter or to the receiver. The locus of points with constant received power approximately describes an ellipse. However, the Friis model (5.1) is only valid in free space or in situations where the antennas have high directivity, which avoids multipath interference. In order to include multipath propagation, an empirical model is often considered. The RSSI is the received power expressed in dBm [5.30]:

$$P_R(dBm)(d_T, d_R) = P_R(dBm)(d_0, d_0) - 10 n_1 log(\frac{d_T}{d_0}) - 10 n_2 log(\frac{d_R}{d_0}) - L_{wall} + X \tag{5.2}$$

Equation (5.2) is split into two parts considering the two existing propagation paths: transmitting to the tag and backscattering to the receiver. In (5.2), d_0 is the reference distance (i.e. the midpoint between transmitter and receiver $d_0 = (d_{Tx-Rx}/2)$, $P_R(d_0, d_0)$ is the average received power at d_0, and n_1 and n_2 are the path loss exponents, whose values depend on the environment and the height of the antennas. Typical values for indoor environments vary between 2.5 and 3. L_{wall} are the losses due to the diffraction and attenuation of the walls and X is a random variable that takes into account the attenuation due to multipath propagation. $P_R(d_0, d_0)$ can be determined experimentally through the regression analysis of measured data and depends on the transmitted power and the gain of the antennas. It is also a function of the height of the antennas and depends on the diffraction. However, in this section, the expression

(5.2) derived from the Friis transmission equation is considered to perform the simulations.

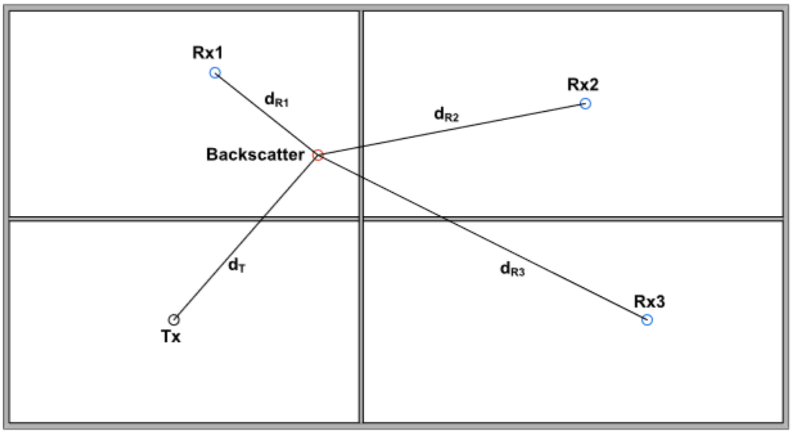

Figure 5.3: Diagram used for the description of the propagation analysis.

A typical deployment scenario is shown in the diagram in Figure 5.3. The attenuation due to path loss between the transmitter and tag is equal from all the receivers, but the power of the received signals depends on the distance between each receiver and the backscatter d_{Ri} and the number of walls that each signal goes through. It is expected that the maximum received power will be that of the receiver that is in the same room as the backscattering tag because it will be closer to it and attenuation due to the walls will not be an issue.

Typical wall attenuation at 900 MHz for a brick wall is 5 dB and 15-18 dB for a double reinforced concrete wall [5.31]. In the model, the distribution presented by the random variable X can be considered of the log-normal type $X(dB) \sim N(0, \sigma)$, where σ (dB) is the standard deviation and experimental results yield values between 2 and 4 dB for a single path [5.32] (in this case a double path due to the backscatter channel is expected). The coverage probability (Prob) is that in which the average received power or RSSI (P_R) is higher than the receiver sensitivity S (dBm). For a log-normal distributed channel this is given by [5.33]:

$$Prob(P_R > S) = \frac{1}{2} erfc(\frac{S - P_R}{\sqrt{2}\sigma}) \tag{5.3}$$

where $erfc$ is the complementary error function. For a σ equal to 8 dB and a received power of 10 dB above the sensitivity (fading margin), the coverage probability is about 90%.

LoRa receiver sensitivity depends too on the noise figure of the receiver and the bandwidth (BW). It is computed from the noise floor plus the required signal-to-noise ratio (SNR) [5.34]:

$$S(dBm) = -174 + 10log(BW) + NF(dB) + SNR(dB) \tag{5.4}$$

where BW is the bandwidth of the LoRa signal and NF is the LoRa receiver noise figure. The SNR is negative and can be approximated as a function of the spreading factor (SF), which can be selected in LoRa transceivers from 7 to 12 [5.34]:

$$SNR(dB) = -7.5 - 2.5(SF - 7) \tag{5.5}$$

One of the reasons why the LoRa transceiver is used in this system is its high sensitivity, which allows the detection of the backscatter in indoor environments in spite of the attenuation typically experienced in such spaces. From (5.4), for a spread factor of 12, a bandwidth of 125 kHz, and assuming a typical noise figure of 6 dB, the receiver sensitivity is -137 *dBm*.

5.2.3 Room-Level Classification

The classification process is schematically described in Fig. 5.4. The LoRa transmitter regularly transmits packets using a counter for packet identification. The transmission time interval (packets transmitted per second) can be configured depending on the desired tracking frequency or application. When it strikes the device, the signal coming from the LoRa transmitter is backscattered towards the receivers located in each room to identify the signal. Each receiver has been tuned to the shifted frequency channel. The received RSSI and SNR measured by the LoRa transceiver and the packet identification number are sent to the MQTT broker. In this case, a Wi-Fi transmission was used because the ESP32 has a built-in Wi-Fi transceiver. However, in the absence of Wi-Fi coverage, the receiving node can be configured to transfer the message via LoRa to a gateway with an internet connection, which will upload the data to the MQTT broker. A custom Mosquitto broker was used in the experiment but other MQTT brokers can also be used [5.35]. There are two modes of operation: the training mode and the normal operation mode. In the former, the data are stored in a SQLLite database for later use in the training of the classifiers. Then, to train the system, data are provided together with the room where the backscatter is, allowing the system to learn the footprint of each backscatter location. To indicate the room where the backscatter is located during the training stage, a message is sent to an MQTT configuration topic using a mobile app. After that, the training data collected are used for training the machine learning model. The MQTT client is implemented in Python using the Eclipse MQTT Paho module. The scikit-learn module was used for machine learning [5.36]. In the normal operation mode, the room number is determined by the measured RSSI and SNR data, which are obtained from the subscription to the respective MQTT topics of the receivers. If any of the receivers do not receive the backscattered packet because they are outside its coverage area, the minimum value of RSSI (sensitivity) and SNR will be assigned. The simplest classification method consists of assigning the room to the index of the receiver with the highest SNR or RSSI. As the resolution in the RSSI measurement is only 1 dBm for the LoRa transceiver used in this work, the use of the SNR measurements seems to be the most appropriate option due to their higher resolution, which tends to yield better results. In any case, the room can be determined with both the RSSI and the SNR measurements, providing the system with a double-check calculation. If advanced machine learning algorithms are used for the room classification, the room index is obtained by running the trained classifier. The simulated and experimental results with different classifiers are described in the next sections.

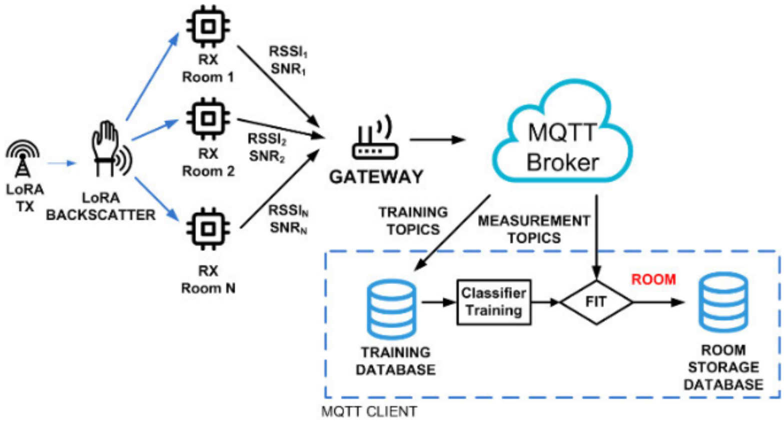

Figure 5.4: Block diagram of the classification procedure

5.3 Simulations

Figure 5.5 shows the received power in dBm computed using the model (5.1) and (5.2) as a function of the tag location for a frequency of 868 MHz. A distance of 50 meters between the transmitter and receiver is considered. Figure 5.5a shows the ideal free-space case, whereas Figure 5.5b shows a scenario with decay factors (n_1 and n_2) of 2.5. The transmitter EIRP is 20 dBm, and the receiver antenna gain 2.2 dBi. The gain of the tag antenna is -1 dBi (the typical surface-mounted antenna gain). In the simulations, the measured tag gain and the ideal square wave waveform are used. An indoor scenario resulted in a considerable reduction in receiver power. However, these simulation results show that a LoRa backscatter can be detected within an area of about 100 m^2, although the attenuation of walls or other objects would decrease this coverage area. Experimental results measured in a house are presented in the next section.

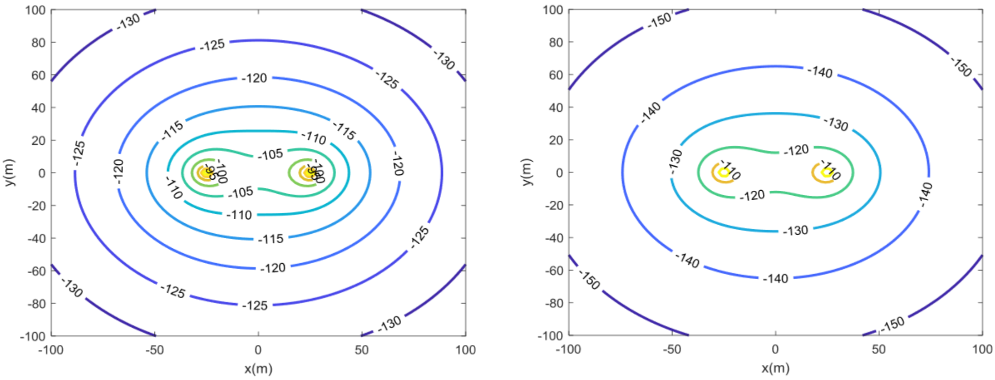

(a) (b)

Figure 5.5: Contour map of the received power as a function of the backscatter location (a) in free space and (b) with multipath considering a propagation decay factor of 2.5

A series of simulations were performed to validate the proposed method. Six rooms of different sizes covering an area of 40 m × 40 m were considered. The received power obtained from the model (5.2) is shown in Figure 5.6. A value of 10 dB was taken for wall attenuation with a standard deviation of 8 dB. The transmitter was located approximately in the center of room one.

Several classifiers can be used to determine the room number associated with the RSSI measured at each one of the receivers. The simplest method consists

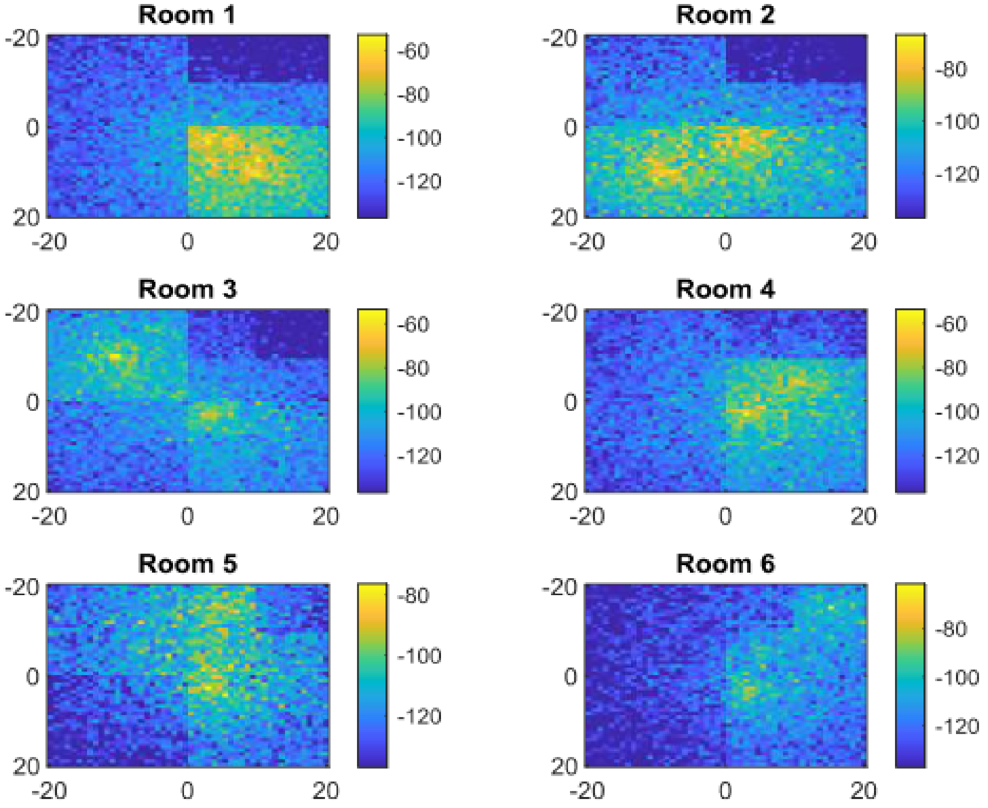

Figure 5.6: Contour map of the received power as a function of the backscatter location for each receiver location.

of determining the room number through the receiver with the best power reception. Figure 5.7 shows the classified rooms for the last simulated scenario using the simplest RSSI classifier, where the room is assigned to the receiver that collects the strongest RSSI signal. This method has the advantage of not requiring a training step. Although this method worked reasonably well in the presence of noise, other classifiers were also analyzed. Classifiers implemented in Python scikit-learn machine learning module [5.37] were used for comparison. The classifiers were trained with 20% of the samples (simulated reception powers for several backscatter locations). The samples were chosen at random and the other 80% were used to test the trained classifier.

Table 5.1 compares the accuracy obtained for each classifier. The best classifier found was linear discriminant analysis (LDA), which achieved an accuracy of up to 91.5%. Table 5.2 shows the confusion matrix C for the linear dis-

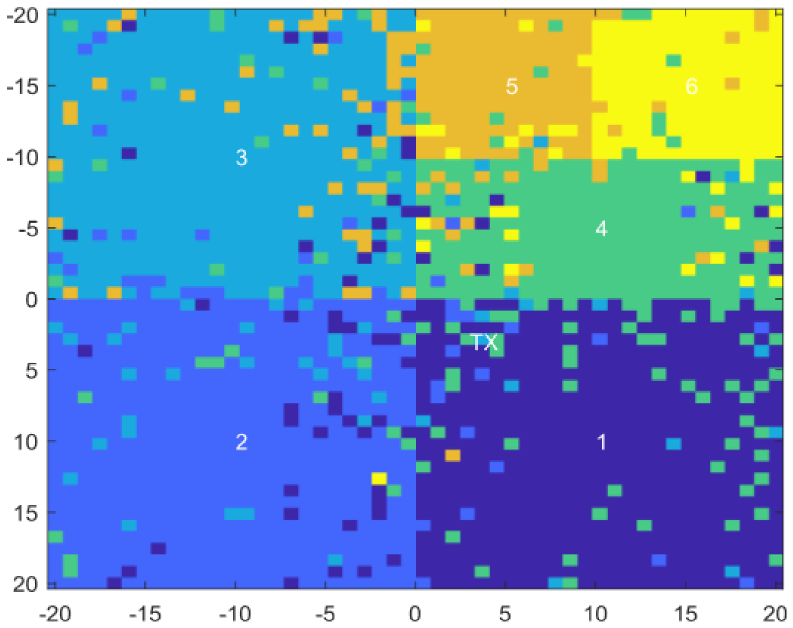

Figure 5.7: Color map that shows the classified room using an RSSI level classifier. Each room is represented by a different color. The position of the receiver is indicated with the room number. The position of the transmitter is also shown

criminant analysis (LDA) classifier. Each element of this matrix Cij is equal to the number of observations known to be in the room i and predicted to be in the room j. For example, in the first row, the first column indicates the room where the backscatter is, in this case room one. The algorithm was correct in its predictions in 93.84% of cases, but in 3.07% of cases it determined that the backscatter was in room two, in 1.54% it predicted room three and in 1.54% room four. The results shown in Table 5.2 have been normalized by the total number of samples. Note that to improve readability the values equal to zero have been left blank. As the table shows, there was a small degree of confusion with neighboring rooms.

Room	HRL	LR	LDA	KNN	CART	NB
1	84	93	94	90	88	90
2	87	91	91	94	89	90
3	85	96	97	93	91	93
4	80	80	90	80	77	82
5	85	72	83	90	79	83
6	92	54	94	89	97	94
Average	85.6	89.3	92.5	91.5	87.0	89.3

Table 5.1: Accuracy (%) as a function of classifier

Room	1	2	3	4	5	6
1	93.84	3.07	1.54	1.54	0	0
2	3.91	91.40	4.69	0	0	0
3	0	0.85	96.58	2.56	0	0
4	4.92	0	3.27	90.16	0	1.64
5	0	0	6.89	3.45	82.75	6.89
6	0	0	0	0	5.71	94.28

Table 5.2: Normalized confusion matrix in % using linear discriminant analysis (LDA)

5.4 Experimental Results

The proposed room-level localization system was tested in a complex scenario like a house. Several experiments were conducted to determine the coverage of the LoRa backscattering system. Figure 5.8 shows a heatmap of the received RSSI for the different rooms equipped with receivers. The backscatter was placed on the wrist of a volunteer moving along different points on a grid that was used to plot the heatmap. The transmitter was located approximately in the center of the house (in the hallway) and a receiver was located in another room separated by walls. The receiving power strength on the receiver increased when the backscatter was near the transmitter or receiver. But reasonable coverage (with an RSSI greater than -122 dBm) was achieved in all situations. In addition, the backscatter signal could also be received by the nearest receivers. In this test, the transmitted channel frequency was 868 MHz and the receiver was tuned to the shifted channels spaced at 300 kHz. The bandwidth was 125 kHz and the spread factor was 12.

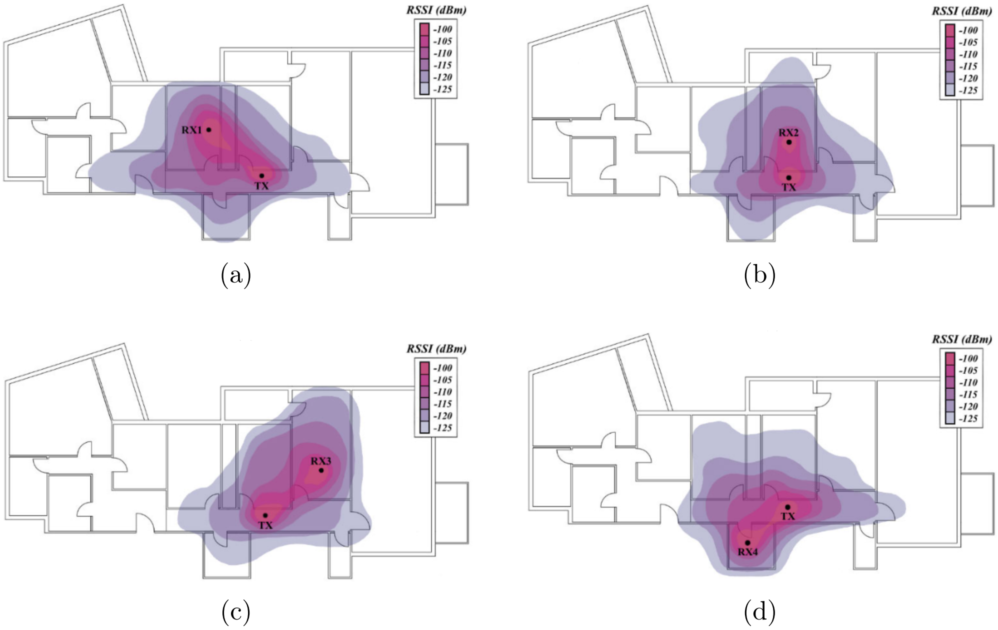

(a) (b)

(c) (d)

Figure 5.8: Measured heatmap of the received power as a function of the backscatter location for: (a) receiver RX1 located in room number one (b) receiver RX2 located in room number two, (c) receiver RX3 located in room number three and (d) receiver RX4 located in room number four (d).

The system was applied to the scenario shown in Fig. 5.8, where the transmitter was located in the center of the hall and four receivers were installed in the adjacent rooms. The training procedure was performed as described in section 5.2. A comparison of the accuracy achieved in each room is summarized in Table 5.3. Considering the method based on the highest SNR level, the degree of accuracy was very good for rooms one and two because the received strength levels were high, whereas in rooms three and four, except for some points, the degree of coverage was much lower, or even non-existent. Applying the same analysis, the accuracy for rooms three and four was worse compared to rooms one and two. This explains the low degree of accuracy for these rooms using the simplest method. However, the other classifiers were able to achieve high degrees of accuracy in all four rooms, regardless of the room's potential coverage. Our experimental results showed that the best average accuracy was obtained with the LDA classifier although the accuracy for room two was worse than that obtained with the other classifiers. In any case, the differences in the average accuracy among classifiers were slight, excluding the highest SNR level classifier. The Gaussian Naïve Bayes classifier (NB) was not analyzed because the measured data in the rooms did not meet the Gaussianity conditions for the method that would allow it to be applied. The normalized confusion matrix for the KNN classifier is shown as an example in Table 5.4. The elements of the principal diagonal that present the highest percentages correspond, as expected, to the neighboring rooms. There were a significant number of cases (10%) that increased the confusion in the classification process between rooms four and one. This is because the coverage area of Rx1 and Rx4 partially overlapped with similar received levels.

Room	HSL	LR	LDA	KNN	CART	SVM
1	82	82	93	90	82	88
2	89	86	83	81	81	88
3	40	97	97	93	93	93
4	56	86	86	82	82	84
Average	66.7	87.7	89.7	87.7	84.5	88.2

Table 5.3: Accuracy (%) as a function of classifier

Room	1	2	3	4
1	92.5	5.0	0.0	2.5
2	7.1	83.3	4.7	4.7
3	0.0	1.7	96.6	1.7
4	10.0	4.0	0.0	86.0

Table 5.4: Normalized confusion matrix in % using linear discriminant analysis (LDA)

5.5 Discussion

This section examines existing indoor localization technologies described in the literature. Although several surveys (e.g [5.1], [5.38]) on localization are available, this section aims to compare the advantages and limitations of the system proposed here in relation to other similar systems. Table 5.5 summarizes some of the properties, advantages and disadvantages of the technologies studied. The different technologies analyzed are described below.

- **WiFi-based localization:** Wi-Fi networks (based on IEEE 802.11 standards) operate on ISM bands and are used to provide internet access to computers and smartphones, especially in indoor environments. Therefore, Wi-Fi is an ideal system for indoor localization and has been widely examined in the literature. Existing access points deployed for communication can be used as reference (anchor) nodes for localization without the need for additional infrastructure. However, it is sometimes necessary to install more anchors to improve accuracy, which increases the cost. Localization techniques based on RSSI measurements are the most common [5.39], [5.40]. However other techniques use the measurement of channel state information (CSI) [5.41] provided by some Wi-Fi boards. ToA has also been proposed, although it requires hardware modifications [5.42]. AoA localization techniques were recently investigated in [5.43], [5.44]. Fingerprinting is a widely used indoor positioning method used with several wireless access technologies including Wi-Fi, BLE, and Zigbee [5.38].

This method can improve accuracy in NLoS environments, but it requires the creation of a database from training measurements and the results depend on the density of reference points.

- **ZigBee-based localization:** Zigbee (IEEE 802.15.4 standard) based localization techniques [5.45], [5.46] share the primary drawback of Wi-Fi-based techniques. But the use of Zigbee networks (mainly used for wireless sensor networks) is not as widespread in indoor environments as Wi-Fi networks, and requires an additional deployment that increases the cost of the localization system.

- **UWB-based localization:** Ultra-wideband (UWB) is one of the wireless solutions that has been the focus of much attention for indoor localization. This interest arises from the fact that the use of large bandwidth yields high time resolution because it is possible to separate multiple reflections from the pulse. Consequently, UWB systems can obtain centimeter-level ranging accuracy under LoS conditions, even in indoor environments with multipath interferences [5.47]. The position is often determined by trilateration from the measured ToA from different anchors distributed in the coverage area. Localization accuracy depends on the number of anchors, their location and the LoS coverage. To address the problem of cost-effective UWB-based localization in complex indoor environments, hybrid trilateration and fingerprint algorithms have been developed [5.48]. The cost of the system depends on the number of anchors. UWB technology is not as extensive as other wireless technologies and the cost of UWB transceivers is still expensive compared with other wireless systems.

- **Bluetooth-based localization:** The latest version of Bluetooth (IEEE 802.15.1) is known as Bluetooth Low Energy (BLE), which achieves a coverage range of 10–20 meters indoors with better energy efficiency compared to previous versions. The RSSI measurement provided by BLE devices can be used for localization [5.49]. However, two BLE-based protocols, iBeacons (by Apple Inc.) and Eddystone (by Google, Inc.), have been designed for context-aware proximity services. From the messages received from the beacon and from the RSSI, users are classified into three range regions (immediate, near, far, or unknown) [5.50]. Based on the user's proximity to any beacon, the mobile application triggers an action (e.g. sends a notification or a discount coupon) [5.51]. Fingerprint approaches based on iBeacon have been proposed in the literature [5.52], [5.53]. Recently, private company U-blox released the XPLR-AOA BLE and Bluetooth 5.1 kits for indoor positioning based on the Angle-of-Arrival (AoA) technique [5.54].

- **RFID-based localization:** RFID systems can be classified into active and passive. Active RFID is often used to track assets outdoors, where great position accuracy (order of meters) is not required and when measurements are taken over long periods of time that require long-lasting batteries. They are based on UHF (ISM 433 or 868 MHz bands) and ISM 2.45 GHz. Essentially, two different types of active RFID tags are available: transponders and beacons. With transponders, communication works by means of backscattering, but using battery-assisted (BAP) devices. Active RFID transponders are commonly used in secure access control and payment systems at toll booths. Battery-assisted UHF tags that comply with Gen 2 standards [5.55] (and therefore, can be read with standard UHF readers) have recently been released which can extend the range of passive RFID systems up to 20 m. In these BAP tags, the uplink read range is limited by the sensitivity of the reader as in passive UHF tags. However, some active RFID tags use beacons tags. These tags use a transmitter that sends out messages every few seconds. The use of transmitters extends the read range but can noticeably reduce the battery life depending on the transmission duty-cycle used. Active tag beacons are very common in the oil and gas industry, and for cargo tracking systems. For example, commercial Tagsense tags use a modified Zigbee transmitter, and Omni-ID integrates BLE and LoRaWAN transceivers. The read range in the open field is about 80 m depending on the antennas used [5.56]. This read range is notably reduced in indoor environments to 20 m [5.57] due to multipath propagation. The sensitivity of a typical reader is on the order of -100 dBm. The price of active RFID tags is between 20 and 100 $ depending on their functionality and whether they must withstand harsh conditions. Although active RFID is designed for outdoor applications, it has been explored for indoor localization applications as well. LANDMARC is one of the most popular indoor localization tech-

UNIVERSITAT ROVIRA I VIRGILI
LONG-RANGE BACKSCATTERING COMMUNICATIONS FOR NEXT GENERATION IOT APPLICATIONS
Marc Lázaro Martí

nologies used in active RFID tags [5.58][5.59][5.60]. Passive tags, on the other hand, have shorter transmission ranges because they do not use a battery. They, therefore, have a lower read range than active RFID tags. UHF RFID can read up to a few meters, but HF RFID and NFC can read up to a few centimeters. Although they have the advantage of low cost, UHF readers are more expensive than the NFC readers available in modern smartphones. A navigation system based on NFC has recently been proposed in [5.61]. The limitations on coverage make passive RFID suitable for proximity applications [5.62].

- **Acoustic-based localization:** Radiofrequency (RF) signals share many characteristics with acoustic signals. Compared to more common RF signals like Wi-Fi, acoustic localization has been gaining strength because its main requirements are microphones and speakers, which are widely equipped on many smart devices [5.63][5.64]. Another advantage of the acoustic signal is that the speed of sound is much lower than the speed of a RF signal, which is a positive factor in achieving higher accuracy. Different localization techniques are being used that combine multiple microphone signals, such as those based on time of arrival (ToA), time difference of arrival (TDoA), Doppler effect, direction of arrival (DOA), and steered response power (SRP) [5.39]. One advantage of these devices is that they can use the microphones built into smartphones [5.65].

- **Ultrasound-based localization:** Ultrasound-based localization technology uses ultrasound waves (typically at 44 kHz) to measure the ToA between a transmitter and a receiver [5.66], [5.67]. Due to the lower velocity of sound compared to that of an electromagnetic wave, accuracies of less than centimeters can be achieved in range measurements. For node synchronization, the ultrasound localization system requires a secondary RF link. One disadvantage of these systems is the dependence of sound velocity on temperature and humidity and the high levels of environmental noise, which reduce accuracy and coverage.

- **Visual-based localization:** Visual localization systems are commercially available on the market (e.g. Kinect [5.68] or Wii [5.69] for games). They do not have interferences from RF devices, but they are affected by environmental lighting conditions and pose privacy issues. Another disadvantage of this technology is the high computational requirements that make it difficult to integrate into smartphones or wearables. These systems also require LOS, limiting their coverage to only a few meters [5.70].

- **Visible light-based localization:** Visible light-based localization techniques use light sensors to measure the position and direction of LED emitters that work something like iBeacons. The localization is based on AoA methods [5.71]. The advantage of this technology is its low cost, which makes it possible to install the LEDs over large areas. However, the biggest drawback with this technology, as with other techniques based on light, is the need for LOS.

- **Lidar-based localization:** LIDARs and infrared cameras are becoming more popular in robotics [5.72] as their accuracy is in the order of millimeters. LIDAR is fast and accurate and it is gaining popularity with car makers due its use in the development of autonomous cars [5.73]. Although LIDAR systems are becoming increasingly common, such systems are still expensive.

- **Infrared-based (IR) localization:** The low cost of IR positioning systems makes them a potential candidate at the room level, though their coverage range and accuracy are limited [5.74]. Technical limitations such as the required LOS between the transmitter and the receiver and the interference of IR waves with fluorescent light and sunlight reduce the widespread usability of these systems. These issues have led researchers to explore alternative approaches to infrared-based indoor positioning.

As already addressed in the introduction of this chapter, the main novelty of the system here proposed is the utilization of a LoRa backscatter for localization. Apart from RFID systems, which also rely on backscattering communication, other wireless systems use communication between a transmitter and a receiver for localization. Consequently, the power consumption of the proposed system is lower than even BLE and Zigbee devices. A low-cost ($<$ 5$) proof-of-concept of a wearable device have been here presented. The prototype can run continuously for 24 days or for more than two years if the refresh rate is reduced to 1/10 seconds with a 500 mAh Lite-on battery. The proposed system has been designed for room-level localization as an alternative to other techniques based on RSSI, such as Wi-Fi, Zigbee or BLE can also be applied. The computational cost of the algorithm is low, and it is implemented on a server. Low power consumption is a key advantage as it eliminates the need for frequent battery replacement, which can be an issue in ADL applications for use with the elderly. This long battery life also means that the system can be used to track assets in indoor environments. The high sensitivity of LoRa receivers and their great immunity to interferences [5.75] due to the robustness of the CSS-modulation scheme allow a higher coverage range than other backscatters, including active RFID based on proprietary protocols. The use of lower frequencies reduces the undesirable effects associated with the attenuation and diffraction by the body compared with systems operating in 2.45 GHz bands. In addition, in some countries, the ISM 433 MHz band can be used for LoRa (e.g. based on Semtech SX1278 [5.30]) allowing the coverage range to be expanded. The result is better for indoor coverage, reducing the number of anchors or reference nodes and improving performance in wearable applications. LoRa is also a low-cost, low-power standardized wireless system that is continuously growing. Therefore, the cost of LoRa transceivers is lower than active UHF RFID readers. Low-cost Wi-Fi nodes with LoRa transceivers are used as receivers, therefore the use of expensive multichannel gateways or routers is not required. For example, in this work, a low-cost LoRa32 shield with a Semtech SX1276 transceiver was used in the experiments. Therefore, the overall cost of the system is lower than UWB and comparable to Wi-Fi or Zigbee based systems. Device-free localization (DFL) techniques have been proposed using the variation of the RSSI received from different signals in a wireless network to detect and count the presence of human activity [89]. Although DFL has several interesting applications, the results are likely to be more sensitive to environmental changes. Fingerprint-based algorithms are often used in DFL. However, the training data requires several measurements with a person standing at different positions to avoid the influence of measurement noise. Also, training environments with multiple people who backscatter the signals is challenging [5.76]. In the proposed system, the multiple signals backscattered on different objects in the scene are filtered from those produced by the LoRa backscatter because they change the frequency to another channel.

Technology	Coverage	Consumption	Accuracy	Cost	Mathod	Advantages	Disadvantages
UWB	30 m	Moderate	cm-m	High	Toa Fingerprint	Interference immunity	Dedicated hardware
Bluetooth	10-20 m	Low	m	Low	RSSI iBeacon	Widely available. Integrated in smartphones.	sensitive to multipath
WiFi	50 m	High	dm-m	Low	RSSI CSI AoA Fingerprint	Widely available.	Sensitive to multipath. Complex processing.
ZigBee	100 m	Moderate	m	Moderate	RSSI Fingerprint	Easy deployment	Sensitive to multipath. Dedicated hardware.
Active RFID	20 m (indoor)	Low	< 1 m	Moderate	RSSI Fingerprint	Long battery life.	Expensive readers. Property tags.
Passive RFID	cm - few m	Very low	< 1 m	Low	RSSI Fingerprint	Tag low cost. No battery	Expensive UHF readers. Short range for HF system.
Ultrasound	Couple of m	Low - Moderate	1.5 - 10 cm	Low	ToA	Widely used for distance measurements.	Enironmental noise. Air temperature and humidity dependence.
Acoustic	Couple of m	Low - Moderate	cm	Moderate	ToA AoA	Smartphones compatibility.	Ambient noise dependence. Requires mic. arrays & loudspeakers.
Infrared	Few meters	Room-level	dm	Low	ToA TDoA	Cheap. Widely adopted for human detection.	Flueorescent & sunlight interference. Required LoS.
Lidar	10 m	Very high.	mm - cm	High	ToA AoA	Commercially available. No RF interference.	Required LoS. No wearable.
Visual	10 m	High	mm - cm	Medium	AoA TDoA RSSI	Commercially available. No RF interference.	Light dependence. Requires LoS.
This work	<100 m	Very low	Room-level	Low	RSSI Fingerprint	Low number of anchors. Wearable. Interference immunity	Requires a database.

Table 5.5: Comparison of the reflection amplifiers proposed in the literature.

5.6 Conclusion

Techniques for estimating the absolute position of users in a coordinate system have been widely researched. Today, applications can locate a person or an object within a building by merely monitoring the room in which that individual or item is located. This chapter presents an indoor localization system with room-level accuracy and a focus on easy setup and a low-cost network. The system is based on the analysis of the backscattered signal strength received by LoRa transceivers deployed in an indoor environment. The backscatter device stands out for its low power consumption and long range. This chapter has explored different methods, ranging from a simple technique that assigns the room to the receiver with the highest measurement value to other more sophisticated techniques based on machine learning. The method based on the highest received signal strength exhibits great accuracy as long as the coverage is good in all rooms. Otherwise, to obtain better accuracy, methods based on machine learning are required. In these cases, a process to train the classification algorithms is necessary. This is a quick and straightforward process that only requires taking random samples in each room, without the need to determine the absolute coordinates at the sampling points. The proposed method also does not require establishing a propagation model, unlike other existing methods in the literature. The use of a low-cost, low-consumption LoRa backscatter device eliminates the need for frequent battery recharging, unlike in devices with higher consumption. Our experimental results show that the LoRa backscatter can be detected through the walls in indoor environments. The LoRa backscatter can be easily integrated into a comfortable wrist band. Due to the high sensitivity of the LoRa system, a large number of anchors are not required. Simulated and experimental results show that only one receiver in each room and a transmitter for every three to four receivers are needed to locate a person at the floor level in a standard home. The wireless network required can be implemented using low-cost modules available on the market without any modification. The back-end system can be implemented in any computer without the need for expensive servers using MQTT protocol.

5.7 Bibliography

[5.1] Faheem Zafari, Athanasios Gkelias, and Kin K Leung. A survey of indoor localization systems and technologies. *IEEE Communications Surveys & Tutorials*, 21(3):2568–2599, 2019.

[5.2] Ali Yassin, Youssef Nasser, Mariette Awad, Ahmed Al-Dubai, Ran Liu, Chau Yuen, Ronald Raulefs, and Elias Aboutanios. Recent advances in indoor localization: A survey on theoretical approaches and applications. *IEEE Communications Surveys & Tutorials*, 19(2):1327–1346, 2016.

[5.3] Jiang Xiao, Zimu Zhou, Youwen Yi, and Lionel M Ni. A survey on wireless indoor localization from the device perspective. *ACM Computing Surveys (CSUR)*, 49(2):1–31, 2016.

[5.4] Fernando Seco, Antonio R Jiménez, Carlos Prieto, Javier Roa, and Katerina Koutsou. A survey of mathematical methods for indoor localization. In *2009 IEEE International Symposium on Intelligent Signal Processing*, pages 9–14. IEEE, 2009.

[5.5] Aswin N Raghavan, Harini Ananthapadmanaban, Manimaran S Sivamurugan, and Balaraman Ravindran. Accurate mobile robot localization in indoor environments using bluetooth. In *2010 IEEE international conference on robotics and automation*, pages 4391–4396. IEEE, 2010.

[5.6] Ka-Ho Lam, Chi-Chung Cheung, and Wah-Ching Lee. RSSI-based LoRa localization systems for large-scale indoor and outdoor environments. *IEEE Transactions on Vehicular Technology*, 68(12):11778–11791, 2019.

[5.7] Ka-Ho Lam, Chi-Chung Cheung, and Wah-Ching Lee. New RSSI-based LoRa localization algorithms for very noisy outdoor environment. In *2018 IEEE 42nd Annual Computer Software and Applications Conference (COMPSAC)*, volume 2, pages 794–799. IEEE, 2018.

[5.8] Yi-Cheng Lin, Chi-Chia Sun, and Kuo-Ting Huang. RSSI measurement with channel model estimating for IoT wide range localization using LoRa communication. In *2019 International Symposium on Intelligent Signal Processing and Communication Systems (ISPACS)*, pages 1–2. IEEE, 2019.

[5.9] You Li, Zhe He, Yuqi Li, Hongliang Xu, Ling Pei, and Yu Zhang. Towards location enhanced IoT: Characterization of LoRa signal for wide area localization. In *2018 Ubiquitous Positioning, Indoor Navigation and Location-Based Services (UPINLBS)*, pages 1–7. IEEE, 2018.

[5.10] Jeremy Landt. The history of RFID. *IEEE potentials*, 24(4):8–11, 2005.

[5.11] Klaus Finkenzeller. *RFID handbook: fundamentals and applications in contactless smart cards, radio frequency identification and near-field communication.* John wiley & sons, 2010.

[5.12] Patrik Moravek, Dan Komosny, Milan Simek, Mojmir Jelinek, David Girbau, and Antonio Lazaro. Investigation of radio channel uncertainty in distance esti-

UNIVERSITAT ROVIRA I VIRGILI
LONG-RANGE BACKSCATTERING COMMUNICATIONS FOR NEXT GENERATION IOT APPLICATIONS
Marc Lázaro Martí

mation in wireless sensor networks. *Telecommunication systems*, 52:1549–1558, 2013.

[5.13] Patrik Moravek, Dan Komosny, Milan Simek, David Girbau, and Antonio Lazaro. Energy Analysis of Received Signal Strength Localization in Wireless Sensor Networks. *Radioengineering*, 20(4), 2011.

[5.14] Danijel Čabarkapa, Ivana Grujić, and Petar Pavlović. Comparative analysis of the bluetooth low-energy indoor positioning systems. In *2015 12th International Conference on Telecommunication in Modern Satellite, Cable and Broadcasting Services (TELSIKS)*, pages 76–79. IEEE, 2015.

[5.15] Zheng Yang, Chenshu Wu, and Yunhao Liu. Locating in fingerprint space: Wireless indoor localization with little human intervention. In *Proceedings of the 18th annual international conference on Mobile computing and networking*, pages 269–280, 2012.

[5.16] Mingfeng Li, Lichen Zhao, Ding Tan, and Xiaozhe Tong. BLE fingerprint indoor localization algorithm based on eight-neighborhood template matching. *Sensors*, 19(22):4859, 2019.

[5.17] Thomas Tegou, Ilias Kalamaras, Konstantinos Votis, and Dimitrios Tzovaras. A low-cost room-level indoor localization system with easy setup for medical applications. In *2018 11th IFIP Wireless and Mobile Networking Conference (WMNC)*, pages 1–7. IEEE, 2018.

[5.18] Geun Yeop Ha, Seung Beom Seo, Hyun Seob Oh, and Wha Sook Jeon. LoRa ToA-based localization using fingerprint method. In *2019 International Conference on Information and Communication Technology Convergence (ICTC)*, pages 349–353. IEEE, 2019.

[5.19] Michiel Aernouts, Rafael Berkvens, Koen Van Vlaenderen, and Maarten Weyn. Sigfox and LoRaWAN datasets for fingerprint localization in large urban and rural areas. *Data*, 3(2):13, 2018.

[5.20] Y Basiouny, M Arafa, and Amany M Sarhan. Enhancing Wi-Fi fingerprinting for indoor positioning system using single multiplicative neuron and PCA algorithm. In *2017 12th International Conference on Computer Engineering and Systems (ICCES)*, pages 295–305. IEEE, 2017.

[5.21] Laslo Gogolak, Silvester Pletl, and Dragan Kukolj. Indoor fingerprint localization in WSN environment based on neural network. In *2011 IEEE 9th International Symposium on Intelligent Systems and Informatics*, pages 293–296. IEEE, 2011.

[5.22] Lersan B Del Mundo, Rafael Lean D Ansay, Cedric Angelo M Festin, and Roel M Ocampo. A comparison of wireless fidelity (Wi-Fi) fingerprinting techniques. In *ICTC 2011*, pages 20–25. IEEE, 2011.

[5.23] Ruoxi Jia, Ming Jin, Zilong Chen, and Costas J Spanos. SoundLoc: Accurate room-level indoor localization using acoustic signatures. In *2015 IEEE International Conference on Automation Science and Engineering (CASE)*, pages 186–193. IEEE, 2015.

[5.24] Paul Martin, Bo-Jhang Ho, Nicholas Grupen, Samuel Munoz, and Mani Srivastava. An ibeacon primer for indoor localization: demo abstract. In *Proceedings of the 1st ACM Conference on Embedded Systems for Energy-Efficient Buildings*, pages 190–191, 2014.

[5.25] Christian Debes, Andreas Merentitis, Sergey Sukhanov, Maria Niessen, Nikolaos Frangiadakis, and Alexander Bauer. Monitoring activities of daily living in smart homes: Understanding human behavior. *IEEE Signal Processing Magazine*, 33(2):81–94, 2016.

[5.26] Stephanie Blackman, Claudine Matlo, Charisse Bobrovitskiy, Ashley Waldoch, Mei Lan Fang, Piper Jackson, Alex Mihailidis, Louise Nygård, Arlene Astell, and Andrew Sixsmith. Ambient assisted living technologies for aging well: a scoping review. *Journal of Intelligent Systems*, 25(1):55–69, 2016.

[5.27] M Johannes Tiusanen. Soil scouts: Description and performance of single hop wireless underground sensor nodes. *Ad Hoc Networks*, 11(5):1610–1618, 2013.

[5.28] Ioan Susnea, Luminita Dumitriu, Mihai Talmaciu, Emilia Pecheanu, and Dan Munteanu. Unobtrusive monitoring the daily activity routine of elderly people living alone, with low-cost binary sensors. *Sensors*, 19(10):2264, 2019.

[5.29] Pavel V Nikitin, KVS Rao, and Roberto D Martinez. Differential RCS of RFID tag. *Electronics letters*, 43(8):1, 2007.

[5.30] Marc Lazaro, Antonio Lazaro, and Ramon Villarino. Feasibility of backscatter communication using LoRAWAN signals for deep implanted devices and wearable applications. *Sensors*, 20(21):6342, 2020.

[5.31] Daniel Pena, Rodolfo Feick, Hristo D Hristov, and Walter Grote. Measurement and modeling of propagation losses in brick and concrete walls for the 900-MHz band. *IEEE Transactions on Antennas and Propagation*, 51(1):31–39, 2003.

[5.32] Antonio Lazaro, David Girbau, and David Salinas. Radio link budgets for UHF RFID on multipath environments. *IEEE transactions on antennas and propagation*, 57(4):1241–1251, 2009.

[5.33] Andrea Goldsmith. *Wireless communications*. Cambridge university press, 2005.

[5.34] Semtech. SX1276/77/78/79—137 MHz to 1020 MHz Low Power Long Range Transceiver. 2020.

[5.35] Roger A Light. Mosquitto: server and client implementation of the MQTT protocol. *Journal of Open Source Software*, 2(13):265, 2017.

[5.36] Oliver Kramer and Oliver Kramer. Scikit-learn. *Machine learning for evolution strategies*, pages 45–53, 2016.

[5.37] Fabian Pedregosa, Gaël Varoquaux, Alexandre Gramfort, Vincent Michel, Bertrand Thirion, Olivier Grisel, Mathieu Blondel, Peter Prettenhofer, Ron Weiss, Vincent Dubourg, et al. Scikit-learn: Machine learning in Python. *the Journal of machine Learning research*, 12:2825–2830, 2011.

[5.38] Ahasanun Nessa, Bhagawat Adhikari, Fatima Hussain, and Xavier N Fernando. A survey of machine learning for indoor positioning. *IEEE access*, 8:214945–214965, 2020.

[5.39] Shaoguo Xie, Yanjun Hu, and Yi Wang. Weighted centroid localization for wireless sensor networks. In *2014 IEEE International Conference on Consumer Electronics-China*, pages 1–4. IEEE, 2014.

[5.40] Bo Yang, Luyao Guo, Ruijie Guo, Miaomiao Zhao, and Tiantian Zhao. A novel trilateration algorithm for RSSI-based indoor localization. *IEEE Sensors Journal*, 20(14):8164–8172, 2020.

[5.41] Linsheng Zhao, Hongpeng Wang, Pengpeng Li, and Jingtai Liu. An improved WiFi indoor localization method combining channel state information and received signal strength. In *2017 36th Chinese Control Conference (CCC)*, pages 8964–8969. IEEE, 2017.

[5.42] Moustafa Youssef, Adel Youssef, Chuck Rieger, Udaya Shankar, and Ashok Agrawala. Pinpoint: An asynchronous time-based location determination system. In *Proceedings of the 4th international conference on Mobile systems, applications and services*, pages 165–176, 2006.

[5.43] Laxima Niure Kandel and Shucheng Yu. VWAN: Virtual WiFi ANtennas for increased indoor localization accuracy. In *2019 IEEE International Conference on Industrial Internet (ICII)*, pages 258–267. IEEE, 2019.

[5.44] Zengshan Tian, Zhongchun Wang, Ze Li, and Mu Zhou. RTIL: A real-time indoor localization system by using angle of arrival of commodity WiFi signal. In *2019 11th International Conference on Wireless Communications and Signal Processing (WCSP)*, pages 1–6. IEEE, 2019.

[5.45] Jan Blumenthal, Ralf Grossmann, Frank Golatowski, and Dirk Timmermann. Weighted centroid localization in zigbee-based sensor networks. In *2007 IEEE international symposium on intelligent signal processing*, pages 1–6. IEEE, 2007.

[5.46] Hening Pram Praditya, Lukman Rosyidi, Riri Fitri Sari, et al. Performance evaluation of RSS fingerprinting method to track ZigBee devices location using artificial neural networks. In *2017 International Conference on Information and Communication Technology Convergence (ICTC)*, pages 268–273. IEEE, 2017.

[5.47] Davide Dardari, Andrea Conti, Ulric Ferner, Andrea Giorgetti, and Moe Z Win. Ranging with ultrawide bandwidth signals in multipath environments. *Proceedings of the IEEE*, 97(2):404–426, 2009.

[5.48] Sandra Djosic, Igor Stojanovic, Milica Jovanovic, Tatjana Nikolic, and Goran Lj Djordjevic. Fingerprinting-assisted UWB-based localization technique for complex indoor environments. *Expert Systems with Applications*, 167:114188, 2021.

[5.49] Ramsey Faragher and Robert Harle. Location fingerprinting with bluetooth low energy beacons. *IEEE journal on Selected Areas in Communications*, 33(11):2418–2428, 2015.

[5.50] Volodymyr Andrushchak, Taras Maksymyuk, Mykhailo Klymash, and Dmytro Ageyev. Development of the iBeacon's positioning algorithm for indoor scenarios. In *2018 International Scientific-Practical Conference Problems of Infocommunications. Science and Technology (PIC S&T)*, pages 741–744. IEEE, 2018.

[5.51] Zhiqiang He, Binyue Cui, Wei Zhou, and Shigeki Yokoi. A proposal of interaction system between visitor and collection in museum hall by iBeacon. In *2015 10th International Conference on Computer Science & Education (ICCSE)*, pages 427–430. IEEE, 2015.

[5.52] Jinbo Zuo, Shuo Liu, Hao Xia, and Yanyou Qiao. Multi-phase fingerprint map based on interpolation for indoor localization using iBeacons. *IEEE Sensors Journal*, 18(8):3351–3359, 2018.

[5.53] Thai-Mai Thi Dinh, Ngoc-Son Duong, and Kumbesan Sandrasegaran. Smartphone-based indoor positioning using BLE iBeacon and reliable lightweight fingerprint map. *IEEE Sensors Journal*, 20(17):10283–10294, 2020.

[5.54] XPLR-AOA-1 kit: Direction finding explorer kit with NINA-B4 Bluetooth 5.1 module. https://www.u-blox.com/en/product/xplr-aoa-1-kit. [Accessed: 17/06/23].

[5.55] Jae-Young Jung, Hyunseok Kim, Heyung-Sub Lee, and Kyung-Whan Yeom. An UHF RFID tag with long read range. In *2009 European Microwave Conference (EuMC)*, pages 1113–1116. IEEE, 2009.

[5.56] Mathieu Cassel, Thomas Dépret, and Hervé Piégay. Assessment of a new solution for tracking pebbles in rivers based on active RFID. *Earth Surface Processes and Landforms*, 42(13):1938–1951, 2017.

[5.57] Shouzhi Xu, Huan Zhou, Changzhi Wu, Chung-Ming Huang, and Sungkon Moon. Spatial signal attenuation model of active RFID tags. *IEEE access*, 6:6947–6960, 2018.

[5.58] Lionel M Ni, Yunhao Liu, Yiu Cho Lau, and Abhishek P Patil. LANDMARC: Indoor location sensing using active RFID. In *Proceedings of the First IEEE International Conference on Pervasive Computing and Communications, 2003.(PerCom 2003).*, pages 407–415. IEEE, 2003.

[5.59] Guang-yao Jin, Xiao-yi Lu, and Myong-Soon Park. An indoor localization mechanism using active RFID tag. In *IEEE International Conference on Sensor Networks, Ubiquitous, and Trustworthy Computing (SUTC'06)*, volume 1, pages 4–pp. IEEE, 2006.

[5.60] Jingyu Wang, Ravindra Kumar Dhanapal, Priyadharshini Ramakrishnan, Balakumar Balasingam, Thiago Souza, and Roman Maev. Active RFID based indoor localization. In *2019 22th International Conference on Information Fusion (FUSION)*, pages 1–7. IEEE, 2019.

[5.61] Wilson E Sakpere, Nhlanhla Boyfriend Wilton Mlitwa, and Michael Adeyeye Oshin. Towards an efficient indoor navigation system: a near field communication approach. *Journal of Engineering, Design and Technology*, 2017.

[5.62] Stavroula Siachalou, Spyros Megalou, Anastasios Tzitzis, Emmanouil Tsardoulias, Aggelos Bletsas, John Sahalos, Traianos Yioultsis, and Antonis G Dimitriou. Robotic inventorying and localization of rfid tags, exploiting phase-fingerprinting. In *2019 IEEE International Conference on RFID Technology and Applications (RFID-TA)*, pages 362–367. IEEE, 2019.

[5.63] Maximo Cobos, Fabio Antonacci, Anastasios Alexandridis, Athanasios Mouchtaris, and Bowon Lee. A survey of sound source localization methods in wireless acoustic sensor networks. *Wireless Communications and Mobile Computing*, 2017, 2017.

[5.64] Manni Liu, Linsong Cheng, Kun Qian, Jiliang Wang, Jin Wang, and Yunhao Liu. Indoor acoustic localization: A survey. *Human-centric Computing and Information Sciences*, 10:1–24, 2020.

[5.65] Huijie Chen, Fan Li, and Yu Wang. EchoLoc: Accurate device-free hand localization using COTS devices. In *2016 45th International Conference on Parallel Processing (ICPP)*, pages 334–339. IEEE, 2016.

[5.66] Faheem Ijaz, Hee Kwon Yang, Arbab Waheed Ahmad, and Chankil Lee. Indoor positioning: A review of indoor ultrasonic positioning systems. In *2013 15th International Conference on Advanced Communications Technology (ICACT)*, pages 1146–1150. IEEE, 2013.

[5.67] Carlos Medina, José Carlos Segura, and Angel De la Torre. Ultrasound indoor positioning system based on a low-power wireless sensor network providing sub-centimeter accuracy. *Sensors*, 13(3):3501–3526, 2013.

[5.68] Jamie Shotton, Andrew Fitzgibbon, Mat Cook, Toby Sharp, Mark Finocchio, Richard Moore, Alex Kipman, and Andrew Blake. Real-time human pose recognition in parts from single depth images. In *CVPR 2011*, pages 1297–1304. Ieee, 2011.

[5.69] Thomas Schlömer, Benjamin Poppinga, Niels Henze, and Susanne Boll. Gesture recognition with a Wii controller. In *Proceedings of the 2nd international conference on Tangible and embedded interaction*, pages 11–14, 2008.

[5.70] Fares Alkhawaja, Mohammad Jaradat, and Lotfi Romdhane. Techniques of indoor positioning systems (IPS): A survey. In *2019 Advances in Science and Engineering Technology International Conferences (ASET)*, pages 1–8. IEEE, 2019.

[5.71] Ye-Sheng Kuo, Pat Pannuto, Ko-Jen Hsiao, and Prabal Dutta. Luxapose: Indoor positioning with mobile phones and visible light. In *Proceedings of the 20th annual international conference on Mobile computing and networking*, pages 447–458, 2014.

[5.72] Yuan Xu, Yuriy S Shmaliy, Yueyang Li, Xiyuan Chen, and Hang Guo. Indoor INS/LiDAR-based robot localization with improved robustness using cascaded FIR filter. *IEEE Access*, 7:34189–34197, 2019.

[5.73] Ryan W Wolcott and Ryan M Eustice. Visual localization within lidar maps for automated urban driving. In *2014 IEEE/RSJ International Conference on Intelligent Robots and Systems*, pages 176–183. IEEE, 2014.

[5.74] Erwin Aitenbichler and Max Muhlhauser. An IR local positioning system for smart items and devices. In *23rd International Conference on Distributed Computing Systems Workshops, 2003. Proceedings.*, pages 334–339. IEEE, 2003.

[5.75] Tallal Elshabrawy and Joerg Robert. The impact of ism interference on lora ber performance. In *2018 IEEE Global Conference on Internet of Things (GCIoT)*, pages 1–5. IEEE, 2018.

[5.76] Neal Patwari and Joey Wilson. RF sensor networks for device-free localization: Measurements, models, and algorithms. *Proceedings of the IEEE*, 98(11):1961–1973, 2010.

UNIVERSITAT ROVIRA I VIRGILI
LONG-RANGE BACKSCATTERING COMMUNICATIONS FOR NEXT GENERATION IOT APPLICATIONS
Marc Lázaro Martí

Chapter 6

Backscattering for Implanted Medical Applications

6.1 Introduction

The performance of wearable and implantable devices is often limited by the lifetime of batteries. A considerable part of the power budget of these devices is spent by the radiofrequency circuits (oscillators, receivers, and transmitters) on wireless communication [6.1]. Recently, backscatter communications have been raising a great interest in a variety of applications including implanted devices [6.2][6.3][6.4][6.5].

In this chapter, we discuss a novel communication method based on the frequency-shifted LoRa backscatter for wearable and deep-implanted devices using Medical Implant Communication Service (MICS) bands and the ISM 433 MHz band. The system is designed for low-data rate transmission since it implements the LoRa packet OOK modulation described in chapter 4. Therefore commercial LoRa transceivers are used for the tag information demodulation. Long-distance links can be achieved using the approach presented in [6.6][6.7]. Therefore, communications based on LoRa backscatter can be useful for communication with deep implants. The strong attenuation of the body is compensated by the sensitivity of the LoRa receivers. To this end, the backscatter must be connected to a specifically designed implanted antenna. The miniaturization of the implanted antenna decreases the radiation efficiency, but this is mitigated by the sensitivity of the system. In this chapter we use off-the-shelf components

UNIVERSITAT ROVIRA I VIRGILI
LONG-RANGE BACKSCATTERING COMMUNICATIONS FOR NEXT GENERATION IOT APPLICATIONS
Marc Lázaro Martí

to design a specific antenna, which is tuned to the desired frequency adjusting the matching network and covering it with a heat-shrinkable sleeve.

The chapter is organized as follows. Section 6.2 describes the system overview with the phantom design, the tag miniaturization, the antenna tuning and the link budget calculation. Section 6.3 presents experimental results with the proposed system. Section 6.4 compares the system with other approaches reported in the literature. Finally, Section 6.5 draws conclusions.

6.2 System Design

6.2.1 System Description

The system consists of a very little backscatter device implementing the already mentioned LoRa packet OOK modulation. For the transceivers, we used two LoRa32 boards, one to transmit and the other to receive the backscattered packets in the adjacent channel. The proposed implanted device works in the Medical Implant Communication Service (MICS) band [6.8], ranging from 401 to 406 MHz. Therefore, the Asian version of the commercial LoRa32 board has been used. In contrast to the European version that integrates an SX1276 operating at 868 MHz, the Asian version integrates an SX1278, which is capable to operate between 137 MHz and 525 MHz, making it suitable to operate in the MICS and in the Industrial Scientific and Medical (ISM) 433 MHz band, which is also frequently used for Implanted Medical Devices (IMD). Alternatively, more expensive LoRa gateways integrate both transmission and multi-channel reception in the same device, making more simple the system deployment, and allowing multiple tags to transmit packets to different channels simultaneously.

The OOK modulation reduces the cost of the implementation and is more than enough to send the information of the tag. However, if higher data rates are required, it can be further improved by demodulating the tag transmission by means of a software-defined radio. The techniques described in chapter 4 to maximize the power backscattered have been used. Therefore, the tag antenna is loaded using an open circuit and a short circuit, using the ADG902 switch. The switch is controlled by a low-power square wave LTC6907 oscillator from Analog Devices [6.9], which can be adjusted with a simple resistor for an output frequency between 40 kHz and 4 MHz. The power consumption of the oscillator is 36 μA for an output frequency of 400 kHz. Moreover, the LTC6907 has 1% frequency accuracy from 0 °C to 70 °C, which is enough for the LoRa-packet OOK modulation. The tag controls the oscillator by means of the low-power AtTiny402 microcontroller. For the antenna, we used a low-profile ceramic antenna from Johansons Technology designed to operate at the 868-900 MHz band. However, with some adjustments (and under the specific implant conditions) it can be successfully adjusted at the MICS and 433 MHz ISM bands. Figure 6.1 shows an image of the prototype and Figure 6.2 shows a spectrogram with the tag successfully modulating the LoRa packets at the 406 MHz band.

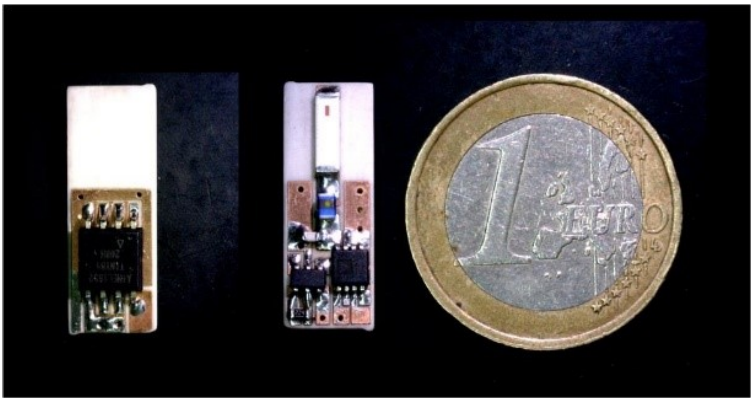

Figure 6.1: Photograph of LoRa backscatter. Bottom layer with the microcontroller and top layer with the RF switch, antenna and oscillator.

As previously described in chapter 4, the backscattered power is maximized if the antenna resonates in the band ($[Im]Z_a = 0$) and the two reflection coefficients have a phase shift of 180° one to each other. Reflection coefficients at each state (open circuit and short circuit) are measured as a function of the frequency using the setup depicted in Figure 4.2 of chapter 4. Markers at 406 and 433 MHz bands show the insertion loss introduced by the ADG902 switch. A loss of 1.6 dB with respect to the ideal short circuit and open circuit case is observed. The measured phase difference between both states is close to 180°.

6.2.2 Phantom Design

In order to develop an antenna for a deep implant, a phantom material needs to be designed to simulate the muscle tissue for the desired frequency range.

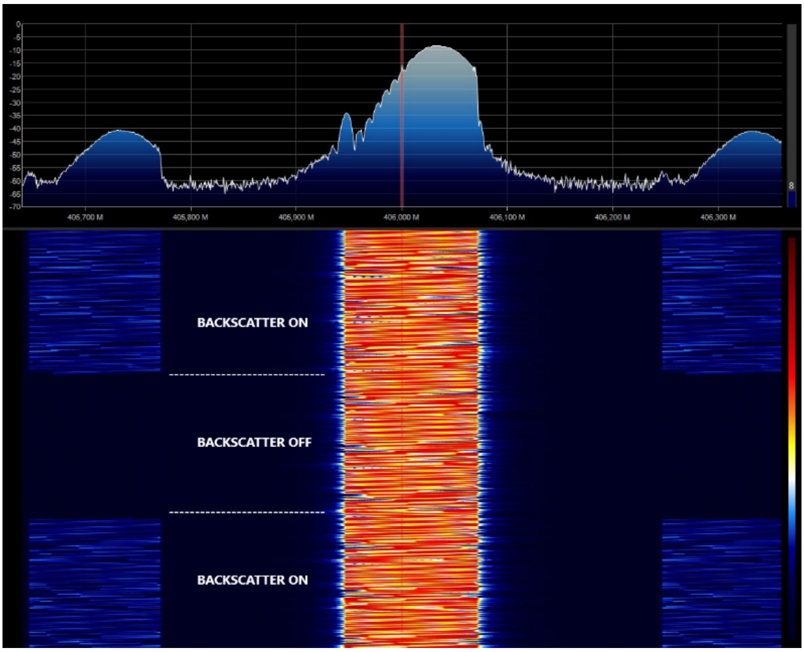

Figure 6.2: Measured spectrogram with the backscatter enabled and disabled for SF = 12, BW = 125 kHz.

The dielectric properties of different tissues have been reported in the literature [6.10]. To this end, several phantom materials have been proposed for different frequency ranges and applications [6.11][6.12][6.13][6.14]. In our case, the dielectric properties must be designed to take into account the shift in the antenna frequency response introduced by the high dielectric constant of the tissues and to simulate the attenuation of the body and the reduction in the radiation efficiency of the antenna due to the high tissue conductivity. In our case, we are interested in finding a simple phantom for the ISM band (400–433 MHz). The dielectric constant of the muscle is about 57 and the conductivity is 0.8 S/m at 406 MHz according to data provided by Gabriel et al. [6.10]. For frequencies higher than 100 MHz, the dielectric constant of the muscle is lower than that of water [6.12] so a phantom based on a saline water solution is considered because antennas can be used in it more easily than in a solid phantom and it is easy to manufacture. In [6.13], a mixture of water with NaCl and sucrose was proposed to design a phantom at 2.45 GHz. The present study follows a similar procedure but adjusts the parameters to the 400–500 MHz band. The permittivity was measured using an open-ended coaxial probe [6.15] from Keysight (slim form

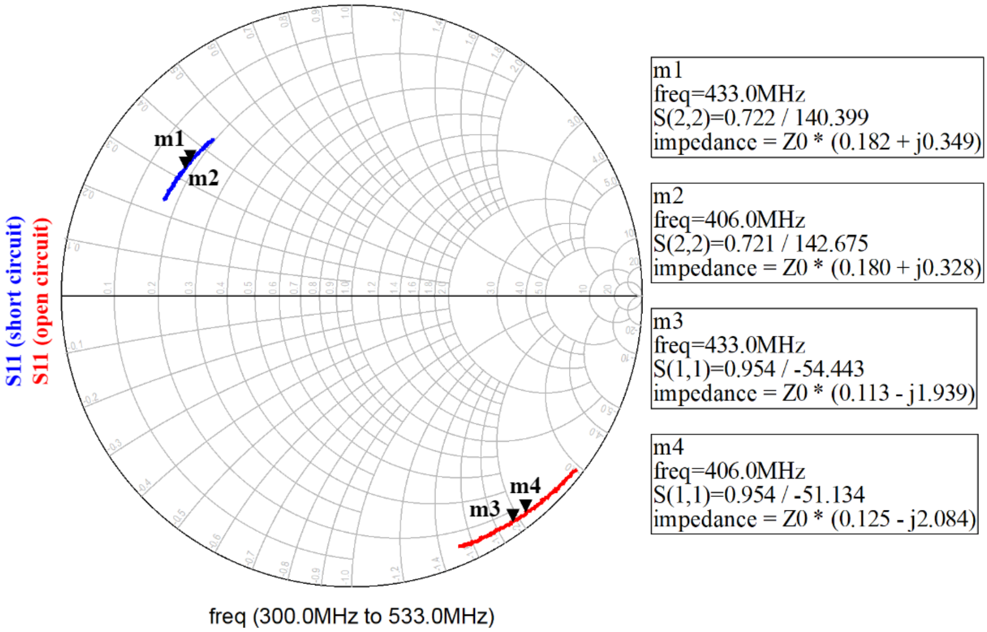

Figure 6.3: Measured reflection coefficients of the ADG902 switch (S_{11} open circuit state (red) and short circuit state (blue)) at the MICS (406 MHz) and 433 MHz ISM bands.

probe 85070E/N1501A model) with a Vector Network Analyzer (VNA) model Keysight PNA E8364C. Figure 6.4a shows the real part and imaginary part of the permittivity as a function of the mass fraction (percentage by weight) of sugar at 406 MHz. The imaginary part remains nearly constant whereas the real part decreases as a function of sugar. It can be shown that for a percentage of about 45% of sugar, the real part is close to the muscle value. Figure 6.4b shows the complex permittivity for a saline water solution with 45% of sugar and changing the quantity of NaCl at 406 MHz. Therefore, adding NaCl can increase the conductivity and adding sugar can reduce the real part. A solution consisting of 45% sucrose, 0.8% NaCl and water (percentages are in weight) was chosen. Figure 7 compares the data reported by Gabriel et al. [6.10] and our measurements at ambient temperature (25 $°C$). The agreement was good in the 400–600 MHz band. The power transported by the wave decreases exponentially in accordance with Lambert's law. The attenuation constant introduced by the tissue can be computed using [6.16]:

$$\alpha\left(\frac{dB}{m}\right) = 8.686\cdot 2\pi f\sqrt{\frac{\mu_0\varepsilon_0\varepsilon'}{2}[\sqrt{1+(\frac{\varepsilon''}{\varepsilon'})^2}+1]} \tag{6.1}$$

where $\varepsilon_c = \varepsilon' - j\varepsilon''$ is the complex relative permittivity, ε_0 and μ_0 are the vacuum permittivity and permeability, respectively, and f is the frequency. Considering the muscle complex permittivity, a typical attenuation of 165 dB/m or a power penetration depth of $d_p = 1/(2\alpha(N_p/m)) = 2.6$ cm is introduced by the muscle at 406 MHz. Equation (7) was derived for incident plane waves in large bodies without considering reflections within the materials at the opposite interface with the air. Ayappa et al. have shown that the above relationship only applies if the thickness of the tissues is larger than the critical length, which is about 5.4 d_p [6.16]. Otherwise, computer simulation models are required to predict more realistic power distributions.

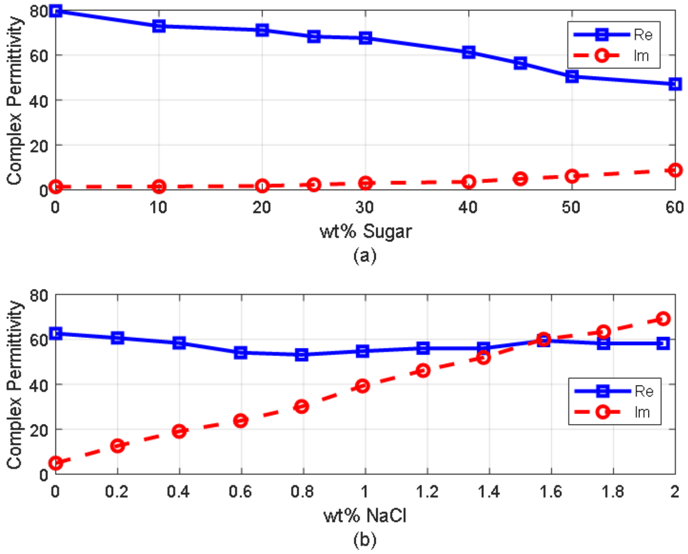

Figure 6.4: (a) Measured dielectric permittivity (real and imaginary part) as a function of sugar mass fraction at 406 MHz, and (b) measured dielectric permittivity (real and imaginary part) as a function of NaCl mass fraction and 45% sugar at 406 MHz.

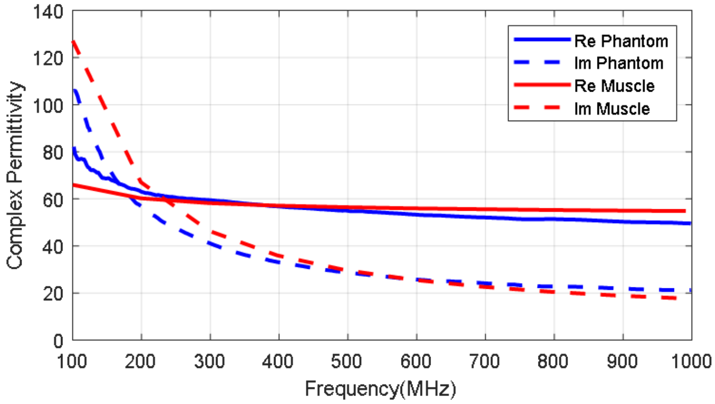

Figure 6.5: Measured dielectric permittivity (real and imaginary part) as a function of frequency compared to muscle tissue data ??.

6.2.3 Antenna for Deep Implanted Backscatter

Several implanted antennas have been proposed in the literature for ISM bands and MICS [6.17][6.18][6.19]. A ceramic (alumina) antenna with a superstrate was proposed in [6.17]. Chip antennas made with low temperature co-fired ceramics (LTCC) are available on the market and are extensively used in wireless modules (ISM band, Bluetooth, GPS, WLAN, etc.). The high permittivity of these materials enables the antennas to be smaller so that they can be integrated into small circuits. In the present study, a miniature commercial LTCC ceramic antenna (0900AT43A0070, Johanson Technology, Camarillo, CA, USA) designed for operation in the air at 900 MHz is used to operate as an implant in the 402–433 MHz band. The antenna is 7.7 mm long, 2 mm wide, and 0.8 mm high. Simulations and experiments were conducted to study the feasibility of commercial ceramic antennas for devices implanted in MICS and the 433 MHz band. The small size of the antenna (0.0715λ in the body) means that it is electrically small compared with the wavelength, so neither the pattern diagram nor the directivity will be greatly affected, and it has an omni-directional radiation pattern. Due to the high permittivity surrounding the antenna, the effective electrical length of the monopole decreases and changes the antenna impedance. This drawback can be overcome with a matching network that has discrete components (inductors and capacitors) as the manufacturer proposes for air but tuned to the impedance of the implanted antenna. However, the main drawback is that the antenna radiation efficiency is reduced by the lossy tissue material close to the antenna. This reduction in radiation efficiency, in turn, reduces the antenna gain, and consequently, the $\Delta\sigma$ and the backscattering power are also lessened.

Implanted medical devices must be covered by a biocompatible material to prevent contamination [6.20] and metallic oxidation, and the possibility of a short-circuit due to the high conductivity of the tissues [6.21]. The coating material acts as a superstrate and the thickness and the material have a considerable influence on the radiation efficiency [6.17]. Increasing the thickness of this coating material or the air gap between the cover and the antenna improves the radiation efficiency [6.21] but also increases the size of the implanted device. Therefore, there is a constraint between radiation efficiency and size. In the present study, we have used rubber silicone ($\varepsilon_r = 2.9$, $\tan\delta = 0.02$) [6.22]. Figure 6.6b shows the reflection coefficient of the antenna connected to a short transmission line (width 1.85 mm) printed on 32 mil Roger RO4003C substrate, within the body with a 1 mm thick coating of silicone. The size of the ground plane was 10 mm × 10 mm. An image is shown in Figure 6.6a. This figure shows that the antenna is completely mismatched in the 400–433 MHz band. Therefore, a matching network is required. Assuming a well-matched design, the realized antenna gain must be close to the antenna gain that does not take into account the antenna mismatch. Figure 6.7 shows the gain, directivity, and radiation efficiency at 406 MHz as a function of the thickness of the silicone coating. The simulations were performed with the full-wave Ansys HFSS simulator including the model provided by the antenna manufacturer. We used a box of muscle tissue ($\varepsilon_r = 57$, $\sigma = 0.8$ S/m) surrounding the antenna to simulate the effect of the body. The antenna directivity is not hardly affected by the thickness of the coating, but the radiation efficiency, and therefore the gain, increases with thickness. The efficiency fluctuates between 9.5% and 16%, which is considerably lower than in air (about 27%). Figure 6.8 shows the effect of the coating permittivity. This figure assumes the coating material to be 1 mm thick. The radiation efficiency increases slightly as the permittivity of the coating increases. However, it should be pointed out that coatings based on ceramic substrates with high permittivity are difficult to drill and cut.

In order to design the matching network with real materials and dimensions, a prototype with an SMA connector was manufactured (Figure 6.9a). The size

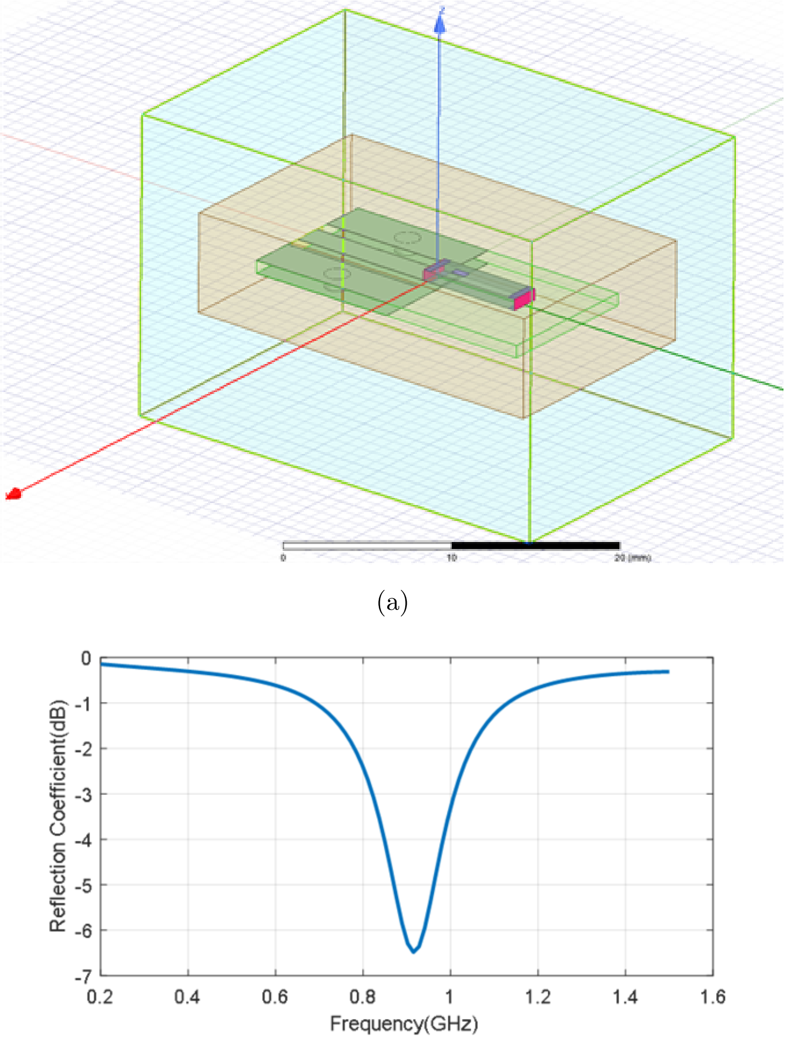

(a)

(b)

Figure 6.6: (a) Image of the simulated antenna with HFSS, (b) simulated antenna reflection coefficient as a function of the frequency for the antenna with a 1-mm thick silicone coating.

UNIVERSITAT ROVIRA I VIRGILI
LONG-RANGE BACKSCATTERING COMMUNICATIONS FOR NEXT GENERATION IOT APPLICATIONS
Marc Lázaro Martí

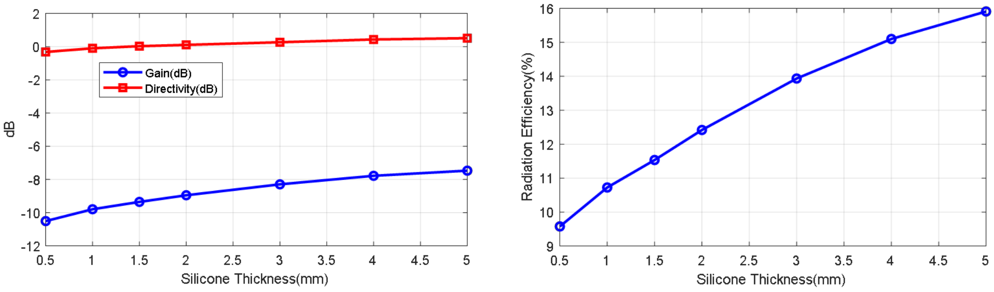

(a) (b)

Figure 6.7: (a) Simulated gain and directivity at $\theta = 0$, $\phi = 0$, and (b) radiation efficiency as a function of the silicone thickness at 406 MHz.

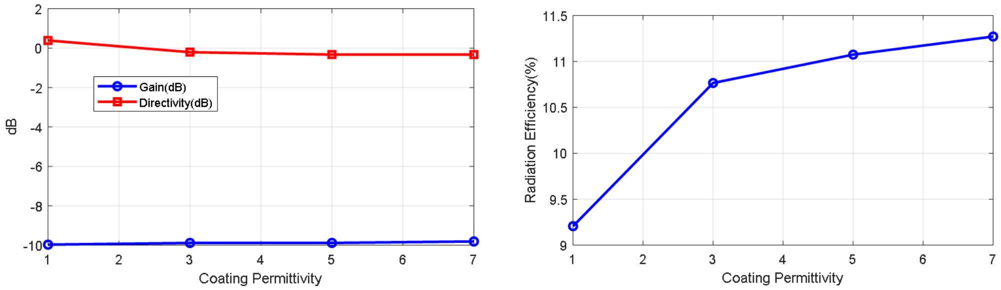

(a) (b)

Figure 6.8: (a) Simulated gain and directivity at $\theta = 0$, $\phi = 0$ and (b) radiation efficiency as a function of the coating permittivity (1-mm thick coating thickness) at 406 MHz.

of the board (7.5 mm × 21 mm) and ground plane (7.5 mm × 12 mm) together with the position of the discrete matching components is the same as in the implanted prototype (Figure 6.1). The impedance of the antenna was measured with a VNA connecting a thru line (zero Ohm SMD resistance), after which the reference plane was shifted to obtain the antenna impedance. Then, an LC matching network was designed using the Smith chart. Figure 6.9b shows the measured reflection coefficient of the antenna in the phantom material before and after the matching network. The frequency band can be tuned by modifying the components of the matching network. A 56 nH inductance in series and a 0.5 pF in parallel were used to match the antenna at 406 MHz and there was less than -10 dB between 387.28 MHz and 469.3 MHz (82.1 MHz bandwidth or 19.2%).

Table 6.1 compares the designed antenna with other printed implanted antennas proposed in the literature in the MICS band ([6.23][6.24][6.25][6.26]) using different miniaturization techniques. The miniature antenna proposed in the present study achieves a high gain and radiation efficiency, and a bandwidth that is moderate but enough to cover the MICS and 433 MHz bands. It is also available commercially, which simplifies the commercialization of future implanted devices.

Reference	Volumen (mm^3)	Antenna Type	Gain (dB)	Efficiency (%)	BW at -10 dB (mHz)
[6.23]	245	PIFA with superstrate	-7	39	115
[6.24]	32.7	Meander patches	-45	0.81	40
[6.25]	190	Spiral patch	-26	0.61	50
[6.26]	705	Alumina capsule $\lambda/2$ SIR	-22	0.4	16
This study	28 (236)[1]	Ceramic SMD	-9.5	10.8	82.1

Table 6.1: Comparison with other antennas in the Medical Implant Communication Service (MICS) band reported in the literature

---

[1] Including a coating of 1mm, a matching network, and a ground plane

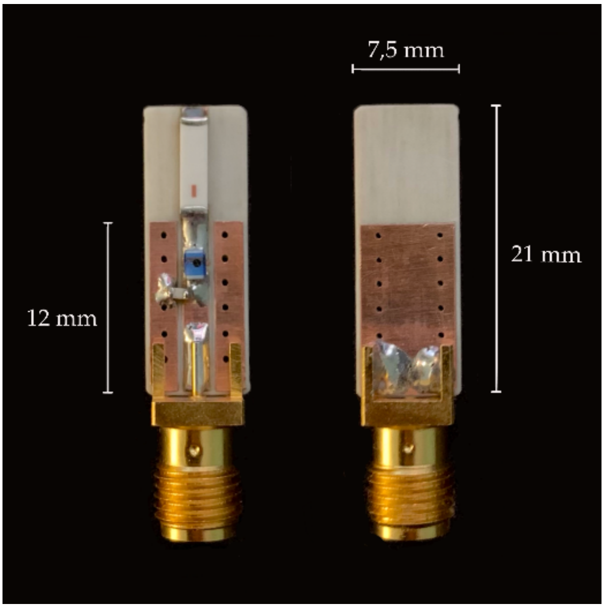

(a)

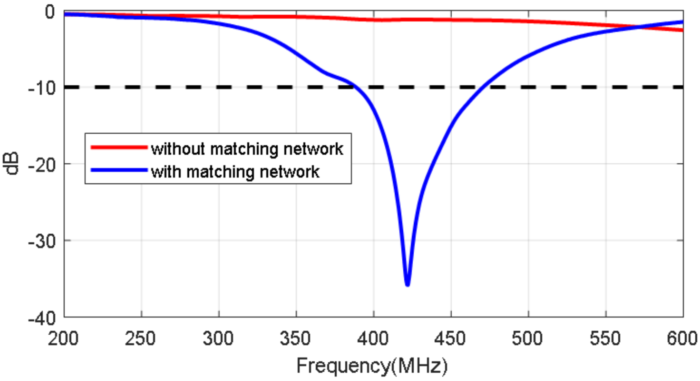

(b)

Figure 6.9: (a) Photography of the prototype manufactured for the antenna characterization, (b) measured reflection coefficient of the antenna in the phantom with and without the matching network.

6.2.4 Link Budget

In this section, we utilize the propagation model presented in section 5.2.3 of chapter 5 to calculate the link budget based on the system parameters. The objective is to determine the maximum depth and coverage area at which the implanted backscatter can be read.

The received power can be calculated using the Friis transmission equation, already presented in section 5.2.3, but now considering the attenuation of the body α(dB/m), and the implant depth d. Therefore, equation (5.1) can be rewritten as:

$$P_R = \frac{P_T G_T}{4\pi d_T^2} \cdot \Delta\sigma \cdot 10^{-0.1\alpha \cdot 2d} \cdot \frac{1}{4\pi d_R^2} \cdot (\frac{\lambda^2}{4\pi}) G_R \tag{6.2}$$

The parameters used in the simulations are listed in Table 6.2. The LoRa receiver sensitivity (S) can be determined using equation 5.4 from chapter 5. It depends on the noise figure of the receiver, the bandwidth (BW), and the signal-to-noise ratio (SNR), which is a function of the spreading factor, as shown in Table 6.3 [6.27][6.28].

LoRa SX1276 transceivers allow operating with one of the following predefined bandwidths: 7.8, 10.4, 15.6, 20.8, 31.5, 41.7, 62.5, 125, 250, 500 kHz. The calculation of the sensitivity in Table 6.3 assumes a typical BW of 125 kHz. Thus, sensitivity decreases if lower bandwidth is used in accordance with equation (5.4) (12 dB for the lower bandwidth compared to 125 kHz). Table 6.3 also shows the time on air and the equivalent bit rate computed from the equations given in [6.27][6.28] considering 10 bytes of payload with a preamble of 6 bytes and a coding rate of CR = 4/5.

However, due to multipath propagation and reflections on the ground and objects in indoor environments, the power decays with exponential factors that are not those given in the Friis model considered in (6.2). The received power or RSSI can be expressed using the empirical model (5.2) of section 5.2.3 without considering the losses introduced by the walls. This model is an extension to the backscatter channel of the empirical propagation model for indoor environments [6.23][6.29]:

---

[2] From measurements shown in Figure 6.3.

[3] Chips/Symbol = 2^{SF}

[4] with a preamble of 6 symbols and CR = 4/5

[5] S can be reduced 12 dB for BW = 7.8 kHz.

Parameter	Value	Unit
Transmission power P_T	20	dBm
Transmission antenna gain G_T	0	dB
Receiver antenna gain G_R	0	dB
Tag antenna gain G_a	-10	dB
Carrier frequency	406	MHz
Attenuation per unit length α	165	dB/m
Exponential decay factors (n_1, n_2)	2.5	
$\|\Delta\Gamma\|^2$	2.8^2	
Modulation factor (m)	$1/\pi^2$	
Noise figure of the receiver (NF)	6	dB
Bandwidth (BW)	125	kHz

Table 6.2: Parameters used to calculate the link budget.

$$P_R(d_{TX}, d_{RX})(dBm) = P_R(d_0, d_0)(dBm) - 10n_1 log(\frac{d_{TX}}{d_0}) - 10n_2 log(\frac{d_{RX}}{d_0}) + X \tag{6.3}$$

In this model, the received power is modeled as an average term and a random term X, where d_0 is a reference distance (e.g., the midpoint between transmitter and receiver $d_0 = (d_{TX-RX}/2)$) and $P_R(d_0, d_0)$ is the average received power at this reference distance. The exponential decay factors n_1 and n_2 are a function of the environment and the antenna height but for indoor environments, they have values of about 2.5–3 [6.30][6.31]. From the Friis equation, $P_R(d_0, d_0)$ is a function of transmitted power and the antenna gains. However, it is also a function of the antenna height and the diffraction. $P_R(d_0, d_0)$ can

Spreading factor SF	Chips/Symbol[3]	SNR (dB)	ToA of a 10-byte packet[4] (ms)	Bit rate (bps)	Sensitivity S (dBm) for BW = 125 kHz[5]
7	128	-7.5	56	5470	-124.5
8	256	-10	103	3125	-127.0
9	512	-12.5	205	1758	-129.5
10	1024	-15	371	977	-132.5
11	2048	-17.5	741	537	-134.5
12	4096	-20	1483	293	-137.0

Table 6.3: Parameters as a function of the Spreading Factor.

be found experimentally by regressing the measured data. Nevertheless, in this section, we perform simulations by considering the following expression derived from the Friis transmission equation (8):

$$\begin{aligned} P_R(d_0, d_0)(dBm) = {} & P_T(dBm) + G_T(dB) + G_R(dB) - 20log(4\pi) + 10log(\frac{\lambda^2}{4\pi}) \\ & + RCS_{dif}(dB) - \alpha(dB/m)2d - 10n_1log(d_0) - 10n_2log(d_0) \\ & + L_{obs}(dB) \end{aligned} \tag{6.4}$$

L_{obs} is a term in dB that accounts for the attenuation for diffraction that depends on the antenna height [6.29]. The losses for ground diffraction can be neglected if the antenna height is higher than $0.6R_1$, where R_1 is the radius of the first Fresnel zone [6.29]:

$$R_1 = \sqrt{\lambda \frac{d_{TX} d_{RX}}{d_{TX} + d_{RX}}} \tag{6.5}$$

UNIVERSITAT ROVIRA I VIRGILI
LONG-RANGE BACKSCATTERING COMMUNICATIONS FOR NEXT GENERATION IOT APPLICATIONS
Marc Lázaro Martí

For a distance between the transmitter and receiver (backscatter) of 2 m, and antennas of the same height, the minimum antenna height is 0.36 m at 406 MHz. Therefore, for a typical antenna height of around 1–2 m, we can expect that the effect of ground diffraction will be small.

The random variable X takes into account the attenuation due to multipath propagation. It can be regarded as a log-normally distributed random variable $X(dB) \sim N(0, \sigma)$, where σ in dB is the standard deviation and experimental results have given values between 2 and 4 dB for a single path [6.31] (in our case we expect it to be double this because of the backscatter channel). The coverage probability ($Prob$), that remember, is the probability that the average received power or RSSI, $P_R(dBm)$, will be higher than the receiver sensitivity S is computed using equation (5.3) of chapter 5.

Two cases were analyzed: monostatic and bistatic. In the monostatic case, the LoRa transmitter and receiver gateway are close together ($d_{TX} = d_{RX}$). Figure 6.10 compares the maximum depth or distance inside the body that the backscatter can communicate for SF = 7 and SF = 12 with BW = 125 kHz. Figure 6.11 shows the maximum depth as a function of the transmitter-to-body distance and receiver-to-body distance in the bistatic case for SF = 7 and SF = 12 with BW = 125 kHz, respectively. In these simulations, the exponential decay factors (n_1 and n_2) were considered to be equal to 2.5. Depths can be greater than 10 cm at 4 m. In the bistatic case, depths can be greater if the transmitter is closer to the body than the receiver.

These simulations have taken into account a fading margin due to multipath propagation of 10 dB. Results show the potential to read low-rate data from implants using frequency-shifted LoRa backscatter. The number of packets per unit of time increases if the spreading factor is low (e.g., SF = 7) as can be seen in Table 3 because the time on air is shorter than at high spreading factors. However, the sensitivity and robustness of the system were better when spreading factors were high. In the bistatic case, to achieve better coverage, it is assumed that the transmitter will be located near the patient (e.g., close to the bed) and the receiver somewhere else in the room.

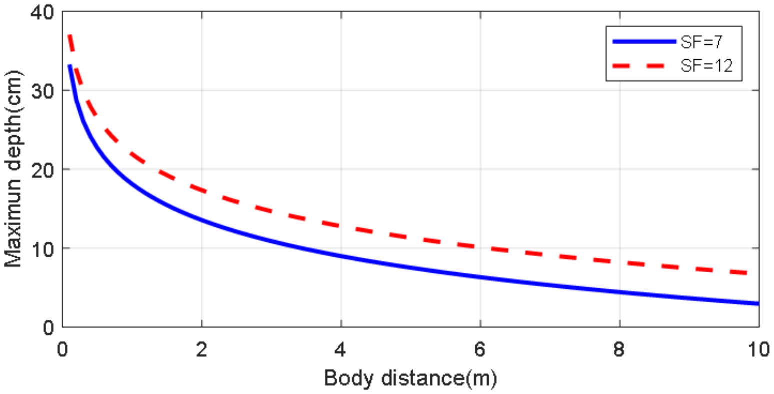

Figure 6.10: Simulated maximum depth for an implanted backscatter as a function of the distance to the body using the parameters of Table 6.1 for the monostatic case with a spreading factor SF = 7 and 12. Propagation model parameters: $n_1 = n_2 = 2.5$, Fade Margin = 10 dB.

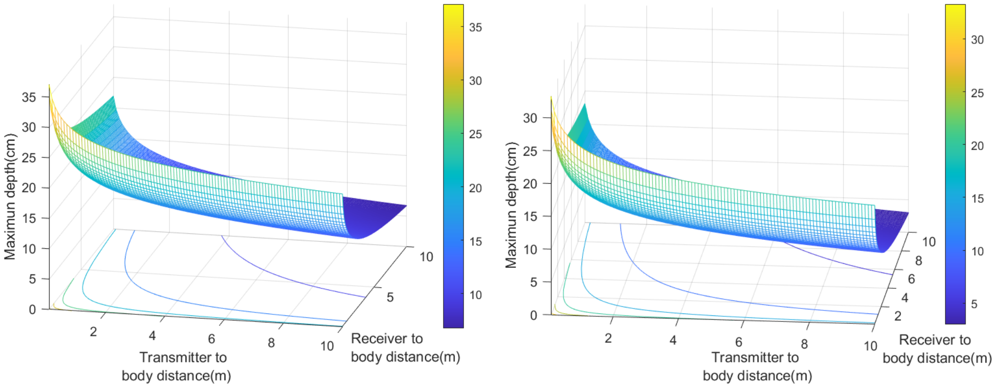

(a) (b)

Figure 6.11: Simulated maximum depth for an implanted backscatter as a function of the distance of the transmitter and receiver to the body using the parameters of Table 6.1 for the bistatic case with a spreading factor SF = 7 (a) and SF = 12 (b). Propagation model parameters: $n_1 = n_2 = 2.5$, Fade Margin = 10 dB.

A simplified scenario shown in Figure 6.12 consists of the transmitter and the receiver and the implanted backscatter on the same plane. All these elements are used to estimate the coverage from the propagation model proposed. In this scenario, it is assumed that the transceivers are fixed and the backscatter can move around different positions.

Figures 6.13 and 6.14 show the simulated coverage results for backscatter at a depth (d) of 5 cm and 10 cm, respectively. They depict the average received power computed with (10)–(11) considering the ideal free space exponential factors $n_1 = n_2 = 2$ and $n_1 = n_2 = 2.5$ as a function of the position of the backscatter. The monostatic and bistatic cases (with a distance between the transmitter and receiver $d_{TX-RX} = 1m$) are shown. For devices implanted on the surface or at small depths (<5 cm), the read range area can be about 4 m × 4 m, whereas for deep implanted devices (10 cm), a read range area of about 1.8 m × 1.8 m can be covered.

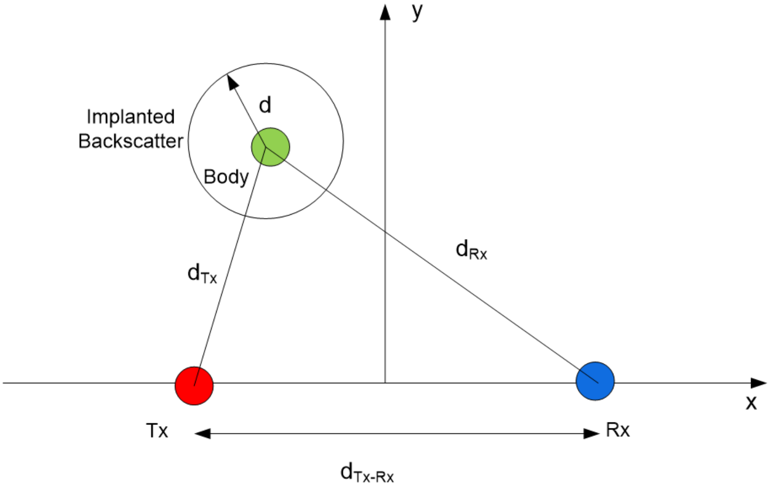

Figure 6.12: Scheme used in the RSSI simulations.

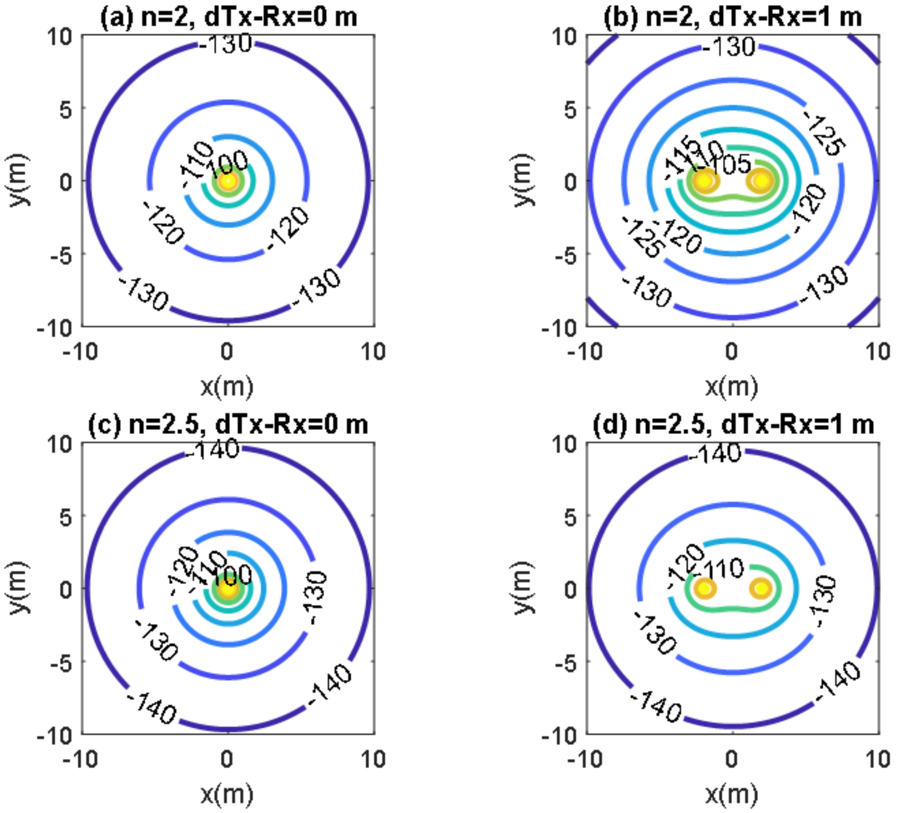

Figure 6.13: Simulated RSSI as a function of the location of the implanted backscatter assuming a depth of 5 cm inside the body for the monostatic case ($d_{Tx-Rx} = 0$ m) and bistatic case ($d_{Tx-Rx} = 1$ m). Path loss exponential factor $n_1 = n_2 = 2$ and $n_1 = n_2 = 2.5$.

UNIVERSITAT ROVIRA I VIRGILI
LONG-RANGE BACKSCATTERING COMMUNICATIONS FOR NEXT GENERATION IOT APPLICATIONS
Marc Lázaro Martí

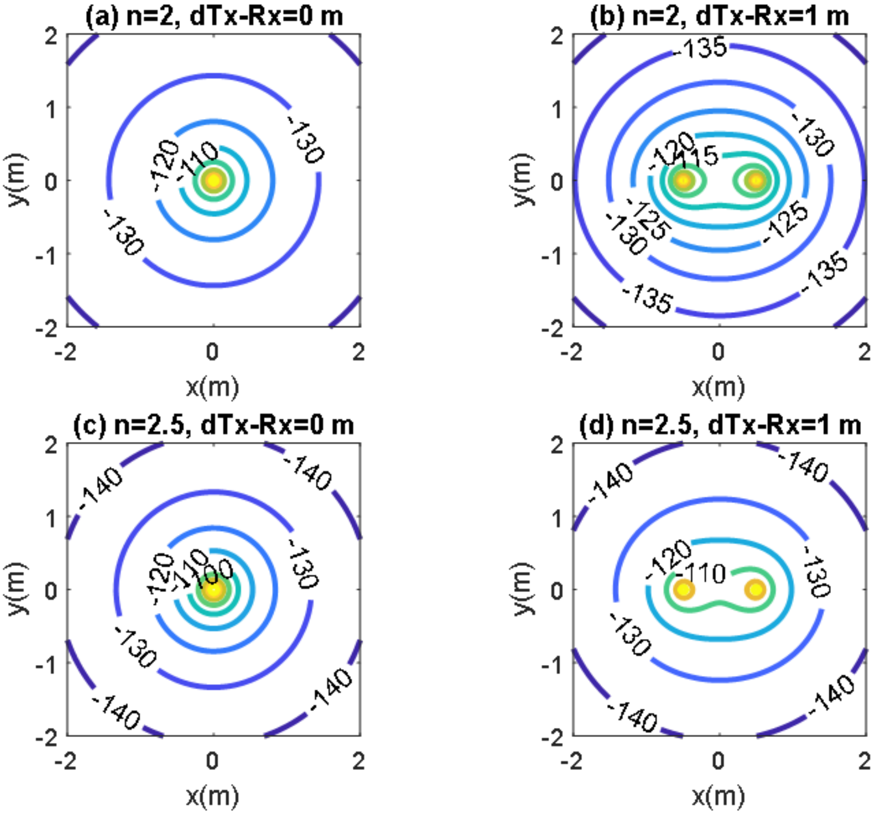

Figure 6.14: Simulated RSSI as a function of the location of the implanted backscatter assuming a depth of 10 cm inside the body for the monostatic case ($d_{Tx-Rx} = 0$ m) and bistatic case ($d_{Tx-Rx} = 1$ m). Path loss exponential factor $n_1 = n_2 = 2$ and $n_1 = n_2 = 2.5$.

6.3 Results

A backscatter prototype has been designed using the load-modulation front-end described in chapter 4. The prototype includes an antenna with a matching network, an RF switch (ADG902) [6.32] used as a modulator, and the low-power oscillator (LTC6907). The microcontroller generates the baseband signal with the test messages. The backscatter is covered with heat-shrink silicone (approximately 1 mm thick). This proof-of-concept prototype is externally biased with a battery pack connected by two wires that are also used to support the device. A photograph is shown in Figure 6.15. In order to check the correct modulation of the backscatter inside the body, it was inserted into a 20 cm diameter cylindrical vessel (see Figure 6.15). The vessel was filled with a mixture of saline solution with sugar described in the previous section. A signal generator was connected to a transmitting antenna and a spectrum analyzer was used as a receiver. Two whip monopoles tuned at 406 MHz were used in the generator and the spectrum analyzer. The distance from the Tx and Rx to the vessel was 1 m. The frequency was swept and the backscattered power was received. Figure 6.16 shows the spectrum in which the sidebands at the modulating backscatter frequency at 406 MHz can be seen. The central peak at this carrier frequency was due to the coupling between the transmitter and receiver. The sideband peaks are spaced from the carrier at the same frequency at which the ADG902 is switching (300 kHz in this experiment). Figure 6.17 shows the measurement of the received power at the sideband as a function of the generator frequency. The maximum received power was around 408 MHz. It is observed that the backscatter covers the desired frequency band, which shows that the antenna was correctly tuned within the phantom.

To test the reliability of the system, some experimental results were done using two LoRa32 boards as a transmitter and receiver. The central frequency of the transmitter was 406 MHz and the oscillation frequency was 300 kHz. The receiver was tuned to 406.3 MHz. The LoRa was configured to transmit and receive packets with SF = 12 and BW = 125 kHz for better sensitivity. Figure 6.18 shows an image of the setup used in the experiments.

Figure 6.19 shows the complementary distribution function (CDF) plot of the received signal strength indicator (RSSI) and the SNR in the shifted channel measured by the LoRa receiver. In order to obtain the data, the receiver was

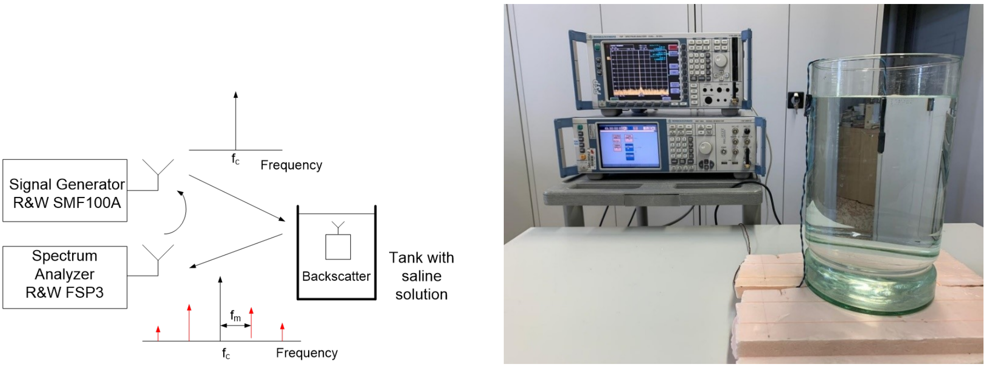

Figure 6.15: Block diagram of the setup used for the characterization of the backscatter and photograph (bottom).

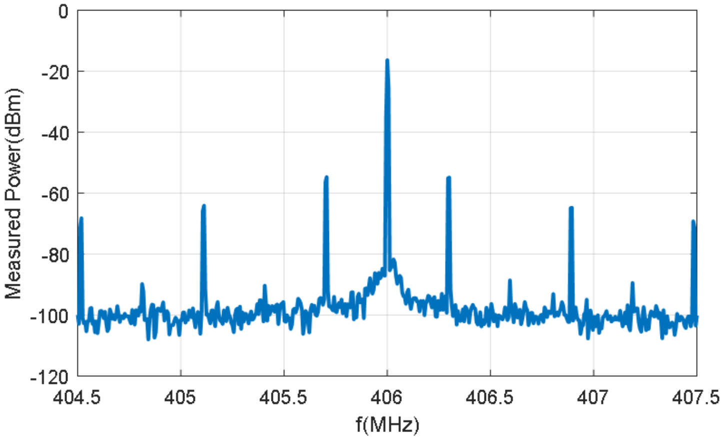

Figure 6.16: Spectrum of the receiver signal when the backscatter is illuminated at 406 MHz using the setup in Figure 17.

tuned to the backscattered channel and was located at random points (uniformly distributed) in the laboratory within a coverage area of 4 × 4m. The distance from the LoRa transmitter to the vessel was 80 cm at a height of 1 m from the ground. The backscatter was immersed in the center of the 20 cm diameter vessel with the phantom solution. We can observe that the RSSI is typically higher than -123 dBm (less than 10% of the locations receive levels below -123 dBm and SNR below -15 dB). Therefore, most locations were above the sensitivity of the receiver, and the packets were successfully backscattered.

In order to show the coverage area, Figure 6.20 shows the heat maps of

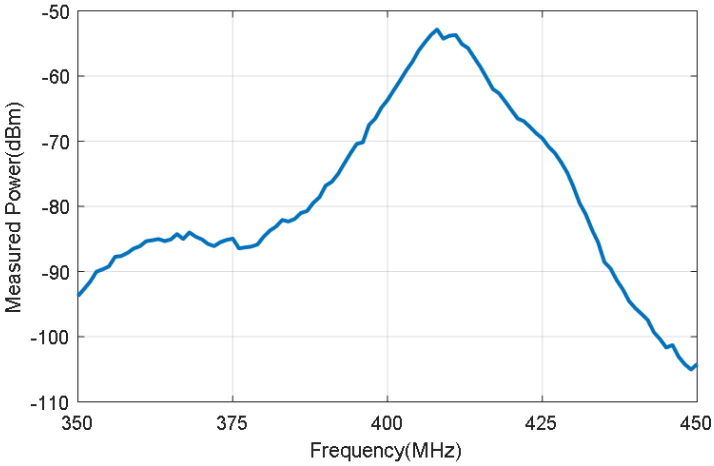

Figure 6.17: First harmonic ($f_c + f_p$) measured power as a function of the frequency with the backscatter immersed in the vessel described in Figure 6.15.

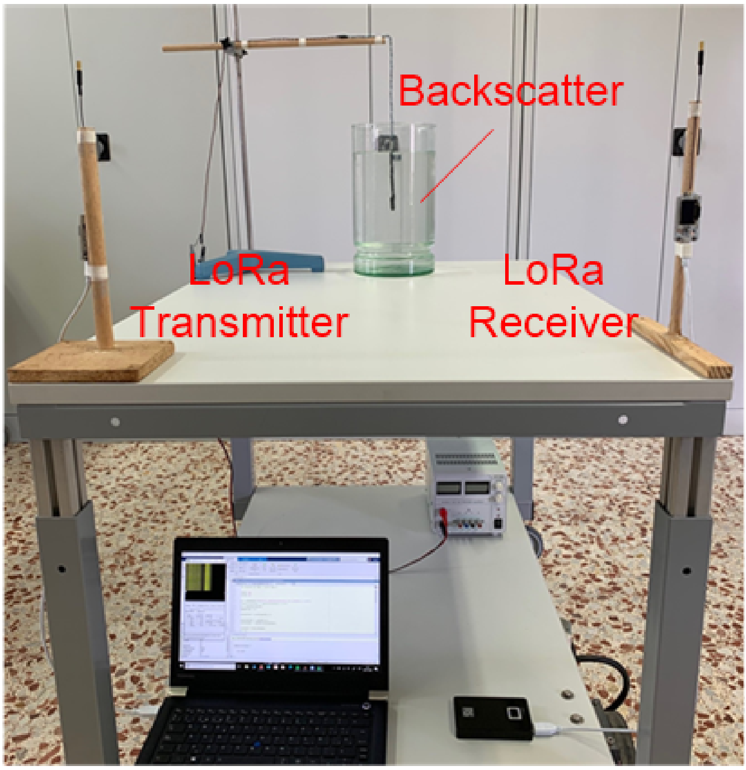

Figure 6.18: Photograph of the experimental setup in the laboratory.

UNIVERSITAT ROVIRA I VIRGILI
LONG-RANGE BACKSCATTERING COMMUNICATIONS FOR NEXT GENERATION IOT APPLICATIONS
Marc Lázaro Martí

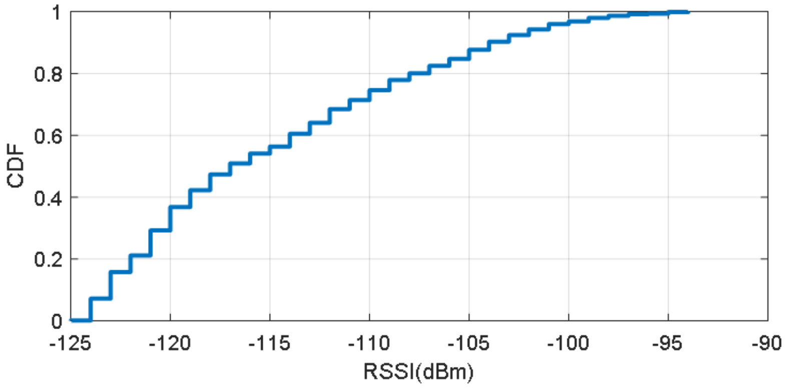

(a)

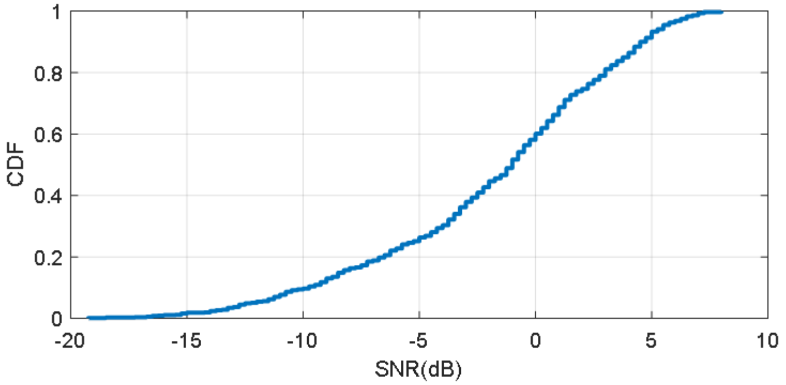

(b)

Figure 6.19: Complementary distribution function of the measured RSSI (a) and SNR (b) with the backscatter immersed in the vessel for a transmitter located 80 cm from the vessel.

the measured RSSI for the transmitter located 80 cm from the vessel with the immersed backscatter prototype centered and immersed at a depth of 10 cm The backscatter prototype and the transmitter are fixed whereas the receiver is moved along different locations in the room (laboratory). Under these circumstances, data can be received within the laboratory (area 5 m × 10 m) and through walls provided the receiver is located in neighboring rooms on the same floor. This result is in accordance with Figure 6.11b which shows that devices implanted at a 10 cm depth can be detected up to 10 m from the receiver when the transmitter is close (80 cm in this case).

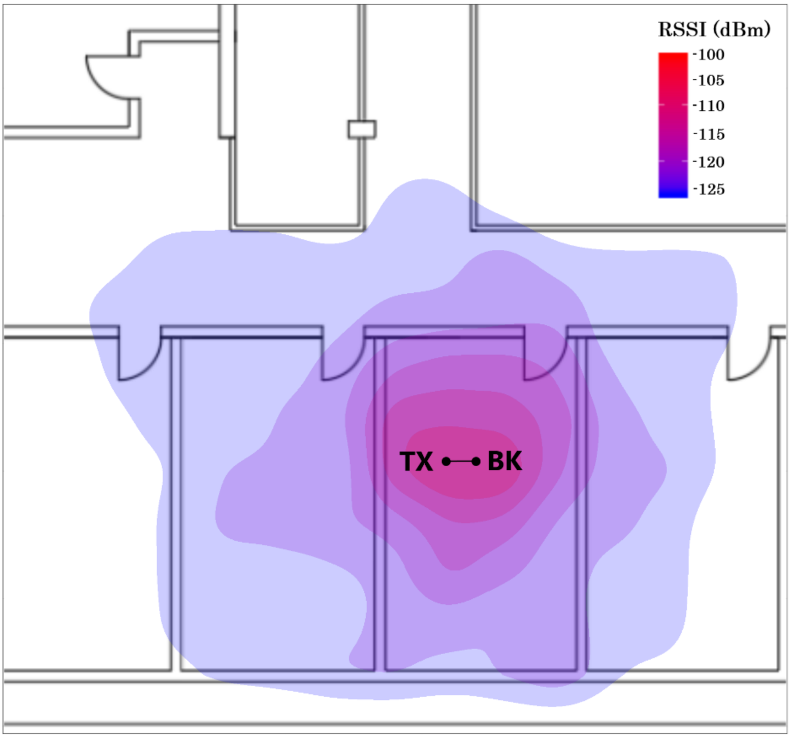

Figure 6.20: Measured RSSI heat map for the transmitter located 0.8 m from the vessel with the backscatter immersed (the points marked as BK and TX indicate the location of the backscatter and the transmitter, respectively).

To emulate the functionality of an implanted sensor, the measurement of the temperature with an external sensor is transmitted using the LoRa packet OOK modulation described in section 4.2.2 of chapter 4. Figure 6.21 shows the received data obtained with frame transmission over 60 min. The transmitter was located 80 cm away from the vessel surface with the backscatter immersed in the phantom liquid at the center of the vessel. The receiver was located at a distance of 1.5 m. In this test, the SF configuration exhibiting the best range was set up (SF = 12), keeping the bandwidth (BW) to 125 kHz to not increase drastically the time on air of the packet. To test the backscatter, the straightforward protocol described in Figure 4.31 of chapter 4 is used to send the temperature test value. The average number of frames lost was 4%. These results pave the way for long-range wireless implanted devices based on LoRa backscattering communication in indoor environments.

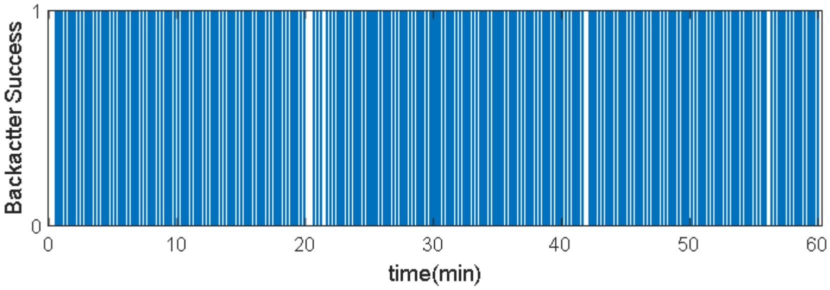

Figure 6.21: Backscattered frames successfully received as a function of the time with the backscatter immersed in the center of the vessel with a phantom liquid and the transmitter located 0.8 m from the vessel.

6.4 Discussion

The use of a frequency band (406–433 MHz) allows to increase the coverage because the propagation losses are lower than at 868/915 MHz or 2.45 GHz ISM band (free space attenuation decays with the square of the frequency) and besides, the walls [6.33] and indoor propagation [6.31] introduce lower attenuation at this frequency band. This helps to counter the fading effect caused by multipath propagation in indoor environments which, in backscattering systems, affects the up and downlinks [6.34][6.35][6.36]. The proposed system could easily use receiver diversity with multiple receivers to sniff shifted channels and prevent selective multipath fading. Channel hopping is not expected to provide significant improvements in the 406 MICS and 433 MHz ISM bands due to the small spacing between channels (less than the channel coherence bandwidth) so the channels are correlated [6.30][6.31]. However, to prevent interference or collision with another system, a listen-before-talk procedure (LBT) can easily be implemented in the LoRa transmitter so that the available channels can be listened to before the packets are sent. The parameters of the channel (frequency, SF, BW) can be transmitted to the receivers using a conventional LoRa link. This is different from the 2.4 GHz band, where channel hopping can be used to counter the effects of multipath propagation (e.g., in Bluetooth) [6.31].

In the following lines, there is a comparison of the technology presented here with other existing wireless technologies for implanted applications. Table 6.4 summarizes some examples of wireless technologies and compares such parameters as the carrier frequency, data rate, implant depth, or read range. These technologies can be classified according to whether are battery-less or not. Each technology has advantages and drawbacks depending on the requirements of the final application. Due to the higher losses of the body, Wireless Power Transfer (WPT) based on inductive links at low-frequency (LF) [6.37] and high-frequency (HF) [6.38][6.39] is the method preferred to power battery-less devices. Data are transferred by load modulation (Load Shift Keying-LSK) or by another wireless link at higher frequencies [6.40]. Depth and power depend on the size of the coils used [6.38], and the communication (read range) can be performed when the coils are close to the body. A drawback of this approach is that it requires specialized readers and ASICs. In [6.40], the authors propose a method based on three coils is proposed to improve the depth and reading range using smartphones equipped with NFC and tags embedding commercial NFC IC with energy-harvesting capabilities.

When the carrier frequency increases, the communication uses far-field and the attenuation increases very quickly with the frequency. Passive UHF RFID systems for identification and sensor communication at small implanted depths (5-15 mm subcutaneous) have been proposed [6.41][6.42]. The communication is by backscattering and a commercial UHF reader can be used. The WPT link is limited by the sensitivity of the UHF RFID IC [6.42] (about -20 dBm for modern ICs such as Impinj Monza R6 and -10 dBm for AMS-SL900A with sensing capabilities). The reader transmitter power is limited by exposure regulations (SAR) [6.42] so when body losses are higher the read range is limited to 0.6-1.6 m depending of the depth of the implant (5 to 15 mm) [6.41].

Battery-implanted devices are used when high performance and high data rate transfer are required. Commercial active implantable transceivers are available on the market. For example, the Microsemi ZL70103 transceiver [6.43] operates in the MICS band and the 433 MHz ISM band at a raw data rate of up to 400 kbps and with wake-up at 3.45 GHz. Its sensitivity is -102 dBm at 200 kbps (with a packet error rate of 10%) and the Tx/Rx average current is 5 mA. Several implanted wireless devices have been proposed for endoscopy [6.44][6.45][6.46][6.47][6.48]. For this application, to download video data, a high data rate is needed; therefore, active transceivers are used. However, the battery lifetime is limited to a few hours, which is enough for the exploration period required. Data rates from 1 Mbps [6.48] to 80 Mbps [6.47] have been achieved using different modulations such as BPSK [6.47], FSK [6.44], QPSK [6.45][6.46], or OFDM [6.48], at frequency bands ranging from 20 MHz to 925 MHz transmitting power between 1 mW and 6 mW. The price to pay is high power consumption and, therefore, the limited lifetime. It is not the best option for long-term monitoring even if the data rate required is small.

Ref.	Technology /Power	Carrier Frequency	Modulation	Implanted Depth	Link Range Outside the Body	Bitrate (bps)	Base Station Receiver Sensitivity (dBm)
[6.37]	Inductive /RF	700 kHz	CW (WPT)	20 mm	BS[6]	-	-
[6.39]	Inductive /RF	13.56 MHz	LSK, ASK	15 mm	BS[6]	2 M	NA
[6.49]	Inductive /RF	10 MHz	PPSK, OOK	8 mm	BS[6]	1.35 M	NA
[6.40]	NFC /RF	13.56 MHz	LSK, ASK	15–20 mm	3 cm	26.4 /848 k[7]	Depends on reader
[6.41][6.42]	UHF RFID /RF	868/915 MHz		5-15 mm	0.6-1 m	40 k	-60/-70
[6.43]	Active /Battery	406/433 MHz 2.45 GHz Wakeup	OOK	-	10-20 cm	400 k	-91
[6.44]-[6.48]	Endoscopy /Battery	20 to 925 MHz	BPSK, QPKS, FSK, OFDM	10–20 cm	BS[6]	-	-85
[6.50]	Backscattering /Battery	600 MHz	FSK	10 cm	BS[6]	1-5	-87
[6.2]	Backscattering /Battery	915 MHz	ASK	6 cm	BS[6]	30	-90
This work	LoRa Backscattering /Battery	406–433 MHz	LoRa	10-20 cm	<4 m	Few bps	-137

Table 6.4: Comparison with other communication technologies for implantable medical devices.

Zero power backscatter gives better power consumption because it does not transmit RF power, which extends the life of the battery although the link attenuation is double that of active transceivers due to the forward and backscattered channel. The proposed backscatter can be used with other modulations such as ASK (OOK) or FSK and the bit rate achieved (a few MHz) is high enough to transfer implanted video camera data. In this case, a CW tone illuminates the backscatter from the transmitter and the backscatter responds by modulating the carrier. A backscatter similar to that described in this study was used in [6.2] to achieve 30 Mbps working at 915 MHz at a depth of 6 cm using a loop antenna. In another study [6.50], a backscatter device implementing an FSK modulation achieved 1-5 Mbps at 600 MHz and a depth of up to 10 cm. In both cases, the reader antennas were located close to the phantom and the reader system was implemented using software-defined radio (SDR). The LoRa backscatter technique proposed in this study can achieve greater depths and read ranges outside the body because of the higher sensitivity of the LoRa modulation, but the main limitation is the low data rate. Another important point is that the proposed system does not require specialized readers because commercial low-cost LoRa transceivers can be used.

6.5 Conclusions

This chapter has shown the feasibility of communication based on receiving backscatter LoRa packets at a shifted channel for implanted devices. A proof-of-concept prototype has been developed. The prototype consists of an RF switch that presents two high reflective coefficients to an antenna controlled by a low-frequency modulating oscillator. A commercial ceramic antenna is tuned using a matching network at the MICS and ISM 433 MHz bands, which provides high miniaturization and high radiation efficiency. The backscatter can be interfaced with a low-power microprocessor to send low-rate data from sensors for monitoring purposes. Although the backscatter can be used with other modulations such as ASK and FSK, the proposed method uses the reflection of LoRa packets to exploit the high sensitivity and robustness of LoRa modulation; therefore, there is no need to integrate high power-consuming FPGAs or other

---

[6] Receiver antenna on body surface.

[7] The data rate depends on standard ISO15693 (26.4 kbps) ISO1443 (up to 848 kbps).

ICs. A complete link budget has been presented which shows the potentiality of the communication technique. The method proposed achieves great implant depths that can be read at distances of up to several meters from the body, so that only one transmitter base station is enough to cover a typical room. Conventional LoRa transceivers are compatible with the proposed backscatter system, which can be used for long-range monitoring in indoor environments for future implanted and wearable devices.

6.6 Bibliography

[6.1] Stewart J Thomas, Jordan S Besnoff, and Matthew S Reynolds. Modulated backscatter for ultra-low power uplinks from wearable and implantable devices. In *Proceedings of the 2012 ACM workshop on Medical communication systems*, pages 1–6, 2012.

[6.2] Jordan S Besnoff and Matthew S Reynolds. Near field modulated backscatter for in vivo biotelemetry. In *2012 IEEE International Conference on RFID (RFID)*, pages 135–140. IEEE, 2012.

[6.3] Deepak Vasisht, Guo Zhang, Omid Abari, Hsiao-Ming Lu, Jacob Flanz, and Dina Katabi. In-body backscatter communication and localization. In *Proceedings of the 2018 Conference of the ACM Special Interest Group on Data Communication*, pages 132–146, 2018.

[6.4] Ali Khaleghi and Ilangko Balasingham. Wireless Capsule Endoscopy Using Backscatter Communication. In *2019 13th European Conference on Antennas and Propagation (EuCAP)*, pages 1–5. IEEE, 2019.

[6.5] Vikram Iyer, Vamsi Talla, Bryce Kellogg, Shyamnath Gollakota, and Joshua Smith. Inter-technology backscatter: Towards internet connectivity for implanted devices. In *Proceedings of the 2016 ACM SIGCOMM Conference*, pages 356–369, 2016.

[6.6] Yao Peng, Longfei Shangguan, Yue Hu, Yujie Qian, Xianshang Lin, Xiaojiang Chen, Dingyi Fang, and Kyle Jamieson. PLoRa: A passive long-range data network from ambient LoRa transmissions. In *Proceedings of the 2018 Conference of the ACM Special Interest Group on Data Communication*, pages 147–160, 2018.

[6.7] Vamsi Talla, Mehrdad Hessar, Bryce Kellogg, Ali Najafi, Joshua R Smith, and Shyamnath Gollakota. Lora backscatter: Enabling the vision of ubiquitous connectivity. *Proceedings of the ACM on interactive, mobile, wearable and ubiquitous technologies*, 1(3):1–24, 2017.

[6.8] Mohd Noor Islam and Mehmet R Yuce. Review of medical implant communication system (MICS) band and network. *Ict Express*, 2(4):188–194, 2016.

[6.9] Analog Devices(Linear Technologies). *Micropower, 40kHz to 4MHz Resistor Set Oscillator in SOT-23*, 6 2005. Rev. A.

[6.10] Sami Gabriel, RW Lau, and Camelia Gabriel. The dielectric properties of biological tissues: II. Measurements in the frequency range 10 Hz to 20 GHz. *Physics in medicine & biology*, 41(11):2251, 1996.

[6.11] Sergio Castelló-Palacios, Concepcion Garcia-Pardo, María Alloza-Pascual, Alejandro Fornes-Leal, Narcís Cardona, and Ana Vallés-Lluch. Gel phantoms for body microwave propagation in the (2 to 26.5) GHz frequency band. *IEEE Transactions on Antennas and Propagation*, 67(10):6564–6573, 2019.

[6.12] Chung-Kwang Chou, Gang-Wu Chen, Arthur W Guy, and Kenneth H Luk. Formulas for preparing phantom muscle tissue at various radiofrequencies. *Bioelectromagnetics: Journal of the Bioelectromagnetics Society, The Society for Physical Regulation in Biology and Medicine, The European Bioelectromagnetics Association*, 5(4):435–441, 1984.

[6.13] Sergio Castelló-Palacios, Ana Vallés-Lluch, Concepcion Garcia-Pardo, Alejandro Fornes-Leal, and Narcís Cardona. Formulas for easy-to-prepare tailored phantoms at 2.4 GHz ISM band. In *2017 11th International Symposium on Medical Information and Communication Technology (ISMICT)*, pages 27–31. IEEE, 2017.

[6.14] David M Peterson, Walker Turner, Kevin Pham, Hong Yu, Rizwan Bashirullah, Neil Euliano, and Jeffery R Fitzsimmons. A Tissue Equivalent Phantom of the Human Torso for in vivo Biocompatible Communications. In *26th Southern Biomedical Engineering Conference SBEC 2010, April 30-May 2, 2010, College Park, Maryland, USA*, pages 414–417. Springer, 2010.

[6.15] Everette C Burdette, Fred L Cain, and Joseph Seals. In vivo probe measurement technique for determining dielectric properties at VHF through microwave frequencies. *IEEE transactions on microwave theory and techniques*, 28(4):414–427, 1980.

[6.16] KG Ayappa, HT Davis, G Crapiste, EA Davis, and J Gordon. Microwave heating: an evaluation of power formulations. *Chemical engineering science*, 46(4):1005–1016, 1991.

[6.17] Pichitpong Soontornpipit, Cynthia M Furse, and You Chung Chung. Design of implantable microstrip antenna for communication with medical implants. *IEEE Transactions on Microwave theory and techniques*, 52(8):1944–1951, 2004.

[6.18] Olive H Murphy, Christopher N McLeod, Manoraj Navaratnarajah, Magdi Yacoub, and Christofer Toumazou. A pseudo-normal-mode helical antenna for use with deeply implanted wireless sensors. *IEEE Transactions on Antennas and propagation*, 60(2):1135–1139, 2011.

[6.19] Asimina Kiourti and Konstantina S Nikita. A review of implantable patch antennas for biomedical telemetry: Challenges and solutions [wireless corner]. *IEEE Antennas and Propagation Magazine*, 54(3):210–228, 2012.

[6.20] PEK Donaldson and E Sayer. A technology for implantable hermetic packages. Part 2: An implementation. *Medical and Biological Engineering and Computing*, 19:403–405, 1981.

[6.21] Francesco Merli, Benjamin Fuchs, Juan R Mosig, and Anja K Skrivervik. The effect of insulating layers on the performance of implanted antennas. *IEEE Transactions on Antennas and propagation*, 59(1):21–31, 2010.

[6.22] Adrian JT Teo, Abhinay Mishra, Inkyu Park, Young-Jin Kim, Woo-Tae Park, and Yong-Jin Yoon. Polymeric biomaterials for medical implants and devices. *ACS Biomaterials Science & Engineering*, 2(4):454–472, 2016.

[6.23] Fu-Jhuan Huang, Chien-Ming Lee, Chia-Lin Chang, Liang-Kai Chen, Tzong-Chee Yo, and Ching-Hsing Luo. Rectenna application of miniaturized implantable antenna design for triple-band biotelemetry communication. *IEEE Transactions on Antennas and Propagation*, 59(7):2646–2653, 2011.

[6.24] Asimina Kiourti, Maria Christopoulou, and Konstantina S Nikita. Performance of a novel miniature antenna implanted in the human head for wireless biotelemetry. In *2011 IEEE International Symposium on Antennas and Propagation (APSURSI)*, pages 392–395. IEEE, 2011.

[6.25] Wen-Chung Liu, Feng-Ming Yeh, and Mohammad Ghavami. Miniaturized implantable broadband antenna for biotelemetry communication. *Microwave and Optical Technology Letters*, 50(9):2407–2409, 2008.

[6.26] Denys Nikolayev, Maxim Zhadobov, Laurent Le Coq, Pavel Karban, and Ronan Sauleau. Robust ultraminiature capsule antenna for ingestible and implantable applications. *IEEE Transactions on Antennas and Propagation*, 65(11):6107–6119, 2017.

[6.27] Semtech. SX1276/77/78/79—137 MHz to 1020 MHz Low Power Long Range Transceiver. 2020.

[6.28] Semtech Corporation. *SX1272/3/6/7/8: LoRa Modem Design Guide*, 7 2013. Rev. 1.

[6.29] Andrea Goldsmith. *Wireless communications.* Cambridge university press, 2005.

[6.30] Antonio Lazaro, David Girbau, and David Salinas. Radio link budgets for UHF RFID on multipath environments. *IEEE transactions on antennas and propagation*, 57(4):1241–1251, 2009.

[6.31] Pere Tuset-Peiró, Albert Anglès-Vazquez, José López-Vicario, and Xavier Vilajosana-Guillén. On the suitability of the 433 MHz band for M2M low-power wireless communications: propagation aspects. *Transactions on Emerging Telecommunications Technologies*, 25(12):1154–1168, 2014.

[6.32] Microchip (Atmel). *ATtiny25/45/85/V: Atmel 8-bit AVR Microcontroller with 2/4/8K Bytes In-System Programmable Flash*, 8 2013. Rev. D.

[6.33] Panu Ali-Rantala, Leena Ukkonen, Lauri Sydanheimo, Mikko Keskilammi, and Markku Kivikoski. Different kinds of walls and their effect on the attenuation of radiowaves indoors. In *IEEE Antennas and Propagation Society International*

Symposium. Digest. Held in conjunction with: USNC/CNC/URSI North American Radio Sci. Meeting (Cat. No. 03CH37450), volume 3, pages 1020–1023. IEEE, 2003.

[6.34] Javier Lorenzo, Antonio Lazaro, David Girbau, Ramon Villarino, and Ernest Gil. Analysis of on-body transponders based on frequency selective surfaces. *Progress in Electromagnetics Research*, 157:133–143, 2016.

[6.35] J Lorenzo, A Lazaro, R Villarino, and D Girbau. Diversity study of a frequency selective surface transponder for wearable applications. *IEEE Transactions on Antennas and Propagation*, 65(5):2701–2706, 2017.

[6.36] S Milici, A Lazaro, J Lorenzo, R Villarino, and D Girbau. Wearable sensors based on modulated frequency selective surfaces. In *2017 47th European Microwave Conference (EuMC)*, pages 942–945. IEEE, 2017.

[6.37] Anil Kumar RamRakhyani, Shahriar Mirabbasi, and Mu Chiao. Design and optimization of resonance-based efficient wireless power delivery systems for biomedical implants. *IEEE transactions on biomedical circuits and systems*, 5(1):48–63, 2010.

[6.38] Dai Jiang, Dominik Cirmirakis, Matthew Schormans, Timothy A Perkins, Nick Donaldson, and Andreas Demosthenous. An integrated passive phase-shift keying modulator for biomedical implants with power telemetry over a single inductive link. *IEEE transactions on biomedical circuits and systems*, 11(1):64–77, 2016.

[6.39] Yu-Po Lin, Chun-Yi Yeh, Pin-Yang Huang, Zong-Ye Wang, Hsiang-Hui Cheng, Yi-Ting Li, Chi-Fen Chuang, Po-Chiun Huang, Kea-Tiong Tang, Hsi-Pin Ma, et al. A battery-less, implantable neuro-electronic interface for studying the mechanisms of deep brain stimulation in rat models. *IEEE transactions on biomedical circuits and systems*, 10(1):98–112, 2015.

[6.40] Antonio Lazaro, Marti Boada, Ramon Villarino, and David Girbau. Study on the reading of energy-harvested implanted NFC tags using mobile phones. *IEEE Access*, 8:2200–2221, 2019.

[6.41] Shubin Ma, Lauri Sydänheimo, Leena Ukkonen, and Toni Björninen. Split-ring resonator antenna system with cortical implant and head-worn parts for effective far-field implant communications. *IEEE Antennas and Wireless Propagation Letters*, 17(4):710–713, 2018.

[6.42] Carolina Miozzi, Giovanni Saggio, Emanuele Gruppioni, and Gaetano Marrocco. Constrained safety-integrity performance of through-the-arms UHF-RFID transcutaneous wireless communication for the control of prostheses. *IEEE Journal of Radio Frequency Identification*, 3(4):236–244, 2019.

[6.43] Microsemi. *ZL70103 Medical Implantable RF Transceiver. MICS-Band RF Telemetry*, 9 2015. Rev. 2.

[6.44] Joonsung Bae, Kiseok Song, Hyungwoo Lee, Hyunwoo Cho, and Hoi-Jun Yoo. A 0.24-nJ/b wireless body-area-network transceiver with scalable double-FSK modulation. *IEEE Journal of Solid-State Circuits*, 47(1):310–322, 2011.

[6.45] Yuan Gao, San-Jeow Cheng, Wei-Da Toh, Yuen-Sam Kwok, Kay-Chuan Benny Tan, Xi Chen, Wai-Meng Mok, Htun-Htun Win, Bin Zhao, Shengxi Diao, et al. An asymmetrical QPSK/OOK transceiver SoC and 15: 1 JPEG encoder IC for multifunction wireless capsule endoscopy. *IEEE journal of solid-state circuits*, 48(11):2717–2733, 2013.

[6.46] Yao-Hong Liu, Li-Guang Chen, Chun-Yu Lin, and Tsung-Hsien Lin. A 650-pJ/bit MedRadio transmitter with an FIR-embedded phase modulator for medical micro-power networks (MMNs). *IEEE Transactions on Circuits and Systems I: Regular Papers*, 60(12):3279–3288, 2013.

[6.47] Hyunwoo Cho, Hyunki Kim, Minseo Kim, Jaeeun Jang, Yongsu Lee, Kyuho Jason Lee, Joonsung Bae, and Hoi-Jun Yoo. A 79 pJ/b 80 Mb/s Full-Duplex Transceiver and a $42.5\mu W$ 100 kb/s Super-Regenerative Transceiver for Body Channel Communication. *IEEE journal of solid-state circuits*, 51(1):310–317, 2015.

[6.48] Wala Saadeh, Muhammad Awais Bin Altaf, Haneen Alsuradi, and Jerald Yoo. A pseudo OFDM with miniaturized FSK demodulation body-coupled communication transceiver for binaural hearing aids in 65 nm CMOS. *IEEE Journal of Solid-State Circuits*, 52(3):757–768, 2017.

[6.49] Christian T Wentz, Jacob G Bernstein, Patrick Monahan, Alexander Guerra, Alex Rodriguez, and Edward S Boyden. A wirelessly powered and controlled device for optical neural control of freely-behaving animals. *Journal of neural engineering*, 8(4):046021, 2011.

[6.50] Ali Khaleghi, Aminolah Hasanvand, and Ilangko Balasingham. Radio frequency backscatter communication for high data rate deep implants. *IEEE Transactions on Microwave Theory and Techniques*, 67(3):1093–1106, 2018.

UNIVERSITAT ROVIRA I VIRGILI
LONG-RANGE BACKSCATTERING COMMUNICATIONS FOR NEXT GENERATION IOT APPLICATIONS
Marc Lázaro Martí

Chapter 7

Backscattering for IoT

7.1 Introduction

People's welfare became the major objective in those times of pandemics. With the arrival of the COVID-19 virus, measures to contain the spread of the disease among the population were taken. Confinement, use of face masks and gloves, temperature controls at the entrance of public places, and social distancing were some of these measures, which stayed in place for a while.

Authorities ordered the population to use wearable devices that complied with the quarantine measures, while telecommunication data was used to monitor crowds. Corporations worked on applications capable of alerting situations in which a person may have come into contact with newly diagnosed COVID-19 patients [7.1]. For this reason, smart mobile applications were proposed for monitoring purposes, such as monitoring employees in industrial environments [7.2].

However, the pandemic has revealed the limitations of current technological deployments, particularly in what concerns the spread of the disease. IoT and smart connected technologies, in combination with data-driven applications, can play a critical role not only in the prevention, mitigation, and continuous remote monitoring of patients, but also in the prompt enforcement of guidelines, rules, and administrative orders to prevent future outbreaks[7.1, 7.3]. The pandemic has accelerated the introduction of IoT in several fields such as E-health, smart hospitals, remote patient monitoring, or supply chain management [7.1, 7.3].

The pandemic became a race against time, where the effectiveness of the aforementioned measures was continually verified. In order to prevent widespread contagion in public places, a protocol for measuring body temperature was established, isolating individuals exhibiting symptoms of COVID, such as fever.

There are several methods for measuring body temperature (e.g. oral, rectal, axillary, or tympanic). Some of these are compared in the literature [7.4]. Despite the number of options, most of them are not feasible outside of a medical environment and even less on a mass scale. Therefore, there is no question why the infrared thermometer was the method of choice for monitoring people's body temperature. An infrared thermometer allows a quick and non-contact measurement, but the massive use of this kind of thermometer made visible some latent drawbacks [7.5]. These include the effect of the distance, the measurement site, or the influence of the environment on the temperature readings. To ensure a correct determination of the temperature, the operators designated for the controls must follow a strict protocol, and anyone who undergoes the measurement requires an acclimatization time when coming from outside. In practice, the system is imprecise and inefficient, despite being the most suitable for mass population control.

Face masks allow the insertion of breathing sensors [7.6] that allow the person to carry out their usual activity despite the discomfort of their use. The mandatory use of face masks to prevent the spread of coronavirus through the air has led to the adoption of smart masks equipped with sensors. The widespread use of the masks allows us to think of other applications and uses different from those expected in medical or hospital environments [7.7] for remote monitoring or in industrial environments [7.8]. Accordingly, a new generation of wearable devices, that receives the name of smart masks, has attracted the interest of different research groups [7.9, 7.10, 7.11, 7.7, 7.12, 7.13, 7.14, 7.15, 7.8]. In [7.7], a personalized smart mask obtained from a 3D scanned face image, whose objective is to minimize skin irritation is proposed. In addition, temperature and strain sensors have been integrated to detect irregular breathing, which is one of the symptoms of respiratory diseases. The strain sensor is used to monitor possible face irritation caused by the tight sealing of the masks. However, the temperature sensor is based on a thermistor connected to a microcontroller that exclusively monitors the air temperature. In [7.9][7.12], a smart mask senses particles of different sizes suspended in the air and close to it, by using an onboard particulate matter (PM) sensor. Another example of a smart mask is proposed

UNIVERSITAT ROVIRA I VIRGILI
LONG-RANGE BACKSCATTERING COMMUNICATIONS FOR NEXT GENERATION IOT APPLICATIONS
Marc Lázaro Martí

in [7.10], where a self-powered device based on a textile triboelectric nanogenerator (TENG) is proposed to electrocute virus-loaded aerosols. Recently, in [7.13] a smart mask with wireless connection using Bluetooth low-energy (BLE) is proposed. It integrates a PhotoPlethysmoGraphy (PPG) pulse-oximeter and a pair of differential barometers, one internal and one external, that acts as a spirometer and are able to measure respiratory pressure during the breathing cycle.

As in the related works described above, this work takes advantage of the acceptance of the face mask and its widespread use in pandemics to add a new functionality: it introduces a novel approach to determine the temperature and breathing rate of the person that uses the smart mask. In addition, the solution is capable of granting or denying access to public areas such as academic, leisure, administration, and healthcare centers based on the wireless reading of the sensors placed in the mask, eliminating the error introduced by the operator, and improving the screening efficiency. In order to automate the system, the smart mask incorporates a low-power communication system based also on LoRa backscatter technique.

One of the most important characteristics of the mask temperature sensor designed, is that it does not depend on the person and ambient variations. Since covid-19 compatible symptoms can also manifest in breathing activity, the mask also includes breath rate monitoring using an integrated air-flow sensor. Finally, effective location mechanisms are included for motion direction detection, allowing automatic occupancy detection in public spaces. This smart mask could also be used for monitoring patients while they wait in hospitals or medical facilities.

System design is challenging for at least two reasons. First, determining body temperature through skin temperature is controversial. The face is highly exposed to drafts and sudden changes in ambient temperature, which directly influences the measurements. Second, the backscatter technique makes synchronization between devices difficult due to the one-way communication, consequently, packet collision is a major problem to manage.

Sustainability must be an essential point to consider in any scientific advance. With an estimated monthly use of 129 billion face masks [7.16] during the hard periods of Covid-19 pandemic, the design of a disposable electronic system integrated into the mask does not appear to be an environmentally friendly solution. The option of integrating the system into a reusable device has been

UNIVERSITAT ROVIRA I VIRGILI
LONG-RANGE BACKSCATTERING COMMUNICATIONS FOR NEXT GENERATION IOT APPLICATIONS
Marc Lázaro Martí

taken into account. Although the electronics do not present disadvantages to be integrated into a dockable prototype, any modification of the mask could affect or invalidate the strict approvals that support it. For this reason, major changes in mask morphology have been avoided. Since this chapter aims to develop a proof of concept, the discussion of the effect of the system in reference to mask approvals is outside its scope.

In an effort to solve the aforementioned problems, the main contributions of the work carried out in this chapter are summarized below:

1. A dual heat flux sensor has been integrated into a commercial FFP2 mask to determine body temperature by using cheek surface temperature

2. A thermistor has been integrated into the mask to measure the temperature of the air flow, thus being able to monitor both the respiratory rate and the episodes of coughing.

3. Transmission is based on backscatter communication of the signal sent by a LoRa transmitter located next to an access door. The position of the sensor can be determined by comparing the power of the backscattered signal received by two LoRa receivers located on both sides of the access door

4. The system uses an inexpensive standard LoRa transceiver without any modifications, so no specialized receivers (e.g. software defined radio) are required.

The chapter is organized as follows: section 7.2 begins with a brief overview of the design and operation of the system and subsequently introduce the duel heat flux sensor employed to measure the body temperature, the system for the breathing monitoring and the wireless communication based on LoRa backscattering. Experimental results are presented in section 7.3. This section starts with the procedure to calibrate the dual heat flow sensor and continues with the results obtained from the measurements of temperature and breathing rate, as well as the detection of cough and positioning. Different non-contact temperature sensor technologies are discussed in section 7.4. Finally, the conclusions from this work are summarized in section 7.5.

UNIVERSITAT ROVIRA I VIRGILI
LONG-RANGE BACKSCATTERING COMMUNICATIONS FOR NEXT GENERATION IOT APPLICATIONS
Marc Lázaro Martí

7.2 System Design

7.2.1 System Overview

Figure 7.1 shows an overall system's operation sketch. The main goal is to filter people quickly and efficiently without the need for an operator. For this purpose, LoRa transceivers are proposed to be placed at the entrance of public venues. Low-cost LoRa radios ensure scalability and commercialization with a low budget. The transmitter is placed at the entrance, while receivers are placed inside and outside the site. This distribution of LoRa transceivers allows implementing a low-resolution localization system by means of the received signal strength (as described in chapter 5). Using this method, it is possible to determine whether or not the subject has crossed the entrance and where it was last detected (exiting or entering). This property can be used to implement an automatic occupancy control system. The attenuation of the wall plays an important role in determining if the person is inside or outside. The use of two receivers has two main advantages, such as increasing the probability of receiving data packets under non line-of-sight (NLoS) propagation conditions and determining if the subject has entered the building by comparing the received signal strength intensity (RSSI) of each receiver. The received power should be higher for the receiver closer to the tag allowing to track the smart mask as it moves. A simple classifier can be established from the RSSI or the signal-to-noise ratio (SNR) measured by the LoRa receiver for the received packets. Unlike other backscatter-based communication systems proposed in the literature that require specific and often expensive SDR receivers, the system proposed here allows the use of commercial devices without having to make any modification. Receivers work as a gateway, sending the data via WiFi to the cloud or a local server. In any system that handles personal data like this one, the privacy of the user must be respected. However, this should be managed at higher layers of the communication protocol by implementing encryption systems, which is currently beyond the scope of this work.

The smart mask integrates two temperature sensors to measure body temperature and monitor the subject's breathing. By placing the temperature sensor inside the mask, multiple measurements can be taken to check body temperature, unlike the single measurement provided by an infrared thermometer. This allows the system to obtain a set of temperatures and store them for fur-

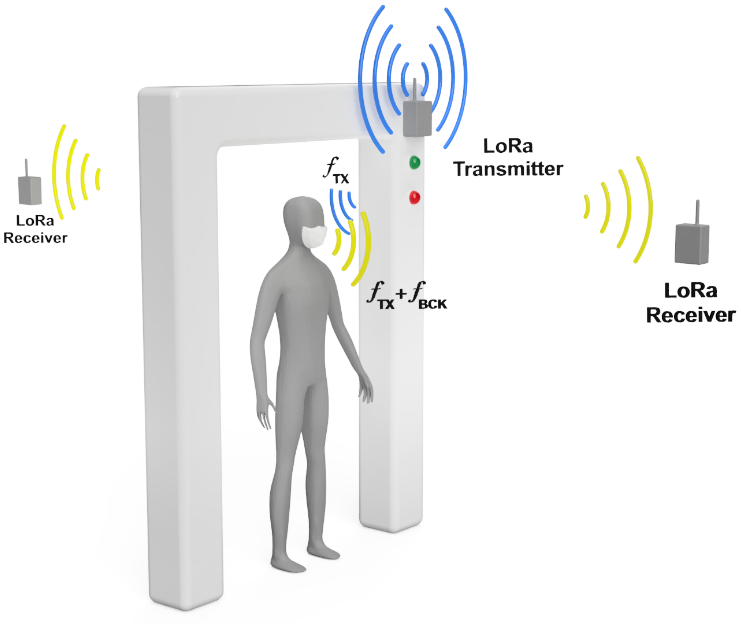

Figure 7.1: Scheme of the system operation. LoRa transmitter is placed at the entrance illuminating the subject wearing the smart mask. LoRa receivers placed inside and outside receive the signal backscattered by the mask. Access is granted or denied depending on the value of the temperature readings.

ther evaluation. The package payload consists of two main parts: the identifier and the sensor data (e.g., temperature or breathing rate). Alternatively, to reduce payload length, temperature and breathing rate can be replaced with an OK/NOK bit. The identifier is crucial for determining the origin of each mask's data, accepting valid identifiers and rejecting those that have crashed. To avoid packet loss due to collisions between multiple smart masks, anti-collision strategies have been implemented. The first strategy involves properly setting the LoRa parameters to reduce the communication range, capturing signals only from masks near the entrance. The second strategy randomly adjusts a waiting time between frame transmissions, minimizing potential collisions between frames from different backscatters. The system denies access to individuals with temperatures outside the standard range, triggering an alert and preventing their entry. In case of irregular measurements, the mask identifier and temperature data are saved, providing a useful history and allowing the system to record nearby mask identifiers for tracking or possible infection alerts. Subsequently, a manual check of the patient's condition can be performed using conventional methods.

7.2.2 Implementation

A schematic of the designed electronic device placed in the smart mask is presented in Figure 7.2. It integrates a dual-heat-flux sensor for determining core body temperature and a thermistor to monitor the breathing cycle of the person wearing the smart mask. A low-power AtTiny402 microcontroller reads and processes the temperature data. Once the data is processed, it is sent to receivers via the LoRa backscatter uplink communication, as described in Chapter 4.

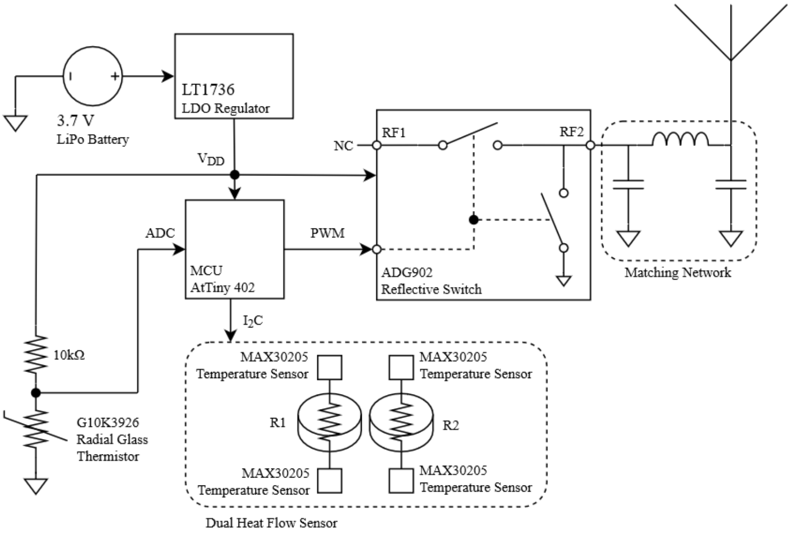

Figure 7.2: Block diagram of the smart mask.

Figure 7.3 shows an image of the prototype coupled to an FFP2 mask. The smart mask is powered by a 500 mAh lithium polymer (LiPo) battery. The system utilizes a load-modulation front-end, implemented with the previously mentioned ADG902. The combined power consumption of the microcontroller and the RF switch does not exceed 620 μA. The critical component in terms of power consumption is the DHF probe, which incorporates four MAX30205 ICs with a supply current of 600 μA each. Consequently, the system's maximum power can reach approximately 3 mA. In a worst-case scenario where all components are running at a 100% duty cycle, the battery life could extend up to 179 hours. The user can recharge the battery periodically once a week. By taking advantage of the MAX30205's shutdown mode with a current draw of less than 3.5 μA and the quick 50 ms temperature conversions, the overall power consumption of the system can be significantly reduced by duty-cycling the DHF sensor's operation. The antenna used is the 0868AT43A0020 ceramic antenna from Johanson Technology, connected to a Pi-matching network.

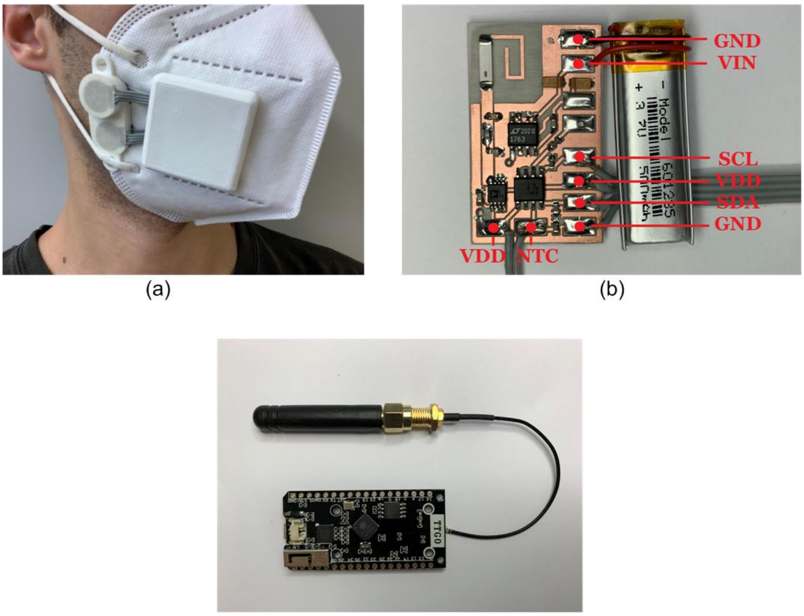

(a) (b)

(c)

Figure 7.3: (a) Photography of the Smart mask, (b) Detail of the PCB board, (c) ESP32 LoRa transceiver.

Three low-cost LoRa32 boards from TTGO, operating at the 868 MHz ISM European band, are used for the transmitter and receivers located inside and outside of the laboratory, as it is shown in Figure 7.4. Both receivers are tuned at the sideband channel where the smart mask backscatters the LoRa packets. The transmitter is installed at the entrance, right in the middle point. The distance between the receivers and the transmitter is set to 2 meters in the experiments. LoRa transceivers are set with a spreading factor (SF) of 7, a bandwidth of 250 kHz, and a preamble length of 6. The air time of the packets is 18 ms. LoRa transmitter frequency is set to 868MHz and backscatter shifting frequency f_{osc} is set to 500 kHz. Consequently, LoRa receiver's frequencies are set to 868.5 MHz. The power of the transmitter is set to 17 dBm.

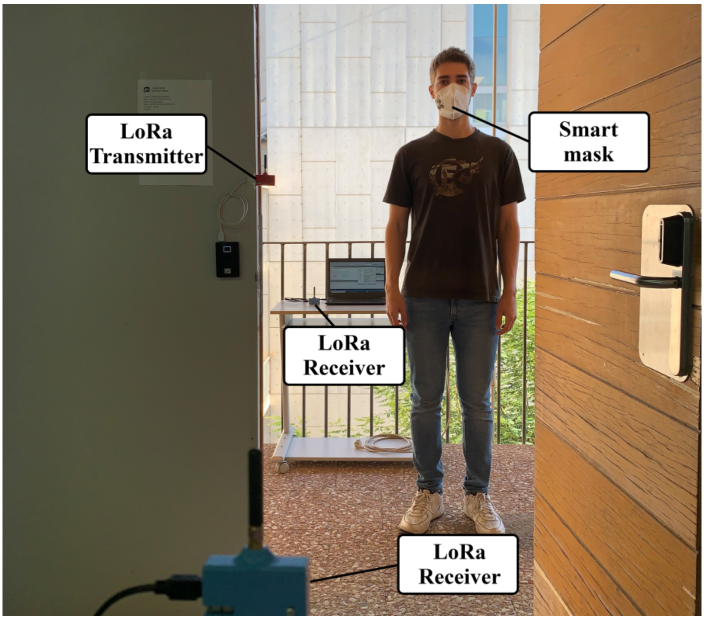

Figure 7.4: Photography of the measurement scenario. LoRa transmitter is placed at the entrance. LoRa receivers are placed inside and outside of the laboratory.

7.2.3 Temperature Sensing

Determining body temperature through the skin has always been a challenge [7.17]. Although conventional thermometers can perform this task precisely, the locations to measure the temperature must be very sheltered. The most common measurement places are the oral, tympanic, axillary, and rectal. All of them are unfeasible for measuring temperature on a large scale or outside of a healthcare environment [7.18]. Infrared thermometers have been the only method capable of handling the pandemic situation due to a quick and non-intrusive way of measuring body temperature, but their accuracy and reliability have been questioned in practice [7.19, 7.20, 7.21, 7.22].

The simplest way to measure body temperature is by measuring skin temperature with a temperature sensor (e.g. with a thermistor or an active integrated circuit sensor). Although this method works well in places where the temperature is stable (e.g. in the armpit), it is not the most ideal system to be integrated into a mask, since it is highly exposed to drafts and changes in temperature. A method for determining deep body temperature is through heat flux sensors.

UNIVERSITAT ROVIRA I VIRGILI
LONG-RANGE BACKSCATTERING COMMUNICATIONS FOR NEXT GENERATION IOT APPLICATIONS
Marc Lázaro Martí

Several works that analyze the performance of this kind of sensor can be found in the literature [7.23, 7.24, 7.25]. In [7.23], a single heat flux sensor based on temperature measurement at two points plus a correction to take into account the influence of ambient temperature is proposed. However, the calibration of the sensors depends on the thermal conductivity of the body. To solve this problem, dual-heat-flux sensors can be used to measure the temperature in four points [7.24].

In a previous work [7.26], two thermistors were used to estimate the body temperature, one installed in the cheekbone and the other outside the mask to measure ambient temperature. With this methodology, it is necessary to calibrate the parameters of the model for each person because they depend on the skin resistance. In addition, the thermistor must be calibrated with great precision. To avoid these problems, a dual-heat-flux (DHF) probe is designed and embedded into the face mask. Figure 7.5 shows the operating diagram of the core temperature probe. It consists of two heat flow sensors integrating four MAX30205 temperature sensors from Maxim Integrated, one MAX30205 pair for each heat flux sensor. This chip has an accuracy of 0.1ºC and is specifically designed to measure the temperature of the human body. Both MAX30205 are isolated from each other with polylactic acid (PLA), which has a thermal conductivity equal to 0.13 $W/m \cdot K$.

According to the second law of thermodynamics, heat will flow from the hottest point to the coolest point until both temperatures are equalized by diffusion. The dual-heat-flux probe can be modeled with an electrical system [7.24, 7.25] described in Figure 7.5. In this analogy, temperatures are represented by the voltages in the nodes and the heat flow is the current that flows between two nodes. Analyzing this circuit, the following equations are obtained:

$$T_{core} = T_1 + \frac{(T_1 - T_2)R_S}{R_1} \tag{7.1}$$

$$T_{core} = T_3 + \frac{(T_3 - T_4)R_S}{R_2} \tag{7.2}$$

where T_1 and T_3 are the temperatures on the skin surface, T_2 and T_4 are the temperatures at the top surface of each heat flux sensor, R_S is the thermal resistance of the skin and the subcutaneous tissue and they have the same value for the two flux sensors. That is a reasonable approximation, considering that both sensors are very close to each other. The problem arises because the thermal resistance R_S of the tissue beneath each heat flux sensor cannot be measured and it is strongly influenced by the hypodermic blood flow and subject to variations between persons. The use of two heat flow sensors solves this problem. Eliminating R_S from 7.1 and 7.2, the core temperature can be obtained from the measured temperatures:

$$T_{core} = T_1 + \frac{(T_1 - T_2)(T_1 - T_3)}{K(T_3 - T_4) - (T_1 - T_3)} \tag{7.3}$$

where K is defined as the ratio of thermal resistances R_1 and R_2 ($K = R_1/R_2$). The ratio K is determined during the calibration procedure from a known T_{core} and the measured temperatures:

$$K = \frac{(T_{core} - T_3)(T_1 - T_2)}{(T_{core} - T_1)(T_3 - T_4)} \tag{7.4}$$

In the implemented prototype, a PLA housing that integrates and isolates the four sensors has been printed with a 3D printer, as can be observed in Figure 7.6. The height of each heat flux sensor is 5 mm and 10 mm, respectively, and the diameters are 20 mm. The body temperature T_{core} can be calculated after estimating the ratio K using (7.3).

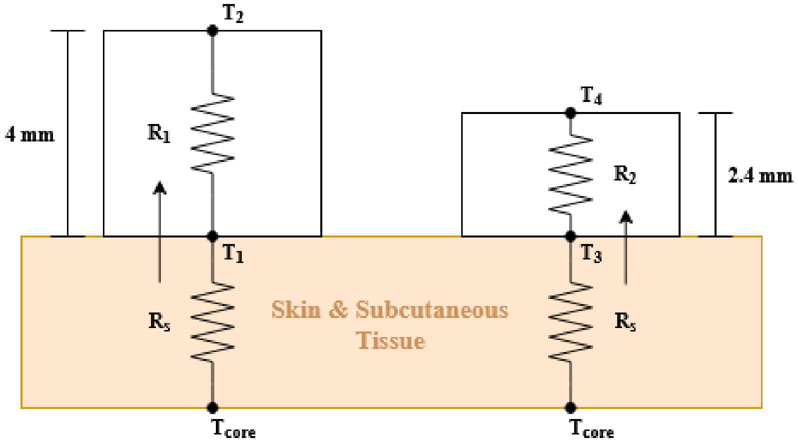

Figure 7.5: Schematic diagram of the dual-heat-flux sensor and its equivalent circuit.

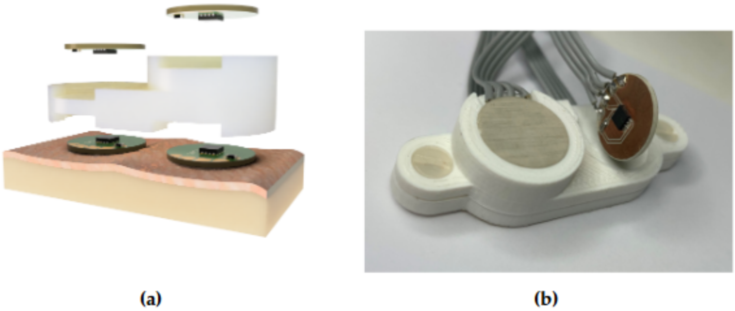

Figure 7.6: Dual heat flow sensor prototype built on a 3D printed PLA support, which acts as an insulator between the four temperature sensors: (a) 3D rendering of the prototype; (b) real prototype.

7.2.4 Breathing monitoring

COVID-19 disease can cause shortness of breath, lung damage, and impaired respiratory function [7.27]. COVID-19 patients can develop a complication known as Acute Respiratory Distress Syndrome (ARDS). With ARDS, patients lose the ability to breath normally and this is known as a respiratory failure that results from severe inflammation in the lungs. Therefore, anomalies in breathing rate can be useful for screening COVID-infected subjects. In addition, an increase in temperature is observed in people after having done some physical exercise [7.28]. Therefore, tracking the breathing rate history can be useful in avoiding false positives.

Figure 7.7 shows the thermal behavior inside the mask (FFP2 type) during a respiration cycle. The temperature in the cheekbone and the lateral part of the mask remains mainly constant, whereas the central part of the mask changes according to the inhaled and exhaled air temperature. Therefore, the dual-heat-flux sensor (DHF) must be installed on the lateral part of the mask to avoid heating associated with breathing. To monitor breathing, a temperature airflow sensor capable of detecting temperature variations is used. The temperature airflow sensor consists of a Negative Temperature Coefficient (NTC) thermistor integrated into the mask and located under the nose. Compared to other temperature sensors, NTC devices are inexpensive and are characterized by both high sensitivity and high non-linearity. In this design, absolute temperature is not required. Consequently, the calibration and the non-linearity of this sensor are not critical issues. In the manufactured prototype, a radial glass

NTC model G10K3976 from TE Connectivity is employed.

The first-order approximation of the Steinhart–Hart equation [7.29] is given by the manufacturer to model the NTC resistance R as a function of the temperature:

$$\frac{1}{T} = \frac{1}{T_0} + \frac{1}{\beta} ln\left(\frac{R}{R_0}\right) \tag{7.5}$$

where T is the temperature in K, $R_0 = 10k\Omega$ is the nominal resistance at T_0 $= 298$ K, and $\beta = 3976$ K is the Steinhart–Hart parameter, which is provided in the thermistor datasheet.

A simple voltage divider composed of the NTC and a resistance with the nominal value of the NTC ($10k\Omega$) connected to the supply voltage V_{cc} is used to obtain the breathing measurement. The voltage output V_{out} of this circuit is acquired with the internal analog-to-digital converter (ADC) of the microcontroller:

$$V_{out} = V_{cc} \frac{R}{R + R_0} \tag{7.6}$$

In order to estimate the limitation in the temperature measurement due to the finite resolution of the ADC, the voltage sensitivity can be obtained by combining 7.5 and 7.6 and derive the result with respect to the temperature:

$$\frac{dV_{out}}{dT} = \frac{dV_{out}}{dR}\frac{dR}{dT} = -V_{cc}\frac{R \cdot R_0}{(R + R_0)^2}\frac{\beta}{T^2} \approx -\frac{V_{cc}}{4}\frac{\beta}{T^2} \tag{7.7}$$

For temperatures in the order of ambient temperature $T \approx T_0$ gives an approximate value of -35 mV/K. Taking into account that the temperature variation due to airflow is on the order of 4 to 5 degrees, the microcontroller's 10-bit ADC provides enough resolution to digitize the output without the need for amplification, thus reducing the number of components.

This temperature signal estimated from the airflow sensor has a small variation over the average temperature of the mask and it is also noisy. Therefore, after the average signal is subtracted, low-pass filtering is applied to reduce noise. Since the filters must be implemented in a low-power microcontroller, exponential moving average (EMA) filters are used to reduce the computational charge and memory. The average temperature $X_{av}[n]$ is estimated using the following recursive equations from the measured temperature samples $X[n]$ [7.30]:

$$X_{av}[n] = \alpha_1 X[n] + (1 - \alpha_1) X_{av}[n-1] \tag{7.8}$$

The output breathing signal $Y[n]$ is obtained from a second exponential moving average filter applied to $X[n]$ after subtracting the average value to reduce noise:

$$Y[n] = \alpha_2 (X[n] - X_{av}[n]) + (1 - \alpha_2) Y[n-1] \tag{7.9}$$

Typical values for α_1 and α_2 are 0.04 and 0.08, respectively.

The breathing rate is usually expressed in breaths per minute (bpm). It can be estimated from the inverse of the interval between two consecutive peaks of the breathing signal. A robust peak detection algorithm described in [7.31] is applied to the filtered breathing signal $Y[n]$. When an interval between two consecutive breathings is longer than 10 seconds, it is considered as apnea. In this case, an apnea index is activated to count the number of apneas during the measurement session.

Compared to conventional airflow sensors used for breath monitoring, the integration of the airflow sensor in the mask allows for comfortable breath monitoring once the obligation to wear the mask is assumed.

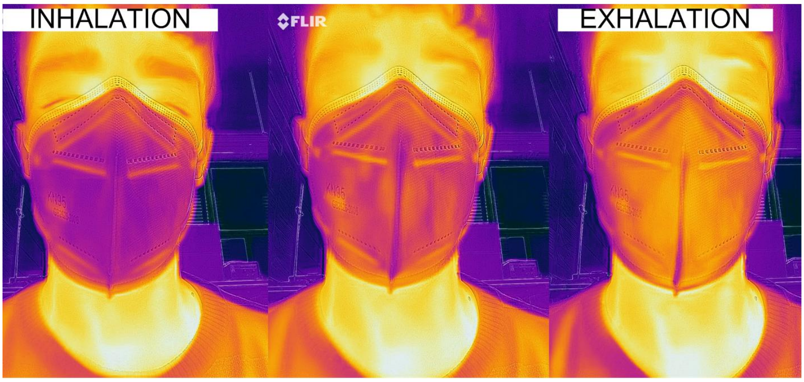

Figure 7.7: Thermal image of a breathing cycle of a subject with a mask.

UNIVERSITAT ROVIRA I VIRGILI
LONG-RANGE BACKSCATTERING COMMUNICATIONS FOR NEXT GENERATION IOT APPLICATIONS
Marc Lázaro Martí

7.3 Results

7.3.1 Calibration of the temperature Sensor

In order to find the thermal resistance ratio K an experimental setup similar to the one proposed in [7.32] is conducted (see schema in Figure 7.8). This experiment allows to set the core temperature and check the calibration. A water bath at a temperature of 37º simulates the nominal temperature of the body. A copper container is placed floating on the water. Rubber sheets were used to emulate the skin and subcutaneous tissue. The thickness of the rubber can be increased by adding more sheets. Rubber material has been chosen because its thermal conductivity ($0.17 W m^{-1} K^{-1}$) is close to the value of the subcutaneous tissue. Then the probe is located on the rubber layer and the thermal resistance ratio K is determined for different thicknesses from the measurement of the four temperature sensors using (7.4). The water temperature is monitored with a thermometer and controlled with a hot plate (with resolution of ±1 ºC). A nearly constant value as a function of the thickness of the rubber layer has been obtained (see the top plot in Figure 7.9). The room temperature is 25ºC. Using the value of the ratio $K = 1.2$ that has been found, the water temperature is estimated from another set of measurements (Figure 7.9). The differences produced could be attributed to poor lateral insulation of the prototype [7.25]. Despite this drawback, the error is typically below 0.5ºC.

From the thermal resistance ratio K found with the latest experimental setup, the core temperature of a subject wearing the face mask can be estimated from (7.3). A set of measurements are shown in the following figures. The experiments have been repeated with different persons and similar conclusions have been achieved. The measured temperatures for each sensor of the DHF sensor, following the notation of Figure 7.5, are shown in Figure 7.10. The estimated core temperature and the measured temperature in the armpit with a thermistor are shown in Figure 7.11. It takes about 100 seconds to reach a value close to the core temperature. Figure 7.11 shows the difference between two sensors once the temperatures reach the thermal equilibrium. The standard deviation error is 0.2ºC which is of the order of the temperature sensor accuracy. When the mask is not worn, the four temperature sensors tend to ambient temperature and, therefore, it is useful to verify the correct placement of the face mask.

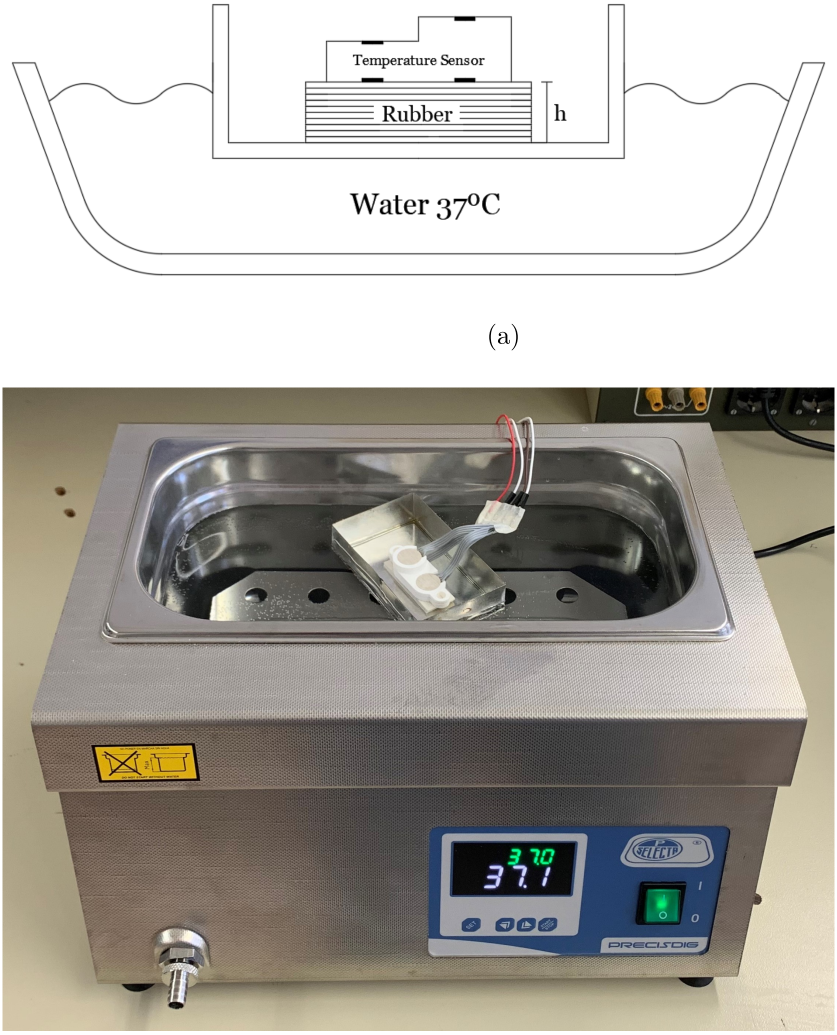

(a)

(b)

Figure 7.8: Scheme of the body simulation method used to calibrate the DHF sensor (a), and photography of the experimental equipment used to calibrate the DHF sensor (b).

7.3.2 Determination of breathing rate and coughing events

An example of breathing rate estimation is shown in the following figures. Figure 7.12 shows the measured temperature by the frontal thermistor installed in the mask close to the nose area, in addition to the core temperature estimated with the DHF probe. Some apneas periods have been simulated by consciously

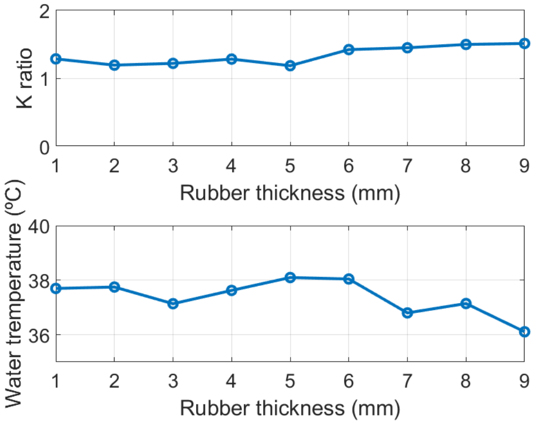

Figure 7.9: Thermal resistance ratio K (top) and estimated water temperature (bottom) as a function of rubber thickness.

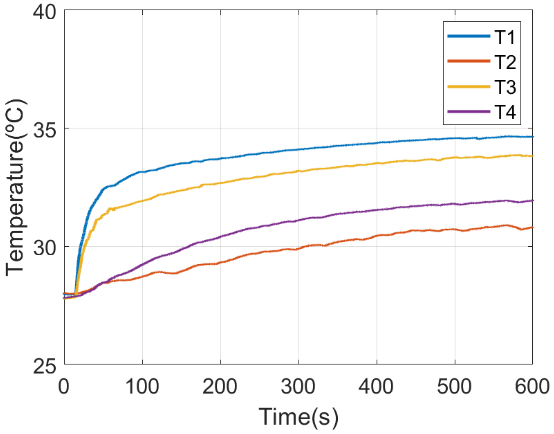

Figure 7.10: Measured temperature for each temperature sensor in the probe as function of the time after installing the smart mask.

stopping breathing. The maximum and minimum peaks obtained with the peak search algorithm are also plotted on the graph. The breath frequency can be obtained from the time position of the maximum peaks (see Figure 7.13). The average breathing is also shown in this figure. Apneas can be identified if the time interval between two consecutive breaths is greater than 10 seconds. An increase in breathing amplitude is observed after the end of each apnea period. The breath frequency can be obtained from the time position of the maximum peaks (see Figure 7.13). The average breathing is also shown in this figure.

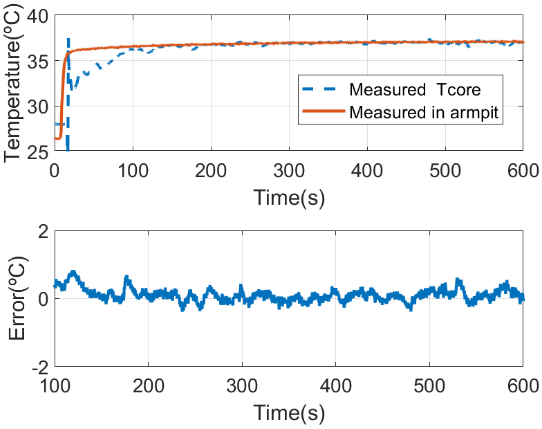

Figure 7.11: Comparison of the estimated core temperature with the dual-heat-flux sensor and measured in the armpit with a thermistor (top) and difference between both measurements after the initial response (bottom).

Apneas can be identified if the time interval between two consecutive breaths is greater than 10 seconds. An increase in breathing amplitude is observed after the end of each apnea period. These figures show how the smart mask can be used to monitor breathing activity. Some simple statistics such as the average breathing rate, the maximum breathing rate, and the apnea count can be saved in the flash memory of the microcontroller. For continuous data logging, an SD memory card can be used to store the complete data over time.

The presence of cough is another symptom associated with COVID. The system has the ability to detect cough events. Figure 7.14 shows the temperature of the thermistor after installing the mask. It can be shown that it takes about 25 seconds to reach the steady state. The figure shows the maximum peaks associated with the breaths. Under these conditions, the amplitude of the peaks remain nearly constant. To show the detection of cough, in this figure, the subject has coughed three times. Coughs cause a rapid rise in temperature of about 1 degree due to the sudden expulsion of air. Therefore, by detecting these peaks and comparing the level with the average of the last 5 temperature peaks, a simple cough counter can be implemented (see graph at the bottom of Figure 7.14).

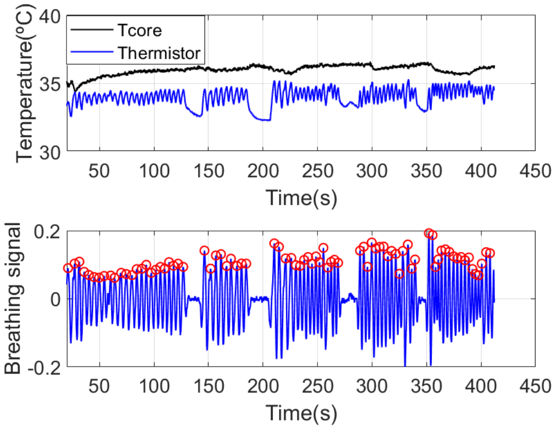

Figure 7.12: Estimated core temperature and measured frontal thermistor temperature for breathing rate estimation (top). Breathing signal after removing and filtering the baseline (bottom).

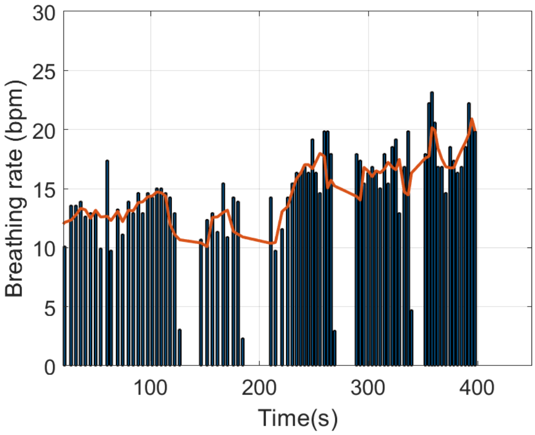

Figure 7.13: Estimated breathing rate (vertical bars) and average breathing rate (red solid line).

7.3.3 Wireless measurement and positioning

In chapter 5 the LoRa backscattering localization system based on the received signal strength has been introduced. The work here proposed focuses on knowing the relative position of the person with respect to the door, establishing if the person is inside or outside the room. Therefore, a simpler classifier that does not require a training procedure is investigated. Some tests have also been done

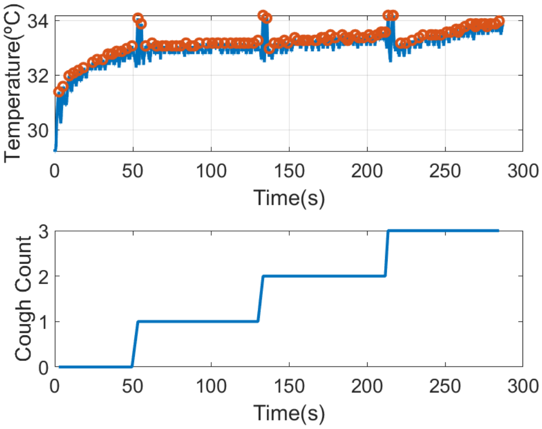

Figure 7.14: Thermistor temperature measured after putting on the mask considering coughing episodes (top). Number of cough episodes detected from maximum temperature peaks (bottom).

to evaluate the feasibility of locating the person from the backscattered signal using the setup shown in Figure 7.15, which corresponds to a typical access control (see Figure 7.4). LoRa ICs are equipped with measured received signal strength intensity (RSSI) and SNR indicators. The values of these measured parameters are stored in the corresponding registers and can be read via the SPI bus by the host processor. Figure 7.15 shows the decrease of the RSSI at receiver number one (placed outside) and the increase at receiver number two (placed inside) as the person walks through the door from outside to inside.

However, from equation (5.1) of chapter 5, the received power would be expected to increase significantly as the person gets closer to the transmitter. Although there is a slight increase, it was expected to be larger. This is attributed to both diffraction effects and the blocking of the direct line of sight produced by the walls and the body itself. The measured RSSI for each receiver presents the crossover at approximately the equidistant point between each receiver and the transmitter. Following (5.1), the power at the receivers should be equal for equal distances between the transmitter and each receiver. This defines a plane located midway between both receivers. However, due to the attenuation of the walls, slight variations in the positioning of the receiver and, in general, a non-symmetrical scenario, a displacement of the crossover point may occur. A threshold difference parameter ($\Delta RSSI$) to establish the crossover point at the door entrance can be considered. The smart mask will be located inside when the difference between the RSSI measured at each receiver is greater than this parameter $\Delta RSSI$:

$$RSSI_2 - RSSI_1 > \Delta RSSI \tag{7.10}$$

This parameter can be determined experimentally when the receivers are installed. The backscatter is placed in the center of the door and then the difference of the measured RSSI values of the two receivers is averaged. An analog decision rule can be applied using the SNR measurements returned by the transceiver.

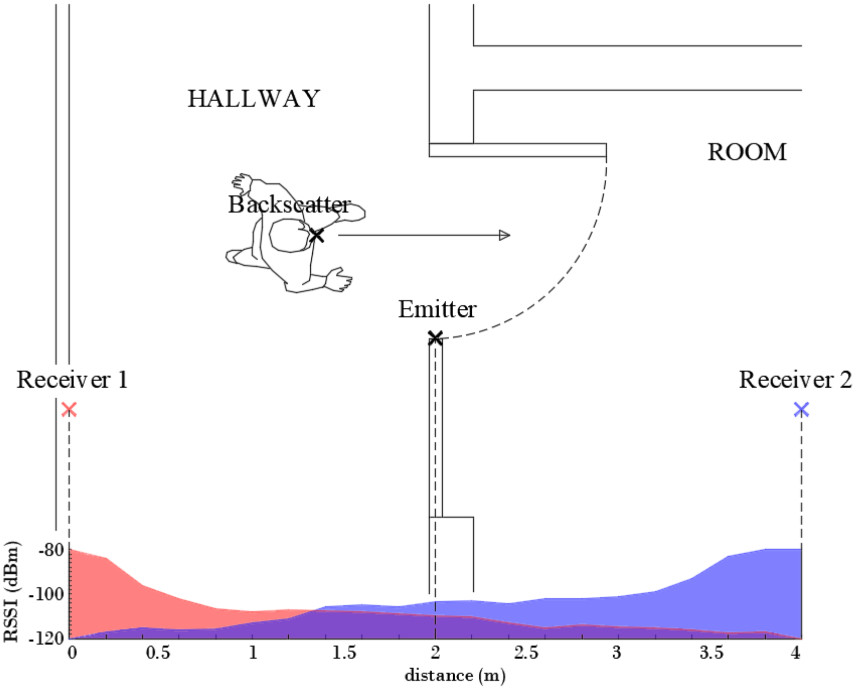

Figure 7.15: Measured RSSI at the two receivers (receiver 1 outdoor and receiver 2 indoor) for a subject crossing a door, as a function of distance.

To study the reception coverage several measurements have been made with the backscatter device within a radius of three meters around the entrance. Figure 7.16 shows the cumulative distribution function (CDF) of the RSSI and the signal to noise ratio (SNR) received for points randomly taken both outside and inside the room. These figures show that the measured RSSI and SNR are higher for the receiver closest to the mask. The average SNR returned by the LoRa transceiver has higher resolution than RSSI, so that, it is preferred to use the measured SNR values than RSSI values. Therefore, a simple classifier based on the measured SNR can be used to determine whether the smart mask is inside or outside the building or room. The smart mask is outside if the SNR of receiver 1 (at the outdoor) is higher than that of receiver 2 (at the indoor). The read range can be increased by varying the LoRa parameters and the power of the transceivers. The LoRa transceivers are connected to internet, and the information gathered is sent by Message Queueing Telemetry Transport (MQTT) protocol to a broker that can be accessed from any web browser or mobile app.

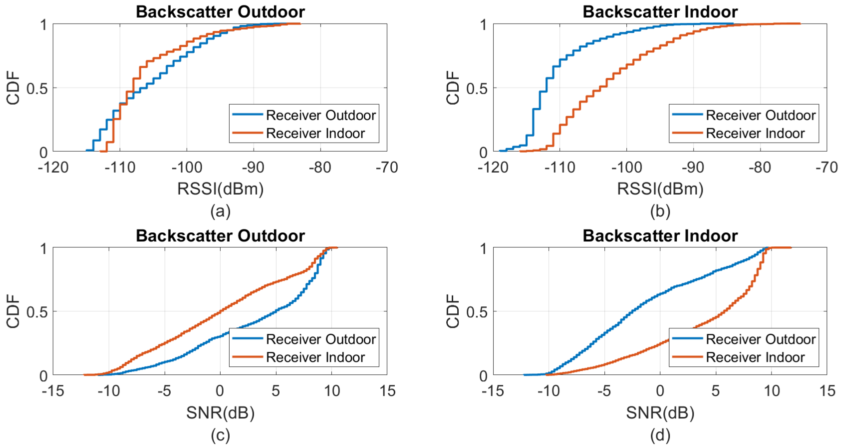

(a)
(b)
(c)
(d)

Figure 7.16: Cumulative distribution function of the RSSI for (a) backscatter outdoor and (b) backscatter indoor, and SNR for (c) backscatter outdoor and (d) backscatter indoor.

In order to investigate the performance of the positioning system, a number of measurements are done in a scenario in which both line-of-sight and multipath propagation effects must be taken into account. Figure 7.17 shows a schematic of the scenario. It consists of a corridor that allows access to the laboratory through the door. Each receiver is 2.4 m away from the door and 1.5 m above the ground. The transmitter is placed on top of the door. The entrance has two doors, one of which is made of metal and is kept closed. RSSI and SNR measurements are performed and recorded in each receiver in sets of backscattered packets measured every 40 cm along the corridor and the entrance of the lab-

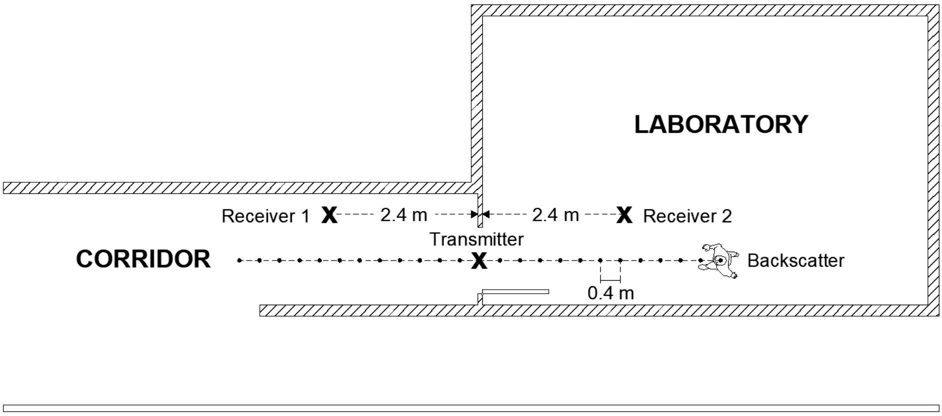

Figure 7.17: Diagram of the scenario used in the measurements.

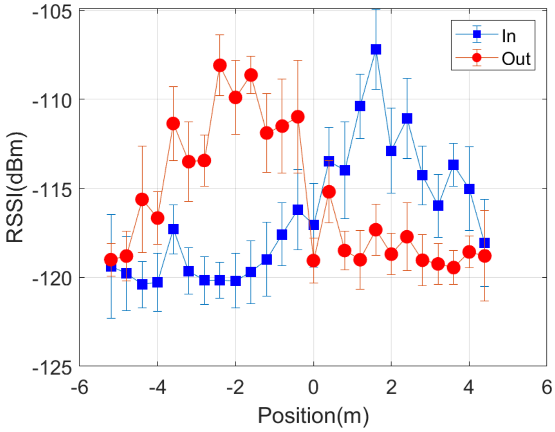

Figure 7.18: Average RSSI measured as a function of the backscatter position with respect to each of the receivers. The standard deviation has been included in the error bars.

oratory, as shown in the diagram in figure 7.17. A total of 1000 measurements are done at each position with the smart mask worn by one person. Figures 7.18 and 7.19 show the average RSSI and SNR values measured at each receiver (receiver 1 outside and receiver 2 inside) and the error bars show the standard deviation obtained. From these data, the decision rule is applied for each measurement cell. Figures 7.20 and 7.21 show the percentage of cases in which the RSSI or SNR measured at the receiver located in the laboratory is greater than

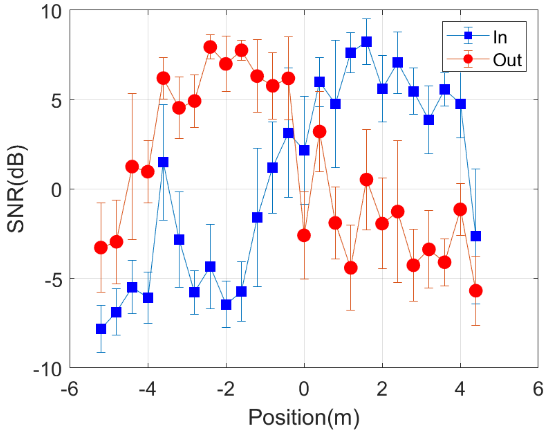

Figure 7.19: Average SNR measured as a function of the backscatter position with respect to each of the receivers. The standard deviation has been included in the error bars.

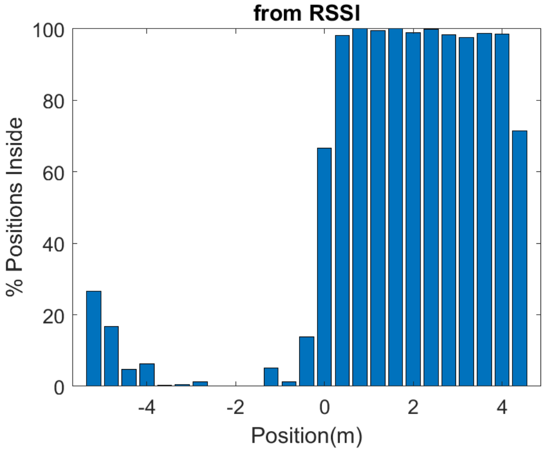

Figure 7.20: Percentage of cases in which the smart mask is classified inside, as a function of the position with respect to each of the receivers, obtained by comparing the measured RSSI of each receiver at each position.

that measured by the receiver located outside. Values close to 0% were found corresponding to the positions furthest from the receptor. The result agrees with the measured RSSI and SNR values that reach their minimum levels, close to the sensitivity of the receiver. These cases can be ignored if they are considered to be outside the cover range. Again, slight better accuracy is observed when using SNR measurements instead of RSSI measurements. Near the door,

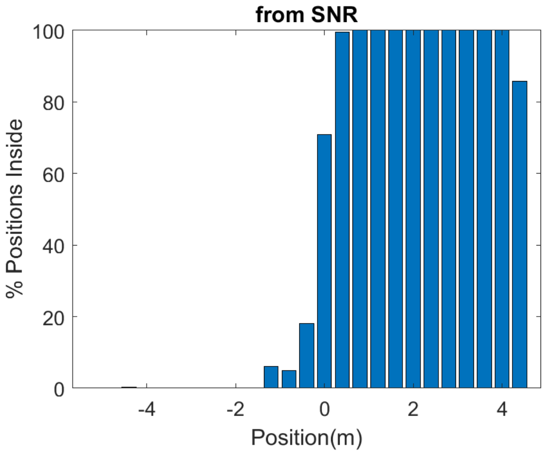

Figure 7.21: Percentage of cases in which the smart mask is classified inside, as a function of the position with respect to each of the receivers, obtained by comparing the measured SNR of each receiver at each position.

the accuracy is about 30% due to the measurement uncertainty and the random nature of propagation. Therefore, it can be estimated that the resolution is about one range cell (± 0.4 m), which is enough for this application. Therefore, the proposed decision rule to classify the relative position with respect to the door can be carried out without the need of a training procedure or the use of a specific propagation model.

To investigate the fluctuations of the RSSI (or SNR) depending on the position, a comprehensive empirical model has been developed. Propagation models applied to wireless signals within buildings have been extensively studied in different contexts such as cordless phones and wireless local area networks (WLANs) [7.33, 7.34]. The proposed model considers the effect of multipath propagation due to reflections on walls, floor and large objects, the shadowing or blockage of the transmitter and receiver due to the proximity of the body, and the attenuation due to walls and doors along the path. The model introduces an additional attenuation to the receiver power given by (5.1):

$$L(dB) = L_{obs}(dB) + L_{multipath}(dB) + L_{blockage}(dB) \tag{7.11}$$

where L_{obs} considers attenuation due to propagation through walls or other materials, and $L_{multipath}$ considers the attenuation due to the multipath interference, which is modeled using the two-slope model:

$$L_{multipath}(dB) = 10 \cdot (n_T - 2) \cdot log\left(1 + d_T/R_{0T}\right) + 10 \cdot (n_R - 2) \cdot log\left(1 + d_R/R_{0R}\right) \tag{7.12}$$

where n_T and n_R are the path loss exponents for a distances greater than the breakpoint distance [7.33], R_{0T} and R_{0R} are the backscatter to the transmitter and the backscatter to the receiver paths, respectively. This model does not consider any obstacle in the first Fresnel region and the path loss exponent is close to 2 (or under 2 due to the corridor behaviour, equivalent to a wave-guide). On the other hand, a path loss exponent larger than 2 is expected when the distance is higher than the breakpoint. To account for the shadowing effect of the transmitter or receiver due to the proximity of the body, an increasing attenuation has been introduced as the backscatter approaches the transmitter or receiver:

$$L_{blockage}(dB) = 10 \cdot n_{bT} \cdot log\left(1 + R_{1T}/d_T\right) + 10 \cdot n_{bR} \cdot log\left(1 + R_{1R}/d_R\right) \tag{7.13}$$

where n_{bT} and n_{bR} are exponent coefficients that control the level of attenuation, and R_{1T} and R_{1R} determine the range extension for the blockage of the transmitter and the receiver, respectively.

Table 7.1 lists the empirical model parameters used in the simulations. Figure 7.22 shows a contour map of the received power (RSSI) simulated for each receiver for the same distances between transceivers and heights than in the scenario of 7.17. Figure 7.23 shows a cut for $y = 0$. Despite the limitations of the model, it justifies the evolution obtained in the measurements performed in this scenario. These figures show the ability of the model to predict the shadowing around the transmitter and receivers, and show the convenience of the decision rule 7.10 based on the highest RSSI (or SNR) that permits to predict if the person has crossed the gate or not(position $x = 0$). Considering a deviation in the RSSI measurements of 2 dB, the resolution is in the order of ±0.5 m, which is in agreement with the experimental results.

Parameter	Symbol	Value
Attenuation due to obstacles	L_{obs}	15 dB
Path loss exponent for transmitter to backscatter path	n_T	3
Path loss exponent for backscatter to receiver path	n_R	3
Breakpoint distance for backscatter path	R_{0T}	1.5 m
Breakpoint distance for backscatter to receiver path	R_{0R}	1.5 m
Blockage exponent for the transmitter	n_{bT}	4.5
Blockage exponent for the receiver	n_{bT}	4.5
Extension of blockage distance in the transmitter	R_{1T}	1.5 m
Extension of blockage distance in the receiver	R_{1T}	1.5 m

Table 7.1: Indoor propagation model parameters.

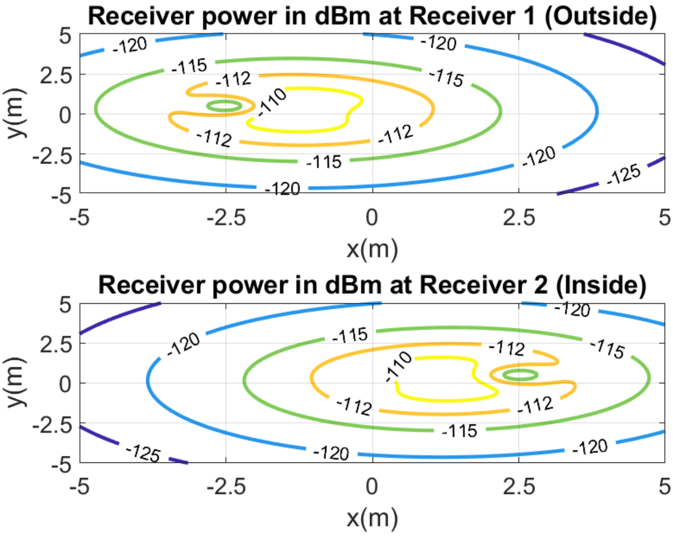

Figure 7.22: Simulated received power (RSSI) at the receiver located inside (top) and outside (bottom).

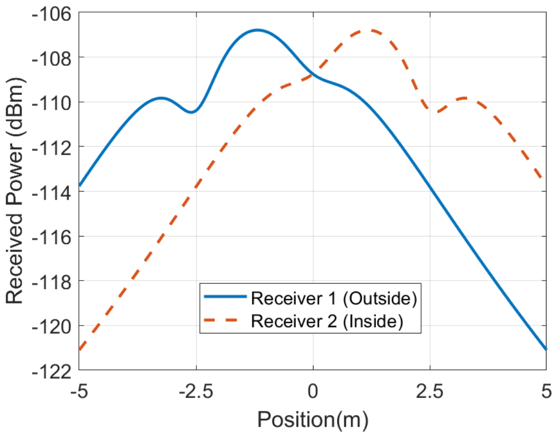

Figure 7.23: Simulated received power (RSSI) as a function of the x-position at y=0.

7.4 Discussion

In this section, a comparison with other technologies (conventional and presented in the literature) are discussed. The comparison is summarized in table 7.2. There are different commercially available methods for measuring body temperature. Body temperature measurement depends on the accuracy of the thermometer, the measurement site, and the skills of the person measuring the temperature. The aim is to measure core temperature, which is defined as the temperature of the large blood vessels in the internal organs and the brain. Temperature measurement using a pulmonary artery catheter is considered the standard. However, this method is difficult to perform and it is considered an invasive measurement method. Therefore, other methods and parts of the body such as the esophagus, the rectum, the armpits and the eardrum are used to measure body temperature [7.35]. Esophageal and rectal measurements are both generally considered valid [7.36] but are not suitable for non-contact or continuous readings. Therefore, methods for measuring body temperature from measurements performed on its surface are considered non-invasive and are preferable for continuous measurements or home use.

Body temperature is measured on the surface of the skin and results from the ambient temperature and the temperature inside the body. The main problem is that it depends on factors such as blood circulation, activity and external

UNIVERSITAT ROVIRA I VIRGILI
LONG-RANGE BACKSCATTERING COMMUNICATIONS FOR NEXT GENERATION IOT APPLICATIONS
Marc Lázaro Martí

temperature, and serves as a regulator of the body's temperature. While the core body temperature remains mainly constant, the surface temperature of the human body can vary considerably (approx. 28 °C - 37 °C). Depending on the ambient temperature, there can be big differences between the temperature of the interior and the surface of the body. The temperatures in hands and extremities decrease several degrees in cold environments.

There are different ear or tympanic measurement devices commercially available. The most common are manual handguns, but recently there are also available portable over-the-ear devices for professional healthcare and for sports monitoring (eg. from Cossinuss GmbH, Munich, Germany).

Axillary temperature measurement is a commonly used method. Modern sensors are based on a thermistor placed in the armpit, which is a place where the temperature remains stable and less influenced by the ambient temperature. Devices designed for continuous measurement are attached with the help of adhesive tape and can record the temperature and send the information via Bluetooth to a mobile application. Commercial examples of this technology are FeverSmart (model WT701, iMobile Healthcare LLC, Philadelphia, PA) and iThermonitor (model WT701, Railing Medical Company, Beijing, China). The main problem of these devices is given by the limitation of arm movements to prevent them from being disconnected or interfering with the measurement, as well as being problematic for measuring the temperature of babies.

UNIVERSITAT ROVIRA I VIRGILI
LONG-RANGE BACKSCATTERING COMMUNICATIONS FOR NEXT GENERATION IOT APPLICATIONS
Marc Lázaro Martí

Ref.	**Technology**	**Advantages**	**Disavantages**
Com.	Infrared Thermometer	Cheap	- Operator needed. - Close detection. - Affected by external environment conditions. - Affected by body thermoregulation.
Com.	Thermo-scanner	Remote detection	- Expensive. - Affected by external environment conditions. - Affected by body thermoregulation.
Com.	Tympanic Thermometer	- Cheap. - Body core temperature estimation.	- Operator needed. - Close detection.
Com.	Axillary Thermometer	- Cheap. - Body core temperature estimation.	- Close detection.
[7.37]	Zero-flux method	- Body core temperature estimation.	- Commercially available - wired. - High power consumption for the heater.
[7.38] [7.39] [7.40] [7.41]	UHF RFID	- Cheap epidermal tag.	- Expensive reader. - Position dependent. - Can be Affected by external environment.
[7.42, 7.25]	BLE and Dual Flow heat	- Wireless measurement. - Body Core temperature estimation - Reading from a smartphone	- Require a head band. - Does not measure breathing or location. - Requires authentication. - Long-range.
[7.43]	NFC	Cheap. Mobile as a reader.	- Measures the skin surface temperature. - Position dependent. - Affected by external environment conditions. - Affected by body thermoregulations. - Short-range.
This work	LoRa Backscatter	- Cheap. - Body core temperature estimation. - Breathing rate estimation. - Low resolution Localization. - Based on commercial LoRa transceivers - Integrated in a mask. - Long-range. - Cough detection.	- Battery assisted. - Low data-rate.

Com.: Commercial available.

Table 7.2: Body temperature measurement methods

In addition to those places where the body surface temperature is similar to the core temperature (such as armpits or eardrums), there are other strategies based on estimating the core temperature obtained from heat flux measurements, such as considered in this work.

Zero-heat-flux (ZHF) method is a non-invasive method [7.44] that is commercially available, for example, 3M commercializes the model SpotOn (3M, St. Paul, MN). Zero-heat-flux thermometers consist of a heater and two thermometers separated by a heat insulator. The heater is controlled to maintain the two temperatures identical. When these conditions are met, an isothermal tunnel from the core body to the skin surface is created. At this point, the subdermal temperature can be measured approximately 1 to 2 cm below the surface of the skin. In well-perfused parts of the body (such as the lateral forehead), the temperature of the tissue below the surface of the skin approaches the core body temperature. This non-invasive method is a useful tool for monitoring brain temperature. However, the current consumption associated with the heater makes this solution unsuitable for battery-powered or wearable devices. In addition, the patient must remain still to avoid the disconnection of the probes on the forehead.

As described in this work, dual-heat-flux sensors are used as an alternative to ZHF sensors with similar accuracy [7.24]. These sensors are installed also in the forehead and are commercially available for clinical use (eg.Tcore product from Dräger, Lübeck, Germany). For instance, in [7.42, 7.25], a dual-heat-flux sensor has been integrated into a headband that allows data to be transmitted to the mobile phone with Bluetooth.

Infrared thermometers are a cheaper solution than infrared camera-based thermal scanners and are widely used to measure forehead temperature to examine people. A comparison of the accuracy of infrared thermometers with a tympanic sensor has been presented in [7.45]; it shows that there are fixed offsets that depend on the site where the measurement is made (forehead or wrist) and therefore, a suspicious person with fever requires a double check. In addition to the accuracy, the other issue arises from the need for a person to perform the measurement and, consequently, the system is not fully automatic.

In the last years, some research groups have developed epidermal temperature sensors based on UHF RFID tags [7.38, 7.39, 7.40, 7.41]. The accuracy depends on the RFID integrated circuit, which embeds the temperature sensor

UNIVERSITAT ROVIRA I VIRGILI
LONG-RANGE BACKSCATTERING COMMUNICATIONS FOR NEXT GENERATION IOT APPLICATIONS
Marc Lázaro Martí

and the RFID communication. These IC have poorer sensitivity than conventional RFID IC without sensing capability due to the extra energy required to bias the analog-to-digital converters as well as the sensors. In addition, losses introduced by the body limit the read range of these epidermal tags to a few meters. A prototype for the measurement of axillary temperature using passive RFID has been proposed in [7.38]. In [7.41] a dual-sensor based on a dual UHF IC embedded in a UHF RFID tag has been proposed to improve the estimation of the body temperature. Although the cost of epidermal tags is low, the readers are expensive and justified if the entire blockchain over RIFD is deployed for other applications (eg. to track the real-time location of assets, employees, or customers), limiting the application for small users.

Recently, large investigation can be found about battery-less sensors based on energy harvesting Near Field Communications devices [7.46]. These RFID tags obtain energy from the RF field to bias low-power microcontrollers and sensors. Contactless epidermal sensors based on battery-less Near Field Communications (NFC) [7.46] integrated into textile has been recently investigated in [7.43]. This approach solves the requirement of a specific reader because a mobile with NFC can be used as a reader, but the read range is limited to few centimeters and gives the measurement of the shell temperature instead of the core temperature. Therefore, the accuracy and the utility for screening depend on the site where the tag is attached. When the tag is in the armpit can be accurate but it is not very practical for automatic screening applications.

The system proposed in this chapter has the advantages of embedding the core temperature sensor in a face mask as well as being fully automatic. On the other hand, the estimation of the relative location can be measured using low-cost infrastructure based on commercial LoRa transceivers. Therefore, an expensive reader and the installation of additional wearable devices are not required. The communication based on backscattering extends battery lifetime. The main drawback is the low data rate due to the mechanism based on backscattering of LoRa packed that avoids the use of custom readers (eg. SDR receivers). Therefore, for screening applications, basic information can be sent to avoid the amount of data (eg. few bits to encode the temperature level, a bit to indicate the correct mask installation, a bit to indicate the usage time of the mask, and few bits to encode the breathing rate). The cost of the mask electronics is on the order of 5€ and a reusable future commercial device can

UNIVERSITAT ROVIRA I VIRGILI
LONG-RANGE BACKSCATTERING COMMUNICATIONS FOR NEXT GENERATION IOT APPLICATIONS
Marc Lázaro Martí

be designed, changing the contaminated mask after use.

7.5 Conclusion

This chapter has proposed a system (addressed as smart mask) for long-range non-invasive wireless core body temperature and breath rate monitoring. It takes advantage of the mandatory use of the face mask in the interiors during pandemics to integrate into it a temperature and breath rate monitoring system without requiring the use of another wearable (bracelet or headband). The implementation of a body temperature and breath control of people using face mask on a door is proposed in order to prevent entering persons with covid19-compatible symptoms. In addition, it can be detected if the person is located inside or outside the control point and its moving direction (if enters or exits) in order to implement a people counter and an occupant registration.

The system relies on backscatter communication as an alternative to other wireless communication system such as a Bluetooth. The latter sometimes requires to authenticate and also some infrastructure to estimate the location using proximity beacons (eg. the location sensors and smartphones). The proposed backscattering system is implemented using low-cost LoRa devices. The high sensitivity of LoRa receivers allows for the detection and collection of information at enough range distance (a few meters). A proof-of-concept prototype has been designed, which detects the core temperature by means of a dual-heat-flux sensor and breath rate by means of measuring the exhaled temperature flow using an NTC. The core temperature sensor output has been compared to the measurement of the temperature in the armpit, obtaining a small difference in the accuracy, but it is enough for non-contact and autonomous screening applications. In addition, the multiple temperature measurements and the breathing rate estimation allow for both verifying correct face mask placement and usage time, avoiding the use of complex identification systems based on cameras and on computer vision. The smart mask also allows for the detection of coughing episodes from the sudden increase in thermistor temperature.

Other sensors could be integrated into smart masks, especially those used in industrial environments that are characterized by their larger size. Consequently, sensors such as those used to detect the presence of toxic gases (eg carbon monoxide or flammable gases) could be added to smart face masks. The transmission rate of the system is limited by the time between LoRa packets. Therefore, the amount of information to transfer is limited. To overcome this issue, in applications where the sensor can be applied to monitor the temperature or breathing during large periods, data can be saved in the memory of the microcontroller and downloaded later for processing. On the other hand, other wireless transmission systems such as Bluetooth Low Energy (BLE) can be employed to transfer the data.

7.6 Bibliography

[7.1] Maanak Gupta, Mahmoud Abdelsalam, and Sudip Mittal. Enabling and enforcing social distancing measures using smart city and its infrastructures: a COVID-19 Use case. *arXiv preprint arXiv:2004.09246*, 2020.

[7.2] M. Shamim Kaiser, Mufti Mahmud, Manan Binth Taj Noor, Nusrat Zerin Zenia, Shamim Al Mamun, K. M. Abir Mahmud, Saiful Azad, V. N. Manjunath Aradhya, Punitha Stephan, Thompson Stephan, Ramani Kannan, Mohammed Hanif, Tamanna Sharmeen, Tianhua Chen, and Amir Hussain. Worksafe: Towards Healthy Workplaces During COVID-19 With an Intelligent Phealth App for Industrial Settings. *IEEE Access*, 9:13814–13828, 2021.

[7.3] Deepti Gupta, Smriti Bhatt, Maanak Gupta, and Ali Saman Tosun. Future smart connected communities to fight covid-19 outbreak. *Internet of Things*, 13:100342, 2021.

[7.4] Partha Pratim Ray. An IR sensor based smart system to approximate core body temperature. *Journal of medical systems*, 41(8):1–10, 2017.

[7.5] Alex Buoite Stella, Paolo Manganotti, Giovanni Furlanis, Agostino Accardo, and Miloš Ajčević. Return to school in the COVID-19 era: considerations for temperature measurement. *Journal of Medical Engineering & Technology*, 44(8):468–471, 2020.

[7.6] Yongliang Cheng, Chunya Wang, Junwen Zhong, Shizhe Lin, Yongjun Xiao, Qize Zhong, Hulin Jiang, Nan Wu, Wenbo Li, Shuwen Chen, et al. Electrospun polyetherimide electret nonwoven for bi-functional smart face mask. *Nano Energy*, 34:562–569, 2017.

[7.7] Noori Kim, Joslyn Lim Jun Wei, John Ying, Haining Zhang, Seung Ki Moon, and Joonphil Choi. A customized smart medical mask for healthcare personnel. In *2020 IEEE International Conference on Industrial Engineering and Engineering Management (IEEM)*, pages 581–585. IEEE, 2020.

[7.8] F Velluzzi, A Fois, AH Dell'osa, F Tocco, AM Bertetto, C Serra, L Melis, U Bertelli, and A Concu. Mechatronic face mask anti covid-19 to remotely record cardiorespiratory variables in farm's workers engaged in jobs at high risk of infection. *International Journal of Mechanics and Control*, pages 61–76, 2021.

[7.9] Rohan Reddy Kalavakonda, Naren Vikram Raj Masna, Anamika Bhuniaroy, Soumyajit Mandal, and Swarup Bhunia. A smart mask for active defense against Coronaviruses and other airborne pathogens. *IEEE Consumer Electronics Magazine*, 10(2):72–79, 2020.

[7.10] Barnali Ghatak, Sanjoy Banerjee, Sk Babar Ali, Rajib Bandyopadhyay, Nityananda Das, Dipankar Mandal, and Bipan Tudu. Design of a Self-powered Smart Mask for COVID-19. *arXiv preprint arXiv:2005.08305*, 2020.

[7.11] Liang Pan, Cong Wang, Haoran Jin, Jie Li, Le Yang, Yuanjin Zheng, Yonggang Wen, Ban Hock Tan, Xian Jun Loh, and Xiaodong Chen. Lab-on-mask for remote respiratory monitoring. *ACS Materials Letters*, 2(9):1178–1181, 2020.

[7.12] Rohan Reddy Kalavakonda, Naren Vikram Raj Masna, Soumyajit Mandal, and Swarup Bhunia. A smart mask for active defense against airborne pathogens. *Scientific Reports*, 11(1):1–9, 2021.

[7.13] Hannah Friederike Fischer, Daniela Wittmann, Alejandro Baucells Costa, Bo Zhou, Gesche Joost, and Paul Lukowicz. Masquare: A Functional Smart Mask Design for Health Monitoring. In *2021 International Symposium on Wearable Computers*, pages 175–178, 2021.

[7.14] Naren Vikram Raj Masna, Rohan Reddy Kalavakonda, Reiner Dizon, and Swarup Bhunia. Smart and Connected Mask for Protection beyond the Pandemic. In *2021 IEEE International Midwest Symposium on Circuits and Systems (MWSCAS)*, pages 676–679. IEEE, 2021.

[7.15] Andrea Fois, Filippo Tocco, Antonio Dell'Osa, Laura Melis, Ugo Bertelli, Alberto Concu, Andrea Manuello Bertetto, and Carmen Serra. Innovative Smart Face Mask to Protect Workers from COVID-19 Infection. In *2021 IEEE International Symposium on Medical Measurements and Applications (MeMeA)*, pages 1–6. IEEE, 2021.

[7.16] Joana C Prata, Ana LP Silva, Tony R Walker, Armando C Duarte, and Teresa Rocha-Santos. COVID-19 pandemic repercussions on the use and management of plastics. *Environmental Science & Technology*, 54(13):7760–7765, 2020.

[7.17] AH Ilsley, AJ Rutten, and WB Runciman. An evaluation of body temperature measurement. *Anaesthesia and intensive care*, 11(1):31–39, 1983.

[7.18] Paul Fulbrook. Core body temperature measurement: a comparison of axilla, tympanic membrane and pulmonary artery blood temperature. *Intensive and Critical Care Nursing*, 13(5):266–272, 1997.

[7.19] CG Teran, J Torrez-Llanos, TE Teran-Miranda, C Balderrama, NS Shah, and P Villarroel. Clinical accuracy of a non-contact infrared skin thermometer in paediatric practice. *Child: care, health and development*, 38(4):471–476, 2012.

[7.20] Shuanglong Cui, Bojun Sun, and Xiaogang Sun. A method for improving temperature measurement accuracy on an infrared thermometer for the ambient temperature field. *Review of Scientific Instruments*, 91(5):054903, 2020.

[7.21] Adrian Shajkofci. Correction of human forehead temperature variations measured by non-contact infrared thermometer. *IEEE Sensors Journal*, 2021.

[7.22] Nicholas Wei-Jie Goh, Jun-Jie Poh, Joshua Yi Yeo, Benjamin Jun-Jie Aw, Szu Cheng Lai, Jayce Jian Wei Cheng, Christina Yuan Ling Tan, and Samuel Ken-En Gan. Design and Development of a Low Cost, Non-Contact Infrared Thermometer with Range Compensation. *Sensors*, 21(11):3817, 2021.

[7.23] Hanns-Christian Gunga, Mariann Sandsund, Randi E. Reinertsen, Frank Sattler, and Jochim Koch. A non-invasive device to continuously determine heat strain in humans. *Journal of Thermal Biology*, 33(5):297–307, 2008.

[7.24] Kei-Ichiro Kitamura, Xin Zhu, Wenxi Chen, and Tetsu Nemoto. Development of a new method for the noninvasive measurement of deep body temperature without a heater. *Medical Engineering and Physics*, 32(1):1–6, 2010.

[7.25] Jingjie Feng, Congcong Zhou, Cheng He, Yuan Li, and Xuesong Ye. Development of an improved wearable device for core body temperature monitoring based on the dual heat flux principle. *Physiological measurement*, 38(4):652, 2017.

[7.26] Marco Lazaro, Antonio Lazaro, Ramon Villarino, and David Gibau. Smart mask for temperature monitoring with LoRa backscattering communication. In *2021 International Multidisciplinary Conference on Computer and Energy Science (SpliTech)*, pages 1–3, 2021.

[7.27] Dean J Miller, John V Capodilupo, Michele Lastella, Charli Sargent, Gregory D Roach, Victoria H Lee, and Emily R Capodilupo. Analyzing changes in respiratory rate to predict the risk of COVID-19 infection. *PLoS One*, 15(12):e0243693, 2020.

[7.28] Xiaojiang Xu, Anthony J Karis, Mark J Buller, and William R Santee. Relationship between core temperature, skin temperature, and heat flux during exercise in heat. *European journal of applied physiology*, 113(9):2381–2389, 2013.

[7.29] John S Steinhart and Stanley R Hart. Calibration curves for thermistors. *Deep sea research and oceanographic abstracts*, 15(4):497–503, 1968.

[7.30] Stefano Milici, Antonio Lázaro, Ramon Villarino, David Girbau, and Marco Magnarosa. Wireless Wearable Magnetometer-Based Sensor for Sleep Quality Monitoring. *IEEE Sensors Journal*, 18(5):2145–2152, 2018.

[7.31] Stefano Milici, Javier Lorenzo, Antonio Lázaro, Ramon Villarino, and David Girbau. Wireless Breathing Sensor Based on Wearable Modulated Frequency Selective Surface. *IEEE Sensors Journal*, 17(5):1285–1292, 2017.

[7.32] T Nemoto and T Togawa. Improved probe for a deep body thermometer. *Medical and Biological Engineering and Computing*, 26(4):456–459, 1988.

[7.33] Cassio Bento Andrade and Roger Pierre Fabris Hoefel. IEEE 802.11 WLANs: A comparison on indoor coverage models. In *CCECE 2010*, pages 1–6. IEEE, 2010.

[7.34] HA Obeidat, Rameez Asif, NT Ali, YA Dama, OA Obeidat, SMR Jones, WS Shuaieb, Mohammed A Al-Sadoon, KW Hameed, AA Alabdullah, et al. An indoor path loss prediction model using wall correction factors for wireless local area network and 5G indoor networks. *Radio Science*, 53(4):544–564, 2018.

[7.35] Shu-Hua Lu and Yu-Tzu Dai. Normal body temperature and the effects of age, sex, ambient temperature and body mass index on normal oral temperature: a prospective, comparative study. *International journal of nursing studies*, 46(5):661–668, 2009.

[7.36] J-Y Lefrant, L Muller, J Emmanuel de La Coussaye, M Benbabaali, C Lebris, N Zeitoun, C Mari, G Saissi, J Ripart, and J-J Eledjam. Temperature measurement in intensive care patients: comparison of urinary bladder, oesophageal, rectal, axillary, and inguinal methods versus pulmonary artery core method. *Intensive care medicine*, 29(3):414–418, 2003.

[7.37] Michiaki Yamakage and Akiyoshi Namiki. Deep temperature monitoring using a zero-heat-flow method. *Journal of Anesthesia*, 17(2):108–115, 2003.

[7.38] Carolina Miozzi, Sara Amendola, A Bergamini, and Gaetano Marrocco. Reliability of a re-usable wireless Epidermal temperature sensor in real conditions. In *2017 IEEE 14th International Conference on Wearable and Implantable Body Sensor Networks (BSN)*, pages 95–98. IEEE, 2017.

[7.39] Francesca Camera, Carolina Miozzi, Francesco Amato, Cecilia Occhiuzzi, and Gaetano Marrocco. Experimental assessment of wireless monitoring of Axilla temperature by means of epidermal battery-less rfid sensors. *IEEE Sensors Letters*, 4(11):1–4, 2020.

[7.40] Carolina Miozzi, Francesco Amato, and Gaetano Marrocco. Performance and durability of thread antennas as stretchable epidermal UHF RFID tags. *IEEE Journal of Radio Frequency Identification*, 4(4):398–405, 2020.

[7.41] C Occhiuzzi, S Parrella, and G Marrocco. Flexible Dual chip on-skin RFID Sensor for Body Temperature Monitoring. In *2020 IEEE International Conference on Flexible and Printable Sensors and Systems (FLEPS)*, pages 1–4. IEEE, 2020.

[7.42] Ming Huang, Toshiyo Tamura, Takumi Yoshimura, Tadahiro Tsuchikawa, and Shigehiko Kanaya. Wearable deep body thermometers and their uses in continuous monitoring for daily healthcare. In *2016 38th Annual International Conference of the IEEE Engineering in Medicine and Biology Society (EMBC)*, pages 177–180, 2016.

[7.43] Yutong Jiang, Kewen Pan, Ting Leng, and Zhirun Hu. Smart textile integrated wireless powered near field communication body temperature and sweat sensing system. *IEEE Journal of Electromagnetics, RF and Microwaves in Medicine and Biology*, 4(3):164–170, 2019.

[7.44] RH Fox, AJ Solman, R Isaacs, AJ Fry, and IC MacDonald. A new method for monitoring deep body temperature from the skin surface. *Clinical Science and Molecular Medicine*, 44(1):81–86, 1973.

[7.45] Hsuan-Yu Chen, Andrew Chen, and Chiachung Chen. Investigation of the impact of infrared sensors on core body temperature monitoring by comparing measurement sites. *Sensors*, 20(10):2885, 2020.

[7.46] Antonio Lazaro, Ramon Villarino, and David Girbau. A survey of NFC sensors based on energy harvesting for IoT applications. *Sensors*, 18(11):3746, 2018.

Chapter 8

General Conclusion

This doctoral thesis has studied the design and implementation of low-power long-range wireless communications using LoRa backscattering. Work has been conducted on both system implementation and application viability analysis for three different fields, contributing to bringing this technology closer to the commercial sector.

Research on backscattering tag front-end design has been carried out. Conventional load-modulated front-end has been compared with a reflection amplifier front-end, showing the increase in the backscattered power, at expenses of higher power consumption. It is worth noting that the power consumption has remained in the μA range, keeping in alignment with the purpose of this thesis. The two most relevant reflection amplifier topologies available in the literature have been implemented using a tunnel diode and a bipolar transistor, both enhancing the radar cross-section of the tag. Although the tunnel diode exhibited a higher individual gain-consumption efficiency, its biasing point poses a challenge for its integration within a tag, since it requires power conversion to interface it with the minimum operation voltage of the digital unit. Therefore, is concluded that, despite the more modest individual behavior, the transistor-based reflection amplifier is more efficient within a full integration context, since it does not require bias voltage conditioning.

After having studied the integration of these amplifiers in backscattering tags, several challenges arise regarding efficiency and operation. The input power dependence of the reflection amplifier makes it susceptible to oscillation when is biased close to the unstable region. Therefore, under specific conditions

UNIVERSITAT ROVIRA I VIRGILI
LONG-RANGE BACKSCATTERING COMMUNICATIONS FOR NEXT GENERATION IOT APPLICATIONS
Marc Lázaro Martí

oscillation may occur, interfering with or completely disrupting the communication of other tags operating in the same frequency band. Additionally, maintaining the reflection amplifier continuously powered is not an efficient practice. In this thesis the integration of a current sensor in the supply line of the reflection amplifier to actively control it, turning it off when the input power exceeds a specific threshold, is proposed. This approach prevents tag oscillation and significantly prolongs battery life.

Tag up-link communication has been implemented by means of two different modulation schemes: a LoRa-packet OOK modulation and a novel down-chirp modulation. The proposed LoRa-packet OOK modulation stands out by its compatibility with commercial-of-the-shelf LoRa transceivers, making the implementation cheap and simple. However, the LoRa packets limit the maximum data-rate to a few bits per second, posing a problem for high data-rate demanding applications. On the other hand, a novel modulation based on down chirps has been proposed, leveraging the inherent gain of LoRa modulation and exhibiting a more efficient use of spectrum. Additionally, a DSSS technique based on a Barker sequence has been implemented, providing an extra processing gain to the proposed modulation. The main disadvantage is that it requires a dedicated receiver to demodulate the signal. Employing an SDR to demodulate the backscatter signal makes the system less attractive but removes the LoRa packet constraint, allowing higher data-rate modulations. Further work exploring the limits of the proposed modulation, both in terms of data-rate and communication range as a function of the power drawn could be carried out.

The communication through backscattering of LoRa packets has been validated with the implementation of three different applications. First, a low-resolution localization system based on the backscattered LoRa packets received signal strength has been successfully implemented. The main advantage that brings this approach is the low power consumption of the tag and the low cost of the overall implementation. Additionally, the system has been enhanced with machine learning techniques, further increasing its reliability. Simulated and experimental results have been provided, and several machine learning algorithms have been compared, showing the individual performance for each of them. Second, the proposed LoRa backscattering communication has been studied for the design of a deep implant. The most significant contribution of this part has been to prove that backscattering communication can operate perfectly even under high attenuation caused by the body's tissues. Despite that, the final design of an implant requires evaluating additional aspects, such as the biocompatibility of the coating and evaluation under more realistic conditions, the LoRa backscattering communication has been proved to operate under the conditions of an implanted device. Lastly, a smart mask capable of measuring body temperature and monitoring respiration, two crucial indicators during the COVID pandemic, has been designed. The wireless communication and a system to determine the users entering and exiting a building have been implemented with the proposed LoRa backscattering technique. With these three applications, the viability of LoRa backscattering modulations has been demonstrated, bringing it closer to future commercial applications.

To conclude the thesis, it is worth mentioning that the research conducted in the field of backscattering communications is extensive, with high-quality contributions constantly emerging in the literature. Unfortunately, in the commercial field, backscattering techniques remain confined to RFID technology. The reason for this is that despite scientific efforts to address and improve the individual aspects of backscattering systems, the lack of standardization in the field poses a barrier to further advancement. Therefore, the next objective within the field of backscattering should be the design of a backscattering development platform with standardized communication protocols compatible with the major wireless technologies: WiFi, Bluetooth, and LoRa. This should be the next goal in backscattering communications and the focus of future work.